UNIVERSITÀ DEGLI STUDI DI PALERMO
Dottorato di Ricerca in Ingegneria Civile, Ambientale, dei Materiali
Indirizzo: Ingegneria strutturale e geotecnica
Dipartimento di Ingegneria
Settore Scientifico Disciplinare – ICAR 09

Design of innovative friction damper devices for earthquake-resilient RC frames with Hybrid Steel-Trussed Concrete Beams

IL CANDIDATO
Ing. Salvatore Pagnotta

IL COORDINATORE
Chiar.mo Prof. Ing. Antonina Pirrotta

Il TUTOR
Chiar.mo Prof. Ing. Piero Colajanni

CO-TUTOR
Dott. Ing. Alessia Monaco

CICLO XXXIII

A Silvia
Per la pazienza e l'incoraggiamento

Ai miei genitori
Per il continuo supporto

ACKNOWLEDGEMENTS

This thesis represents the result of a long-wanted journey, which widened my horizon above all my expectations.

I would like to thank several people met during this journey which have considerably contributed to my personal and professional growth.

My first and most felt acknowledgement is dedicated to my advisor, Prof. Piero Colajanni, for his unwavering support and relentless guidance throughout these years. I would like to thank him for all the time dedicated to me, which has contributed significantly to realize my life dream of becoming a structural engineer.

I am thankful to my co-tutor, Dr. Alessia Monaco, for her helpful contribution in the development of the research topic.

I want to thank also Prof. Lidia La Mendola for her active participation to my research.

Acknowledgements are due to Prof. Gianvittorio Rizzano and Dr. Massimo Latour for the fruitful research period spent at the University of Salerno.

Moreover, I am grateful to Prof. George C. Clifton and Dr. Shahab Ramhormozian for having given me the opportunity to join to their research group at the University of Auckland and Auckland University of Technology.

I would like to thank Dr. Mauro Scurria and Eng. Nicola Cancelliere for the useful discussions during the development of the innovative solutions proposed.

A special thank goes also to Marco Ferrotto, the profound friendship with him has been of great support all over these years.

A heartfelt thought goes to my colleagues Francesco, Giovanni, Gabriele, Fabio, Maria, Bharat, Vincenzo, for the unforgettable moments spent together.

I will not thank enough my parents, for being there ready to share every little detail of my work. This research would have been much more arduous without their constant help.

Last but not least, from the bottom of my heart I would like to thank the love of my life, Silvia, for always being by my side during all the challenges encountered throughout the years spent together.

RINGRAZIAMENTI

Questa tesi rappresenta il risultato di un percorso profondamente voluto, che ha allargato i miei orizzonti al di sopra di ogni aspettativa.

Vorrei ringraziare diverse persone incontrate durante questo viaggio che hanno notevolmente contribuito alla mia crescita personale e professionale.

Il mio primo e più sentito riconoscimento è rivolto al mio relatore, Prof. Piero Colajanni, per il suo incrollabile sostegno e la sua instancabile guida in questi anni. Lo ringrazio per tutto il tempo a me dedicato, che ha contribuito in modo significativo a realizzare il sogno della mia vita di diventare un ingegnere strutturista.

Sono grato alla mia co-tutor, Ing. Alessia Monaco, per il suo utile contributo allo sviluppo del tema oggetto della ricerca.

Ringrazio anche la Prof.ssa Lidia La Mendola per la sua attiva partecipazione alla mia ricerca.

Un sentito ringraziamento va anche al Prof. Gianvittorio Rizzano e all'Ing. Massimo Latour per il proficuo periodo di ricerca trascorso presso l'Università degli Studi di Salerno.

Sono inoltre grato al Prof. George Clifton e all'Ing. Shahab Ramhormozian per avermi dato l'opportunità di unirmi al loro gruppo di ricerca presso la *University of Auckland* e la *Auckland University of Technology*.

Ringrazio il Dott. Mauro Scurria e l'Ing. Nicola Cancelliere per le utili riflessioni durante lo sviluppo delle soluzioni innovative proposte.

Un ringraziamento particolare è rivolto a Marco Ferrotto, la cui profonda amicizia è stata di grande sostegno in tutti questi anni.

Un affettuoso pensiero va ai miei colleghi Francesco, Giovanni, Gabriele, Fabio, Maria, Bharat, Vincenzo, per gli indimenticabili momenti trascorsi insieme.

Non ringrazierò mai abbastanza i miei genitori, per essere stati sempre lì pronti a condividere ogni piccolo dettaglio del mio lavoro. Questa ricerca sarebbe stata molto più ardua senza il loro costante aiuto.

Infine, dal profondo del cuore vorrei ringraziare l'amore della mia vita, Silvia, per essere sempre stata al mio fianco durante tutte le sfide affrontate negli anni trascorsi insieme.

ABSTRACT

This thesis focuses on the design of innovative friction damper devices for earthquake-resilient Reinforced Concrete (RC) frames realized with Hybrid Steel-Trussed Concrete Beams (HSTCBs). These devices fall within the framework of the recently-proposed low-damage design strategy for structures built in earthquake-prone areas, on the basis of which the structures are designed to experience negligible damage when subjected to seismic events. The comprehensive solution proposed aims at introducing a feasible option for building earthquake-resilient RC Moment Resisting Frames (MRFs), having been proposed very few solutions for this structural scheme so far. Innovative solutions are proposed for both Beam-to-Column (BCC) and Column-to-Foundation (CFC) connections. For each connection, an analytical design procedure is proposed, and a 3D FEM model is developed and tested.

The capability of the proposed connections in ensuring earthquake-resilient RC frames is assessed by comparing the seismic performance of traditional and innovative RC frames realized with HSTCBs.

As a background to research on dissipative friction connections for MRFs with HSTC beams, two issues affecting the latter structural typology are investigated, namely shear capacity assessment and mechanical performance of HSTCB-column joints. With regard to the former issue, a design-oriented analytical model based on the truss mechanism with variable inclination of the concrete strut is proposed. Concerning the other issue, an approach is derived for the application, in FE software packages, of an-already-existing macro model developed to simulate the cyclic behavior of RC beam-column joints, extending it to the case of HSTC beams.

“Quelli che s’innamorano di pratica sanza scienzia
son come ‘l nocchier ch’entra in navilio senza timone o bussola,
che mai ha certezza dove si vada”

Leonardo da Vinci, Trattato della Pittura

TABLE OF CONTENTS

LIST OF NOTATIONS AND ABBREVIATIONS

A_{PBC}	Cross-sectional area of a PerfoBond Connector
A_b	Rebar cross-sectional area
A_{res}	Resisting area of bolt
A'_s	Cross-sectional area of the top longitudinal reinforcement
A_s	Cross-sectional area of the bottom longitudinal reinforcement
A_{sw}	Cross-sectional area of the web bars
A_{tw1}	Cross-sectional area of the first order of transverse reinforcement
A_{tw2}	Cross-sectional area of the second order of transverse reinforcement
AFC	Asymmetric Friction Connection
B_f	Distance between axis of the friction device oriented along the strong axis and the column face
B_h	Horizontal component of the amplified sliding force of the friction connection
B_{sc}	Distance between axis of the self-centring system oriented along the strong and the column face
B_v	Vertical component of the amplified sliding force of the friction connection
B_v	Sliding force of the friction connection
CDP	Concrete Damage Plasticity
CLT	Cross Laminated Timber
DDSTC	Dissipative Double Split Tee Connection
E_h	Strain hardening modulus of steel
E_{eq}	Equivalent elastic modulus of the stack of disc springs
E_{tb}	Elastic modulus of the steel of threaded bars
F_{PBC}	Shear resistance of a PerfoBond Connector
F_d	Sliding force of the friction connection
F_{pc}	Preloading force acting on the bolt
F_{sc}	Applied preload of each threaded bar
G_F	Fracture energy of concrete
GHM	Gen_Hyst Model
H_f	Distance between axis of the friction device oriented along the

	strong axis and the column face
H_{sc}	Distance between axis of the self-centring system oriented along the strong and the column face
HSTCB	Hybrid Steel-Trussed Concrete Beam
K_{ds}	Global stiffness of the stack of disc springs
K_{tb}	Axial stiffness of the threaded bar
K_y	Rotational elastic stiffness of the bar-slip mechanism
K_θ	Rotational stiffness of the column base connection
$M(x)$	Bending moment acting on the beam related to the x axis
$M_{Ed,PBC,hog}$	Design bending moment of the PerfoBond Connector in the case of hogging moment
$M_{Ed,PBC,sag}$	Design bending moment of the PerfoBond Connector in the case of sagging moment
M_b	Moment strength provided by the friction forces acting at the spherical bearing
M_{cr}	Bending moment at concrete cracking
M_d	Design bending moment of the friction connection
M_f	Moment strength provided by the friction devices
M_{sc}	Moment strength provided by the sel-centring system
M_y	Yielding bending moment
M_u	Ultimate bending moment
M_0	Decompression moment
$M_{0,af}$	Moment capacity provided by the axial force
$M_{1,w}$	Moment capacity provided by the web friction pads
MRF	Moment Resisting Frame
N	Axial force
O	Centre of rotation
PAI	Park and Ang damage Index
PBC	PerfoBond Connector
PC	Prestressed/precast Concrete
PHM	Polygonal Hysteretic Model
R	Radius of curvature of the spherical cap and the concave bearing
RC	Reinforced Concrete
RSBC	Rotational Slotted Bolted Connection
RSFJ	Resilient Slip Friction Joint
SAFC	Column base connection with AFC oriented along the strong axis
SCSHJ	Self-centring Sliding Hinge Joint
SHJAFC	Sliding Hinge Joint with Asymmetric Friction Connection
T	Tensile force acting on the horizontal chord

T_b	Tensile force acting on the bottom longitudinal bars
T_p	Tensile force acting on the bottom plate of the HSTCB
T_w	Dowel action provided by the inclined web rebar
$V_c(x)$	Shear force acting on the beam related to the axis
V_{cr}	Shear force at the concrete cracking
V_{hog}	Shear force due to hogging moment
V_{sag}	Shear force due to sagging moment
V_y	Shear force at the peak strength
WAFC	Column base connection with AFC oriented along the weak axis
a	Shear span
b_w	Cross-section minimum web width
d	Effective depth of the beam or column
d_b	Nominal rebar diameter
f_c	Compressive strength of concrete
f_{cd}	Design compressive strength of concrete
f'_{cd}	Design reduced compressive strength of concrete
f_s	Bar stress at the concrete core perimeter
f_{ub}	Ultimate strength of steel of preloaded bolts
f_y	Yielding stress of steel
f_{yd}	Design tensile strength of steel
f_{yb}	Yielding stress of the bottom longitudinal bars
f_{yp}	Yielding stress of the bottom plate of the HSTCB
f_{yw}	Yielding stress of the transverse reinforcement
h	Cross-sectional height
h_{stack}	Height of the stack of disc springs
h_{str}	Total height of the building
h_0	Conical disc height
$j_o(x)$	Coefficient to calculate the internal lever arm of the beam related to the axis
k_s	Coefficient that depends on the shape of the slotted hole
l_e	Rebar segment whose stresses are below the yield value
l_y	Rebar segment whose stresses are beyond the yield value
n_b	Number of bolts of the friction connection
n_{fb}	Number of bolts of the flange friction connection
n_{fs}	Number of surfaces in contact on which the friction forces are generated with reference to the web friction device
n_{par}	Number of springs stacked in parallel
n_s	Number of surfaces in contact on which the friction forces are generated

n_{ser}	Number of springs stacked in series
n_{tb}	Number of threaded bars for self-centring column base connections
n_w	Number of inclined web bars
n_{wb}	Number of bolts of the web friction connection
n_{ws}	Number of surfaces in contact on which the friction forces are generated with reference to the web friction device
r_f	Ratio between the effective and maximum clamping force calculated according to EN 1993:1-8, acting on the bolts employed in the flange friction pads
r_{tb}	Ratio between the effective and maximum clamping force calculated according to EN 1993:1-8, acting on the threaded bars
r_w	Ratio between the effective and maximum clamping force calculated according to EN 1993:1-8, acting on the bolts employed in the web friction pads
s_{tw1}	Spacing of the first order of transverse reinforcement
s_{tw2}	Spacing of the second order of transverse reinforcement
s_y	Slip at yielding of the longitudinal reinforcement
s_u	Ultimate slip of the longitudinal reinforcement
t_s	Ratio between the effective and the code-consistent preload applied to the bolt
v	Non-dimensional shear strength
x_c	Neutral axis
z	Internal lever arm, equal to 0.9 d
$z_{1,2,3}$	Internal lever arm of the beam-to-column friction connection
$\Phi(\varphi_0)$	Parameter depending on the bearing geometry
Ω_μ	Overstrength factor
α_1	Angle of inclination, with respect to the beam axis, of the first order of transverse reinforcement
α_2	Angle of inclination, with respect to the beam axis, of the second order of transverse reinforcement
γ	Slip parameter for PHM and GHM
γ_{M2}	Safety factor for bolted connections
γ_{M3}	Safety factor for friction connections
δ	Stiffness degradation for PHM and GHM
δ_{sc}	Deflection of the stack of disc springs
ε_{eq}	Equivalent longitudinal strain at the maximum allowable deflection

θ	Slope of the web concrete stress field
$\theta_{c,1,2,3}$	Rotation demand at the beam ends
θ_y	Yield rotation of the connection
θ_u	Ultimate rotation of the connection
μ	Friction coefficient
μ_b	Friction coefficient acting on the spherical bearing
μ_c	Friction coefficient acting on the beam ends
ν'	Coefficient to be applied to the compressive strength of concrete f_c to take into account the biaxial stress state
$\tilde{\sigma}_{cw}$	Non-dimensional stress of the web concrete
$\tilde{\sigma}_{lw}$	Non-dimensional stress of the web longitudinal reinforcement
$\tilde{\sigma}_{tw1}$	Non-dimensional stress of the first order of transverse reinforcement
$\tilde{\sigma}_{tw2}$	Non-dimensional stress of the second order of transverse reinforcement
τ_E	Bond stress in case of elastic steel
τ_Y	Bond stress in case of yielded steel
ϕ_{cr}	Rotation at concrete cracking
ϕ_y	Rotation at yielding
φ_0	Angle complementary to the zenith angle
ω_{lw}	Mechanical ratio of the web longitudinal reinforcement
ω'_s	Mechanical ratio of the top longitudinal reinforcement
ω_s	Mechanical ratio of the bottom longitudinal reinforcement
ω_{tw1}	Mechanical ratio of the first order of transverse reinforcement
ω_{tw2}	Mechanical ratio of the second order of transverse reinforcement

CHAPTER 1

INTRODUCTION

1.1 Background and motivation

The most used approach for the design of earthquake-resistant structures is based on the *capacity design* concept. This design technique involves the identification of structural members, belonging to the structural system, which are required to dissipate the seismic energy. In ordinary Reinforced Concrete (RC) frames, this task is entrusted to the formation of plastic hinges at beam end sections, adequately designed to obtain the required strength, ductility and dissipative capacity.

The success of the above design approach lies in its capability of providing economic and performing structural systems. Nevertheless, several seismic events that have hit different highly-seismic areas all over the world during the last years (e.g. Northridge, 1994; Christchurch, New Zealand, 2011), have shown all the inherent drawbacks of the *capacity design* as it has been used so far. As a matter of fact, many buildings designed according to the most recent methodologies and codes, resisted well to the mainshock-aftershocks sequence. However, they experienced an amount of damage both on structural and non-structural components, such as to make it economically convenient to demolish and rebuild the whole building rather than to repair it (Pampanin 2015). Furthermore, in the case of seismic events of reduced intensity, the minor damage that is often recorded in buildings requires repairs that hinder an immediate occupancy of the structure in the aftermath of the earthquake, resulting in an additional source of economic loss. In addition, seismic-damaged buildings often represent a source of danger for the areas surrounding them, for which public authorities use to forbid the fruition of these areas until the buildings are repaired or demolished. These aspects negatively affect the activities of an earthquake-hit community usually for a long period of time after the end of the mainshock-aftershock sequence.

All the above said, traditional Moment Resisting Frames (MRFs), based on a “high damage” concept, prove environmentally, economically and

socially unsustainable in areas with high-rate of seismic events.

Within this framework, a new design philosophy has been gaining in popularity in earthquake-prone areas over the last few decades, aimed at guaranteeing that the structure experiences negligible damage even after large earthquakes (Takagi and Wada 2019). This behaviour can be achieved by placing in appropriate positions of the structure energy-dissipating devices (e.g. yielding, friction, viscoelastic, viscous) able to absorb the seismic energy and thus preserving the primary structural members from damage. These devices, as well as the structures endowed with them, are defined as *innovative*, because they aim to overcome the above-described shortcomings which characterize the *traditional* structures and their connections. This new approach answers the need expressed by stakeholders to have buildings that experience minor or no damage during the mainshocks, and subsequent aftershocks, in order to be operative as soon as possible after the seismic sequence.

In this context, focusing the attention on solutions based on friction developed for MRFs, several research groups proposed different devices to be used at the Beam-to-Column Connection (e.g. Khoo et al. 2015; Latour, Piluso, and Rizzano 2015, 2018; Latour et al. 2018; Ramhormozian et al. 2018). The main goal of these devices is to dissipate seismic energy by exploiting friction forces generated through sliding of plates made with several materials (e.g.: coated steel, polymer, composite) and clamped together by means of preloaded bolts (Khoo et al. 2012a; Latour, Piluso, and Rizzano 2014; Tsampras et al. 2016).

However, two main drawbacks affect the performance of MRFs having Beam-to-Column Connections (BCCs) realized with Friction Damper Devices (FDDs) only, namely the formation of plastic hinges at the column bases and the large increment of the average residual interstorey drift.

To remedy these defects, MRFs have to be coupled with Column-to-Foundation Connections (CFCs) that combine friction devices and self-centring systems (e.g. preloaded threaded bars with stacks of disc springs) designed to provide a flag-shaped hysteretic response, and thus able to both provide dissipative capacity and reduce structural residual drift ratios (Borzouie et al. 2015, 2016; Freddi, Dimopoulos, and Karavasilis 2017, 2020; Hashemi et al. 2017; Hashemi et al. 2018; Hashemi et al. 2019; Latour et al. 2019).

Several friction device configurations have been developed for steel structures, starting from the pioneering works of Grigorian and Popov (1994) and Yang and Popov (1995). Solutions have also been proposed for timber

structures (Hashemi et al. 2017), while very few studies concern friction devices employed in RC structures (Belleri et al. 2017; Morgen and Kurama 2004; Morgen and Kurama 2008; Song, Guo, and Chen 2014; Tsampras et al. 2018; Zhang et al. 2018).

The reasons why so few solutions were developed for earthquake-resilient RC MRFs are the difficulty to design efficient yet economic damage-proof connections between friction devices and surrounding RC members, particularly in the case of cast-in-situ concrete, and the necessity to modify significantly the construction process introducing specific procedures, which could rise excessively the construction cost making these solutions out of the market.

A structural solution that can be adopted to solve the above shortcomings is the Hybrid Steel-Trussed Concrete Beam (HSTCB). As a matter of fact, among the several existing versions of HSTCBs, those endowed with a bottom steel plate, which make them more similar to structural steel members, can be more easily endowed with a friction device.

HSTCBs are an effective tool for partial industrialization of the construction process of framed RC structures. Thanks to reinforcement formed by a steel truss, HSTCBs are able to cover long spans with small section depths, often contained within the thickness of the slab. However, this characteristic requires the use of a large amount of reinforcement in the beam-column joints, often employing large diameter bars. Thus, both the beam ends and the joint panel become vulnerable to the effects of cyclic actions, like those induced by seismic excitation.

Even if at the beam ends the presence of a properly-designed transverse reinforcement, which provides confinement to the concrete, is usually able to reduce the loss of both stiffness and strength due to cyclic actions, large diameter bars inside a small-sized joint panel cause concrete cracking and damage, inducing a loss of bond. This phenomenon causes degrading hysteresis cycles, which may lead to a reduced structural dissipative capacity (Colajanni et al. 2016).

To prevent this phenomenon, the use of a suitably-designed BCC based on friction, characterized by an increased lever arm of the bending moment transferred between beam and joint, can be considered the appropriate solution to reduce the shear force acting on the joint panel, preventing it from being damaged.

The advantage of the proposed solution lies in the use of HSTCBs endowed with a bottom steel plate, which eases the addition of a friction device.

1.2 Aims

In the light of the foregoing, the present thesis proposes a comprehensive solution for earthquake-resilient RC frames realized with HSTC beams. Innovative friction damper devices for both BCC and CFC will be developed, with the aim of achieving the following properties:

- elastic behaviour up to the yielding moment, which corresponds to the moment value for which friction device(s) start(s) to slide;
- capacity to attain the design ultimate rotation experiencing negligible damage;
- limiting the damage experienced by the connection to specific structural elements, designed to be replaceable;
- avoiding the damaging of the surrounding RC members;
- cyclic response characterized by wide and stable hysteresis loops;

For each connection developed, the following phases will be carried out:

- proposing an analytical formulation for the design of the connection;
- developing a 3D FEM model representative of the connection;
- discussing the numerical results to evaluate the suitability of the connection with respect to the above-mentioned properties.

Once the devices were proposed, the final step of the thesis is to investigated whether the use of such devices is effective in ensuring earthquake-resilient RC frames. To do so, a comparison between the seismic performance of RC frames realized with HSTCBs and endowed or not with the proposed connections is carried out.

With reference to HSTCBs, a study on this structural typology preliminary to its use in the proposed BCCs, have revealed that the shear capacity evaluation and the mechanical performance of HSTCB-column joints are still topics deserving further research efforts. For these reasons, this thesis will investigate these topics as well, with the following aims:

- proposing a design-oriented model for shear strength evaluation of HSTCBs;
- deriving an approach for the application, in FE software packages, of an already-existing macro model developed to simulate the cyclic behaviour of RC beam-column joints, extending it to the case of HSTC beams.

1.3 Outline

An overview of the main characteristics of HSTCBs is reported in Chapter 2, focusing the attention on the shear capacity evaluation and the mechanical performance of HSTCB-column joints.

A state-of-the-art of friction damper devices developed for BCCs and CFCs is reported in Chapter 3. Each solution is commented, highlighting advantages and drawbacks. On the basis of these considerations, a guideline is outlined, which will be used to define the proposed connections.

Chapter 4 presents an analytical model for the evaluation of shear capacity of HSTCBs, that can be used also in the case of RC beams having transverse reinforcement arranged with two different inclinations.

Chapter 5 deals with the definition of a strategy for the use, in FEM analyses, of an already-existing macro model able to reproduce the cyclic response of RC beam-column joints, in the case of HSTC beams.

Chapter 6 proposes three different HSTCB-column friction connections, characterized by an increasing level of both detailing and performance. The first one is characterized by a pin connection and vertical and horizontal slotted holes, the second one is characterized by a T stub connection and curved slotted holes, the third one is characterized by a vertical central plate passing throughout the beam height.

A self-centring connection for the column base section is proposed in Chapter 7, characterized by friction devices, preloaded threaded bars and disc springs. Moreover, a spherical bearing is introduced, so that the axial load acting on the column negligibly affects the moment capacity of the connection.

The comparison between traditional and innovative RC frames realized with HSTCBs is carried out in Chapter 8. Concerning the BCC, one of the solutions proposed in Chapter 6 will be used. As regards the CFC, the connection developed in Chapter 7 will be employed. With reference to the cyclic behaviour of beam-column joints, this will be evaluated as reported in Chapter 5.

Lastly, concluding remarks and recommendations for future research are drawn in Chapter 9, followed by references.

CHAPTER 2

HYBRID STEEL-TRUSSED CONCRETE BEAMS

This chapter focuses on the Hybrid Steel-Trussed Concrete Beams (HSTCBs), describing the main characteristics of this structural typology. The different resisting mechanisms, with respect to ordinary RC beams, are analysed as well. Particular attention is paid to those topics deemed worthy of further studies, such as shear strength and strength of HSTCB-column joint. To shed light on the former, some analytical models able to take into account the peculiarities of HSTCBs are described, in order to better understand how the different resisting mechanisms are interpreted. With regard to the latter, i.e. joint strength, geometrical and mechanical characteristics of RC joints realized with HSTCBs are discussed, focusing on their performance when subjected to cyclic actions.

2.1 Description of the structural typology

The Hybrid Steel-Trussed Concrete Beam (HSTCB) is a structural typology widely used in several areas of the world, such as Southern Europe, Middle East and Latin America. It is constituted by a steel truss encased in a concrete core. The steel truss is realized by a steel plate or a precast prestressed concrete slab, which constitutes the bottom chord, several longitudinal bars positioned in the upper part of the cross-section, representing the top chord, and a group of transverse bars welded to the two chords, constituting the diagonals of the truss. In Figure 2.1 are showed several configurations of the HSTC beams characterized by the following features: the typology of bottom chord, made up of steel plate or precast prestressed concrete slab (a), steel angles (g); truss arrangement, which can be spatial (a, b) or multi-planar (c); dimensions and arrangement of the cross-section with respect to the slab, i.e. slab beam (d, g), regular (downstand) (e) or inverted (upstand) (f); type and arrangement of transverse reinforcement, constituted by V-shaped single inclined bars (h) or by a continuous bar (i), or by a vertical and an inclined bar, subjected to compressive and tensile force, respectively (c). With regard

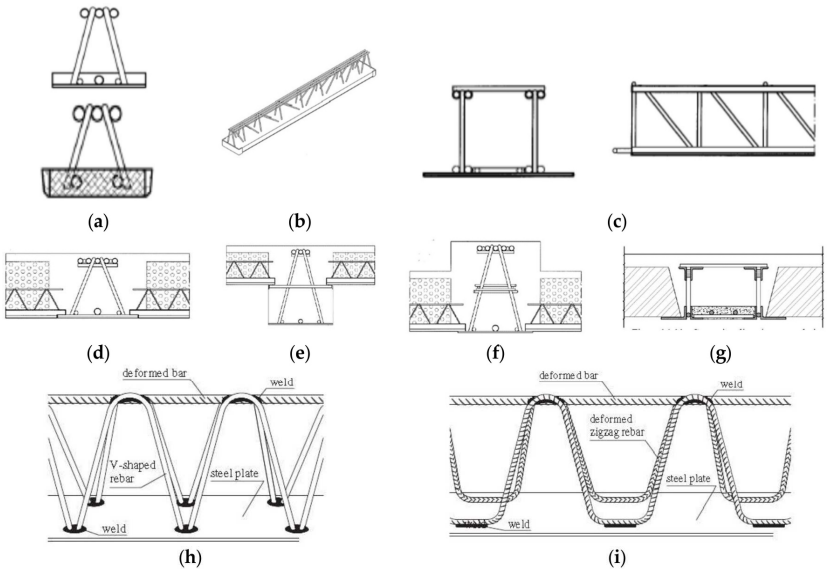

Figure 2.1 HSTC beams characterized by: steel plate or precast prestressed concrete slab (a), spatial truss (b), multi-planar truss (c), slab beam with bottom steel plate (d), regular (downstand) (e), inverted (upstand) (f), slab beam with bottom chord constituted by steel angles (g), transverse reinforcement realized with bent bars having V shape (h), transverse reinforcement made of continuous bent bars (i) (taken from Colajanni et al. 2018a)

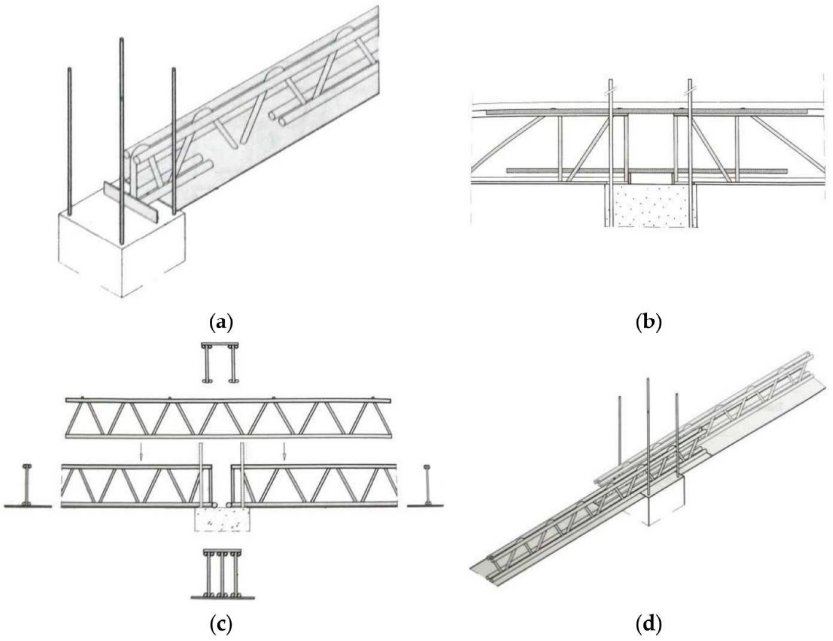

Figure 2.2 Beam-column connections for HSTC beams: bearing constituted by longitudinal bars welded on the top side of the bottom plate and connected by a vertical plate at their end section (a), added top and bottom longitudinal bars (b), added coupled trusses across the joint (c), offset of the truss within the joint (d) (taken from Colajanni et al. 2018a)

to the connection to the column, several solutions have been developed, some of them illustrated in Figure 2.2: bearing constituted by longitudinal bars welded on the top side of the bottom plate and connected by a vertical plate at their end section (a); added top and bottom longitudinal bars (b); added coupled planar trusses across the joint (c); offset of the truss within the joint (d).

Among the several configurations of HSTCBs described above, this thesis focuses on the one constituted by a steel plate on the bottom chord, on which may be welded longitudinal rebars, transverse reinforcement constituted by single inclined bars bent to a V shape and sometimes stirrups also, and top chord realized by at least one longitudinal rebar.

HSTC beams are a convenient structural solution to partially industrialize the construction process, reducing the site operations and the construction costs. Moreover, the capability of covering long spans with reduced cross-section depth eases the architectural layout design.

Three different construction phases characterize the use of HSTCBs:

- *Phase zero*: HSTCB is realized in the workshop and transferred to the construction site;
- *Phase one*: HSTCB is placed in the construction site, and it is subjected to dead and live loads constituted by its own weight, the slab(s), the wet concrete and the construction live load.
- *Phase two*: when the concrete is cured, steel truss and concrete core behave as a single structural member.

Phase one and *Phase two* are illustrated in Figure 2.3. It has to be noted that the HSTC beam should be withstood during the *Phase one* by acrow props, and not directly by the column, in order to avoid contact between the column and the bottom plate, preventing the buckling of the latter when subjected to hogging moment in *Phase Two*. Moreover, for clarity's sake, in Figure 2.3 beams in the orthogonal direction and slabs are not shown.

2.2 Mechanical behaviour of HSTCBs

Over the last two decades, several studies have focused on the mechanical behaviour of HSTCBs during *Phase one* and *Phase two.* As a matter of fact, three main phenomena drives the design of HSTCBs during *Phase one*:

- local buckling of the steel elements constituting the truss;
- lateral-torsional buckling of the whole truss (Vincenzi and Savoia 2010);

- resistance of the welded connections between the diagonal bars and the chords (Colajanni et al. 2013).

With reference to *Phase two*, other aspects need attention, such as those associated to the use of HSTCBs in RC frames sited in seismic areas:

- Assessment of moment and shear strength of the composite beam (Badalamenti 2010; Badalamenti et al. 2010; Campione et al. 2016; Chisari and Amadio 2014; Colajanni et al. 2017c; Monti and Petrone 2015; Tesser and Scotta 2013);
- Stress transfer mechanisms between steel truss and concrete core (Aiello 2008; Cancelliere et al. 2012; Colajanni et al. 2014a, 2015, 2017a, 2018a, 2018b; Monaco 2014; Puhali and Smotlack 1980; Tullini and Minghini 2013);
- Behaviour of beam-column joints (Amadio et al. 2008; Amadio et al. 2011; Colajanni et al. 2016; Ju et al. 2007; Kuramoto et al. 2004);
- Creep deformations (Sassone and Chiorino 2005).

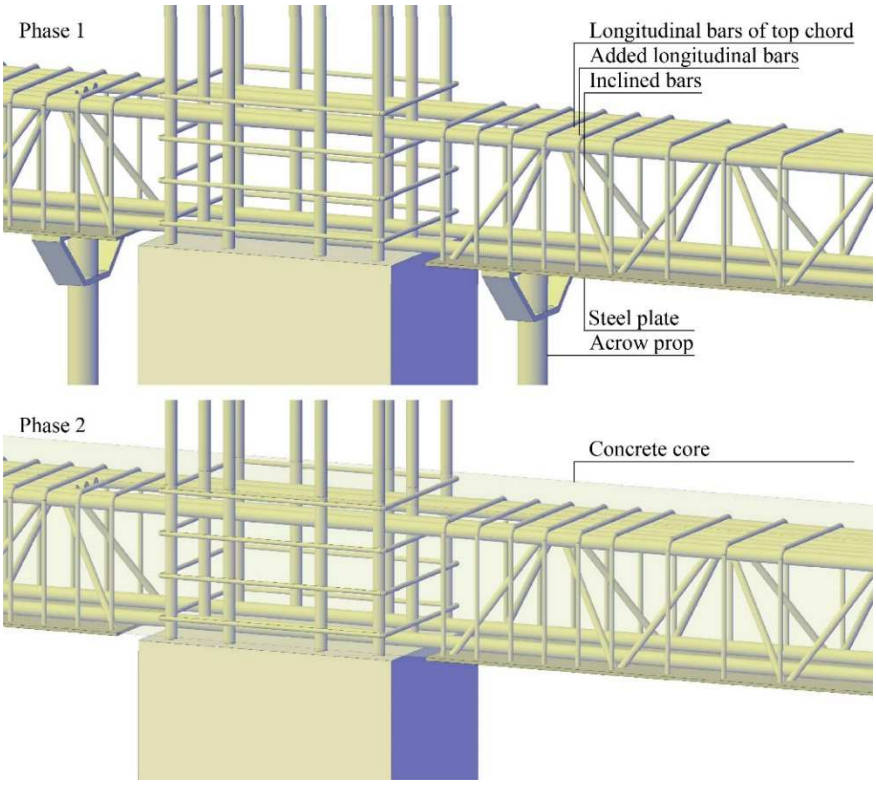

Figure 2.3 Construction phases characterizing the use of HSTC beams

In the following sections, some of the above aspects concerning *Phase two*, that are of greatest interest to the purpose of this research (namely moment, shear and beam-column joint strengths), are described in detail.

2.2.1 Moment strength

Experimental observations

The simultaneous presence of bottom plate, top longitudinal bars and added rebars near beam ends requires a careful evaluation of the contribution of each element to the effective flexural capacity. To this aim, several experimental campaign have been carried out by researchers during the last years, also aiming at assessing the capacity design criteria regarding the overstrength values for flexural and shear strength of the beam itself, of the column and the joint. For example, Colajanni et al. (2015a) tested specimens, represented in Figure 2.4, whose geometrical and mechanical characteristics are representative of slab-thick beam positioned on the first floor of a two-storey residential RC building sited in a seismic area characterized by a Peak Ground Acceleration (PGA) of 0.35 g.

The results showed that, in the absence of specific details to anchor the bottom plate and the longitudinal bars of the truss within the joint, the moment strength of the HSTC beam at the connection with the column is provided only by the longitudinal bars passing through the joint. On the contrary, with regard to the contribution in compression of the steel truss, the results obtained through tests with and without reversed cyclic load gave different indications. As a matter of fact, in the case of tests without load reversal, top chord or bottom plate contribute to increment the ductility of the section, when subjected to compressive forces. On the other hand, these contributions are negligible in the case of reversed cyclic actions, mainly at the top chord, even if it should be ensured by bond between steel and concrete, while smaller

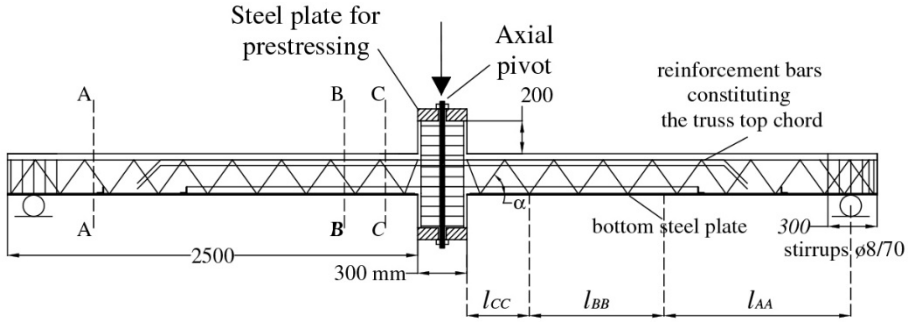

Figure 2.4 Scheme of constraints and load condition of the continuous composites trussed beams subjected to three-point bending tests (taken from Colajanni et al. 2015a)

reduction affects the bottom plate, probably because a portion of these stresses are directly transferred by the contact between bottom plate and column. However, this contact could potentially lead to the buckling of bottom plate.

Interpretation issues

Based on the above findings, to design HSTCBs on the safe side, contact between bottom plate and column should be avoided, while moment strength of beam end section should be assessed by considering added rebars only and neglecting any contribution provided by the truss. By using these assumptions, moment-rotation behaviour of plastic hinges of HSTC beams can be evaluated by means of the common principles used in structural engineering for ordinary RC members (i.e. cross-sections remain planar during bending, tensile strength of concrete is neglected, perfect bond between longitudinal bars and surrounding concrete). When considering the non-linear behaviour of plastic hinges within structural models, both lumped or distributed plasticity models can be used. The former is represented by a zero-length element, usually located at mid-section of plastic hinge length, and whose moment-rotation curve aims at reproducing, in a very simplified yet computationally efficient way, the mechanical behaviour of plastic hinges. The latter (i.e. distributed plasticity model) employs the fibre approach to reproduce the moment-rotation behaviour of cross-section, associating to each fibre a uniaxial stress-strain curve. The mechanical response of cross-section is obtained by integration of the stress-strain curves of all the fibres in which the section was discretized. The paramount advantage of this approach is that it does not require calibration of parameters to reproduce moment-rotation behaviour of structural members subjected to combined biaxial bending moment-axial force. Also, spread of inelasticity through the structural member is not restrained, thus plastic hinges do not have predetermined lengths. This approach leads to more refined results and negligible input required to the user. However, the trade-off is the significant increment of the computational effort, with respect to that required by using the lumped plasticity model. Nevertheless, in the following sections will be adopted the distributed plasticity model to assess the non-linear responses of subassembly (Chapter 5) and frames (Chapter 8).

2.2.2 Shear strength

Experimental observations

Layout of steel truss and its interaction with concrete core, in which is

embedded, makes HSTCBs different from standard RC beams. Thus, several experimental campaigns have been carried out over the last decade focusing on the assessment of their shear strength (e.g. Chisari and Amadio 2014; Colajanni et al. 2017c; Monti and Petrone 2015). Experimental results showed peculiar behaviour and superior performance of HSTCBs, with respect to standard RC beams, thanks to the presence of steel truss with two orders of transverse reinforcement. To better understand shear behaviour of HSTCBs, results described in Colajanni et al. (2017c) are reported here. These Authors tested several HSTCBs constituted by a steel bottom plate, a group of longitudinal bars at the top chord and web components of the truss realized with reversed V-shaped rebars. Five specimens were subjected to three-point bending tests, three of them experiencing sagging moment (i.e. bottom steel plate in tension), the other two hogging moment (i.e. bottom steel plate in compression). Geometrical characteristics and test layout of the specimens are reported in Figure 2.5.

Results showed that, in the case of shear failure caused by crushing of concrete strut, steel truss was still able to provide a residual resisting capacity after the attainment of the peak shear force acting on the beam. Moreover, it was noticed that the bottom steel plate played a critical role in resisting mechanism of HSTCBs to shear force. In fact, in the case of sagging moment, the bottom steel plate separated from concrete core of the beam, contributing to the shear strength acting as a dowel (Figure 2.6a). On the contrary, in the case of hogging moment, the part of bottom steel plate between two consecutive inclined bars buckled due to the compressive force acting on it (Figure 2.6b). This phenomenon was registered because the bottom steel plate was connected to the remaining part of the beam by means of inclined bars only. It should be noticed that, to effectively prevent bottom plate buckling, a group of vertical transverse reinforcement, or a couple of longitudinal bars could be welded to the plate.

Interpretation issues

Reliable interpretation of shear behaviour of HSTCBs able to take into account the above phenomena calls for the development of specific analytical models. As a matter of fact, shear capacity models suggested by European or Italian design code, based on truss mechanism with variable inclination of concrete strut and dedicated to standard RC beams only (i.e. with one order of transverse reinforcement) were demonstrated to be inadequate and too conservative in predicting the shear strength of HSTC beams (Colajanni et al. 2017c; Colajanni et al. 2019). The same Authors demonstrated that the

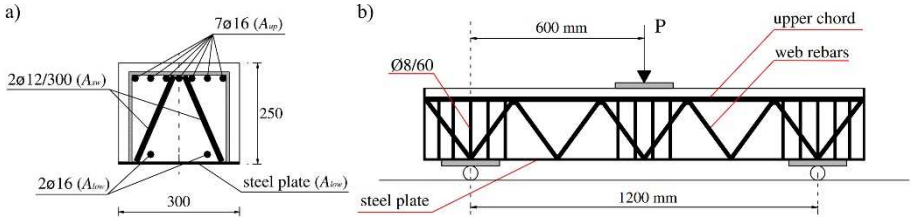

Figure 2.5 Geometrical characteristics and test layout of specimens tested in Monaco (2014) (taken from Monaco 2014)

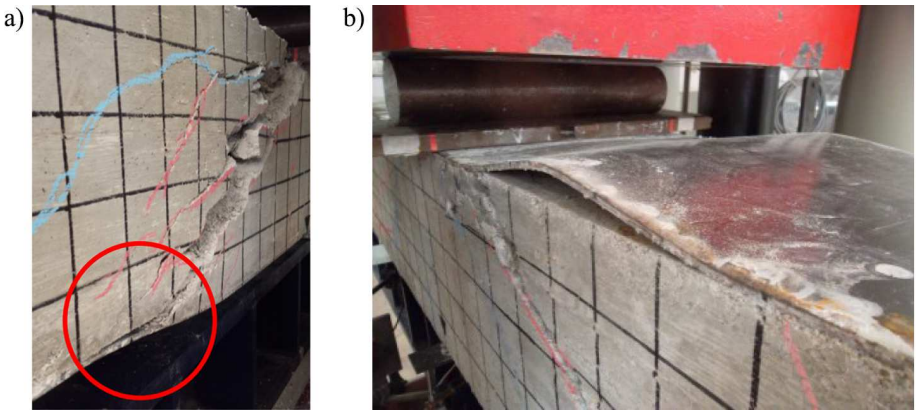

Figure 2.6 Dowel effect (a) and buckling (b) of bottom steel plate (taken from Monaco 2014)

capacity models provided by ACI or CSA, based on the additive approach and, thus, able to consider the second order of transverse reinforcement characterizing HSTCBs, are too conservative as well.

For this reason, during the last decade, several analytical models have been developed to assess the shear strength of HSTC beams. To this aim, in the literature were presented adapted models derived for RC structures and models derived for HSTCBs. With regard to the former, models were formulated which consider two orders of transverse reinforcement. Among these models, three of them, which are considered the most reliable and significant, are described below in order to better understand how the mechanics of these beams can be interpreted.

Campione et al. (2016) model

The model developed by Campione et al. (2016) is based on an additive approach in which the shear strength of HSCTBs is assessed similarly as for standard RC beams, considering the inclined rebars of the truss as the transverse reinforcement of the beam. In addition, the shear contribution provided by the bottom plate of the truss is taken into account. With reference to the shear contribution provided by the concrete, both arch and beam effects

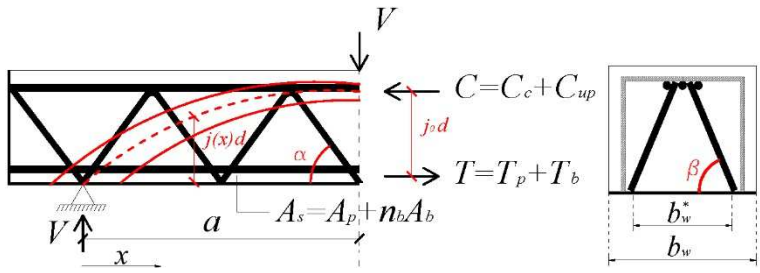

Figure 2.7 Arch and beam effects in the HSTC beam (taken from Colajanni et al. 2019)

are considered, as shown in Figure 2.7.

The compressive force acting on the top chord of the beam C is the sum of the contributions provided by compressed concrete C_c and top longitudinal bars of the truss C_{up}. Similarly, the tensile force acting on the bottom chord of the beam T is the sum of the contributions provided by bottom plate T_p and bottom longitudinal bars T_b, if any. Therefore, the cross-sectional area of the bottom chord is equal to the sum of those provided by bottom plate A_p, and bottom longitudinal bars A_b.

Concerning the beam segment shown in Figure 2.7, the vertical equilibrium is satisfied if the bending moment $M(x)$ and the shear force $V_c(x)$ are consistent with the tensile force T acting on the bottom chord, and the lever arm of internal forces $j_o(x)d$, as expressed below:

$$V_c(x) = \frac{dM(x)}{dx} = T\frac{d\left(j_o(x)d\right)}{dx} + j_o d\frac{dT(x)}{dx} = V_1 + V_2 \qquad (2.1)$$

Eq. (2.1) highlights the contributions provided by beam and arch effect, the former depending on a constant value of the internal lever arm, while the latter depending on a variable value of $j_o d$. It should be noted that the shear contribution provided by beam and arch effects are limited by the failure of concrete in compression, as thoroughly described in Campione et al. (2016). Calculating the tensile force T acting on the bottom chord, the shear contributions provided by the two mechanisms V_1 and V_2 are given as follows:

$$V_1 = \left(T_b + T_p\right) j_o \frac{d}{a} \qquad (2.2)$$

$$V_2 = j_o\, d\left(q_{res,b}\,\pi \sum_{i=1}^{n_b} D_i + q_{res,p}\, b_w^* + \sum_{i=1}^{n(x)} T_{wi}\,\delta\left(x - \overline{x}_i\right)\right) \qquad (2.3)$$

in which d is the effective depth of the beam, D_i is the diameter of each

rebar, b^*_w the effective width of the bottom plate, T_{wi} the dowel action provided by each inclined bar, $q_{res,b}$ and $q_{res,p}$ are the residual bond stress in the bottom rebars and the bottom plate, respectively. The unit step function $u\left(x-\overline{x}_i\right)$ and its derivative $\delta\left(x-\overline{x}_i\right)$ are used to model the difference in the tensile force acting on the bottom chord due to the dowel effect T_{wi} provided by each inclined bar. The internal forces T_b, T_p and T_{wi} may be calculated as follows:

$$T_b\left(x=a\right)=\min\left\{A_b\ f_{yb};q_{res,b}\ a\,\pi\sum_{i=1}^{n_b}D_i\right\} \tag{2.4}$$

$$T_p\left(x=a\right)=\min\left\{A_p\ f_{yp};q_{res,p}\ b_w^*\ a+\sum_{i=1}^{n_w}T_{wi}\ u\left(x-\overline{x}_i\right)\right\} \tag{2.5}$$

$$T_{wi}=A_{sw}\ f_{yw}\left(\cos\alpha+0.4\,r\sin\alpha+0.04\,r^2\sin\alpha\tan\alpha\right)\sin\beta \tag{2.6}$$

where f_{yb} and f_{yp} are the yielding stresses of the bottom longitudinal bars and bottom plate, respectively; n_b and n_w are the number of bottom longitudinal bars and inclined bars, respectively; A_{sw} is the cross-sectional area of the web bars, inclined of an angle α with respect to the beam axis and β with respect to the vertical axis of the beam cross-section, respectively; r is the ratio between ultimate and yielding stress of the web bars. Lastly, the shear contribution provided by the web bar is calculated as follows:

$$V_{sw}=A_{sw}\ f_{yw}\sin\alpha\sin\beta \tag{2.7}$$

The total shear strength V_r is calculated as the sum of the contributions provided by Eqs. (2.1) and (2.7), by using Eqs. (2.2)-(2.6):

$$V_r=V_c+V_{sw}=\left(V_1+V_2\right)+V_{sw} \tag{2.8}$$

Colajanni et al. (2014b) model

Recently, in Colajanni et al. (2014b) a mechanical model for evaluating the shear capacity of beams containing two orders of transverse reinforcement with different inclinations has been derived. The model is based on the stress field approach, and it is formulated assuming that the resisting mechanism to shear force at the Ultimate Limit State (ULS) is constituted by the following elements (Figure 2.8):

- two longitudinal chords, the top compressed chord formed by the

concrete and its reinforcement, and the bottom tensile one formed by the bottom longitudinal reinforcement and the prestressing reinforcement (if any);

- four elements arranged along the web, carrying the shear action, formed by the concrete strut, two orders of stirrups, and longitudinal reinforcement (if any).

The model is based also on the following assumptions:

1. both the stirrups and the longitudinal web reinforcement (if any) are subjected only to axial force (i.e. dowel action is considered elsewhere, as explained below);
2. compared to the size of the structural members, the spacing of the stirrups and of the web longitudinal bars is so small that their actions can be modelled via different uniform stress fields;
3. the concrete stress field in the web is inclined by the angle θ to the longitudinal axis, which may differ from $\beta \sim 45°$, which is the alignment of the first cracks in a structural member subjected merely to bending and shear (like a beam at the Service Limit State, SLS); the maximum shear capacity is achieved for $cot\theta$ varying in the range $1 \leq cot\theta \leq 2.5$; more severe limitations must be imposed in elements where flexural ductility is demanded;
4. the constitutive laws of the materials are consistent with the theory of plasticity;
5. the contributions to the shear capacity of dowel action and aggregate interlock are indirectly taken into account by introducing (through the angle θ) different orientations for the principal directions of the stress fields and the cracks;
6. the contribution due to the tensile strength of the concrete (V_{ct}) is neglected;
7. the arch action, which plays a remarkable role in the D (Disturbed) regions, is neglected; hence, the validity of the model is limited to B (Bernoulli) regions.

It has to be pointed out that according to Nielsen and Hoang (2011), assumption no. 2 may be used for beams with a transverse minimum shear reinforcement mechanical ratio of $0.16/f_c^{0.5}$, being f_c the concrete strength in compression.

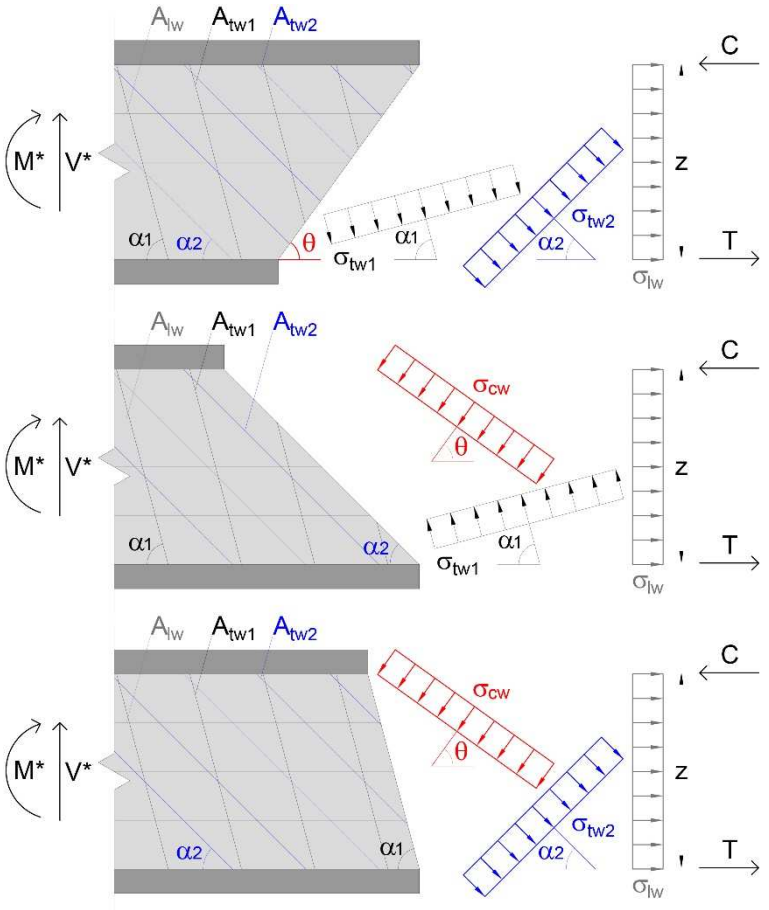

Figure 2.8 Distinct beam segments obtained through three differently-oriented sections parallel to either one of the two sets of transverse reinforcement or concrete stress field direction

Formulated by means of a suitable modification of a model proposed in previous papers (Recupero et al. 2003, 2005), it is a generalization and an alternative derivation of the classical model currently proposed in EN 1992:1-1. In both these two models, and in those derived from them (Colajanni et al. 2017b), the evaluation of shear strength is obtained, according to the static theorem of the theory of plasticity (Prager 1959; Nielsen and Hoang 2011), using the commonly-named "lower-bound solution". The latter exploits a numerical procedure that maximizes the element shear capacity by varying the stress in the two orders of transverse reinforcement and the value and inclination of the web concrete compressive stress field. Each order of stirrups can experience both tension or compression, on the basis of the arrangement and the amount of reinforcement. Four components contribute to the stress

field used to represent the internal forces acting in the beam web, being two representatives of the two sets of transverse reinforcement inclined by the angles α_1 and α_2 respectively, one representative of the concrete strut inclined by the angle θ and one representative of the longitudinal web reinforcement.

The mechanical model is formulated by using the following notation: A_{tw1}, A_{tw2}, and s_{tw1}, s_{tw2} are the cross-sectional areas of the transverse web reinforcements with inclinations α_1 and α_2 and their spacings, respectively; b_w and h are the web minimum width and the cross-section depth, respectively; f_{yd} and f'_{cd} the design tensile strength of steel and the design reduced compressive strength of concrete, respectively. Therefore, assuming A_{twi} the cross-sectional area of the generic order of stirrups, the respective mechanical ratios are:

$$\omega_{twi} = \frac{A_{twi} f_{yd}}{b_w s_{twi} f'_{cd} \sin\alpha_i} \qquad i = 1,2 \tag{2.9}$$

At the same time, the mechanical ratio of web reinforcement is equal to:

$$\omega_{lw} = \frac{A_{lw} f_{yd}}{b_w h f'_{cd}} \tag{2.10}$$

where A_{lw} is the cross-sectional area of the web longitudinal rebars. Moreover, the non-dimensional shear strength is equal to:

$$v = \frac{V}{b_w z f'_{cd}} \tag{2.11}$$

where z is the lever arm of internal forces acting on the section. It should be reminded that, the web concrete being subjected to a biaxial state of stress and cracked in shear, the design compressive strength of concrete f_{cd} has to be multiplied by an efficiency coefficient ν' (≤ 1), obtaining the reduced design compressive strength $f'_{cd} = \nu' f_{cd}$. The values of ν' recommended by EN 1992:1-1 or by NTC 2018, namely $\nu' = 0.6(1-f_{ck}/250)$ or $\nu' = 0.5$, respectively, can be used. The non-dimensional stresses of the two orders of reinforcement and of the web concrete are calculated as follows:

$$\tilde{\sigma}_{cw} = \frac{\sigma_{cw}}{f'_{cd}} \qquad \tilde{\sigma}_{twi} = \frac{\sigma_{twi}}{f_{yd}} \quad i = 1,2 \tag{2.12}$$

In order to assess the shear strength of a RC beam, three distinct beam segments are obtained through three differently-oriented sections parallel to

either one of the two sets of transverse reinforcement or concrete contribution to the stress field direction (Figure 2.8). The equilibrium equations along the vertical axis for each of the three segments read:

$$v = \tilde{\sigma}_{tw1}\omega_{tw1}\left(\cot\theta+\cot\alpha_1\right)\sin^2\alpha_1+\tilde{\sigma}_{tw2}\omega_{tw2}\left(\cot\theta+\cot\alpha_2\right)\sin^2\alpha_2 \quad (2.13)$$

$$v = \tilde{\sigma}_{cw}\sin^2\theta\left(\cot\theta+\cot\alpha_2\right)+\tilde{\sigma}_{tw1}\omega_{tw1}\left(\cot\alpha_1-\cot\alpha_2\right)\sin^2\alpha_1 \quad (2.14)$$

$$v = \tilde{\sigma}_{cw}\left(\cot\theta+\cot\alpha_1\right)\sin^2\theta+\tilde{\sigma}_{tw2}\omega_{tw2}\left(\cot\alpha_2-\cot\alpha_1\right)\sin^2\alpha_2 \quad (2.15)$$

As already said, the mechanical model assesses the shear resistance of a RC beam employing the static theorem of the theory of plasticity, which provides an evaluation of the shear capacity as the maximum value among the possible solutions validating the equilibrium conditions (2.13)-(2.15) and satisfying the following conditions of plastic admissibility:

$$0 \le \tilde{\sigma}_{cw}, \left|\tilde{\sigma}_{tw1}\right|, \left|\tilde{\sigma}_{tw2}\right| \le 1 \quad (2.16)$$

By combining (2.13) and (2.14) or (2.13) and (2.15) with (2.16), the following inequalities, representing the plastic admissible condition for the stress field acting on the concrete strut, are derived:

$$0 \le (\tilde{\sigma}_{tw1}\omega_{tw1}\sin^2\alpha_1+\tilde{\sigma}_{tw2}\omega_{tw2}\sin^2\alpha_2)\left(1+\cot^2\theta\right) \le 1 \quad (2.17)$$

(2.17) clarifies the interaction between the inclination of the concrete strut and the stress fields of the two orders of stirrups. With the aim of assessing the shear resistance of RC beams via the "lower-bound solution", the shear capacity obtained through (2.13) (or (2.14) and (2.15)) has to be maximized, by varying $\tilde{\sigma}_{tw1}$, $\tilde{\sigma}_{tw2}$, and $cot\theta$ within the ranges given in (2.16) and (2.17).

Monti and Petrone (2015) model

Monti and Petrone developed a model to assess the shear resistance of HSTC beams on the basis of a critical observation of several numerical analyses. The failure mechanism detected by the Authors is characterized by the yielding of *n* pairs of inclined bars before the concrete failure. By using the strut and tie approach, a statically indeterminate model of the structure is individuated, characterized by concrete struts of unknown dimensions. The resisting mechanism is characterized also by the dimensions of the beam cross-section, diameter and spacing of inclined bars. The dimension of the concrete truss is assessed by minimizing the strain energy for unit of resisting

mechanism stiffness, after the evaluation of the internal forces acting on the elements constituting the HSTC beam by means of the force method. On these bases, an analytical approach to assess the shear resistance can be formulated. Furthermore, the Authors derived a corresponding simplified approach, by assuming that the concrete strut withstands the increment of shear force acting on the beam in proportion to its stiffness, rather than its strength. In detail, the simplified approach is developed by assuming that the concrete strut is capable of carrying the increment of the internal forces caused by the stiffness loss when the first couple of inclined bars yields, until a second couple yields as well (Figure 2.9). Therefore, the shear resistance can be computed by means of the following code-consistent equation:

$$V = \kappa f_{yw} A_{sw} \sin\alpha \tag{2.18}$$

in which

$$\kappa = \frac{n_t - 2\left(1-\delta_p\right)}{n_t - 2\left(n_s - \delta_p\right)} \tag{2.19}$$

where n_t is the number of inclined bars subjected to tensile force, $n_s = n$ is the number of yielded inclined bars, $d_p = 0$ or $d_p = 1$ have to be assumed in the case of load applied at the top or the bottom of the beam, respectively. A graphical explanation of the parameter κ is shown in Figure 2.9, where H is the internal force acting on the chords, h is the internal lever arm, p is the vertical reaction force, s is the spacing of the diagonal bars, L is the beam length, ΔV is the increment of shear strength provided by the yielding of two couple of diagonal bars.

Discussion

The above-described models evaluate the shear capacity of HSTC beams interpreting the several shear resisting mechanisms differently. Nevertheless, the results they give are generally accurate. Each capacity model is characterized by advantages and limitations. In fact, Campione et al. model combines reliability with design-oriented formulation, but it is not compatible with EN1992-1-1 framework. By contrast, Colajanni et al. model is constituted by equations compatible with EN1992-1-1 that provide reliable results. However, its iterative procedure hinders a daily use by professional engineers. Lastly, Monti and Petrone model provides, in its simplified approach, a design-oriented formulation, which is partially compatible with

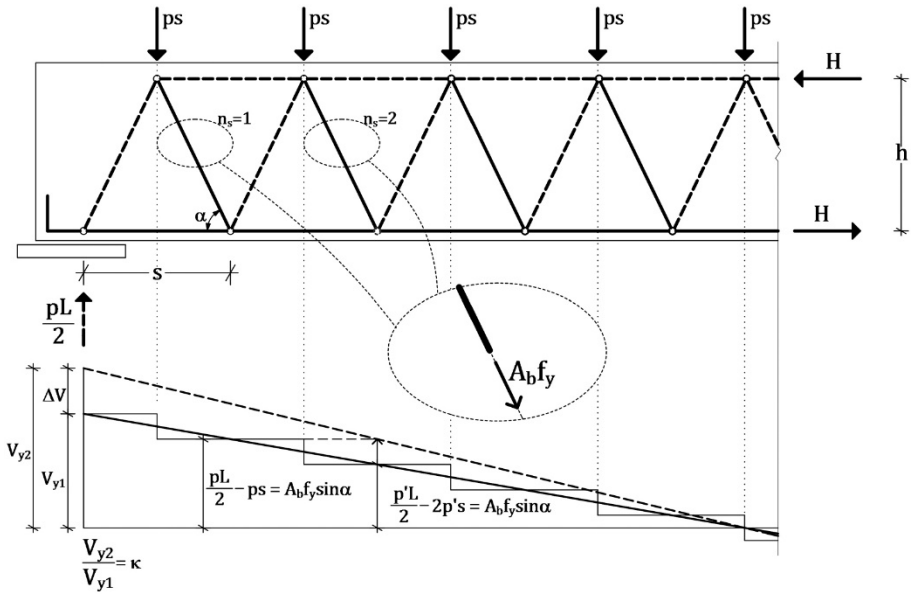

Figure 2.9 Graphical explanation of the parameter κ (taken from Monti and Petrone 2015)

that of EN1992-1-1. Yet, among the three models analysed here, it gives the least accurate results (Colajanni et al. 2019). For these reasons, in Chapter 4 will be presented a mechanical model that combines all the advantages of the above models, namely accurate results, design-oriented formulation, and compatibility with EN1992-1-1 framework.

2.2.3 Beam-column joint strength

In HSTCBs, when the connection between beams and columns is realized by means of added rebars, as in the configuration that will be analysed, the joint can be classified as a standard RC one. However, what characterizes beam-column joints made with HSTC beams are the geometrical and mechanical peculiarities of the latter. In fact, these beams typically have small cross-section depth (usually equal to the slab depth) and large amount of longitudinal reinforcement (often concentrated in rebars with large diameters). As well known, a high ratio between rebar diameter and column cross-section height leads to high bond stresses and, thus, to potentially decreasing performance affecting the response of the joint when subjected to cyclic actions. In addition, due to its small dimensions, which hinder the possibility to arrange a proper amount of transverse reinforcement, RC panel zone is subjected to high shear stresses causing shear distortion, significantly influencing the overall cyclic performance of the joint. This topic will be

extensively analysed in Chapter 5. In this section, to provide an insight into the mechanics of beam-column joints realized with HSTCBs, the experimental campaign carried out by Colajanni et al. (2016b) is described below.

Experimental observations

The three subassemblies tested were representative of internal beam-column joints, each of them constituted as follows (Figure 2.10): two half-columns having cross-section 300 mm width and 400 mm depth, reinforced with 10 rebars of 20 mm diameter; two HSTCBs made with a truss having a 5-mm thick lower steel plate, 3ϕ16 bars constituting the upper chord and inclined transverse ϕ12 bars positioned at a 300 mm spacing. The beam cross-section is equal to 300 × 250 mm. The bending moment capacity of the beam end section is obtained ignoring the truss contribution and considering only the added top and bottom longitudinal reinforcement, namely 4ϕ24 and 2ϕ24 bars, respectively. The column was subjected to an axial load of 800 kN, and the reversed cyclic loading was imposed near to the column base section. The scheme of constraints, load condition and geometrical characteristics of specimen no. 2 is reported in Figure 2.10.

The load-displacement curve of specimen no.2 is plotted in Figure 2.11. The results showed a degrading behaviour in terms of strength, stiffness and pinching of hysteretic cycles. This behaviour was mainly due to the poor performance of the joint, which exhibited severe crackings at the end of the test (Figure 2.12).

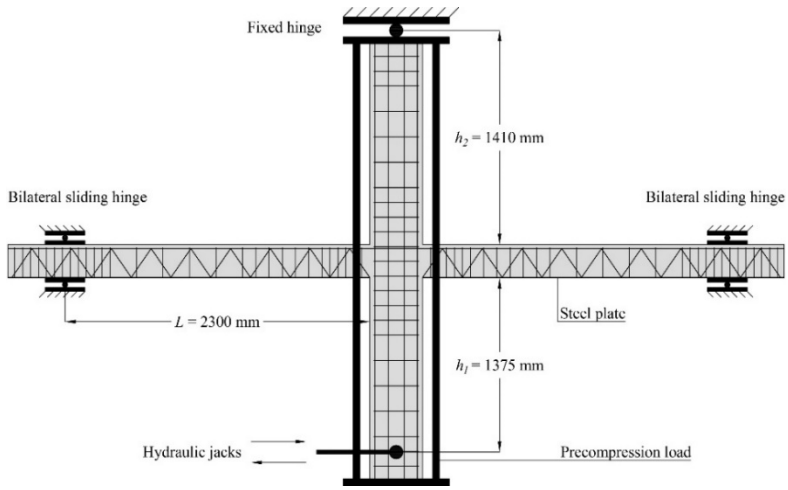

Figure 2.10 Scheme of constraints and load condition of the specimens tested to reversed cyclic actions (adapted from Monaco 2014)

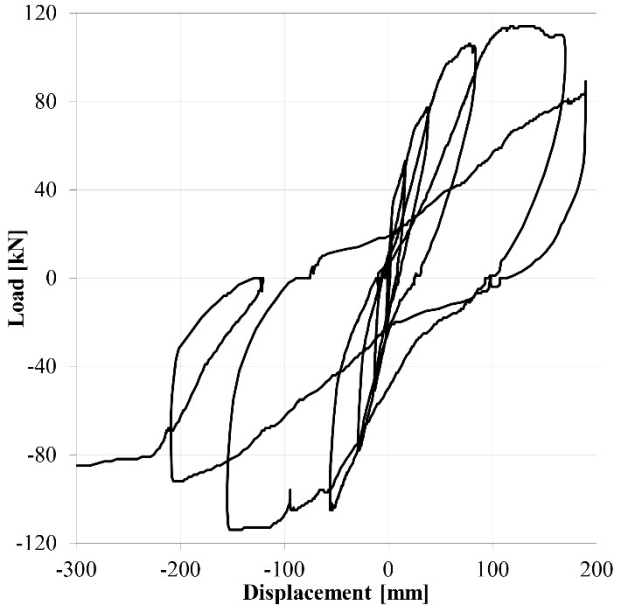

Figure 2.11 Force-displacement curve of specimen no.2 (adapted from Monaco 2014)

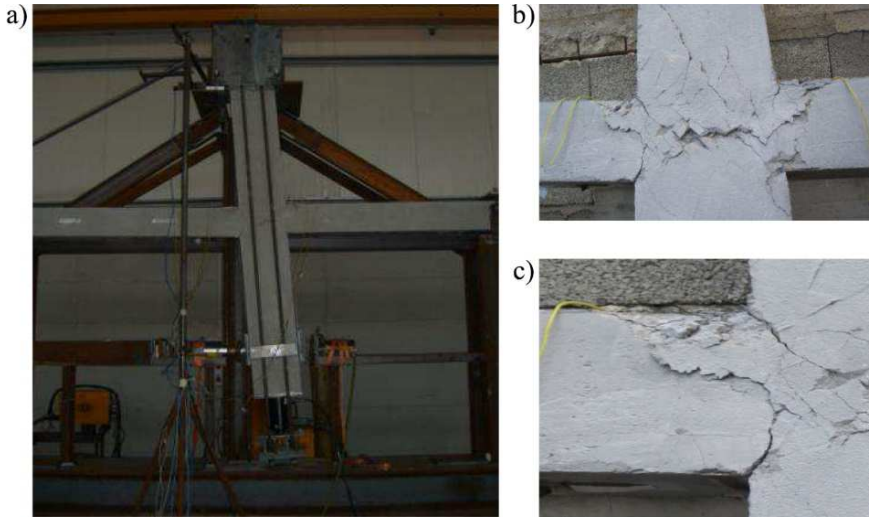

Figure 2.12 Specimen no.2 at the end of cyclic test (taken from Monaco 2014)

Interpretation issues

Generally speaking, it is difficult to exactly reproduce the cyclic response of beam-column joints (Mitra and Lowes 2007). In fact, joint behaviour depends on several resisting mechanisms which are difficult to account for rigorously. At the same time, each resisting mechanism shows a mechanical behaviour that depends not only on the loading history, but also on the

interaction with the other resisting mechanisms. For these reasons, several simplifying assumptions must be done when reproducing cyclic performance of joints. Modelling of joints can be done at the microscopic or macroscopic level. The first one is typically adopted to reproduce experimental results of tested subassemblies. To do so, 3D FEM software packages are used, able to accurately reproducing geometry and reinforcement layout of beam-column subassemblies. However, reliable results are obtained only by calibration of several parameters (e.g. those reproducing mechanical behaviour of concrete and its bond with the steel reinforcement). This operation is usually done on the basis of the experimental results themselves. Also, computational effort and modelling complexity furtherly hamper this approach. For these reasons, the second approach, namely modelling at the macroscopic level, is widely used, being accurately investigated since 1990s. It consists in reproducing the cyclic performance of joints by means of one or more zero-length elements whose force-displacement or moment-rotation curves synthetically describe the mechanical behaviour of the main resisting mechanisms of subassemblies. This approach, being computationally efficient, is suitable when a refined non-linear modelling of RC structures is required.

Several joint models have been developed to evaluate the abovementioned cyclic behaviour, and there is no consensus in the scientific community on a model that is suitable for all configurations (Pan et al. 2017). Among the most renowned models (described in Pan et al. 2017), in the present research will be adopted the model proposed by Lowes and Altoontash (2003), able to account for the two main mechanisms influencing the cyclic performance of beam-column joints, namely shear distortion of panel zone and relative rotation between beam and column due to slippage of longitudinal rebars within panel zone. This topic will be fully addressed in Chapter 5.

Discussion

The structural deficiencies arisen during experimental tests on subassemblies realized with HSTC beams call for the adoption of innovative solutions. As a matter of fact, the ordinary procedure to avoid joint failure would be increasing its strength by adding transverse reinforcement within the panel zone. However, due to the small dimensions of the panel zone, and the already high amount of longitudinal and transverse reinforcement, a further increment in shear reinforcement ratio would be impractical. An effective solution would be the use of High Strength Fibre Reinforced Concrete (HSFRC), although this solution does not prevent plastic hinge formation at beam end. Therefore, in Chapter 6, innovative solutions for beam-to-column

connection will be proposed, able to avoid damaging of both panel zone and beam end. To dissipate seismic energy, these solutions are endowed with friction devices that, by lengthening internal lever arm of moment transferred between beam and column, reduce shear forces acting on the panel zone.

2.3 Conclusions

Since the first patent applied during the Sixties, HSTC beams have been used in the construction industry as a cost-effective solution having enhanced performance, with respect to ordinary RC beams. This Chapter showed the remarkable effort of the scientific community over the last years, in clarifying most of the peculiar aspects of HSTCB mechanics. However, it is deemed that some of them deserve further studies, such as the assessment of shear strength and the enhancement of performance of beam-column joints. In fact, with respect to the former, numerous capacity models were developed to assess the shear resistance of HSTC beams. These models interpret the shear behaviour of these beams in quite different ways, providing however reliable results. Therefore, it can be stated that there is no scientific consensus on the correct interpretation of the mechanical behaviour of HSTCBs subjected to shear force. In addition, none of them combines reliability, design-oriented formulation, and compatibility with EN1992:1-1 shear model. For this reason, in Chapter 4 a new analytical model based on the truss mechanism is proposed, which includes all the above-mentioned characteristics. Concerning the beam-column joint performance, experimental tests showed that the combination of small beam depth with longitudinal bars with large diameters led to cyclic response influenced by degrading stiffness and strength. Due to the small dimensions of joints, it is impractical to use high amount of transverse reinforcement, which are commonly used to limit these phenomena. Therefore, effective solutions still need to be developed to limit or prevent damaging in joints. To this aim, the use of innovative systems at the beam-to-column connections is deemed as a viable solution, since they are already employed in steel MRFs effectively. Within this framework, in Chapter 6 are proposed different innovative solutions for beam-column connection, characterized by the use of friction devices to dissipate seismic energy. These connections are consistent with the low-damage design philosophy, preventing not only damage of joints, but also plastic deformations of beam ends.

CHAPTER 3

STATE OF THE ART ON FRICTION CONNECTIONS FOR LOW-DAMAGE STRUCTURES

During the past three decades, energy dissipated by means of frictional sliding has been investigated as a viable alternative to that absorbed by plastic deformations of sacrificial structural members (e.g. beam end sections of Moment Resisting Frames (MRFs)). Several solutions were developed for the most common structural typologies (e.g. MRFs, shear walls, braced frames). Many different friction connections were proposed for steel structures, some solutions were also designed for timber structures, while few studies concerned friction devices employed in RC/PC structures. In this chapter, the main and most recent solutions developed for MRFs and shear walls, which are of major interest for the aim of the present research, are described. Furthermore, pros and cons for each solution are highlighted, focusing the attention on dissipative capacity, stability of hysteresis loops, kinematic during sliding phase, forces acting on bolts, self-centring capability. In addition, to provide a more comprehensive point of view on the state of the art, some of the most relevant and innovative solutions for the low-damage beam-to-column connections based on metallic hysteretic dampers are shown. Lastly, the common issues affecting all friction connections, namely characteristics of friction shim and bolt preload, are discussed. Based on the above considerations, a guideline can be outlined, which can help to define solutions for beam-to-column and column-to-foundation connections for RC frames with HSTCBs.

3.1 Beam-to-column friction connections

Main energy dissipation source of standard MRFs realized according to capacity design approach is provided by plastic hinges located at beam-to-column connections. The reason why so many innovative solutions for beam-to-column connections have been developed for steel structures over the last

25 years lays on the poor performance some of them showed during Northridge (1994) and Kobe (1995) destructive earthquakes. These events represented a game-changer for the structural engineers' community. As a matter of fact, pre-Northridge beam-to-column connections were usually realized by welding beam flanges on column flange. The plastic hinge was supposed to form starting from the welds connecting beam and column. This constructional detail led to unpredicted stress concentration causing numerous premature failures and limited connection ductility. For this reason, all post-Northridge connections have the common goal of avoiding any damage to the elements connecting beam and column.

With regard to energy dissipation, this can be ensured, for instance, by formation of ordinary plastic hinge in beam segment sufficiently distanced by column flange, and characterized by dog-bone section (e.g. Plumier 1997), or by introducing innovative systems. Among the latter, in the following sections are described the most significant solutions for beam-to-column connections characterized by friction dampers or metallic hysteretic dampers. The latter are taken into account because most of them were developed before the development of the bulk of the friction-based connections actually reported in the literature, and thus, several technological aspects, as well as the issues encountered, are in common between the two groups of solutions.

A main difference between the two types of dampers is that those based on yielding of metallic members are suitable in those areas characterized by a low rate of seismic events. In fact, these dampers often undergo severe damage when subjected to a destructive earthquake, usually requiring their replacement with consequent downtime of the building. On the contrary, the dampers based on friction are able to withstand several earthquakes over their life-time with a minimum maintenance, and thus being more effective in achieving an earthquake-resilient structure. In addition, the metallic hysteretic-based dampers have a mechanical response which can be predicted with great accuracy, the mechanical properties of steel having low level of scatter. This characteristic leads to low overstrength factors to be used in the design of the structural members surrounding the dampers, in order to ensure the elastic behaviour of these members. In contrast, friction-based dampers have a mechanical response which is characterized by a high variability, which is due to the difficulty both to exactly predict the friction coefficient of a material, and to evaluate the effective preload acting on the bolts. These phenomena oblige the designer to use high values of the overstrength factor to protect the structural members from damaging.

3.1.1 Connections based on friction dampers

The beam-to-column connections based on friction can be grouped into four different categories depending on the layout of the dissipative system:

- asymmetric connections with one or more friction shims to one side only;
- asymmetric connections with one or more friction shims per side;
- symmetric connections with additional steel element(s) and two or more friction shims;
- symmetric connections with two or more friction shims per side.

The connection is defined symmetric if the steel plates, which transfer the friction forces between beam and column, are arranged to obtain aligned resultant forces (so that the bolts are not subjected to prying forces).

Rotational Slotted Bolted Connection

One of the first solutions proposed for friction devices applied at beam-to-column joints, was reported in Grigorian and Popov (1994) and Yang and Popov (1995), and belongs to the fourth group (Figure 3.1). The system is constituted by two T stubs, each of these bolted to the beam flanges and cover by a cap plate. At each interface T stub-beam flange and T stub-cap plate is inserted a friction shim. Beam web is bolted to the column flange via vertical steel angles, in which the central bolt acts as the centre of rotation, while the other bolts are inserted through slotted holes.

The advantage of this solution is that, having a properly defined centre of rotation, the kinematic of the connection is readily predictable. However, the position of the centre of rotation causes sensible gap opening during rotation between column flange and top beam flange, leading to potential damage to the slab. In addition, particular attention should be given to the design of the bolt representing the centre of rotation, named pivot bolt, as well as the plates connected by it. As a matter of fact, the first of the two specimens tested by Yang and Popov (1995), named 7A, showed that no element constituting the connection was damaged at the end of the test, except for the pivot bolt, whose shank was bent by shear. In addition, reversed cyclic action enlarged the hole on the beam web through which the pivot bolt was inserted. For this reason, for the second specimen, named 7B, was adopted a larger pivot bolt and the beam web was reinforced.

Experimental tests employed brass as friction shim material. The results showed that, despite the brass provided exceptionally stable cyclic behaviour,

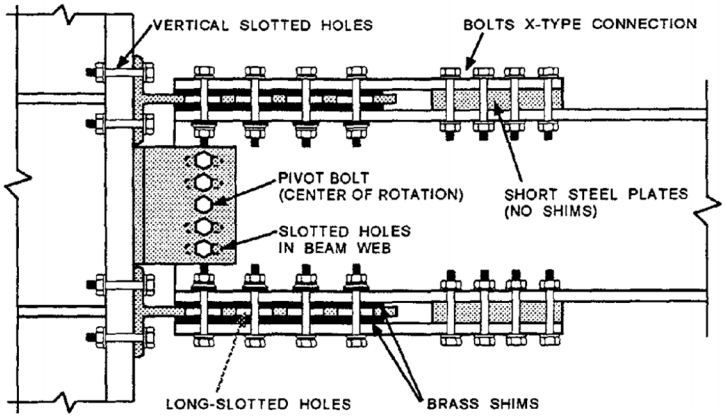

Figure 3.1 Symmetric connections with two or more friction shims per side: *Rotational Slotted Bolted Connection* (RSBC) (taken from Yang and Popov 1995)

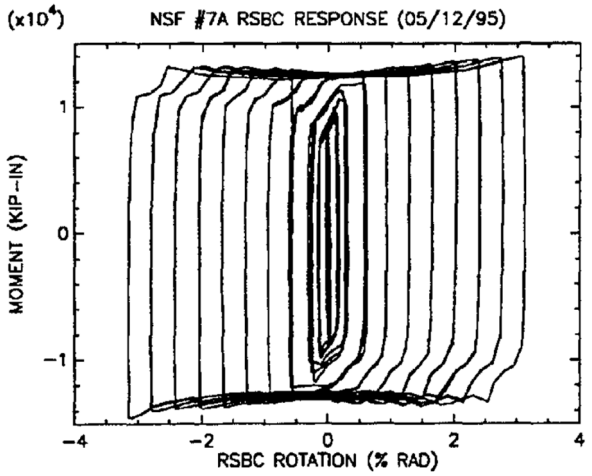

Figure 3.2 RSBC experimental moment-rotation curve (taken from Yang and Popov 1995)

as shown in Figure 3.2, its friction coefficient was quite low and required to build a connection with many friction surfaces and bolts to obtain a proper moment strength. Furthermore, moment of the connection during sliding phase showed a slight hardening behaviour. This can be explained by the fact that, once the connection started to rotate, T stubs were bent, and the bending moment acting on them contributed to increase the moment of the whole connection. With regard to the shape of corners of hysteresis loops, this is due to the slippage of brass pads during load reversal, caused by clearance hole.

Despite the several flaws affecting the proposed solution, it can be stated that the tested connections behaved outstandingly well. It is worth remembering that this solution was pioneering and the application of such friction connections to structural engineering was at the very beginning.

Sliding Hinge Joint with Asymmetric Friction Connection

Among the most recent connections developed at the University of Auckland and University of Canterbury plays an important role the connection that belongs to the first group, which is named Sliding Hinge Joint with Asymmetric Friction Connection (SHJAFC) (Chanchi Golodrino et al. 2019; Khoo et al. 2015; Ramhormozian et al. 2018) (Figure 3.3). The solution solves two main drawbacks affecting the RSBC, namely the centre of rotation constituted by a pivot bolt, to which particular attention has to be paid during structural design to avoid any damage to the bolt itself and to the plates connected by it, and the gap opening between top flange of beam and column flange, which could potentially lead to damage of the slab. In this solution, the beam is connected to the column by means of two horizontal steel plates, which are welded to the column flange next to the beam. The connection between these steel plates and the beam is made with bolts, where the upper ones realize a standard bolted friction connection, while the lower ones are inserted through slotted holes to allow the rotation of the beam. Between the bottom beam flange and the lower plate is inserted a friction shim, which provides adequate dissipative capacity to the connection. A cap plate is bolted to the bottom side of the lower plate, inserting between the latter ones another friction shim. A vertical plate is welded to the column flange and bolted to the beam web by means of two horizontal rows of bolts. The top one is a standard bolted connection, while the bottom one is characterized by horizontal slotted holes to allow the rotation of the beam. Moreover, with the aim of increasing the dissipative capacity of the connection, a cap plate is bolted to the outer side of the web plate. Between the cap plate and web plate, and between the

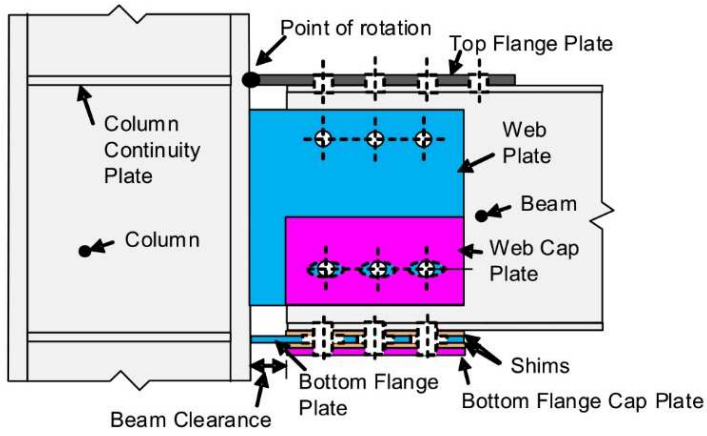

Figure 3.3 Asymmetric connections with one or more friction shims: *Sliding Hinge Joint* (SHJ) (a), Asymmetric Friction Connection (AFC) (b) (taken from Khoo et al. 2015)

web plate and the beam web two friction shims are inserted.

The connection starts to rotate when the friction forces provided by the shims inserted between bottom beam flange and bottom plate, beam web and web plate, are achieved. Increasing the rotation of the system, the total friction force doubles when the friction shims inserted between the bottom and web plates and the cap plates begin to slide (Figure 3.4).

During the design step of the SHJAFC, special attention must be paid to the Serviceability Limit State and to the wind loads. As a matter of fact, due to the above-mentioned moment-rotation behaviour, the connection could start to rotate when subjected to loads different from those caused by the design earthquake. Furthermore, the asymmetric arrangement of the friction device leads to bolts contemporarily subjected to moment, shear and axial load, which, in early versions of this connection, caused plastic deformations of bolts shanks. This phenomenon decreased clamping force leading to hysteretic cycles characterized by a progressive reduction of the sliding force. To solve this issue, bolts have to be kept within the elastic range and coupled

with disc springs able to absorb the elongation undergone by bolts shanks (Ramhormozian et al. 2017).

When SHJAFC is endowed with friction pads having an hardness much higher than that of constructional steel, it provides wide and stable hysteretic cycles, with a slight progressive increase of sliding force (Figure 3.5). This phenomenon is due to the formation of asperities on the surfaces in contact.

From the pioneering configurations developed at the end of the last century, during the last decade the SHJ has been further developed in order to be self-centring (Khoo et al. 2012b, 2013). This behaviour is obtained by adding at the bottom beam flange a stack of preloaded ring springs inserted in a box-shaped case. A bar is inserted through the ring springs and is bolted to the column flange. The system is designed to deform the ring springs in

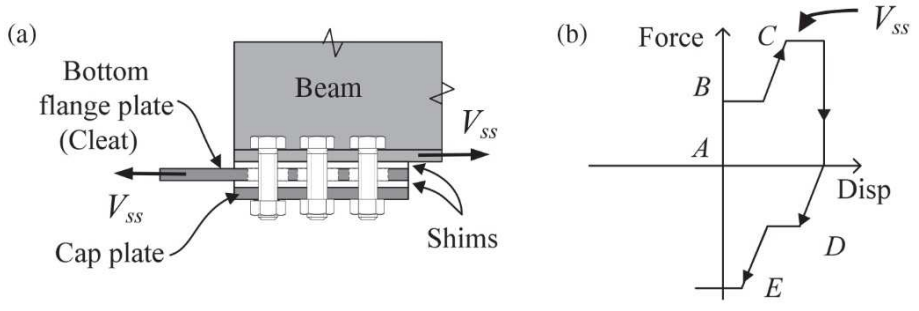

Figure 3.4 Asymmetric Friction Connection (AFC) (a) and its moment-rotation curve (b) (from Khoo et al. 2015)

compression only for both hogging and sagging moment (Figure 3.6).

The ring springs are constituted by inner and outer rings, whose surfaces in contact are inclined. When the stack of ring springs is compressed, these surfaces slide each other once the friction forces acting on them are overcome, causing a compression in the inner rings and a tension in the outer ones. Since these rings behave elastically up to a displacement equal to the length of the surfaces in contact, when the axial load is removed, they slide back to their original position, dissipating energy thanks to the friction forces generating on the surfaces in contact. This characteristic makes the ring springs a valid option to obtain a low-damage connection characterized by both dissipation capacity and self-centring behaviour.

As can be seen in Figure 3.7 (ii), the moment-rotation curve of a joint provided by a stack of ring springs (herein named Ring Spring Joint, RSJ), has the typical flag-like shape of the self-centring connections. A joint combining ring springs and SHJAFC (herein named Self-Centring Sliding Hinge Joint, SCSHJ) provides the moment-rotation curve plotted in

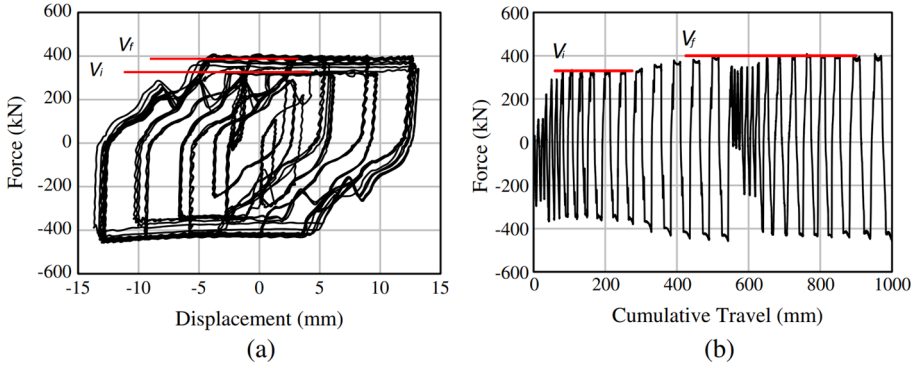

Figure 3.5 Asymmetric Friction Connection force-displacement curve (a) and force-cumulative travel (b) (taken from Khoo et al. 2015)

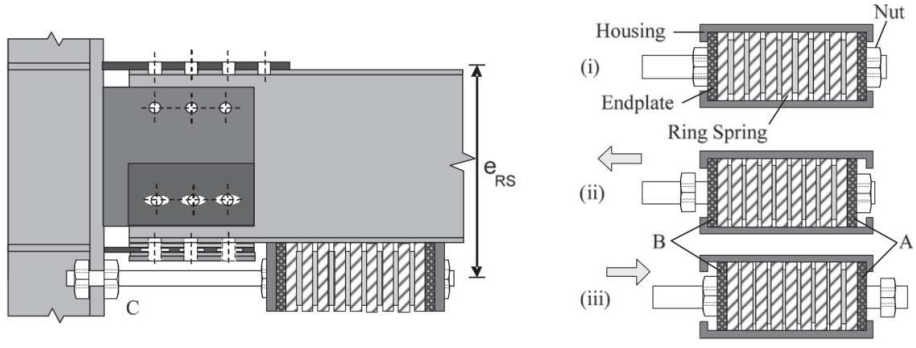

Figure 3.6 *Self-Centring Sliding Hinge Joint* (SCSHJ) (taken from Khoo et al. 2012b)

Figure 3.7 (iii), which is no longer self-centring due to the contribution provided by the AFC. However, the residual drift is less than that given by the SHJAFC, proving the beneficial effect of the ring springs to the self-centring capability of the whole joint.

Experimental tests carried out on different combinations of moment strength provided by the AFC and the stack of disc springs pointed out that the more is the percentage of moment strength provided by the AFC on the whole moment strength of the connection, the less is the self-centring capacity of the connection itself. For instance, in Figure 3.8 is shown the moment-rotation curve of a self-centring SHJAFC characterized by a percentage of moment capacity provided by preloaded ring springs P_{RS} of 52.4%. It can be seen that, despite P_{RS} was more than half of the whole moment capacity of the connection, significant residual drift was still obtained. Therefore, P_{RS} should be increased by using a more performing, and thus more expensive, self-centring system. In addition, the connection behaved according to design requirements for rotation up to 25 mrad. Above this value, the vertical component of the displacement due to the rotation was no more negligible and the moment strength increased rapidly. This is due to the fact that the

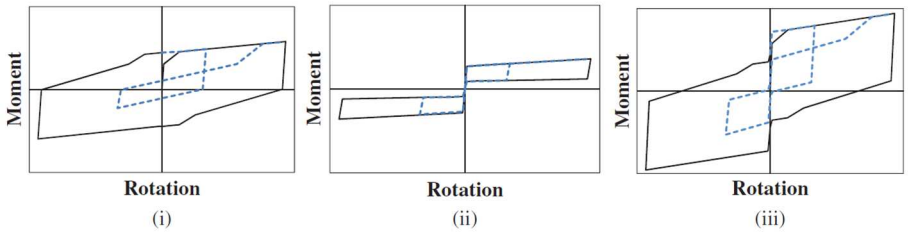

Figure 3.7 Idealized moment-rotation responses of: SHJ (i), RSJ (ii), and SCSHJ (iii) (taken from Khoo et al. 2013)

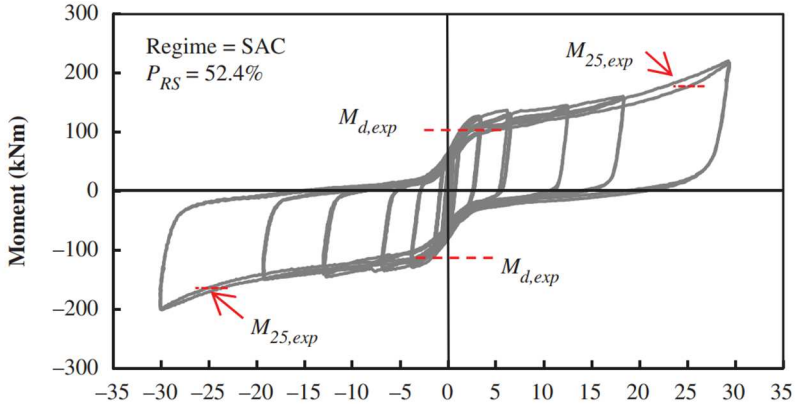

Figure 3.8 SCSHJ experimental moment-rotational curve (taken from Khoo et al. 2013)

connection was not designed to accommodate large displacement in the vertical direction, thus some damage could have been experienced by the connection. Moreover, in the case of seismic event leading to rotation well above 25 mrad, the increment in the moment strength of the connection could have led to the formation of plastic hinge at the beam end or, worse, to damaging the column. For this reason, a real application of this connection should select an appropriate overstrength factor to design the members surrounding the connection to prevent any damage.

Dissipative Double Split Tee Connection

A solution belonging to the second group has been developed at the University of Salerno, Italy, and it is named Dissipative Double Split Tee Connection (DDSTC) (Latour et al. 2015). The connection is made with two T stubs, bolted to the beam flanges, on which slotted holes are realized to allow the sliding of the bolts (Figure 3.9). Between T stub and beam flange is inserted a friction shim, which provides energy dissipation capacity. The connection is designed in order to allow the vertical component of the displacement due to the rotation by means of the deflection of T stubs. The latter ones are supposed to undergo plastic deformations at the base section and then to be replaced after the seismic event. This configuration does not have a defined centre of rotation, leading to potential significant damage to the slab. Experimental tests have shown remarkable performance characterized by an adequate dissipative capacity and a slight hardening behaviour due to bending moment acting on T stubs flanges, as already seen in the RSBC (Figure 3.10). The solution simplifies the configuration of the

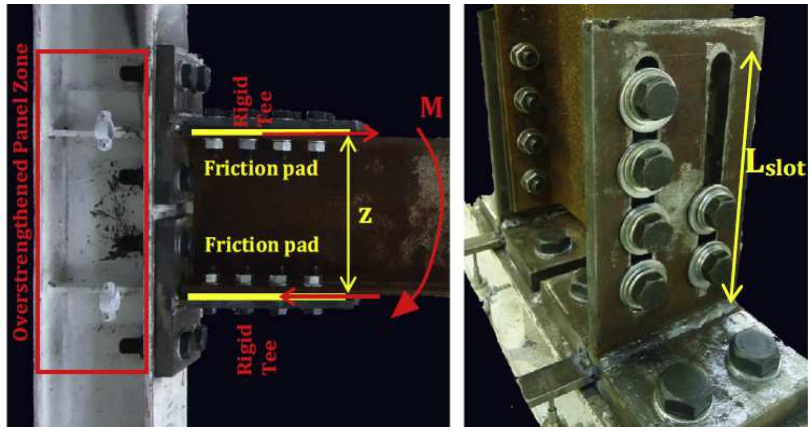

Figure 3.9 Asymmetric connections with one friction shim per side: *Dissipative Double Split Tee Connection* (DDSTC) (taken from Latour et al. 2015)

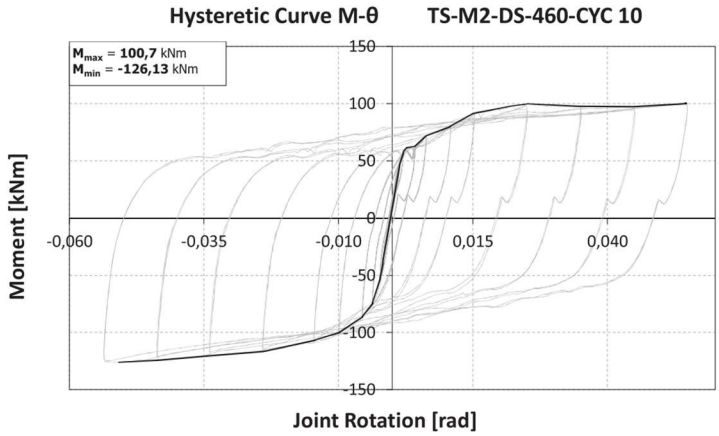

Figure 3.10 DDSTC experimental moment-rotation curve (taken from Latour et al. 2015)

RSBC by removing cap plates and pivot bolt. The reduction of number of surfaces on which friction forces are generated, which would lead to a lower moment capacity of the connection, is compensated by using friction shims having higher friction coefficient. However, by doing so the friction connections become asymmetric and the bolts are subjected to combined axial force-shear force-bending moment that, as discussed in the SHJAFC, might lead to plastic deformations of bolts shanks, potentially causing decreasing clamping forces and poor cyclic performance of the connection.

Removable friction dampers for low-damage connections

The same Authors, in collaboration with the University of Naples "Federico II", Italy, propose two other solutions, one with the dissipative friction sliding plates in horizontal direction, the other one with friction sliding plates oriented in vertical direction, belonging to the third group (Latour et al. 2018a, 2018b). These solutions aim at solving three main flaws of the previous solution, i.e. the lack of a centre of rotation, the asymmetric configuration of the friction connections, and the relatively small moment capacity, which is due to a combination of small internal lever arm of the connection and small number of friction surfaces for each side (i.e. equal to 1). Both of these solutions exploit an additional steel element which is bolted to the bottom beam flange with the aim of increasing the internal lever arm of the connection and, thus, reducing the forces acting on the panel zone. This additional steel element is an I-shaped profile in case of horizontal dissipative device, while is T-shaped in case of vertical one. Another advantage provided by the additional steel element is that it allows to double the surfaces on which friction forces are generated, considerably improving the performance of the

connections. The upper part of the beam is connected to the column flange by means of a T stub which is bolted to both the column and the beam. In both the solutions, the centre of rotation is expected to form at the base section of the upper T stub. The solution with the horizontal dissipative device is constituted by three steel angles which are bolted to the I-shaped profile, using one friction pad for each steel angle (Figure 3.11).

On the other hand, the solution with the vertical dissipative device employs two steel angles, requiring the realization of two groups of slotted holes, one vertically-oriented on the steel angles, and the other one horizontally-oriented on the T-shaped profile (Figure 3.12). By doing so, bolts are able to move in any direction. By contrast, in the solution with horizontal dissipative device, the displacement component in vertical direction is absorbed by the

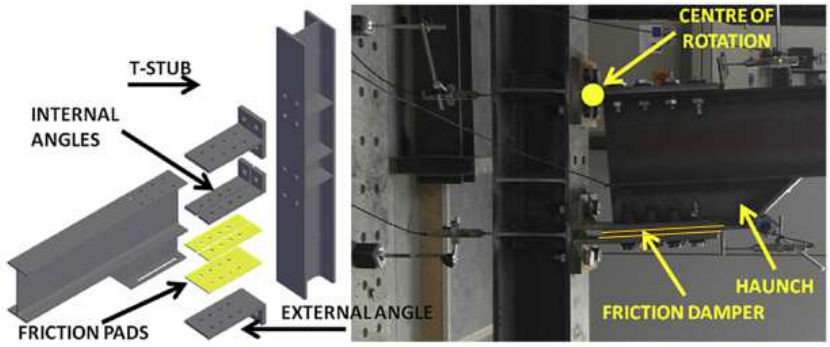

Figure 3.11 Symmetric connections with additional steel element(s) and two or more friction shims arranged horizontally (from Latour et al. 2018a)

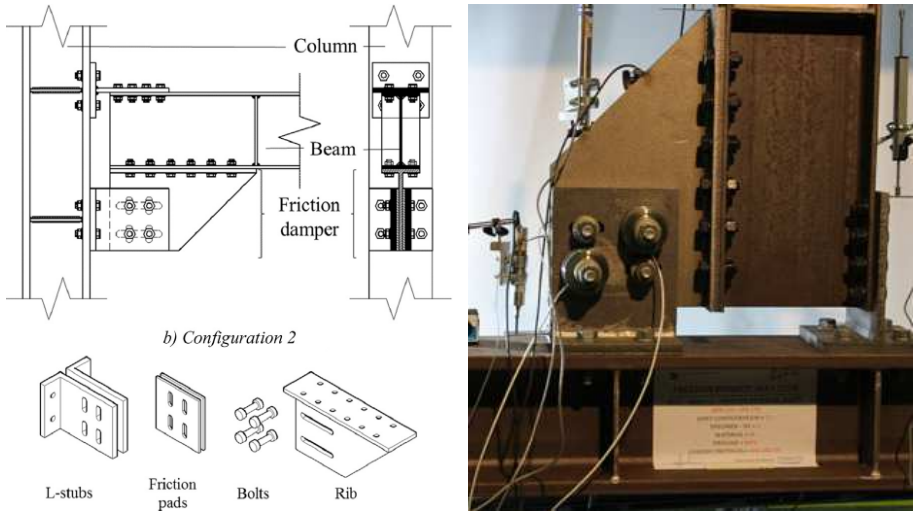

Figure 3.12 Symmetric connections with additional steel element(s) and two or more friction shims arranged vertically (taken from Latour et al. 2018b)

deformation of the lower steel angles. Differently from the horizontal system, in which low damage of the lower steel angles is admitted, the vertical one prevents any damage of the friction connection. However, bolts belonging to the friction device experience plastic deformations due to the contact between horizontal slotted holes of the T-shaped profile and bolts shanks. In fact, these bolts have to be dragged up and down by the T-shaped profile, along the vertical direction, in order to allow the rotation of the connection. With regard to the mechanical behaviour, the horizontal system shows an increment of the moment capacity, in both direction, due to the progressive plasticization of the lower steel angles (Figure 3.13a). As for the vertical system, the contact between bolts shanks and horizontal slotted holes causes an increment of the moment capacity which depends on the amount of bolts shanks dragged by the T-shaped profile. For this reason, the backbone curve of the moment-rotation behaviour showed a sawtooth-like shape (Figure 3.13b).

Moment capacity increment due to these phenomena has to be properly taken into account when designing the members connected to the friction connection with the aim of avoiding damage formation.

As will be explained in the following chapters, the solution with the vertical dissipative device will be adapted to develop the first proposed beam-to-column connection. Therefore, it is worth outlining the design procedure of the above connection.

The force F_d for which the connection starts to slide can be calculated as follows:

$$F_d = \frac{M_d}{z} \tag{3.1}$$

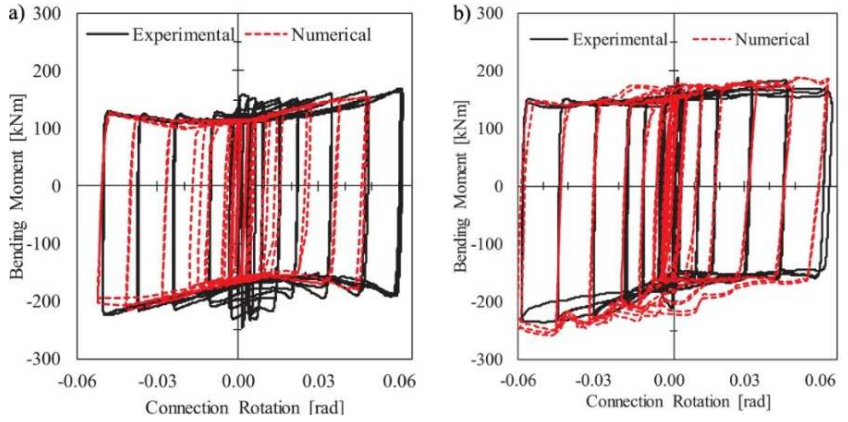

Figure 3.13 Moment-rotation behaviour of the horizontal system (a) and the vertical one (b) (taken from Latour et al. 2018b)

in which M_d is the design bending moment and z is the lever arm, being the distance between the centre of rotation and the axis of sliding. According to EN1993:1-8, the sliding force F_d can be obtained as:

$$F_d = \frac{k_s n_b n_s \mu}{\gamma_{M3}} F_{pc} \tag{3.2}$$

where: - k_s coefficient that depends on the shape of the slotted hole; - n_b the number of bolts; - n_s the number of surfaces in contact; - μ the friction coefficient; - γ_{M3} safety factor; F_{pc} is the preloading force of each bolt. The coefficient k_s is introduced to take into account the loss of preloading and the variation of friction coefficient which characterize bolted connections having shape of holes different to the circular one. However, in the case of low-damage connections, which are characterized by long slotted holes, when the friction coefficient is obtained by means of experimental tests on specimens having holes with this type of geometry, the coefficient k_s looses significance and can be set to 1.

The preloading force F_{pc} can be assessed as follows:

$$F_{pc} = 0.7 t_s f_{ub} A_{res} \tag{3.3}$$

in which f_{ub} is the ultimate strength of steel, A_{res} is the resisting area of bolt, while t_s is a parameter ranging between 0.3 and 0.6, introduced to keep bolt within the elastic range and, thus, limit preload losses due to creep phenomena (Ferrante Cavallaro et al. 2017, 2018).

Self-centring friction connection for PC MRFs

The solution proposed in Morgen and Kurama (2004, 2008), shown in Figure 3.14, was developed for Precast Concrete (PC) structures and belongs to the fourth group. The connection between column and beam is made using only two bolts, both inserted through curved slotted holes. Each dissipative device is constituted by four friction shims (Figure 3.15). Moreover, beam and column are connected with one or more unbounded post-tensioned tendons, which are positioned at the mid height of the beam cross-section, providing self-centring behaviour to the connection.

In Figure 3.16 are represented the theoretical moment-rotation curve of the self-centring connection, as well as the contribution provided by friction devices and post-tensioned tendons. The latter is characterized by a bilinear-elastic behaviour, in which moment value M_{bp} is tuned by means of preload force acting on the tendons, while second branch stiffness is ruled by axial

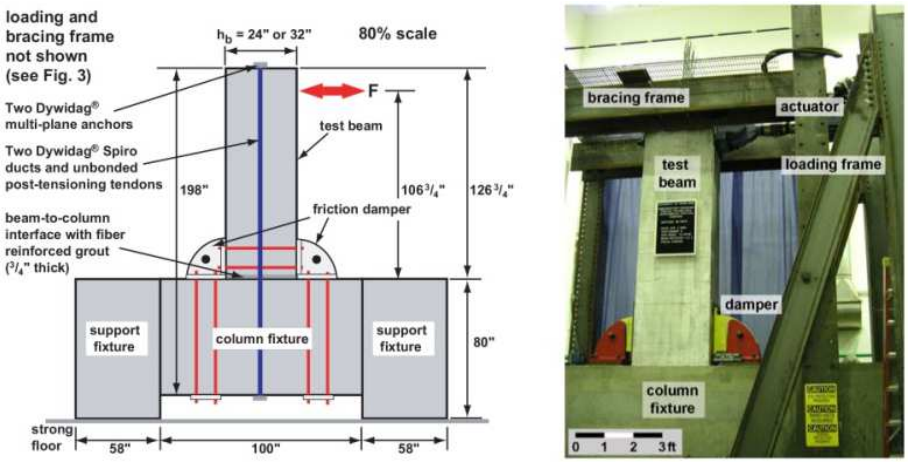

Figure 3.14 Symmetric connections with two or more friction shims per side for PC structures (taken from Morgen and Kurama 2004)

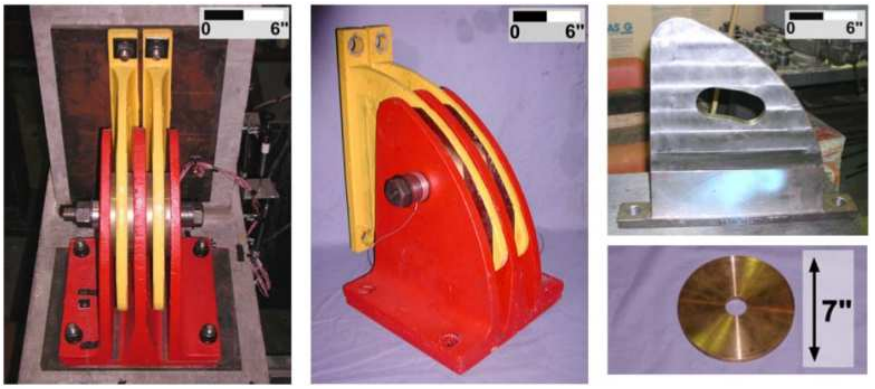

Figure 3.15 Friction device layout (taken from Morgen and Kurama 2004)

stiffness of tendons. It should be noted that the theoretical contribution given by post-tensioned tendons does not dissipate energy, these behaving elastically. Yet, this is not fully confirmed by experimental tests, as can be seen in Figure 3.17, in which are reported two moment-rotation curves of a subassembly endowed with post-tensioned tendons and including or not friction dampers. In both cases, the more was the rotation achieved by the connection, the less was the moment value for which the gap at beam-column interface opens (i.e. without dampers equals to M_{bp}, Figure 3.17a; with dampers equals to M_{bd}, Figure 3.17b). This phenomenon was due to concrete cracking and crushing at interface between beam and column, being the latter ones in contact. As a matter of fact, this contact is required to transfer the shear force between beam and column, otherwise, in the presence of friction connections, these would withstand this force and their functioning would be

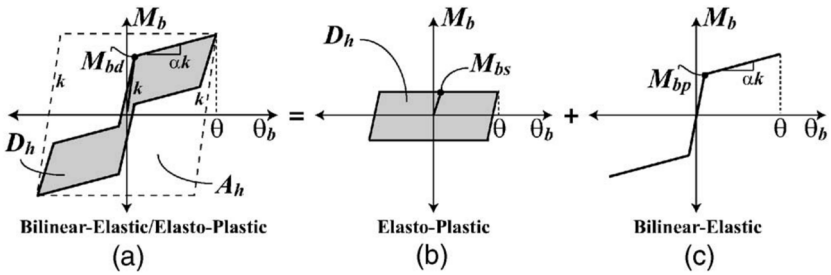

Figure 3.16 Theoretical moment-rotation curves of: self-centring friction connection (a), friction dampers only (b), post-tensioned tendons only (c) (taken from Morgen and Kurama 2007)

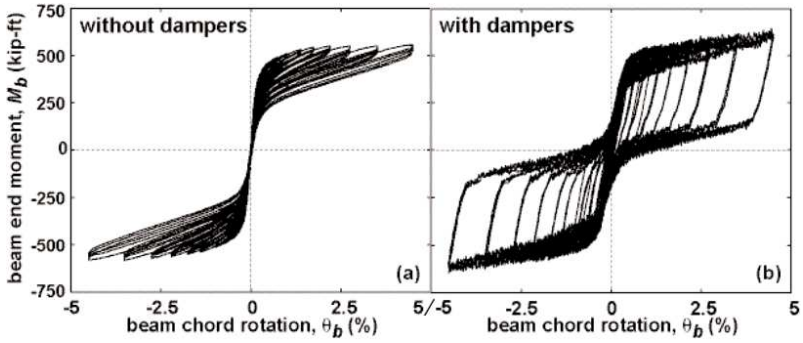

Figure 3.17 Experimental moment-rotation curve of the beam-column joint endowed with post-tensioned tendon only (a) and coupled with friction dampers (b) (taken from Morgen and Kurama 2004)

hampered. Moreover, progressive damage of concrete leads also to hysteretic cycles with small amplitude in the case of subassembly without dampers. On a final note, the results provided by post-tensioned tendons are promising in terms of dissipative and self-centring capacities. However, it has to be stressed that this structural typology requires to tension the tendons in the construction site once the PC members are placed, limiting its use to relevant constructions only.

Discussion

Among the several solutions presented in this section, those developed by Latour et al. (2018a, 2018b) might be deemed the most balanced ones, being characterized by wide and stable hysteresis loops, bolts subjected to symmetric forces, ease of realization, and cost-effectiveness. SHJ is an unquestionably excellent solution for beam-to-column connection, and the AFC compactness does not introduce any obstacle to architectural layout design. However, doubling of the sliding force during the functioning of the connection raises some concerns during the design procedure. In addition, the

asymmetric configuration of the friction device calls for paying particular attention to the design of bolts. In fact, these are subjected to combined axial force-shear force-bending moment, and bolts shanks are particularly prone to plastic deformations. However, the latter should be avoided since they could reduce clamping force of bolts and, thus, deteriorate cyclic performance of the connection. Regarding the self-centring version of the SHJAFC, it seems to provide performance which do not justify the increment of cost of the whole connection. Despite of their promising results, the use of friction connections coupled with unbounded post-tensioned tendons in PC structures requires specific procedures during construction process, which could significantly rise construction costs and make more convenient using other structural typologies. In Table 3.1 are summarized advantages and shortcomings of the preceding friction-based beam-to-column connections.

Table 3.1 Advantages and shortcomings of the beam-to-column connections analysed

	Advantages	**Shortcomings**
Rotational Slotted Bolted Connection (RSBC)	Properly defined centre of rotation	Position of the centre of rotation far from the slab
	Stable cyclic behaviour	Numerous friction surfaces and bolts
Sliding Hinge Joint (SHJ)	Low number of friction surfaces and bolts	Moment capacity dependent on the rotation
	Position of the centre of rotation near the slab	Bolts subjected to moment, shear and axial load
Self-Centering Sliding Hinge Joint (SCSHJ)	Increased self-centring capacity with respect to the standard SHJ	High cost of the ring springs
		No detail to absorb the vertical component of the displacement due to the rotation
Dissipative Double Split Tee Connection (DDSTC)	Low number of friction surfaces and bolts	No defined centre of rotation
	Stable cyclic behaviour	Bolts subjected to moment, shear and axial load
Removable friction dampers for low-damage connections	Position of the centre of rotation near the slab	Damage of the steel angles (horizontal configuration)
	Symmetric configuration of the friction device	Damage of the bolts of the device (vertical configuration)
	Stable cyclic behaviour	
Self-centring friction connection for PC MRFs	Almost ideal self-centring behaviour	Difficulty in setting up the connection on the construction site
	Compact and efficient friction device	Damage of the concrete at the beam-to-column interface

3.1.2 Connections based on metallic hysteretic dampers

The beam-to-column connections based on metallic hysteretic dampers are characterized by the introduction of a structural member designed to provide energy dissipation obtained via plastic deformations of metallic material. Generally speaking, these passive energy dissipation systems have the advantage to be inexpensive and effective in avoiding damage of the surrounding structural members. Most of the solutions were proposed for steel structures, in which the introduction of these dampers is easy and direct. Some of these solutions are characterized by a damper inserted in the connection between the bottom flange of the beam and the column flange (such as those proposed by Koetaka et al. (2005) and Oh et al. (2009)), while other solutions investigate the introduction of dampers within the beam height (e.g. Shen et al. (2011)). Lastly, some Authors explore the possibility to consider the T stubs of a double split T stub connection as metallic hysteretic dampers of an innovative beam-to-column connection (e.g. Latour and Rizzano (2015)).

Koetaka et al. (2005)

The connection proposed by Koetaka et al. (2005) was originally developed to connect steel beams to weak-axis oriented I-shaped steel columns. Beam and column are connected by splice plates at the beam top flange, and by U-shaped metallic hysteretic dampers at the beam bottom flange (Figure 3.18). The centre of rotation of the connection is supposed to form at the end of the beam top flange, in order to cause negligible damage to the slab.

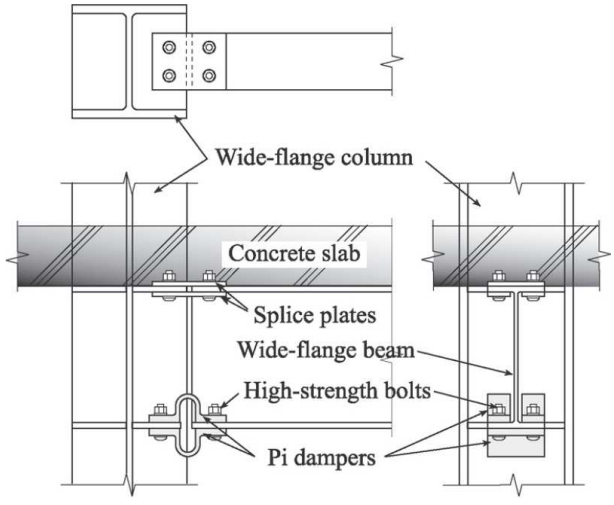

Figure 3.18 Connection layout (taken from Koetaka et al. 2005)

The metallic hysteretic damper, which is named “pi”, is designed to provide stable cyclic behaviour and satisfactory ductility capacity. The “pi”

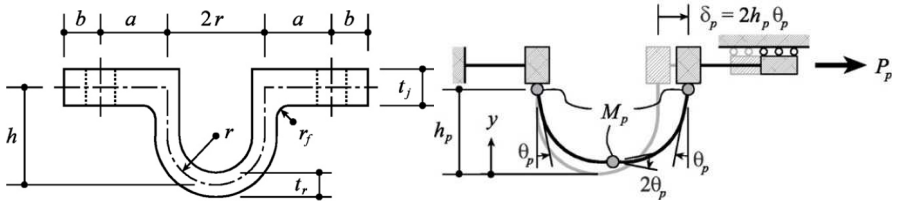

Figure 3.19 “Pi” damper: layout and failure mechanism (taken from Koetaka et al. 2005)

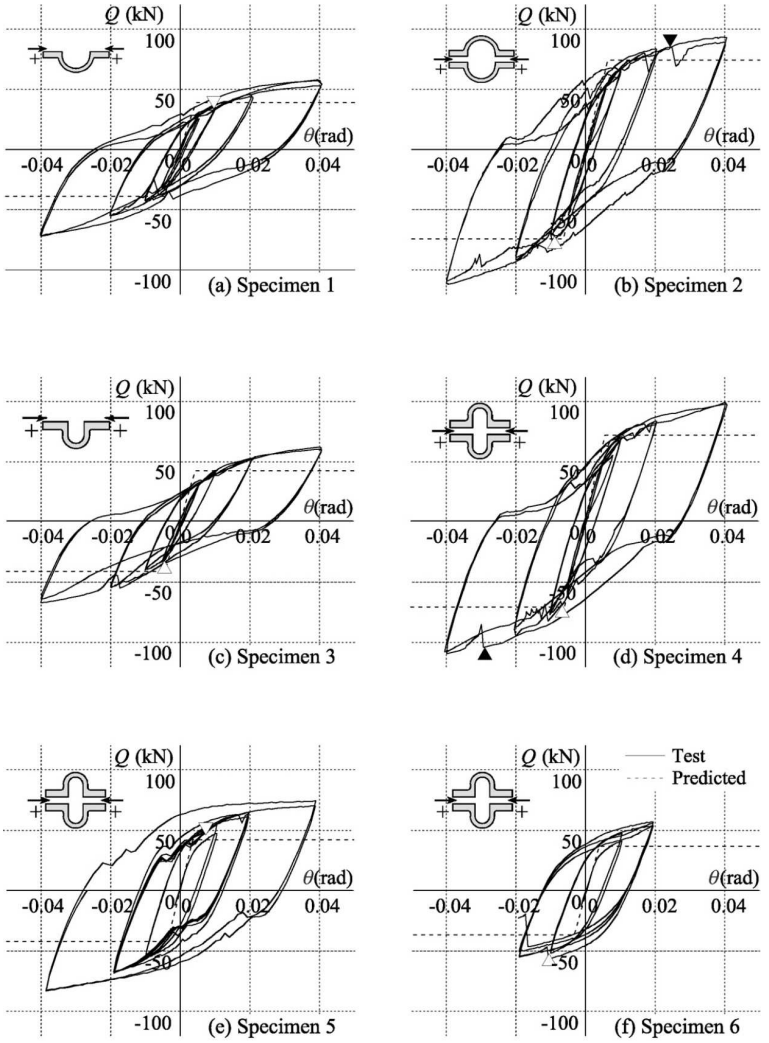

Figure 3.20 Moment-rotation curves of beam-column joints endowed with the “Pi” damper (taken from Koetaka et al. 2005)

damper dissipates energy by means of flexural yielding occurring on the U-shaped portion, which is characterized by a smaller cross-sectional area with respect to that of the contiguous horizontal portions. The collapse mechanism of the "pi" damper occurs with the formation of three plastic hinges, two at the base sections of the U-shaped portion and one at the mid-section (Figure 3.19). The elements constituting the connection are connected by means of high-strength bolts, in order to be easily replaceable in the aftermath of a seismic event. The experimental results shown in Figure 3.20, which report the behaviour of different geometrical configurations, demonstrate the reliability of such a connection. However, despite the stable cyclic behaviour, the hysteresis loops are pinched due to the slippage occurring at the joints of the "pi" dampers.

Oh et al. (2009)

The connection proposed by Oh et al. (2009) is constituted by a slit damper arranged at the beam bottom flange and a T stub at the beam top flange. The slit damper consists of two rows of steel plates having several vertical slotted holes. These plates are connected to a weak-axis oriented steel cantilever on the bottom side, and to a steel plate on the top side (Figure 3.21). The beam-to-column connection is designed to dissipate energy by plastic deformations of the slit damper, while the other elements are supposed to behave elastically. The centre of rotation is supposed to form near the base section of the T stub web. This configuration ensures limited damage to the slab above the top flange of the beam. Similarly to the preceding connection, the connections of slit damper and T stub to beam and column are made with bolts with the aim of ensuring replaceability of the elements when damaged by an earthquake.

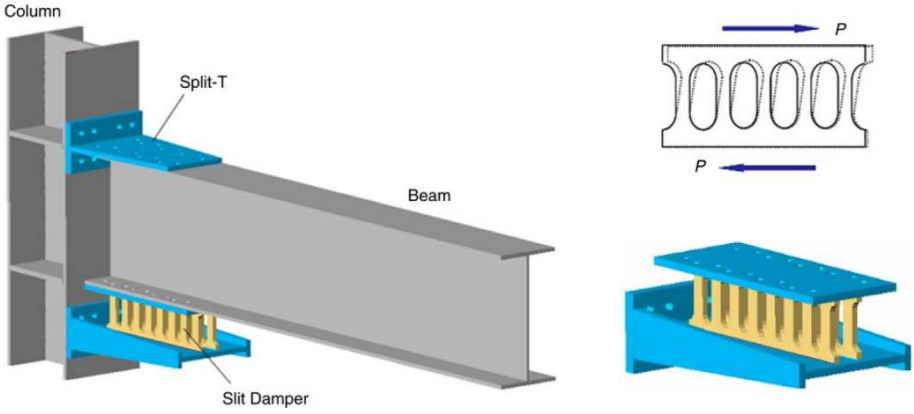

Figure 3.21 Connection layout (taken from Oh et al. 2009)

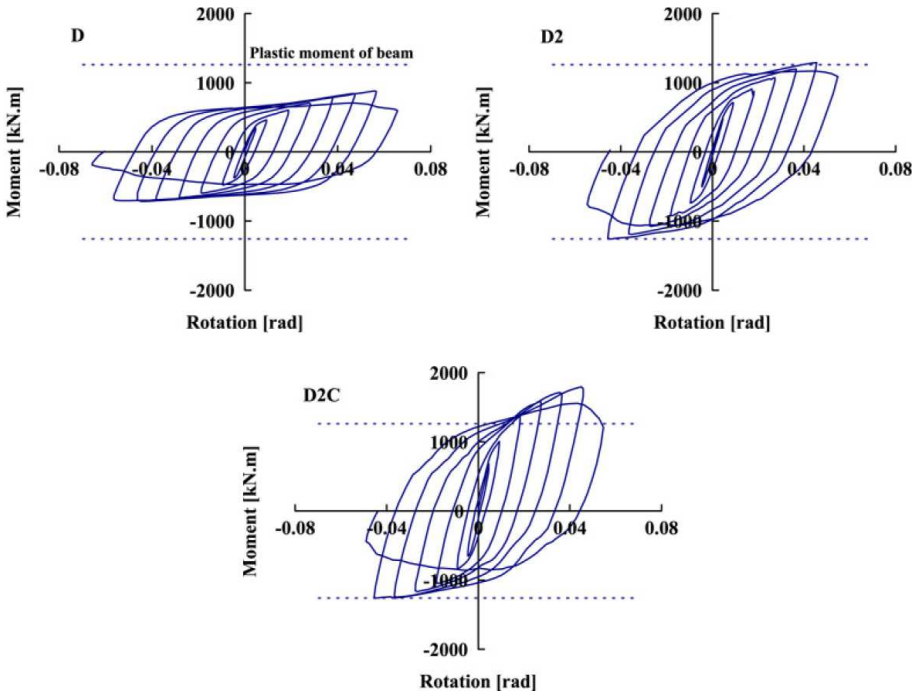

Figure 3.22 Moment-rotation curves of beam-column joints endowed with slit dampers (taken from Oh et al. 2009)

Experimental results showed exceptionally wide and stable hysteresis loops for a rotation at least equal to 40 mrad, after which fracture of the slit damper was observed (Figure 3.22).

Shen et al. (2011)

The connections proposed by Shen et al. (2011) focus on the concept of replaceable link. They are based on the principle introduced by the Reduced Beam Section (RBS) proposed by Plumier (1997), in which beam flanges are trimmed at a certain distance from the column face in order to force the formation of the plastic hinge in that portion of beam and protect the beam-to-column welds. Instead of trimming the beam flanges, these connections are characterized by a replaceable link with reduced flexural capacity than that of the beam to which is connected. Two different replaceable links were proposed, one with web elements bolted to the beam web, the other one with W-section elements bolted with end-plate connections to the beam (Figure 3.23). Differently from the above-described solutions, these connections concentrate plastic rotations far from the column face, and the centre of rotation is far from the slab. These features could lead to damage of the slab

above the beam. Four tests were carried out on beam-to-column subassemblies endowed with these replaceable links. The moment-rotation curves shown in Figure 3.24 prove the reliability of the proposed connections. In the case of bolted web link, the hysteresis loops are slightly pinched due to slippage of the bolted connection, while ensured a stable moment capacity for rotation up to 60 mrad. With regard to the W-section element, the hysteresis loops obtained are wide and stable, however the moment capacity reduced above 40 mrad of rotation due to buckling of flanges (Figure 3.24).

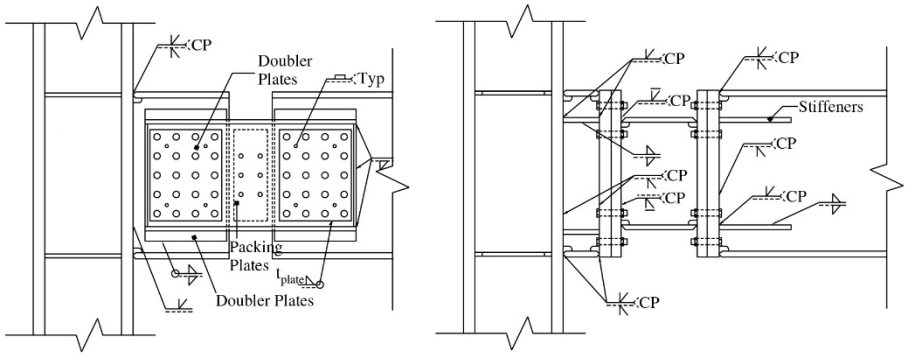

Figure 3.23 Connection layout (taken from Shen et al. 2011)

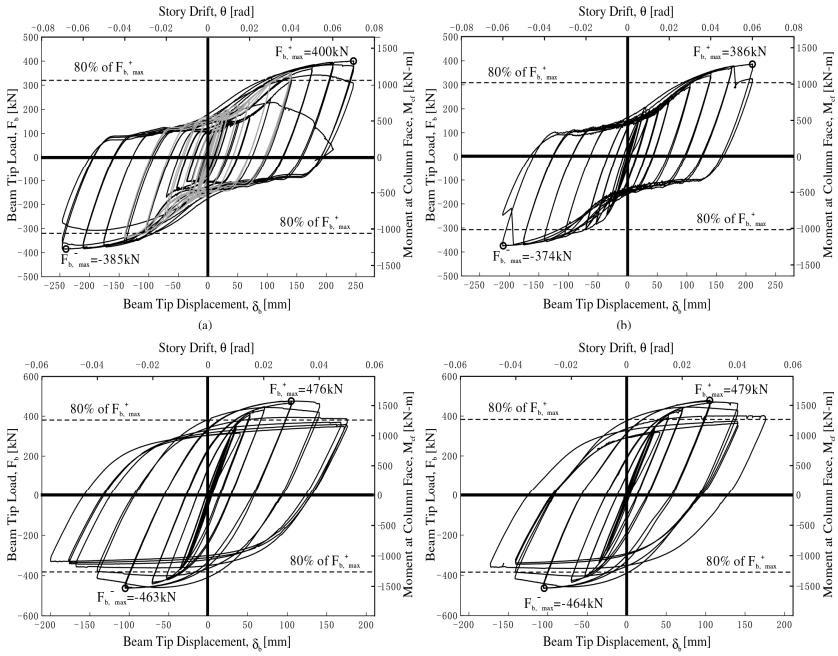

Figure 3.24 Moment-rotation curves of beam-column joints endowed with replaceable links (taken from Shen et al. 2011)

Latour and Rizzano (2015)

The connection proposed by Latour and Rizzano (2015) is constituted by a Double Split T stub (DST) joint, in which the portion of T stub flange between the bolt rows and the T stub web is cut to obtain several hourglass-shaped parts. These weakened elements lead to a partial strength joint, which ensures adequate dissipation capacity avoiding damage of the surrounding structural members (Figure 3.25). Consistently to the preceding solutions, this connection is characterized by bolted connections in order to give the opportunity to substitute the elements which undergo plastic deformations. The centre of rotation is supposed to form near the base section of the top T stub web in the case of hogging moment, on the bottom T stub web in the case of sagging moment. This characteristic implies that the top flange of the beam could move away from the column face in the case of a severe seismic event, causing damage to the slab. Experimental test on a beam-column subassembly endowed with the X-shaped DST joint provided a remarkable dissipative behaviour which was stable for a rotation slightly greater than 80 mrad (Figure 3.26).

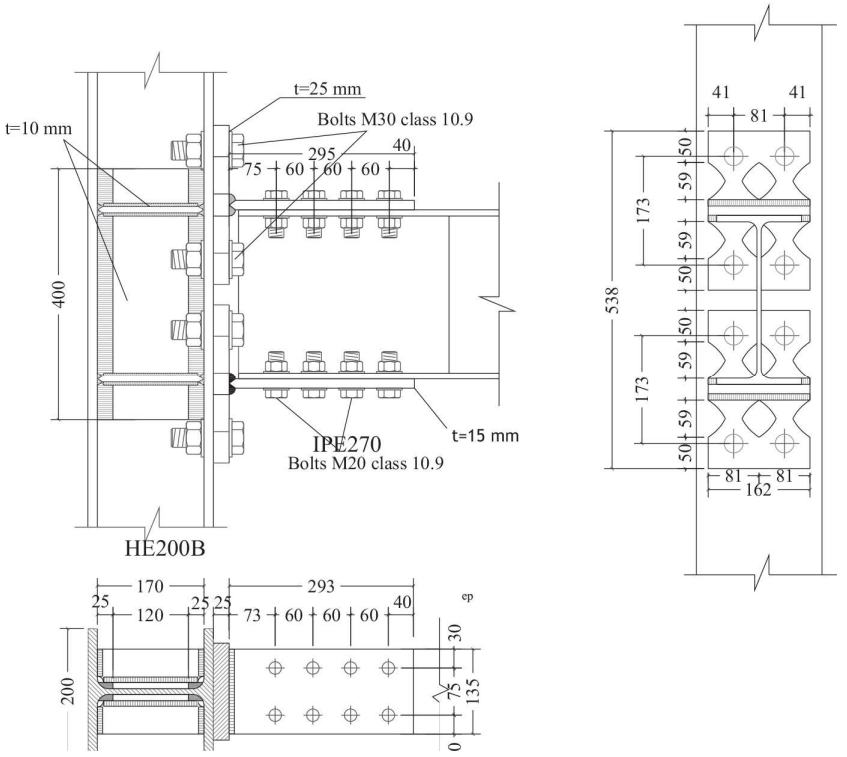

Figure 3.25 X-shaped double split T stub joint (taken from Latour and Rizzano 2015)

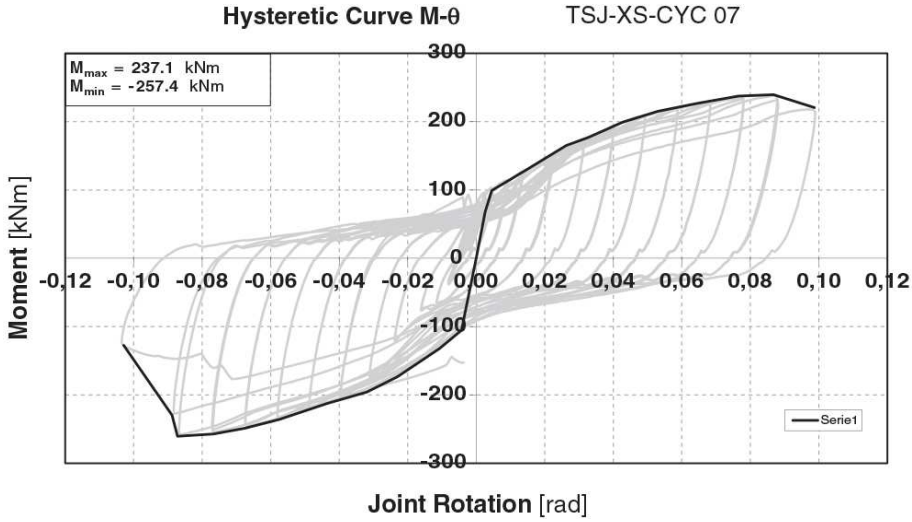

Figure 3.26 Moment-rotation curve of a beam-column joint endowed with X-shaped double split T stubs (taken from Latour and Rizzano 2015)

Discussion

Among the different solutions described in this section, that proposed by Latour and Rizzano (2015) might be considered the most balanced one, being characterized by wide and stable hysteresis loops up to remarkably high values of rotation, compactness, ease of realization, and cost-effectiveness. The solution proposed by Koetaka et al. (2005) provides undeniably excellent performance. Nevertheless, it was developed only for columns oriented along the weak axis with reference to the beam-to-column connection, and thus, an appropriate connection should be investigated in the case of strong-axis aligned columns. Moreover, to solve the pinched hysteresis loops due to the slippage of the bolted connection of the "pi" damper, number or diameter of the bolts involved in these connections should be increased. However, the dimensions of the damper, as well as those of the surrounding members, could be insufficient to increase the bolted connections. The main limitation is due to the fact that the "pi" damper should be aligned vertically with respect to the assumed centre of rotation, which is localized at the splice plates connecting the top flange of the beam to the column, with the aim of avoiding any vertical force acting on the damper which could hamper its functioning (assuming that the shear force is totally carried by the splice plates). Concerning the solution proposed by Oh et al. (2009), two main disadvantages can be highlighted. The first one is that this damper device is much more cumbersome if compared to those proposed by Koetaka et al. or Latour and Rizzano. The second one is the relatively ultimate rotation ensured by the device, namely the rotation after

which a significant reduction of strength is shown, which is about 40 mrad. Lastly, with regard to the solutions proposed by Shen et al. (2011), they require the use of several additional structural components which raise the cost of realization. Moreover, it is difficult to fulfil the damage avoidance criterion due to the possible damaging of the slab, being the centre of rotation far from it.

3.2 Column-to-foundation friction connections

Current seismic design of MRFs is based on strong column-weak beam design approach. According to the latter, when a structure is subjected to a destructive earthquake, it behaves consistent with beam sidesway mechanism, in which plastic hinges form not only at beam ends, but also at base sections of first-storey columns. For this reason, to satisfy the low-damage design philosophy, solutions to prevent damaging of base columns have to be developed. In this regard, scientific community has been developing a significant number of innovative solution since the last decade only. This delay, with respect to beam-to-column connections, might be explain because first column-to-foundation connections were realized only by the following solutions:

- in the case of steel MRFs, pinned connections at base columns are economical and easy-to-use. If a steel structure endowed with low-damage beam-to-column devices and pinned connection at base columns shows unacceptable residual drifts in the aftermath of an earthquake, it can be recentred;
- in the case of PC MRFs, post-tensioned tendons coupled with partially unbounded rebars across column-to-foundation connection have been used for several years as a cost-effective and straightforward solution for base columns.

However, both the above solutions show several flaws. Concerning steel MRFs, recentring an out-of-plumb structure is technically difficult, expensive and requires time to bring the necessary tools. Additionally, surrounding buildings, which could have been damaged or collapsed, might obstacle this operation. Concerning PC MRFs, partially unbounded rebars obstacle a complete self-centring of the connection, because their presence widens hysteretic cycles, increasing residual drift. Moreover, rebars are subjected to buckling and fracture, phenomena that hinder their performance.

For the reasons above, several research groups all over the world have

recently developed different solutions for column base connection, often inspired by beam-to-column ones. Among the several column-to-foundation connections proposed in the literature, the attention is focused on those using friction devices to dissipate energy. Moreover, some of them are coupled with specific systems (e.g. preloaded threaded bars) able to provide self-centring capabilities to the connection. Below are described some of the most significant solutions realized for steel and PC structures.

Steel column base with Asymmetric Friction Connections

Different solutions were proposed by University of Auckland and University of Canterbury, that are characterized by energy dissipation obtained through friction forces developed by the relative rotation of the column member with respect to the foundation flange plates having vertically-oriented slotted holes (Borzouie et al. 2015, 2016; MacRae et al. 2009). These flange plates belong to AFCs, which are oriented along the Weak axis (WAFC, Figure 3.27a) or the Strong one (SAFC, Figure 3.27b).

Due to the rocking behaviour of the column, the self-centring capacity of the connection is provided by the axial force acting on the column. However, this effect could be hampered in the case of variations of axial forces acting on external columns due to the seismic action. Moreover, in the case of moment along strong-axis, the column is supposed to rotate around one of the column flange base. For moment along the weak-axis, the column is supposed to rotate around the column flange edges parallel to the strong-axis. In the case of biaxial moment, the column should rotate around one of the external corner of the column flanges. It is obvious that this condition is not possible due

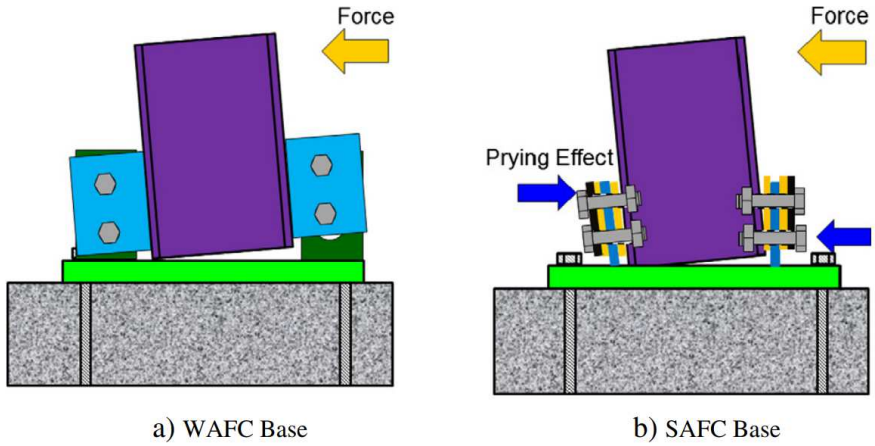

Figure 3.27 Column base connections with AFCs Weak-axis aligned (a) and Strong-axis aligned (b) (taken from Borzouie et al. 2015)

to the presence of the axial force and the compressive component of the bending moment. Such kinematic behaviour provokes significant stress concentrations in the above parts of the column, leading to potential local plasticization and buckling of the steel plates.

Experimental moment-rotation curves on WAFC and SAFC column bases along strong and weak axis are plotted in Figure 3.28. With regard to moment along strong axis, both solutions provide the designed flag-shaped hysteretic cycles. By contrast, poor self-centring capacity is provided in the case of moment along weak axis, with significant difference with respect to the expected backbone curve (red line).

Steel column base with post-tensioned strands and friction devices

The solution proposed by Freddi et al. (2017, 2020) employs post-tensioned bars, other than axial force, to provide self-centring capacity, while friction devices are used for energy dissipation. Compared to the aforementioned solution, this one is endowed with a circular steel plate with rounded edges employed as rocking base. This solution avoids stress concentration and, therefore, damage of surfaces in contact (Figure 3.29).

A shear key is introduced at the centre of the foundation base plate to

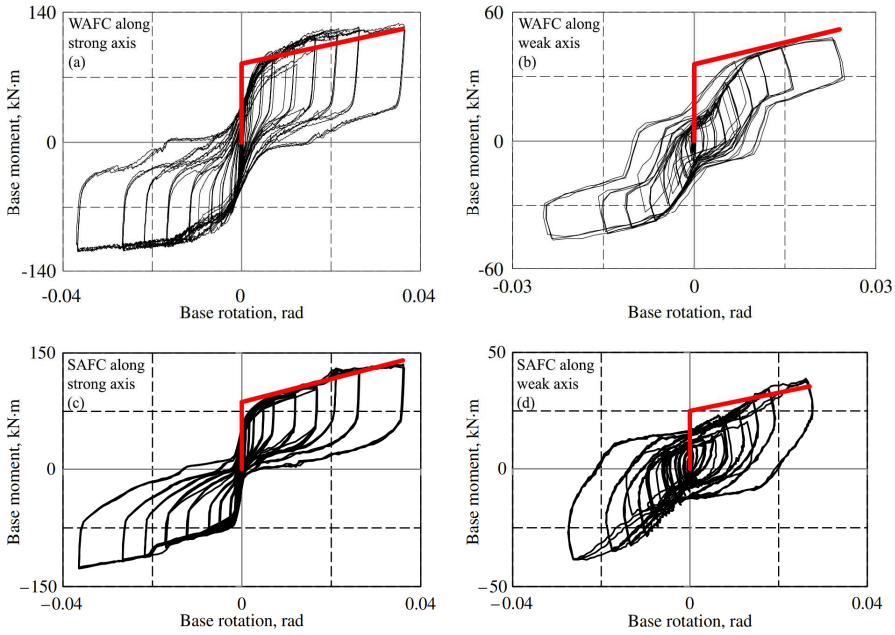

Figure 3.28 Experimental moment-rotation curves of: WAFC along strong axis (a) and weak axis (b); SAFC along strong axis (c) and weak axis (d) (taken from Borzouie et al. 2015, 2016)

prevent undesirable translation of the column in case of friction force between circular steel section and base plate is overcome. Like the solutions developed in New Zealand, the mechanical behaviour is influenced by the axial force acting on the column. In Figure 3.30 are reported the experimental moment-rotation curves of the connection in the case of: axial force and post-tensioned strands (Type B), including strong-axis aligned friction devices (Type C); including weak-axis aligned friction devices (Type D). Type B curve shows the expected theoretical bilinear elastic behaviour of a connection realized with post-tensioned strands, with negligible capacity of energy dissipation. Speaking of the latter, this is successfully obtained by adding friction devices,

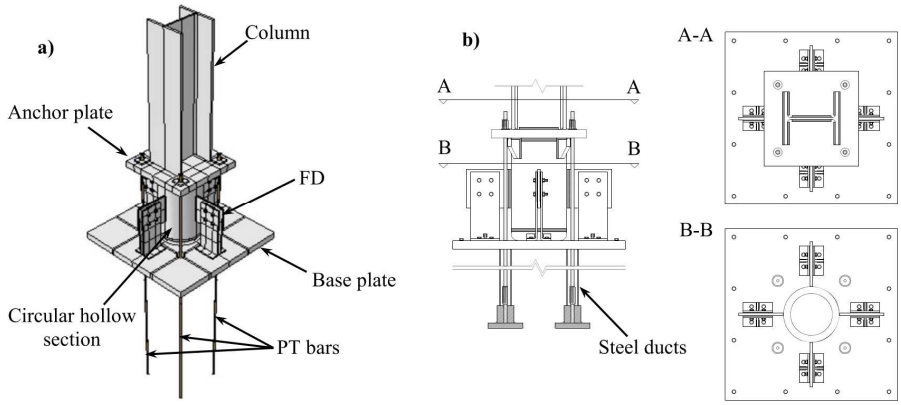

Figure 3.29 Column base connection with friction devices, post-tensioned bars and circular steel plate (taken from Freddi et al. 2017)

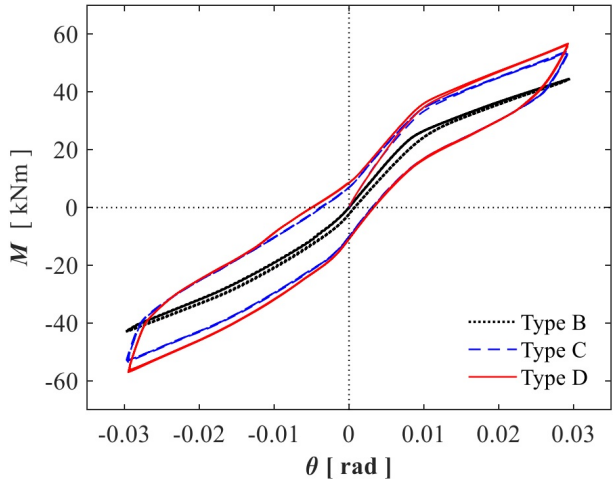

Figure 3.30 Experimental moment-rotation curves of the connection proposed by Freddi et al. (2020) in the case of: axial force and post-tensioned strands (Type B); including strong-axis aligned friction devices (Type C); including weak-axis aligned friction devices (Type D) (taken from Freddi et al. 2020)

as can be seen in Type C and D curves. Differences between the two curves is significant only at large drifts, because, due to the rotation of the connection, the centre of rotation moves towards the outer perimeter of the circular steel plate. This lengthens the lever arm between the centre of rotation and friction devices oriented along weak-axis, increasing their contribution to the whole moment capacity of the connection. Self-centring capacity is adequate, residual drift of the largest imposed cycle being about 5 mrad, usually considered as an acceptable threshold (e.g. McCormick et al. 2008).

Steel column base with preloaded threaded bars and friction devices

The solution developed at the University of Salerno, Italy, and University of Coimbra, Portugal, is characterized by a slotted column splice endowed with friction dampers arranged above a standard full-strength column base connection (Latour et al. 2019). More precisely, the symmetrical friction devices are characterized by vertically-oriented slotted holes in the upper part of the connection above the splice to allow the rotation of the column. Friction devices are arranged both on the flanges and the web of the column. The self-centring capability is provided by the combination of axial force and preloaded threaded bars. The latter ones are arranged at the mid-height of the column and are coupled with a stack of disc springs to prevent plastic deformations (Figure 3.31).

This connection is influenced by the same issue that affects the other ones, namely the variation of the contribution provided by the axial force to the whole moment strength due to seismic actions. Moreover, like New Zealander solutions, the connection is supposed to rotate around an edge or a corner when subjected to moment acting on one or two directions, respectively. Moment-rotation curve of one of the specimens tested in Latour et al. (2019) is reported in Figure 3.32. The connection provided wide and stable flag-shaped hysteretic cycles, with excellent self-centring capability.

To understand how this type of connection are designed, the main equations used are reported below.

A design moment capacity of the connection M_d is assumed, considering the moment capacity of the connected members equal to ΩM_d, where Ω is a suitable overstrength factor. To ensure self-centring behaviour of the connection, the moment capacity provided by threaded bars and axial force (decompression moment M_0) must be greater than or equal to that provided by friction pads, M_1.

The design shear capacity V_d is provided by web friction pads. Consistently with what is suggested by Ferrante Cavallaro et al. (2017, 2018), the clamping

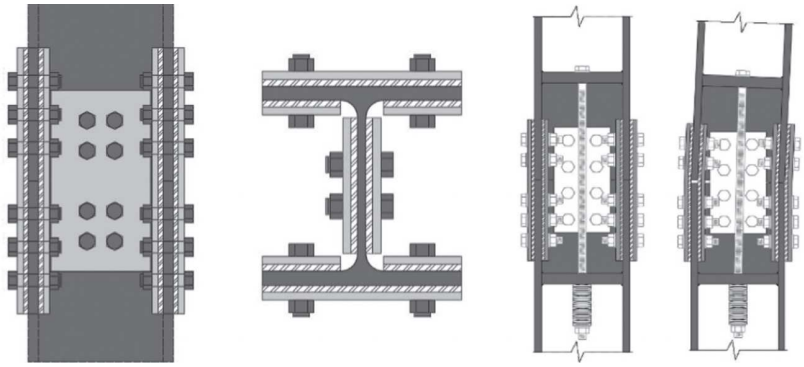

Figure 3.31 Column base connection with friction devices, preloaded threaded bars coupled with stacks of disc springs (taken from Latour et al. 2019)

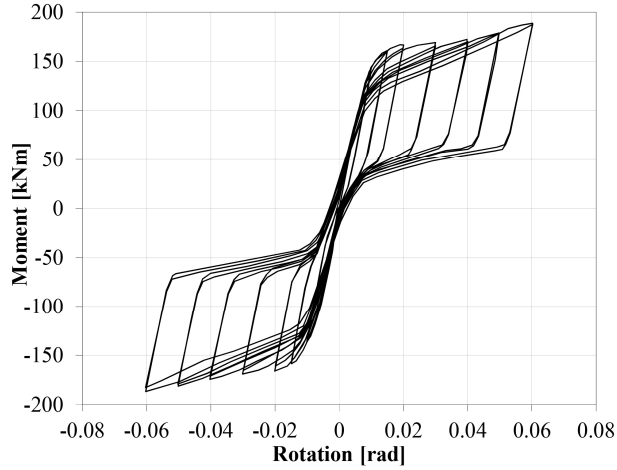

Figure 3.32 Experimental moment-rotation curve of the connection with friction devices, preloaded threaded bars coupled with stacks of disc springs (adapted from Latour et al. 2019)

force should be limited in the range 30-60% of the clamping force calculated according to EN 1993:1-8 (2005), in order to reduce the preload loss. For this reason, the ratio between the effective and maximum clamping force acting on the bolts employed in the web friction pads is computed as follows:

$$r_w = \frac{V_d}{\mu n_{ws} n_{wb} F_p} \tag{3.4}$$

μ being the friction coefficient, n_{ws} the number of friction interfaces, n_{wb} the number of bolts, and F_p the code-consistent clamping force. The moment capacity provided by the web friction pads is equal to:

$$M_{1,w} = r_w \mu n_{ws} n_{wb} F_p \frac{h}{2} \tag{3.5}$$

where the lever arm of the friction force is approximated to $h/2$. The ratio between the effective and maximum clamping force of the latter is:

$$r_f = \frac{M_{1,f}}{\mu n_{fs} n_{fb} F_p h} \tag{3.6}$$

in which n_{fs} is the number of interfaces and n_{fb} the number of bolts both referred to the flange. The moment capacity associated to the threaded bars $M_{0,tb}$ is the difference between the decompression moment M_0 and the bending moment associated to the axial force acting on the column, $M_{0,af.}$ The ratio between effective and maximum preload force to be applied to each bar is given by:

$$r_{tb} = \frac{M_0 - M_{0,af}}{n_{tb} F_{tb} \frac{h}{2}} \tag{3.7}$$

where n_{tb} is the number of bars and F_{tb} the maximum preloading force. Hence, the effective preload force is $F_{tb,eff} = r_{tb}\, F_{tb}$. With the aim of ensuring the elastic behaviour of the threaded bars, a group of disc springs has to be designed and coupled to the bars. An ultimate rotation of the system θ_u has to be selected based on the drift demand of the structure. The rotation θ_u leads to a gap-opening Δ, which has to be satisfy by a stack of disc springs, suitably arranged in series and in parallel. Once the global stiffness K_{ds} of the stack of disc springs is defined, the last step to define the moment-rotation behaviour of the connection is to calculate the stiffness of the branch after the attainment of M_d. Firstly, the stiffness of the threaded bar is computed as follows:

$$K_{tb} = \frac{E_{tb} A_{tb}}{l_{tb}} \tag{3.8}$$

where E_{tb} is the Young modulus of steel, A_{tb} is the cross-sectional area of threaded bar, l_{tb} is the threaded bar length. Then, the rotational stiffness of the connection considering both the stiffness of the threaded bars and the group of disc springs is expressed as:

$$K_\theta = \frac{1}{\frac{4}{h^2}\left(\frac{1}{n_{tb} K_{tb}} + \frac{1}{n_{tb} K_{ds}}\right)} \tag{3.9}$$

Column-to-foundation connections for RC/PC and timber structures

With regard to RC/PC structures, several solutions were developed, mainly focused on the use of post-tensioned tendons arranged within columns or shear walls (e.g. Priestley et al. 1999; Larkin et al. 2012a, 2012b). The energy dissipation devices are generally constituted by partially unbounded rebars connecting the member base and the foundation (Figure 3.33), but also the use of friction dampers was investigated (Li et al. 2020). During the rocking behaviour of the RC/PC members, the high stress concentration in the areas where compressive forces are transferred to the foundation lead to damage in the concrete cover.

Depending on the compressive strength of concrete and on the type and amount of transverse reinforcement, the damage could extend to the concrete core, limiting the low-damage capacity of the system. Moreover, rebars could buckle or fracture, reducing the energy dissipating capacity of the connection. It should be stressed that the tendons in the lateral force-resisting systems have to be anchored to the foundation and post-tensioned once the members are placed in the construction site, in the case of precast concrete structures. Moreover, particular attention has to be paid to the tension applied to the tendons, to their protection against corrosion and to potential loss of preload over their life cycle. These aspects hinder a widespread use of this technology.

It is worth mentioning the solution, initially developed for Cross Laminated Timber (CLT) shear walls, named Resilient Slip Friction Joint (RSFJ) (Hashemi et al. 2017). It is constituted by a symmetric bolted connection having two central plates with slotted holes and two cap plates, clamped together by high strength bolts. The surfaces in contact between the

Figure 3.33 Ducts for tendons before concrete casting within the footing (a); energy dissipation elements constituted by rebars embedded within the footing (b) (taken from Larkin et al. 2012a)

central plates and the cap plates are inclined and the preloaded bolts are coupled with disc springs, characteristics that provide both self-centring and dissipative capacity to the connection (Figure 3.34).

Experimental tests on RSFJs showed extraordinary stable flag-shaped hysteretic cycles (Figure 3.34e). Thanks to its compact shape, and its performance that can be adjusted by scaling its components, the RSFJ is an extremely versatile device. As a matter of fact, this device was successfully investigated as a tool to obtain low-damage structures also for steel MRFs at beam-to-column connections (Hashemi et al. 2018), steel tension-compression and tension-only braces (Hashemi et al. 2019; Bagheri et al. 2020), timber braces (Yousef-Beik et al. 2021).

Discussion

Among the above-presented solutions, the one of Latour et al. might be considered the most balanced solution between performance, ease of realization and cost-effectiveness. The one proposed by Freddi et al. is clearly the nearest to the goal of damage-free connection thanks to its circular plate at the column base. However, it seems cumbersome and complex to realize in a construction site. Those proposed by Borzouie et al. are the simplest and

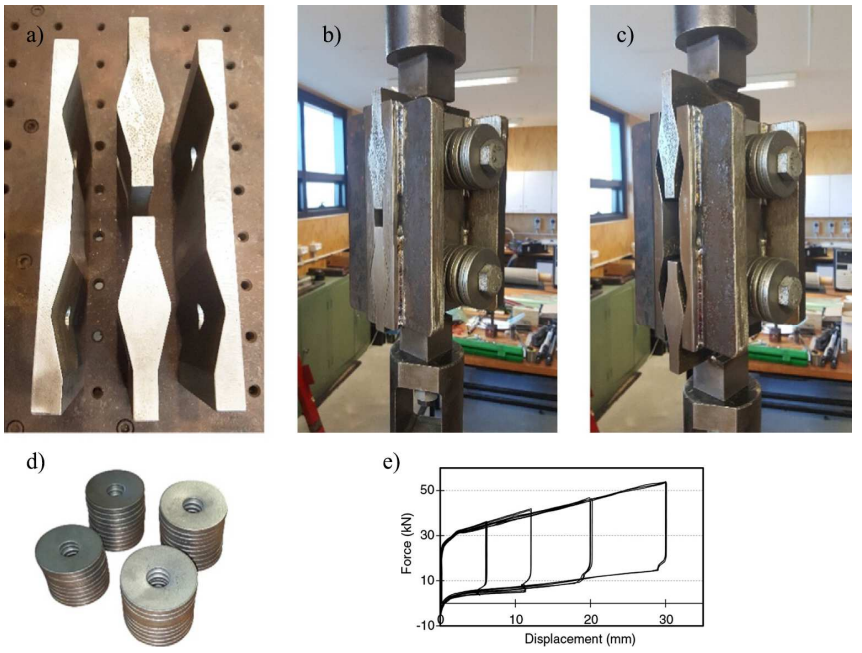

Figure 3.34 Resilient Slip Friction Joint: central slotted plates and cap plates (a); at rest (b); at the maximum displacement (c); stacks of disc springs (d); experimental force-displacement curve (e) (taken from Hashemi et al. 2017)

most economical, nevertheless provide satisfying performance. It should be stressed that Latour et al. and Borzouie et al. solutions are more prone to damage than that of Freddi et al., and in the case of damaged members (e.g. column or base joint), their substitution is challenging.

Concerning solutions for RC/PC structures, despite their promising results, they did not find a significant use in the construction market due to their difficulty to be realized in a construction site.

As regards RSFJ, this surely represents one of the most successful combinations between friction device, preloaded bolts and disc springs, and its main features must be kept in mind when developing a new solution for column-to-foundation connection. In Table 3.2 are summarized advantages and shortcomings of the preceding column-to-foundation connections.

All the preceding connections exploit the axial load acting on the column to achieve the self-centring capacity. This strategy answers to the need of

Table 3.2 Advantages and shortcomings of the column-to-foundation connections analysed

	Advantages	**Shortcomings**
Steel column base with AFC	Ease of realization	Self-centring capacity depending on the axial load
		The connection is supposed to rotate around an edge or a corner
Steel column base with post-tensioned strands and friction devices	Circular plate at the column base	Self-centring capacity depending on the axial load
	Adequate self-centering capacity	Cumbersome and complex to realize
Steel column base with preloaded threaded bars and friction devices	Ease of realization	Self-centring capacity depending on the axial load
	Adequate self-centering capacity	The connection is supposed to rotate around an edge or a corner
Self-centering connection for RC/PC structure	Reduced damage undergone by the column base	Potential buckle or fracture of the element costituting the energy dissipating devices
		Damage of the concrete at the column-to-foundation interface
		Difficulty in setting up the connection on the construction site
Resilient Slip Friction Joint (RSFJ)	Compact and efficient friction device	Difficulty to be inserted in a MRFs
	Stable cyclic behaviour	

reducing the dimensions of the structural components of the connections dedicated to the self-centring capacity, and thus their costs. However, the variability of the axial load due to the seismic action causes a significant variability of the moment capacity of the connection, for which higher overstrength factors must be used to avoid damage to the surrounding members. For this reason, when designing an earthquake-resilient MRF, the use of a connection which exploits the axial force to self-centre should carefully evaluate the above-mentioned advantages and shortcomings.

3.3 Common issues affecting friction connections

The above-mentioned structural solutions are highly influenced by two issues:

- characteristics of friction shim;
- bolt preload.

As for the first one, over the last years several research groups have focused their attention on the research of materials whose characteristics are optimal for this type of use. In Figure 3.35 a typical experimental test for the assessment of the friction properties of materials is illustrated (Latour et al. 2014). The specimen is constituted by two steel plates, one with normal clearance hole and the other one with slotted holes, connected by means of a double cover butt joint. Between the two steel plates and the cover plates are inserted two friction shims. The test is carried out by imposing to one of the two steel plates a displacement history. For instance, in Figure 3.36 the force-displacement curve of a specimen employing non-superficially-treated steel

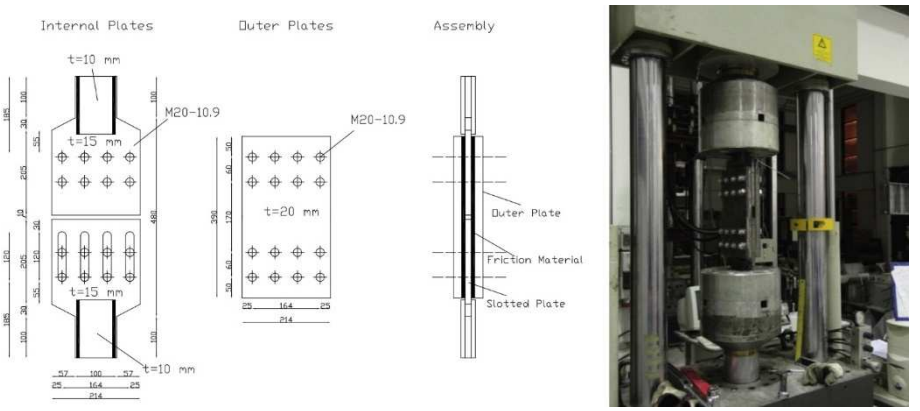

Figure 3.35 Typical experimental test for the assessment of the friction properties of materials (taken from Latour et al. 2014)

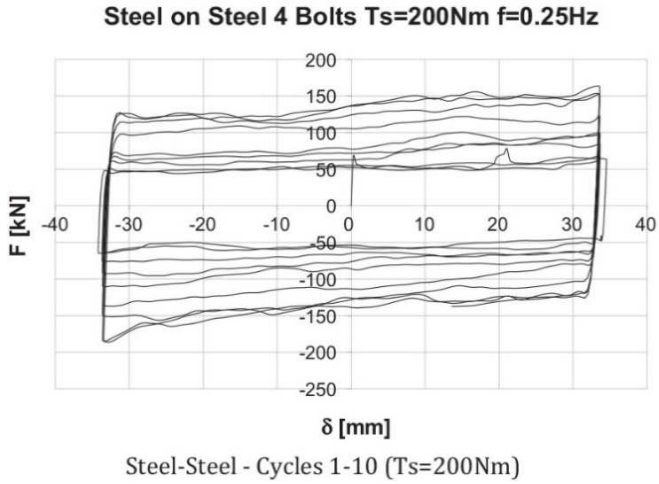

Figure 3.36 Force-displacement curve of a specimen employing non-superficially-treated steel as friction shims (taken from Latour et al. 2015)

as friction shims is reported. It can be noticed that, by incrementing the number of cycles, the required force to activate the slippage of the slotted steel plate increased considerably, tripling the initial value during the last cycles. This phenomenon was due to the increasing roughness of the surfaces in contact, which led to a higher friction coefficient. On the other hand, when superficially-treated steel is used as friction shims, the test outcomes can be the opposite, i.e. flattening of the superficial asperities which leads to a lower friction coefficient and, consequently, to a decreasing resistance of the friction connection. It is clear that these phenomena may hamper the cyclic behaviour of dissipative friction connections. For this reason, the optimal friction material has to provide a high friction coefficient in order to maximize the connection performance, and whose value remains stable during the cycles. Moreover, materials which might show relaxing phenomena (e.g. polymeric) should be avoided. Lastly, material durability must be taken into account, because the environmental conditions in which the connection is used could change the material properties during its life cycle.

Regarding the second issue, i.e. bolt preload, this is influenced by the procedure used to apply the preload and short- and long-term loss of preload. As a matter of fact, by using the common procedures to apply the preload (e.g. torque method) it is impractical to apply exactly the required preload. In Figure 3.37 the effective preload applied to a group of 15 bolts M20 class 10.9 is shown. The applied preload is measured by using a donut cell load between the bolt head and the steel plate through which the bolt is inserted. As can be seen, the variation is remarkable, having preloads at fractiles 95% and 5%

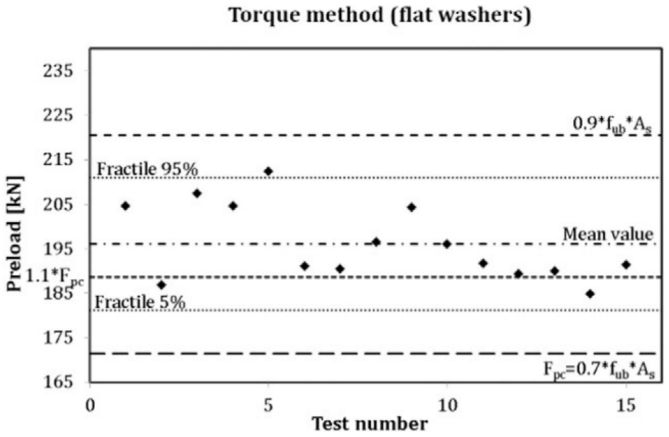

Figure 3.37 Effective preload applied to a group of 15 bolts M20 class 10.9 (taken from Ferrante Cavallaro et al. 2018)

equal to 212 kN and 182 kN, respectively. Therefore, such a variation of bolt preload affects the cyclic behaviour of friction connections. Other than the above-mentioned uncertainties, many studies have investigated the short- and long-term loss of bolt preload (e.g. Heistermann et al. 2013; D'Antimo et al. 2020). The loss of preloading is caused by several phenomena, such as the technique to apply the preload, creep of the material constituting the coating, relaxation due to the flattening of the asperities. The loss of preloading can be divided in three different phases (short-, mid-, and long-term), each one influenced by different aspects. In detail, the short-term loss, which occurs in the first 12-18 h after the application of the preload, represents most of the overall loss of preloading over time, and is mainly due to the tightening procedure. Then, the mid-term loss is observed during the first 30 days after the installation, and its magnitude is influenced by environmental temperature, issues regarding the tightening procedure, and applied external loads. After that, the long-term loss influences the remaining part of the life of the structure, and normally after 4-6 months the rate of loss assumes a constant value.

The evaluation of the loss of preloading over time is of paramount importance since it significantly influences the response of a structure when subjected to a seismic event. For this reason, the assessment of the seismic behaviour of a structure endowed with the above-described innovative connections should be carried out by considering several scenarios at different time in which the preload acting on the bolts changes consistently.

With the purpose of minimizing the loss of preloading, as already mentioned before, several Authors (e.g. Ferrante Cavallaro et al. 2017, 2018)

suggest to limit the bolt preload between 30% and 60% of the maximum value calculated by means of EN 1993:1-8.

3.4 Conclusions

On the basis of the analysis of the solutions found in the literature, the following considerations are drawn, which will be used to define the solutions for the beam-to-column and column-to-foundation connections, that are the aims of the present research.

With regard to the beam-to-column connection:

- symmetric dissipative system ensures a stable response in terms of bending moment capacity, at the same time reducing the stresses experienced by the bolts;
- steel angles connected to the vertical dissipative device remain within the elastic range, simplifying the constructional system with respect to the horizontal dissipative device;
- T stubs and/or L stubs of horizontal dissipative device(s) provide a bending moment contribution during sliding phase;
- the vertical dissipative device, as arranged by Latour et al. (2018), exhibits an undesired contribution as well, provided by the bolts of friction device that have to be dragged up and down during the sliding phase;
- the dissipative device used only at the lower part of the beam does not interfere with the other layers at the upper part of the beam, reducing or avoiding the damaging of the slab;
- the kinematic behaviour of the beam-to-column connection is predictable only if it is known a priori the position of the centre of rotation;
- separating the beam end section and the column face prevents that damage can occur at this interface;

With regard to the column-to-foundation connection:

- the use of combined friction devices and threaded bars coupled with stacks of disc springs is able to provide both energy dissipation capacity and self-centring behaviour;
- the circular steel plate with rounded edges at the column base is effective in preventing stress concentration and, therefore, potential damage of the elements.

With regard to the friction connection:

- loss of bolt preload due to plastic deformations has to be properly reduced inserting spring washers;
- loss of bolt preload due to short- and long-term effects can be reduced employing a bolt preload comprised between 30 and 60% of the maximum bolt preload calculated by means of EN 1993:1-8.

CHAPTER 4

ANALYTICAL EVALUATION OF SHEAR CAPACITY OF HSTC BEAMS

In this chapter, a design-oriented analytical model for shear strength evaluation of HSTCBs that can be extended to Reinforced Concrete (RC) beams with transverse reinforcement with two different inclinations also, is proposed. The model is based on the truss mechanism analogy with variable inclination of the concrete strut, and it is formulated with the aim of representing an extension of EN 1992:1-1 framework to RC beams with two orders of stirrups. The analytical procedure proposed aims at assessing the internal forces acting on the two differently-inclined orders of web steel rebars, as well as the magnitude of the compressive force acting on the concrete strut, and its inclination, for any layout and amount of shear reinforcement. Comparison between shear strength predictions provided by the model and test results available in the literature confirms the accuracy of the model.

4.1 Introduction

Shear failure in RC elements is one of the most undesirable modes of failure due to its rapid progression. Diagonal cracks are the warning signs of incipient shear failure. Usually, the inclined shear cracks start at the middle height of the beam or at the location of the longitudinal reinforcement, and extend towards the compression zone. In order to prevent shear cracking or reduce its width, web reinforcement has to be provided. Since the principal tensile stresses act in an inclined direction, the most effective configuration is obtained when the shear reinforcement is inclined along the direction of the principal tensile force. This circumstance makes the typical configuration of the web bar of the HSTCB beams particularly efficient in providing shear strength to the beam. However, the evaluation of HSTCBs shear strength, in the framework of model currently proposed in EN 1992:1-1 is challenging since they adopt a transverse reinforcement arranged with two different

inclinations (Amadio et al. 2011; Campione et al. 2016; Chisari and Amadio 2014; Colajanni et al. 2017a).

In the American code and past European codes, where shear strength was evaluated on the basis of the additive contributions due to concrete and steel reinforcement, the strength of reinforcement with multiple inclinations could easily have been taken into account by adding their contributions. Currently, the European design codes (e.g. EN 1992:1-1) contain no specific provisions for the abovementioned structural cases, and their design can be performed only by adjusting the existing models developed for other structural typologies. As already explained in Chapter 2, in the literature there are several models able to assess the shear strength of HSTCBs (or beams with two orders of transverse reinforcement). However, some of them are not design-oriented and, therefore, difficult to use (e.g. Colajanni et al. 2014b), and others are not fully consistent with the shear model presented in EN 1992:1-1 and, therefore, difficult to include in current European codes (e.g. Campione et al. 2016; Monti and Petrone 2015).

Within this framework, in this chapter an analytical model for the assessment of shear strength of HSTCBs is presented. The model is based on the truss mechanism analogy with variable inclination of concrete strut, which is the same approach used in the shear model proposed in EN 1992:1-1. For this reason, the design-oriented model proposed is developed in order to represent an extension of EN 1992:1-1 model not only to HSTCBs, but also to ordinary RC beams having transverse reinforcement arranged in two directions. The implication of different layout and amount of web reinforcement is analysed and the effectiveness of the proposed model is validated against experimental results.

4.2 Formulation of the analytical model

The design-oriented model here proposed, similarly of that commonly derived for ordinary RC beams, is based on a truss resisting mechanism characterized by variable inclination of a concrete strut. The resisting mechanism of the truss, schematized in Figure 4.1, is constituted by a steel bottom chord, a compressed concrete top chord, two orders of web bars arranged with two different inclinations α_1 and α_2, and a concrete web strut inclined by the angle θ, inclination yet to be determined. It has to be emphasized that, in ordinary RC beams the truss model can be interpreted as a "calculation model" that is equivalent to the actual multiple truss model shown in Figure 4.2a, while for HSTCBs the single truss model can be either

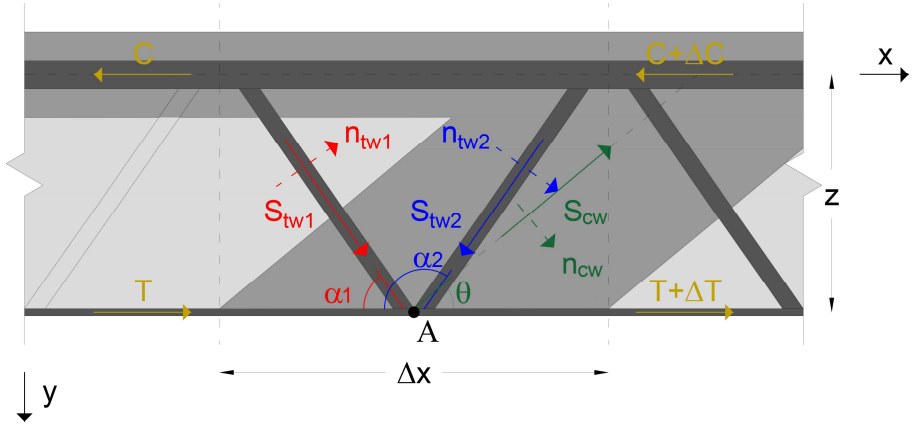

Figure 4.1 Truss mechanism analogy with variable inclination of concrete strut

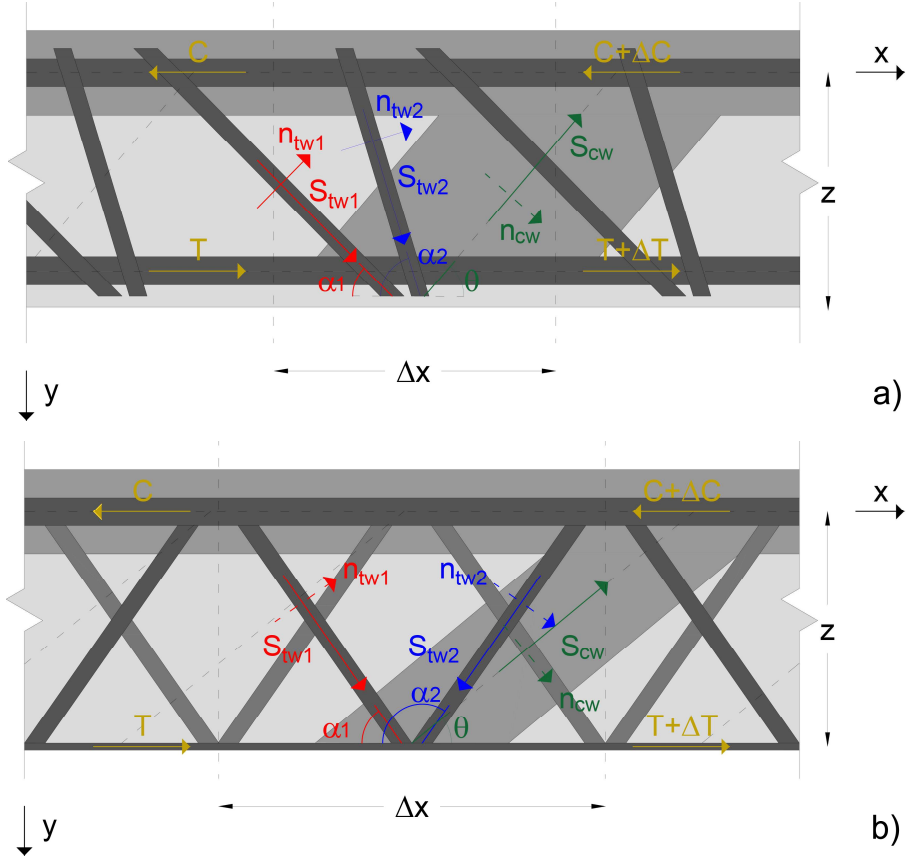

Figure 4.2 Multiple truss model: in ordinary RC beams (a); in HSTCBs with web bars shifted by half spacing length (b)

a physical model, when web reinforcement has a single web rib, or a calculation model, again equivalent to an actual multiple truss model, when

the HSTCBs have a multiple web bars, like the one in Figure 4.2b which presents two web bars shifted by half spacing length.

The proposed model is formulated by using the following notation: A_{tw1}, A_{tw2}, and s_{tw1}, s_{tw2} are the cross-sectional areas of the transverse web bars and their spacings, respectively; b_w and h are the web minimum width and the cross-section depth, respectively; f_{yd} and f'_{cd} the design yielding strength of steel and the design reduced compressive strength of concrete, respectively.

The above notation is able to consider steel truss with web bars of different diameter in the α_1 and α_2 directions, while different s_{tw1}, s_{tw2} spacings are also considered to generalize the model, in order to be applicable also to ordinary RC beams, while in HSTCB the two parameters, namely the inclination α and the spacing s are not independent. Assuming A_{twi} the cross-sectional area of the generic order of web bars, the respective mechanical ratios are:

$$\omega_{twi} = \frac{A_{twi} f_{yd}}{b_w s_{twi} f'_{cd} \sin\alpha_i} \qquad i = 1,2 \tag{4.1}$$

Moreover, the non-dimensional shear strength is equal to:

$$v = \frac{V}{b_w z f'_{cd}} \tag{4.2}$$

in which z is the lever arm of internal forces acting on the section. It should be reminded that, being the web concrete subjected to a biaxial state of stress and cracked in shear, the design compressive strength of concrete f_{cd} has to be multiplied by an efficiency coefficient ν' (≤ 1), obtaining the reduced design compressive strength $f'_{cd} = \nu' f_{cd}$. The values of ν' recommended by EN 1992:1-1 or by NTC 2018, namely $\nu' = 0.6(1-f_{ck}/250)$ or $\nu' = 0.5$, respectively, can be used. The non-dimensional stresses of the two orders of web bars and of the web concrete are calculated as follows:

$$\tilde{\sigma}_{cw} = \frac{\sigma_{cw}}{f'_{cd}} \qquad \tilde{\sigma}_{twi} = \frac{\sigma_{twi}}{f_{yd}} \quad i = 1,2 \tag{4.3}$$

In order to assess the shear strength of a RC beam, the direction cosines of the versors orthogonal to the elements constituting the truss (Figure 4.1) are defined as follows:

$$n_{tw1} = \begin{vmatrix} \sin\alpha_1 \\ -\cos\alpha_1 \end{vmatrix} \qquad n_{tw2} = \begin{vmatrix} \sin\alpha_2 \\ -\cos\alpha_2 \end{vmatrix} \qquad n_{cw} = \begin{vmatrix} \sin\theta \\ -\cos\theta \end{vmatrix} \tag{4.4}$$

The vectors of the forces acting on the elements constituting the truss are defined below, with respect to a coordinate system having x-direction parallel to the beam axis, and y-direction normal to the beam axis:

$$S_{tw1} = \begin{vmatrix} S_{tw1}\cos\alpha_1 \\ S_{tw1}\sin\alpha_1 \end{vmatrix} \qquad S_{tw2} = \begin{vmatrix} S_{tw2}\cos\alpha_2 \\ S_{tw2}\sin\alpha_2 \end{vmatrix}$$
$$S_{cw} = \begin{vmatrix} S_{cw}\cos\theta \\ -S_{cw}\sin\theta \end{vmatrix} \qquad \Delta T = \begin{vmatrix} -\Delta T \\ 0 \end{vmatrix} \tag{4.5}$$

in which S_{tw1}, S_{tw2}, S_{cw} and ΔT are equal to:

$$S_{cw} = \sigma_{cw}\, b\, \Delta x \sin\theta \qquad S_{twi} = \sigma_{twi}\frac{A_{twi}}{s_{twi}}\,\Delta x \quad i = 1,2$$
$$\Delta T = \Delta C = \frac{\Delta M}{z} = \frac{V\,\Delta x}{z} \tag{4.6}$$

The equilibrium equation of the node A in Figure 4.1 reads:

$$S_{tw1} + S_{tw2} + S_{cw} + \Delta T = 0 \tag{4.7}$$

By projecting the vector equilibrium equation in each of the three directions orthogonal to the compressed concrete strut θ, or to one of the two web bars, α_1 and α_2 respectively, three equations are obtained, in each of which only two resisting contributions appear. The three equations are obtained via the scalar product between the aforementioned vector and the vectors of the forces acting on the truss (Figure 4.1).

The equilibrium equation in the direction orthogonal to the concrete strut is equal to:

$$n_{cw}^T\, S_{tw1} + n_{cw}^T\, S_{tw2} + n_{cw}^T\, \Delta T = 0 \tag{4.8}$$

By using Eqs. (4.4) and (4.5), it is obtained:

$$\begin{aligned} &S_{tw1}\sin\theta\cos\alpha_1 + S_{tw1}\cos\theta\sin\alpha_1 + \\ &+S_{tw2}\sin\theta\cos\alpha_2 + S_{tw2}\cos\theta\sin\alpha_2 - \Delta T\sin\theta = 0 \end{aligned} \tag{4.9}$$

Rearranging Eq. (4.9), it yields:

$$\begin{aligned} &S_{tw1}\left(\sin\theta\cos\alpha_1 + \cos\theta\sin\alpha_1\right) + \\ &+S_{tw2}\left(\sin\theta\cos\alpha_2 + \cos\theta\sin\alpha_2\right) - \Delta T\sin\theta = 0 \end{aligned} \tag{4.10}$$

Substituting S_{tw1}, S_{tw2} and ΔT as defined in Eqs. (4.6), it follows:

$$\begin{aligned}&\sigma_{tw1}\frac{A_{tw1}}{s_{tw1}}\Delta x\sin\theta\left(\cot\theta+\cot\alpha_1\right)\sin\alpha_1+\\&+\sigma_{tw2}\frac{A_{tw2}}{s_{tw2}}\Delta x\sin\theta\left(\cot\theta+\cot\alpha_2\right)\sin\alpha_2-\frac{V\Delta x}{z}\sin\theta=0\end{aligned}\tag{4.11}$$

Each term is divided by Δx and $\sin\theta$:

$$\begin{aligned}&\sigma_{tw1}\frac{A_{tw1}}{s_{tw1}}\left(\cot\theta+\cot\alpha_1\right)\sin\alpha_1+\\&+\sigma_{tw2}\frac{A_{tw2}}{s_{tw2}}\left(\cot\theta+\cot\alpha_2\right)\sin\alpha_2-\frac{V}{z}=0\end{aligned}\tag{4.12}$$

Eq. (4.12) is divided by $b_w f'_{cd}$, while the first two terms are multiplied and divided by f_{yd} and $\sin\alpha_1$:

$$\begin{aligned}&\frac{\sigma_{tw1}}{f_{yd}}\frac{A_{tw1}\,f_{yd}}{b_w\,s_{tw1}\,f'_{cd}\sin\alpha_1}\left(\cot\theta+\cot\alpha_1\right)\sin^2\alpha_1+\\&+\frac{\sigma_{tw2}}{f_{yd}}\frac{A_{tw2}\,f_{yd}}{b_w\,s_{tw2}\,f'_{cd}\sin\alpha_2}\left(\cot\theta+\cot\alpha_2\right)\sin^2\alpha_2-\frac{V}{b\,z\,f'_{cd}}=0\end{aligned}\tag{4.13}$$

Introducing Eqs. (4.1) and (4.3) in (4.13), it is obtained the first equation to calculate the shear strength:

$$v=\tilde{\sigma}_{tw1}\omega_{tw1}\left(\cot\theta+\cot\alpha_1\right)\sin^2\alpha_1+\tilde{\sigma}_{tw2}\omega_{tw2}\left(\cot\theta+\cot\alpha_2\right)\sin^2\alpha_2\tag{4.14}$$

The equilibrium equation in the direction normal to the α_1 inclined bar is:

$$n_{tw2}^T S_{cw}+n_{tw2}^T S_{tw1}+n_{tw2}^T\Delta T=0\tag{4.15}$$

By using Eqs. (4.4) and (4.5), it is obtained:

$$\begin{aligned}&S_{cw}\cos\theta\sin\alpha_2+S_{cw}\sin\theta\cos\alpha_2+\\&+S_{tw1}\cos\alpha_1\sin\alpha_2-S_{tw1}\sin\alpha_1\cos\alpha_2-\Delta T\sin\alpha_2=0\end{aligned}\tag{4.16}$$

Rearranging Eq. (4.16), it is obtained:

$$\begin{aligned}&S_{cw}\left(\cos\theta\sin\alpha_2+\sin\theta\cos\alpha_2\right)+\\&+S_{tw1}\left(\cos\alpha_1\sin\alpha_2-\sin\alpha_1\cos\alpha_2\right)-\Delta T\sin\alpha_2=0\end{aligned}\tag{4.17}$$

Substituting S_{cw}, S_{tw1} and ΔT as reported in Eqs. (4.6), it follows:

$$\sigma_{cw}\, b_w\, \Delta x \sin^2\theta \left(\cot\theta + \cot\alpha_2\right)\sin\alpha_2 + \\ +\sigma_{tw1}\frac{A_{tw1}}{s_{tw1}}\Delta x\left(\cot\alpha_1 - \cot\alpha_2\right)\sin\alpha_1 \sin\alpha_2 - \frac{V\Delta x}{z}\Delta x \sin\alpha_2 = 0 \tag{4.18}$$

Each term is divided by Δx and $\sin\alpha_2$:

$$\sigma_{cw}\, b_w \sin^2\theta \left(\cot\theta + \cot\alpha_2\right) + \\ +\sigma_{tw1}\frac{A_{tw1}}{s_{tw1}}\left(\cot\alpha_1 - \cot\alpha_2\right)\sin\alpha_1 - \frac{V}{z} = 0 \tag{4.19}$$

Eq. (4.19) is divided by $b_w\, f'_{cd}$, while the second term is multiplied and divided by f_{yd} and $\sin\alpha_1$:

$$\frac{\sigma_{cw}}{f'_{cd}}\sin^2\theta\left(\cot\theta + \cot\alpha_2\right) + \\ +\frac{\sigma_{tw1}}{f_{yd}}\frac{A_{tw1}\, f_{yd}}{b_w\, s_{tw1}\, f'_{cd}\sin\alpha_1}\left(\cot\alpha_1 - \cot\alpha_2\right)\sin^2\alpha_1 - \frac{V}{b_w\, z\, f'_{cd}} = 0 \tag{4.20}$$

Substituting Eqs. (4.1) and (4.3) in (4.20), it is obtained the second equation to calculate the shear strength:

$$v = \tilde{\sigma}_{cw}\sin^2\theta\left(\cot\theta + \cot\alpha_2\right) + \tilde{\sigma}_{tw1}\,\omega_{tw1}\left(\cot\alpha_1 - \cot\alpha_2\right)\sin^2\alpha_1 \tag{4.21}$$

The equilibrium equation in the direction normal to the α_2 inclined web bar is equal to:

$$n_{tw1}^T\, S_{cw} + n_{tw1}^T\, S_{tw2} + n_{tw1}^T\, \Delta C = 0 \tag{4.22}$$

By using Eqs. (4.4) and (4.5), it is obtained:

$$S_{cw}\cos\theta\sin\alpha_1 + S_{cw}\sin\theta\cos\alpha_1 + \\ +S_{tw2}\cos\alpha_2\sin\alpha_1 - S_{tw2}\sin\alpha_2\cos\alpha_1 - \Delta C\sin\alpha_1 = 0 \tag{4.23}$$

Rearranging Eq. (4.23), it yields:

$$S_{cw}\left(\cos\theta\sin\alpha_1 + \sin\theta\cos\alpha_1\right) + \\ +S_{tw2}\left(\cos\alpha_2\sin\alpha_1 - \sin\alpha_2\cos\alpha_1\right) - \Delta C\sin\alpha_1 = 0 \tag{4.24}$$

Substituting S_{cw}, S_{tw2} and ΔC as defined in Eqs. (4.6), it follows:

$$\sigma_{cw}\, b_w\, \Delta x \sin^2\theta \left(\cot\theta + \cot\alpha_1\right)\sin\alpha_1 + \\ +\sigma_{tw2}\,\frac{A_{tw2}}{s_{tw2}}\,\Delta x\left(\cot\alpha_2 - \cot\alpha_1\right)\sin\alpha_1 \sin\alpha_2 - \frac{V\Delta x}{z}\sin\alpha_1 = 0 \tag{4.25}$$

Each term is divided by Δx and $\sin\alpha_1$:

$$\sigma_{cw}\, b_w \sin^2\theta \left(\cot\theta + \cot\alpha_1\right) + \\ +\sigma_{tw2}\,\frac{A_{tw2}}{s_{tw2}}\left(\cot\alpha_2 - \cot\alpha_1\right)\sin\alpha_2 - \frac{V}{z} = 0 \tag{4.26}$$

Eq. (4.26) is divided by $b_w\, f'_{cd}$, while the second term is multiplied and divided by f_{yd} and $\sin\alpha_2$:

$$\frac{\sigma_{cw}}{f'_{cd}}\sin^2\theta\left(\cot\theta + \cot\alpha_1\right) + \\ +\frac{\sigma_{tw2}}{f_{yd}}\,\frac{A_{tw2}\, f_{yd}}{b_w\, s_{tw2}\, f'_{cd}\sin\alpha_2}\left(\cot\alpha_2 - \cot\alpha_1\right)\sin^2\alpha_2 - \frac{V}{b_w\, z\, f'_{cd}} = 0 \tag{4.27}$$

By using Eqs. (4.1) and (4.3) in (4.27), it is obtained the third equation to calculate the shear strength:

$$v = \tilde{\sigma}_{cw}\left(\cot\theta + \cot\alpha_1\right)\sin^2\theta + \tilde{\sigma}_{tw2}\,\omega_{tw2}\left(\cot\alpha_2 - \cot\alpha_1\right)\sin^2\alpha_2 \tag{4.28}$$

Consistently with the static theorem of the theory of plasticity, the shear strength provided by the truss is obtained maximizing the resisting contribution of each element of the truss, as defined in Eqs. (4.14), (4.21) and (4.28), and satisfying the following conditions of plastic admissibility:

$$0 \le \tilde{\sigma}_{cw}, \left|\tilde{\sigma}_{tw1}\right|, \left|\tilde{\sigma}_{tw2}\right| \le 1 \tag{4.29}$$

By combining (4.14) and (4.21), or (4.14) and (4.28) with (4.29), the following inequalities, representing the plastic admissible condition for the force acting on the concrete strut, are derived:

$$0 \le (\tilde{\sigma}_{tw1}\omega_{tw1}\sin^2\alpha_1 + \tilde{\sigma}_{tw2}\,\omega_{tw2}\sin^2\alpha_2)\left(1+\cot^2\theta\right) \le 1 \tag{4.30}$$

(4.30) represents the interaction between the inclination of the concrete strut and the internal forces of the two orders of web bars. It should be noted that the equilibrium equations ((4.14), (4.21) and (4.28)) and the plastic

admissible conditions ((4.29) and (4.30)) are the same of the mechanical model proposed by Colajanni et al. (2014b) (i.e. (2.13)-(2.15), (2.16) and (2.17), respectively), despite the different initial assumptions (truss mechanism vs. stress field). However, in Colajanni et al. (2014b) the mechanical model exploits an iterative procedure to calculate the shear strength of RC beams by varying $\tilde{\sigma}_{tw1}$, $\tilde{\sigma}_{tw2}$, and $cot\theta$ within the plastic admissible conditions. This operation constitutes the main drawback of the mechanical model, because it hampers its use during the design phase. For this reason, in the following section an analytical procedure is for the first time developed to obtain equations able to provide the optimal values of the three above-mentioned parameters (e.g. $\tilde{\sigma}_{tw1}$, $\tilde{\sigma}_{tw2}$, and $cot\theta$), for any configuration and amount of transverse reinforcement, limited only to the absence of web longitudinal reinforcement ($\omega_{lw} = 0$).

4.3 Analytical evaluation of shear strength

In order to derive the analytical expression of the values of the three aforementioned parameters, preliminarily it has to be recognized that, since the truss model is one time redundant, according to the Nielsen's limit analysis application to the concrete members (Nielsen and Hoang 2011), the collapse condition is attained when at least two of the three components of the truss fail, i.e. reach their normalized stress limit values ±1.

Two different cases are now considered, depending on the inclination of the two web bars, namely the first case in which both α_1, and α_2 are $\leq 90°$, and the second case where $\alpha_1 \leq 90°$, and $\alpha_2 > 90°$. The former is consistent with ordinary RC beam layout, and is used to exploit a more effectiveness of reinforcement placed along the inclined direction of the principal tensile stress; the second one is distinctive of HSTCBs or over-reinforced sections, where the shear strength is limited by the capacity of the concrete web, as in thin-walled bridge sections.

4.3.1 $\alpha_1, \alpha_2 \leq 90°$

The maximum force acting on the concrete strut is obtained when its stress limit is reached ($\tilde{\sigma}_{cw} = 1$), i.e. (4.30) provides:

$$\tilde{\sigma}_{cw} = (\tilde{\sigma}_{tw1}\omega_{tw1}\sin^2\alpha_1 + \tilde{\sigma}_{tw2}\omega_{tw2}\sin^2\alpha_2)(1+\cot^2\theta) = 1 \qquad (4.31)$$

From (4.31) the expression of $cot\theta$ can be derived as follows:

$$\cot\theta = \sqrt{\frac{1}{\tilde{\sigma}_{tw1}\omega_{tw1}\sin^2\alpha_1 + \tilde{\sigma}_{tw2}\,\omega_{tw2}\sin^2\alpha_2} - 1} \qquad (4.32)$$

If the internal forces acting on the concrete strut and the two web bars are maximized, i.e. $\tilde{\sigma}_{tw1} = \tilde{\sigma}_{tw2} = 1$ and $\tilde{\sigma}_{cw} = 1$, the slope of the web concrete stress field can be evaluated as:

$$\cot\theta = \sqrt{\frac{1}{\omega_{tw1}\sin^2\alpha_1 + \omega_{tw2}\sin^2\alpha_2} - 1} \qquad (4.33)$$

Three cases can be considered, depending on the value of $cot\theta$ provided by (4.33):

- $1 \le cot\theta \le 2.5$: in this case, the shear strength can be easily evaluated by one of (4.14), (4.21) and (4.28), assuming $\tilde{\sigma}_{cw} = 1$, and $\tilde{\sigma}_{tw1} = \tilde{\sigma}_{tw2} = 1$ and $cot\theta$ provided by (4.33), since all provide the same value;
- $cot\theta > 2.5$: the shear strength is governed by the failure of the web bar in tension ($\tilde{\sigma}_{tw1} = \tilde{\sigma}_{tw2} = 1$), the limit value ($cot\theta = 2.5$) has to be assumed, and the dimensionless design shear strength v is evaluated by (4.14); the force acting on the concrete strut can be derived from the right-hand side of (4.31) assuming $\tilde{\sigma}_{tw1} = \tilde{\sigma}_{tw2} = 1$ and $cot\theta = 2.5$;
- $cot\theta < 1$: when (4.33) provides $cot\theta < 1$, and the concrete strut fails in compression, and one of the transverse reinforcement can be in the elastic range. Assuming $\alpha_1 < \alpha_2$, and setting $cot\theta = 1$, (4.30) reads:

$$(\tilde{\sigma}_{tw1}\omega_{tw1}\sin^2\alpha_1 + \tilde{\sigma}_{tw2}\,\omega_{tw2}\sin^2\alpha_2) \le 0.5 \qquad (4.34)$$

By direct inspection of (4.21) and (4.28), it can be stated that, since $cot\alpha_1 > cot\alpha_2$, the maximum shear strength is obtained as the minimum value given by the above equations (4.21) and (4.28), being:

$$\tilde{\sigma}_{tw1} = 1 \quad (a) \qquad \tilde{\sigma}_{tw2} = -1 \quad (b) \qquad (4.35)$$

In order to detect which of the two web bars yields, i.e. which of (4.21) and (4.28) provides the minimum shear strength and which of (4.35a)

and (4.35b) is true, (4.35a) and (4.35b) are assumed, and the inequality (4.21) < (4.28) can be rearranged in the following form:

$$\omega_{tw1}\sin^2\alpha_1 \le 0.5+\omega_{tw2}\sin^2\alpha_2 \tag{4.36}$$

Thus, if (4.36) is true, the web bar inclined of α_1 yields in tension ($\tilde{\sigma}_{tw1} = 1$), the shear strength is given by (4.21), while the stress in the web bar inclined of α_2 is:

$$\tilde{\sigma}_{tw2} = \left(0.5-\omega_{tw1}\sin^2\alpha_1\right)/\left(\omega_{tw2}\sin^2\alpha_2\right) \tag{4.37}$$

If inequality (4.36) is false, the web bar inclined of α_2 yields in compression ($\tilde{\sigma}_{tw2} = -1$), the shear strength is given by (4.28), while the stress in the web bar inclined of α_1 is:

$$\tilde{\sigma}_{tw1} = \left(0.5+\omega_{tw2}\sin^2\alpha_2\right)/\left(\omega_{tw1}\sin^2\alpha_1\right) \tag{4.38}$$

In order to represent the above conditions, the Cartesian plane of web bar mechanical ratios $\omega_{tw1} - \omega_{tw2}$ is considered, in which the following regions are detected:

Region 1. By means of (4.33), assuming $cot\theta > 2.5$, the following relation can be derived:

$$\omega_{tw1}\sin^2\alpha_1+\omega_{tw2}\sin^2\alpha_2 \le 7.25^{-1} \tag{4.39}$$

In this region, $cot\theta = 2.5$, $\tilde{\sigma}_{tw1} = \tilde{\sigma}_{tw2} = 1$ and the shear strength is developed at the yielding in tension of the two web bars;

Region 2. By means of (4.33), assuming $1 \le cot\theta \le 2.5$, the following condition is obtained:

$$7.25^{-1} \le \omega_{tw1}\sin^2\alpha_1+\omega_{tw2}\sin^2\alpha_2 \le 0.5 \tag{4.40}$$

In this region $\tilde{\sigma}_{tw1} = \tilde{\sigma}_{tw2} = 1$ and $cot\theta$ is given by (4.33); web concrete and the two web bars fails at the same time;

Region 3. By means of (4.33), assuming $cot\theta < 1$, the following conditions are obtained:

$$\omega_{tw1}\sin^2\alpha_1+\omega_{tw2}\sin^2\alpha_2 > 0.5 \qquad \omega_{tw1}\sin^2\alpha_1-\omega_{tw2}\sin^2\alpha_2 \le 0.5 \tag{4.41}$$

In this region $\tilde{\sigma}_{tw1} = 1$, $cot\theta = 1$, and $\tilde{\sigma}_{tw2}$ is provided by (4.37);

Region 4. By means of (4.36) the following condition is obtained:

$$\omega_{tw1}\sin^2\alpha_1-\omega_{tw2}\sin^2\alpha_2>0.5 \tag{4.42}$$

In this region $\tilde{\sigma}_{tw2}$ = -1, $cot\theta$ = 1 and $\tilde{\sigma}_{tw1}$ is provided by (4.38).

It should be emphasized that (4.14) and (4.33) constitute a direct extension of the equations contained in EN 1992:1-1 for evaluating the shear capacity of RC beams with a single order of transverse reinforcement.

4.3.2 $\alpha_1 \le 90°$, $\alpha_2 > 90°$

First of all, this layout is analysed considering the web bar with lower inclination (α_1) yielding in tension. If the failure of the concrete strut and the web bar with lower inclination is assumed, i.e. $\tilde{\sigma}_{cw} = \tilde{\sigma}_{tw1} = 1$, by (4.30) the following analytical expression of the stress in the second order of web bar $\tilde{\sigma}_{tw2}$ as a function of the concrete stress field slope θ is obtained:

$$\tilde{\sigma}_{tw2}=\frac{\sin^2\theta-\omega_{tw1}\sin^2\alpha_1}{\omega_{tw2}\sin^2\alpha_2} \tag{4.43}$$

By replacing (4.43) into (4.14) the following expression of the normalized shear strength is obtained:

$$\begin{aligned} v=&\tilde{\sigma}_{tw1}\omega_{tw1}\left(\cot\theta+\cot\alpha_1\right)\sin^2\alpha_1+\\ &+\frac{\left(\sin^2\theta-\omega_{tw1}\sin^2\alpha_1\right)\omega_{tw2}\left(\cot\theta+\cot\alpha_2\right)\sin^2\alpha_2}{\omega_{tw2}\sin^2\alpha_2} \end{aligned} \tag{4.44}$$

The value of shear strength provided by (4.44) has to be maximized with respect to the inclination of the web concrete strut θ. Therefore, taking the derivative with respect to θ, and setting it equal to zero, the following equation is obtained:

$$dv(x)/d\theta=2\sin\theta\cos\theta\left(\cot\theta+\cot\alpha_2\right)=0 \tag{4.45}$$

(4.45) can be rearranged in the following form:

$$\cot^2\theta+2\cot\theta\cot\alpha_2-1 \tag{4.46}$$

Thus, the positive solution of (4.46) is:

$$\cot\theta=-\cot\alpha_2+\sqrt{\cot^2\alpha_2+1} \tag{4.47}$$

If the possible inclination of the second order of web bar is considered only in the range $90° < \alpha_2 \leq 135°$, $cot\theta$ will be found in the range $1 \leq cot\theta \leq 2.5$. By replacing (4.47) into (4.43), two different cases can be found, namely:

- $-1 \leq \tilde{\sigma}_{tw2} \leq 1$: i.e. the stress satisfies the condition of plastic admissibility (4.29); thus the shear strength can be evaluated employing (4.14), (4.21) and (4.28), assuming $\tilde{\sigma}_{cw} = \tilde{\sigma}_{tw1} = 1$ and calculating $\tilde{\sigma}_{tw2}$ and $cot\theta$ by means of (4.43) and (4.47) respectively;
- $\tilde{\sigma}_{tw2} > 1$ or $\tilde{\sigma}_{tw2} < -1$: since the solution would violate the plastic admissibility condition, $\tilde{\sigma}_{tw2} = \pm 1$ is assumed (with the sign chosen depending on which of conditions (4.29) is violated by (4.43)), and $cot\theta$ is evaluated exploiting the following expression:

$$\cot\theta = \sqrt{\frac{1}{\omega_{tw1}\sin^2\alpha_1 \pm \omega_{tw2}\sin^2\alpha_2} - 1} \tag{4.48}$$

The result of (4.48) will be comprised in one of the three following ranges:

- $1 \leq cot\theta \leq 2.5$: in this case, the shear strength is given by any of (4.14), (4.21) and (4.28), which all provide the same value;
- $cot\theta > 2.5$: in this case, $cot\theta = 2.5$ is assumed, and v is evaluated through (4.14). The force acting on the concrete strut can be derived by the stress value calculated by (4.31);
- $cot\theta < 1$: when $cot\theta$ provided by (4.48) is less than one, the collapse is due to the failure of the web concrete and one of the web bars, and thus the other web bar can be in the elastic range. Analysing (4.21) and (4.28), it is observed that the maximum shear strength is obtained in each of the two equations by assuming respectively:

$$\tilde{\sigma}_{tw1} = 1 \quad (a) \qquad \tilde{\sigma}_{tw2} = -1 \quad (b) \tag{4.49}$$

Evidently, only one of (4.49a) and (4.49b) can be true, while the other stress has to ensure coincidence between the strength values provided by (4.21) and (4.28). Thus, the actual shear strength is equal to the minimum provided by (4.21) and (4.28) in which (4.49a) and (4.49b) respectively are assumed. In order to recognize the web bar mechanical ratio amount for which (4.49a) and (4.49b) is true, it is necessary to evaluate whether (4.21) or (4.28) gives the minimum shear strength

when (4.49a) and (4.49b) are assumed. Thus, (4.49a) holds, i.e. the first order of web bar yields in tension, if the following inequality is true:

$$\omega_{tw1} \sin^2 \alpha_1 \leq 0.5 + \omega_{tw2} \sin^2 \alpha_2 \tag{4.50}$$

In this case the shear strength can be easily evaluated by (4.21) where $cot\theta = 1$, and (4.49a) is assumed, and the stress in the second order of web bar can be evaluated employing (4.37). By contrast, if (4.50) is false, it turns out that failure is due to the failure of the web concrete and the second order of web bar at the same time, both in compression. Thus, the shear strength is provided by (4.28), where $cot\theta = 1$ and (4.49b) have to be assumed. The stress in the first order of web bar can be evaluated exploiting (4.38).

Thus, as done for the previous case, in the Cartesian plane of the web bar mechanical ratios $\omega_{tw1} - \omega_{tw2}$ the regions characterized by the previously evaluated solutions are:

Region 1: by means of imposing $cot\theta > 2.5$ in (4.48), the following condition is derived:

$$\omega_{tw1} \sin^2 \alpha_1 + \omega_{tw2} \sin^2 \alpha_2 \leq 7.25^{-1} \tag{4.51}$$

In this region $cot\theta = 2.5$, and $\tilde{\sigma}_{tw1} = \tilde{\sigma}_{tw2} = 1$ have to be assumed, and the failure is due to yielding of the two web bars;

Region 2: in this region, the web bars still both yield in tension ($\tilde{\sigma}_{tw1} = \tilde{\sigma}_{tw2} = 1$) and the concrete strut inclination is provided by (4.48). The upper border of this region is determined by imposing the condition that $cot\theta$ must reach the value provided by (4.47). Thus, by equating (4.33) and (4.47), the following expression of the upper boundary of region 2 is obtained:

$$\omega_{tw1} \sin^2 \alpha_1 + \omega_{tw2} \sin^2 \alpha_2 = \frac{1}{2}\left(1 + \cos \alpha_2\right) \tag{4.52}$$

Therefore, the region within $\tilde{\sigma}_{tw1} = \tilde{\sigma}_{tw2} = 1$ and $cot\theta$ provided by (4.48) is bounded by the following conditions:

$$\frac{1}{7.25} < \omega_{tw1} \sin^2 \alpha_1 + \omega_{tw2} \sin^2 \alpha_2 \leq \frac{1}{2}\left(1 + \cos \alpha_2\right) \tag{4.53}$$

In this region both the web concrete and two orders of web bars fails at the same time.

Region 3: this region is characterized by $\tilde{\sigma}_{tw1} = 1$, a fixed value of $cot\theta$ given by (4.47) and the elastic behaviour of the second order of web bar. Its stress can be evaluated by (4.43) once (4.47) is retained, as follows:

$$\tilde{\sigma}_{tw2} = \frac{0.5\left(1+\cos\alpha_2\right) - \omega_{tw1}\sin^2\alpha_1}{\omega_{tw2}\sin^2\alpha_2} \tag{4.54}$$

The boundaries of the region are determined by the second order web bar yielding in tension (4.52) or in compression, i.e. $\tilde{\sigma}_{tw2} = -1$; replacing the latter in (4.54) provides:

$$\omega_{tw1}\sin^2\alpha_1 - \omega_{tw2}\sin^2\alpha_2 = 0.5\left(1+\cos\alpha_2\right) \tag{4.55}$$

Thus, the region within which $\tilde{\sigma}_{tw1} = 1$, $\tilde{\sigma}_{tw2}$ given by (4.54) and $cot\theta$ given by (4.47) is bounded by:

$$\omega_{tw1}\sin^2\alpha_1 + \omega_{tw2}\sin^2\alpha_2 > 0.5\left(1+\cos\alpha_2\right) \tag{4.56}$$

$$\omega_{tw1}\sin^2\alpha_1 - \omega_{tw2}\sin^2\alpha_2 \le 0.5\left(1+\cos\alpha_2\right) \tag{4.57}$$

Region 4: in this region the two orders of web bar yield, the first one in tension ($\tilde{\sigma}_{tw1} = 1$) and the second one in compression ($\tilde{\sigma}_{tw2} = -1$) and $cot\theta$ is given by (4.48). The upper bound is found by imposing the condition that (4.48) has to provide the value $cot\theta = 1$. The boundaries of this region are defined by the following inequalities:

$$0.5(1+\cos\alpha_2) \le \omega_{tw1}\sin^2\alpha_1 - \omega_{tw2}\sin^2\alpha_2 \le 0.5 \tag{4.58}$$

Region 5: further increment of web bar mechanical ratios beyond the upper limit of region 4, i.e. when:

$$\omega_{tw1}\sin^2\alpha_1 - \omega_{tw2}\sin^2\alpha_2 > 0.5 \tag{4.59}$$

means that the tensile web bar stress $\tilde{\sigma}_{tw1}$ is in the elastic range and is given by (4.38), and $\tilde{\sigma}_{tw2} = -1$, $cot\theta = 1$ are the other parameter values. It has to be emphasized that for both the two aforementioned cases, namely α_1, $\alpha_2 \le 90°$, and $\alpha_1 \le 90°$, $\alpha_2 > 90°$, region 1 and region 2 are those of major practical interest, while the other regions describe the behaviour of beams over-reinforced in shear, and are only of practical interest in a few special cases.

4.3.3 Tensile and compressive chord failure

The model is able to detect premature failure of either the compressive or the tensile chord due to shear-flexure interaction. To this aim, the following two equations are proposed to calculate the internal forces in the top and bottom chords:

$$\tilde{T}(x) = \tilde{m}(x) + 0.5\left[\omega_{tw1}\tilde{\sigma}_{tw1}\left(\cot^2\theta - \cot^2\alpha_1\right)\sin^2\alpha_1 + \right.$$
$$\left. + \omega_{tw2}\tilde{\sigma}_{tw2}\left(\cot^2\theta - \cot^2\alpha_2\right)\sin^2\alpha_2\right] \quad (4.60)$$

$$\tilde{C}(x) = \tilde{m}(x) - 0.5\left[\omega_{tw1}\tilde{\sigma}_{tw1}\left(\cot^2\theta - \cot^2\alpha_1\right)\sin^2\alpha_1 + \right.$$
$$\left. + \omega_{tw2}\tilde{\sigma}_{tw2}\left(\cot^2\theta - \cot^2\alpha_2\right)\sin^2\alpha_2\right. \quad (4.61)$$

in which the non-dimensional bending moment is equal to:

$$\tilde{m}(x) = v\frac{x}{z} \qquad 0 \le x \le a \quad (4.62)$$

(4.60) and (4.61) are consistent with the evaluation of the additional tensile force in the bottom chord due to shear required by EN1992:1-1. The strength of the two chords has to satisfy the two following conditions of "plastic admissibility":

$$\tilde{T}(x) \le \omega_s \quad (4.63)$$

$$-\omega_s' \le \tilde{C}(x) \le \xi / \nu' + \omega_s' \quad (4.64)$$

where $\xi = x_c/z$ is the non-dimensional neutral axis depth, A'_s, $\omega'_s = (A'_s f_{yd})/(b_w z f'_{cd})$ and A_s, $\omega_s = (A_s f_{yd})/(b_w z f'_{cd})$ are the areas and the mechanical ratios of the longitudinal reinforcement in the compression and tension chords, respectively.

If the optimal parameters determined as described in the previous section do not satisfy either (4.63) or (4.64), the beam shear strength is ruled by the chord strength.

Substituting v with (4.14), (4.60) and (4.61) can be arranged as follows:

$$\cot^2\theta+\frac{2a}{z}\cot\theta+ \\ +\frac{\tilde{\sigma}_{tw1}\omega_{tw1}\sin^2\alpha_1\cot\alpha_1\left(\frac{2a}{z}-\cot\alpha_1\right)+\tilde{\sigma}_{tw2}\omega_{tw2}\sin^2\alpha_2\cot\alpha_2\left(\frac{2a}{z}-\cot\alpha_2\right)-2\tilde{T}(x)}{\tilde{\sigma}_{tw1}\omega_{tw1}\sin^2\alpha_1+\tilde{\sigma}_{tw2}\omega_{tw2}\sin^2\alpha_2}=0 \tag{4.65}$$

$$\cot^2\theta-\frac{2a}{z}\cot\theta+ \\ -\frac{\tilde{\sigma}_{tw1}\omega_{tw1}\sin^2\alpha_1\cot\alpha_1\left(\frac{2a}{z}-\cot\alpha_1\right)+\tilde{\sigma}_{tw2}\omega_{tw2}\sin^2\alpha_2\cot\alpha_2\left(\frac{2a}{z}-\cot\alpha_2\right)+2\tilde{C}(x)}{\tilde{\sigma}_{tw1}\omega_{tw1}\sin^2\alpha_1+\tilde{\sigma}_{tw2}\omega_{tw2}\sin^2\alpha_2}=0 \tag{4.66}$$

The optimal value of the three variables appearing in (4.65) and (4.66), i.e.: $\tilde{\sigma}_{tw1}$, $\tilde{\sigma}_{tw2}$ and $cot\theta$, should be determined according the amount of transverse mechanical ratios ω_{tw1} and ω_{tw2}. For instance, if the beam belongs to *"Case 1, Region 2",* the three parameter values are: $\tilde{\sigma}_{tw1} = \tilde{\sigma}_{tw2} = 1$ and $cot\theta$ variable. Consequently, $\tilde{\sigma}_{tw1} = \tilde{\sigma}_{tw2} = 1$ are assumed and $cot\theta$ is the only variable parameter in (4.65) and (4.66). According to this procedure, for each of the aforementioned cases/regions of ω_{tw1}-ω_{tw2} plane, the optimal values of two of the three parameters is known, and (4.65) or (4.66) can be solved to determine the third optimal value. In order to clarify the procedure in case of chord failure, the example below elucidates the flow chart of the strength evaluation. Once the shear capacity has been calculated by means of (4.14), (4.21) or (4.28), the internal forces acting on the tension and compression chords are computed using (4.60) and (4.61). Subsequently, the plastic admissibility conditions regarding the two chords are checked employing (4.63) or (4.64). If one of the two inequalities is not verified (e.g. $\tilde{T}(x) > \omega_s$) the limit is assumed (e.g. $\tilde{T}(x) = \omega_s$) and the $cot\theta$ related to the flexural failure is computed using (4.65), where $\tilde{\sigma}_{tw1} = \tilde{\sigma}_{tw2} = 1$.

The minimum amount of the bottom longitudinal reinforcement that ensures the shear failure of the beam can be calculated equating the external bending moment associated to the shear resistance of the beam (i.e. (4.62))

and the non-dimensional bending moment resistance associated to the tensile chord failure. The latter is computed by imposing the equality in (4.63) and substituting it in (4.60), as follows:

$$\tilde{m}(x) = \omega_s - 0.5\Big[\omega_{tw1}\tilde{\sigma}_{tw1}\left(\cot^2\theta - \cot^2\alpha_1\right)\sin^2\alpha_1 + \\ + \omega_{tw2}\tilde{\sigma}_{tw2}\left(\cot^2\theta - \cot^2\alpha_2\right)\sin^2\alpha_2\Big] \tag{4.67}$$

By equating (4.62) and (4.67) the mechanical ratio of the longitudinal reinforcement in the tensile chord that ensures the concurrent shear and flexural failure can be calculated as follows:

$$\omega_s = 0.5\Big[\omega_{tw1}\tilde{\sigma}_{tw1}\left(\cot^2\theta - \cot^2\alpha_1\right)\sin^2\alpha_1 + \\ + \omega_{tw2}\tilde{\sigma}_{tw2}\left(\cot^2\theta - \cot^2\alpha_2\right)\sin^2\alpha_2\Big] + v\frac{x}{z} \tag{4.68}$$

The non-dimensional shear resistance is computed using the procedures described in the previous sections, thus the only variable to be calculated in (4.68) is ω_s. If the mechanical ratio calculated by means of the above equation is greater than or equal to the mechanical ratio of the longitudinal reinforcement in the tensile chord of a generic beam, the RC member experiences flexural failure, otherwise the beam is shear critical. In order to elucidate the design implications related to the proposed model, in the following section some numerical analyses are carried out.

4.4 Model validation

The numerical model proposed in Colajanni et al. (2014b) was validated there, and in subsequent papers (Colajanni et al. 2016a, 2019). Here, in order to demonstrate the effectiveness of the proposed procedure for evaluation of parameter optimal values, prediction of some experimental results available in the literature, some on HSTC beams and others on ordinary RC beams with web reinforcements arranged along two different inclinations, is performed. The test results reported in Campione et al. (2016); Chisari and Amadio (2014); Mohammadyan-Yasouj et al. (2015); Richart (1927) are employed to carry out the validation. Beams tested by Campione et al. (2016); Chisari and Amadio (2014) are HSTCBs, while those tested by Mohammadyan-Yasouj et al. (2015); Richart (1927) are ordinary RC beams. Geometrical and mechanical characteristics as well as loading conditions of these specimens are reported in Table 4.1. In the beam strength evaluation, the mean values of

the material strength reported in the papers describing the experimental results were considered, without the use of partial safety factors. In the case of shear

Table 4.1 Geometrical and mechanical details of the investigated beams (TM: test method, 3P: three point bending, 4P: four point bending)

	ID	b_w mm	d mm	a mm	f_c MPa	$f_{y,s}$ MPa	$f_{y,l}$ MPa	A_s mm^2	A'_s mm^2	$A_{tw,1}$ mm^2	$A_{tw,2}$ mm^2	s_1 mm	s_2 mm	α_1 °	α_2 °	TM
Campione et al. (2016)	*A-1.2*	300	248	600	24	509	395	1500	1407	226	226	300	300	54	126	3P
	A-2.1	300	248	600	16	509	415	1902	1407	226	226	300	300	54	126	3P
	A-2.2	300	248	600	16	509	415	1902	1407	226	226	300	300	54	126	3P
	B-1	300	212	600	16	509	489	1407	1500	226	226	300	300	54	126	3P
	B-2	300	212	600	24	509	489	1407	1500	226	226	300	300	54	126	3P
Chisari and Amadio (2014)	*R0-B-B*	500	308	1338	39	551	397	8000	5024	402	402	450	450	30	90	3P
	R0-B-S	500	308	1338	39	402	397	8000	5024	402	402	450	450	30	90	3P
	R0-S-B	500	308	1338	39	551	397	8000	5024	402	402	450	450	30	90	3P
	R3-B-B	500	298	1338	39	551	423	11768	5024	402	402	450	450	30	90	3P
	R3-B-S	500	298	1338	39	402	423	11768	5024	402	402	450	450	30	90	3P
	R3-S-B	500	299	1338	39	551	402	11768	5024	402	402	450	450	30	90	3P
	R5-B-B	500	294	1338	39	551	433	14280	5024	402	402	450	450	30	90	3P
	R5-B-S	500	294	1338	39	402	433	14280	5024	402	402	450	450	30	90	3P
	R5-S-B	500	295	1338	39	551	404	14280	5024	402	402	450	450	30	90	3P
Mohammadyan-Yasouj et al. (2015)	*WB6*	750	210	700	29	620	466	2211	678	170	157	300	150	90	50	3P
Richart (1927)	*284.1*	203	254	610	18	439	436	791	0	36	36	152	152	60	90	4P
	284.5	203	254	610	20	383	447	791	0	81	81	152	152	60	90	4P
	290.3	203	254	610	19	444	414	645	0	81	81	152	152	60	90	4P
	290.5	203	254	610	19	403	392	645	0	41	41	152	152	60	90	4P

failure (S), when the beams are in region 1, two different shear capacities are computed depending on the maximum value of $cot\theta$ that is assumed (i.e. $cot\theta_{max}$=2.5 or $cot\theta_{max}$=3.0).

Conversely, when chord failure in tension occurs (TC), the shear strength provided by the model does not change whatever $cot\theta_{max}$ is employed, because the shear resistance is limited by the chord capacity. Moreover, it has to be noticed that specimen 290.3 from Richart (1927), an ordinary RC beam having high transverse mechanical ratio values ω_{tw1} and ω_{tw2} belonging to region 2, achieves tensile chord failure, while the second order of transverse reinforcement is in the elastic range.

The results shown in Table 4.2 highlight that the model reproduces the experimental data well, with an acceptable underestimation in the case of a concrete stress field inclination limited to 21.8 degrees ($cot\theta_{max}$=2.5), while a slight overestimation is registered when $cot\theta_{max}$ is equal to 3.0 instead of 2.5, as required by EN1992:1-1. These result are consistent with those reported in Colajanni et al. (2014b).

In general, the model predictions are accurate both when shear or chord failure occurs.

Table 4.2 Comparison between theoretical and experimental results

	ID	V_{exp} [kN]	Model proposed ($cot\theta_{max}$ = 2.5)	Model proposed ($cot\theta_{max}$ = 3.0)	Failure	$\tilde{\sigma}_{tw1}$	$\tilde{\sigma}_{tw2}$	cotθ	Reg.
Campione et al. (2016)	*A-1.2*	288.87	1.15	1.15	TC	1	1	1.56	2
	A-2.1	211.15	0.85	0.99	S	1	0.56	1.96	3
	A-2.2	230.65	1.16	1.16	S	1	0.56	1.96	3
	B-1	167.97	0.91	1.06	S	1	0.56	1.96	3
	B-2	259.77	0.77	0.89	TC	1	1	1.75	2
Chisari and Amadio (2014)	*R0-B-B*	538.88	1.15	1.15	TC	1	1	2.44	1
	R0-B-S	541.38	0.85	0.99	S	1	1	Max	1
	R0-S-B	535.75	1.16	1.16	TC	1	1	2.44	1
	R3-B-B	674.69	0.91	1.06	S	1	1	Max	1
	R3-B-S	581.44	0.77	0.89	S	1	1	Max	1
	R3-S-B	582.69	1.06	1.23	S	1	1	Max	1
	R5-B-B	655.92	0.92	1.07	S	1	1	Max	1
	R5-B-S	610.23	0.72	0.84	S	1	1	Max	1
	R5-S-B	642.77	0.95	1.10	S	1	1	Max	1
Mohammadyan-Yasouj et al. (2015)	*WB6*	317.5	0.92	0.92	TC	1	1	1.33	1
Richart (1927)	*284.1*	118.84	0.94	0.94	TC	1	1	2.28	1
	284.5	122.62	1.11	1.11	TC	1	1	1.3	1
	290.3	96.16	1.15	1.15	TC	1	0.69	1	2
	290.5	87.48	1.03	1.03	TC	1	1	1.7	1
Avg.			0.97	1.03					
CoV			0.15	0.13					

Below some parametric analyses are carried out aiming at illustrating the effect of different values of ω_{tw1} and ω_{tw2}. Since continuous variation of the latter parameters are considered, the analysis represents better the behaviour of ordinary RC beams, where continuous variation of ω_{tw1} and ω_{tw2} can be obtained via variation in stirrup spacing, inclination, and bar diameter, rather than behaviour of HSTCBs where spacing and inclination are correlated.

Thus, in a first case, two transverse stirrup orders with inclinations α_1 = 45° and α_2 = 90° are considered, while in the second one the inclinations are α_1 = 90° and α_2 = 120°. In Figure 4.3, in the Cartesian plane of the mechanical transverse reinforcement ratios ω_{tw1} and ω_{tw2} the boundaries of the four/five regions are represented. The values of the coordinates of the characteristic points are reported in Table 4.3. In Figures 4.4a and 4.4b, for the first case, the values of $cot\theta$ and non-dimensional shear strength vs. the amount of web bar reinforcement ω_{tw1} and ω_{tw2} are represented in the range $0 \leq \omega_{twi} \leq 0.6$ (i = 1, 2), showing the greater efficiency of the first order of web reinforcement placed with a slope of α_1 = 45° with respect to the case in which the reinforcement are vertical (α_2 = 90°).

In Figures 4.5a and 4.5b, the non-dimensional stresses for the two orders of web reinforcement varying the amount of the web reinforcement ratios ω_{tw1} and ω_{tw2} respectively are shown. It can be observed that the first order of web reinforcement always yields in tension, except for $\omega_{tw1} \geq 1$, corresponding to region 4, in which the bars are in the elastic range. Conversely, the second

Table 4.3 Values of the coordinates of the characteristic points highlighted in Figure 4.3

Points	ω_{tw1}	ω_{tw2}
A	$(2\sin^2\alpha_1)^{-1}$	0
B	0	$(2\sin^2\alpha_2)^{-1}$
$C = E$	$(7.25\sin^2\alpha_1)^{-1}$	0
$D = F$	0	$(7.25\sin^2\alpha_2)^{-1}$
G	$(1+\cos\alpha_2)/(2\sin^2\alpha_1)$	0
H	0	$\left[2(1-\cos\alpha_2)\right]^{-1}$
I	$(2\sin^2\alpha_1)^{-1}$	0

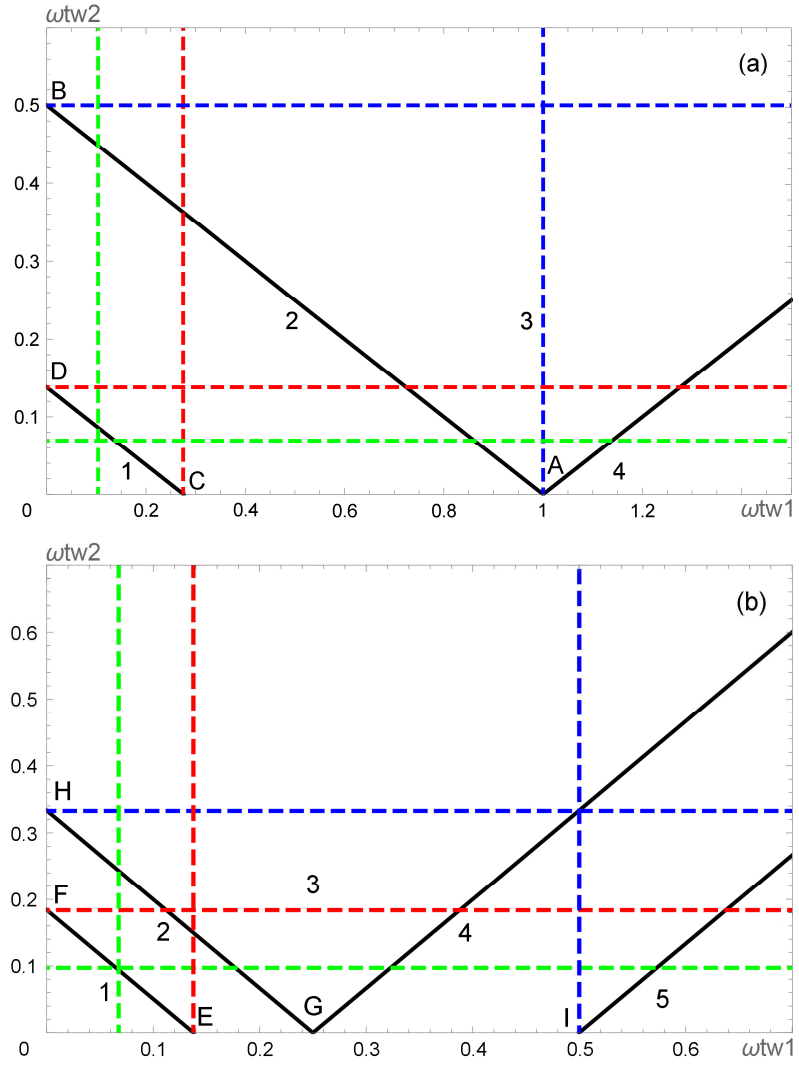

Figure 4.3 Regions for evaluation of shear strength vs. ω_{tw1} and ω_{tw2}: (a) Case 1: $\alpha_1 = 45°$ and $\alpha_2 = 90°$; (b) Case 2: $\alpha_1 = 90°$ and $\alpha_2 = 120°$

order of web reinforcement yields in tension only when a small amount of web reinforcement is employed, i.e. regions 1 and 2. Incrementing ω_{tw2} over the upper boundary of region 2 leads the α_2 inclined web reinforcement to have a stress in the elastic range. Lastly, if ω_{tw1} is also increased, the second order will yield in compression. In Figure 4.6a the curves of the non-dimensional shear strength vs. ω_{tw2} (amount of vertical web reinforcement) for the three characteristic values of ω_{tw1} (inclined web reinforcement), represented in Figure 4.3a with a dashed line of the same colour as used in Figure 4.6a, are shown. The green curve represents the case in which the

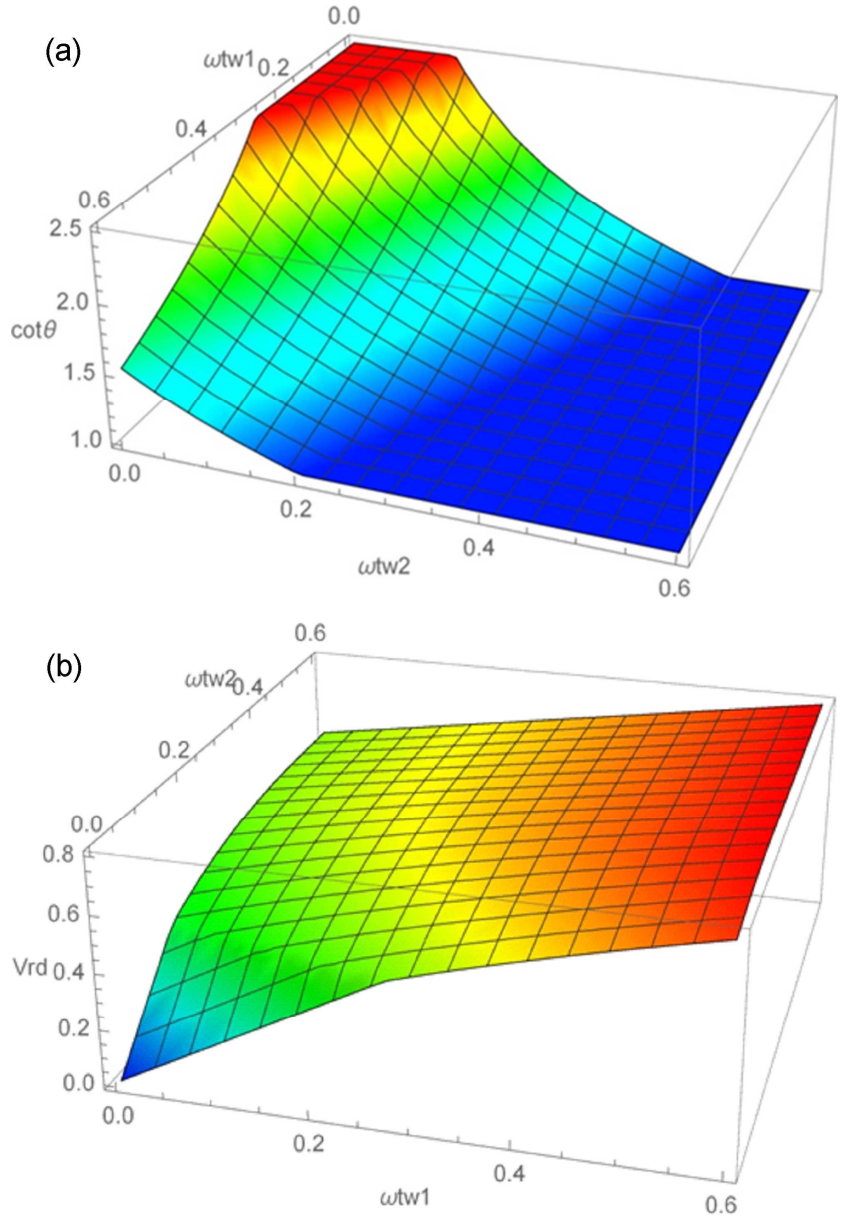

Figure 4.4 Case 1: inclination of web concrete stress field (cotθ) (a) and non-dimensional shear strength (b) vs. ω_{tw1} and ω_{tw2}

amount of inclined web reinforcement is equal to the minimum value of stirrups required by NTC 2018 in ordinary RC beams, $\omega_{twi,\,min} = 1.5\, f_{yd} / (1000\, f'_{cd}\, \sin \alpha_i) = \{0.1\ (i = 1),\ 0.07\ (i = 2)\}$. The red curve refers to the case in which the inclined web reinforcement alone is able to provide the condition of failure of two inclined web reinforcements and web concrete at the same

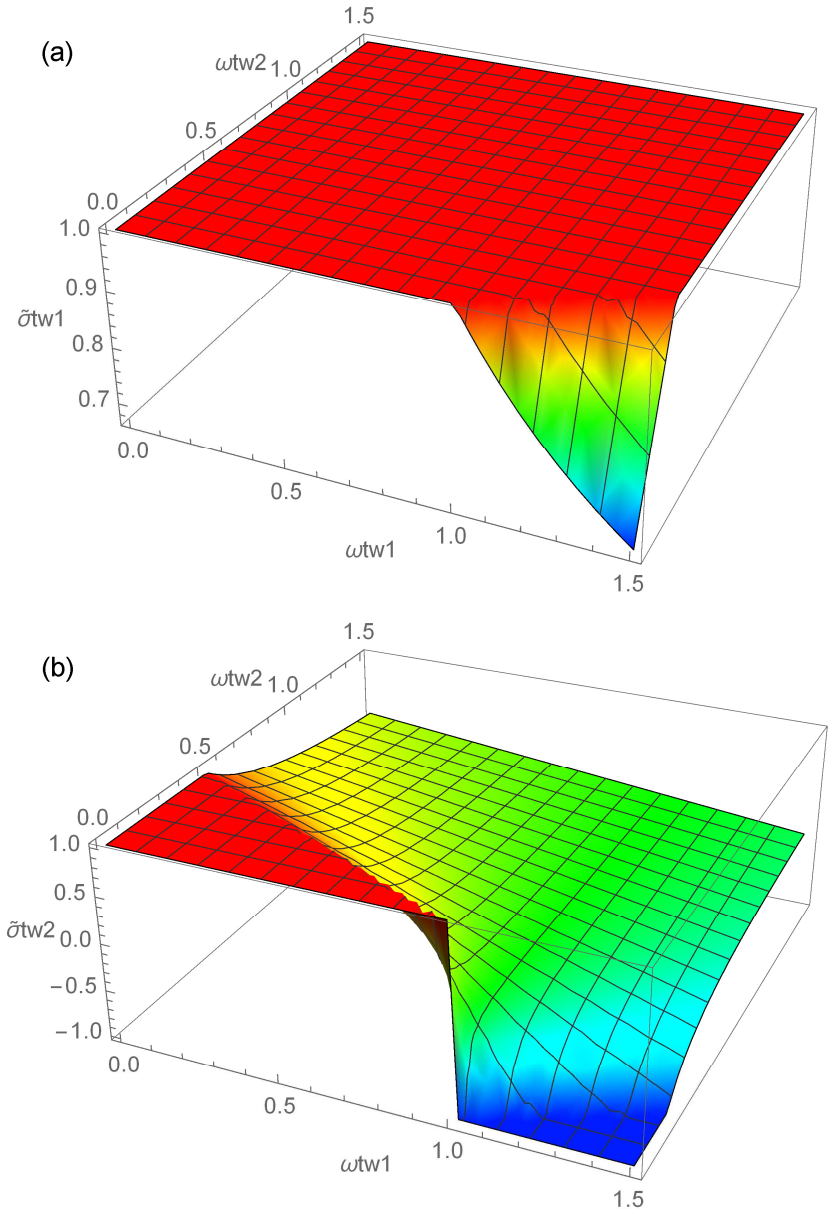

Figure 4.5 Case 1: non-dimensional stress (first order (a), second order (b)) of transverse reinforcement vs. ω_{tw1} and ω_{tw2}

time, while the blue one corresponds to the maximum shear strength that can be obtained with a single order of web reinforcement. The curves show that vertical web reinforcement are only effective when a small amount of inclined web reinforcement are placed in the beam ($\omega_{tw1,\ min} = 0.1$). In Figure 4.6b the corresponding curves of the non-dimensional shear strength vs. ω_{tw1} for a fixed

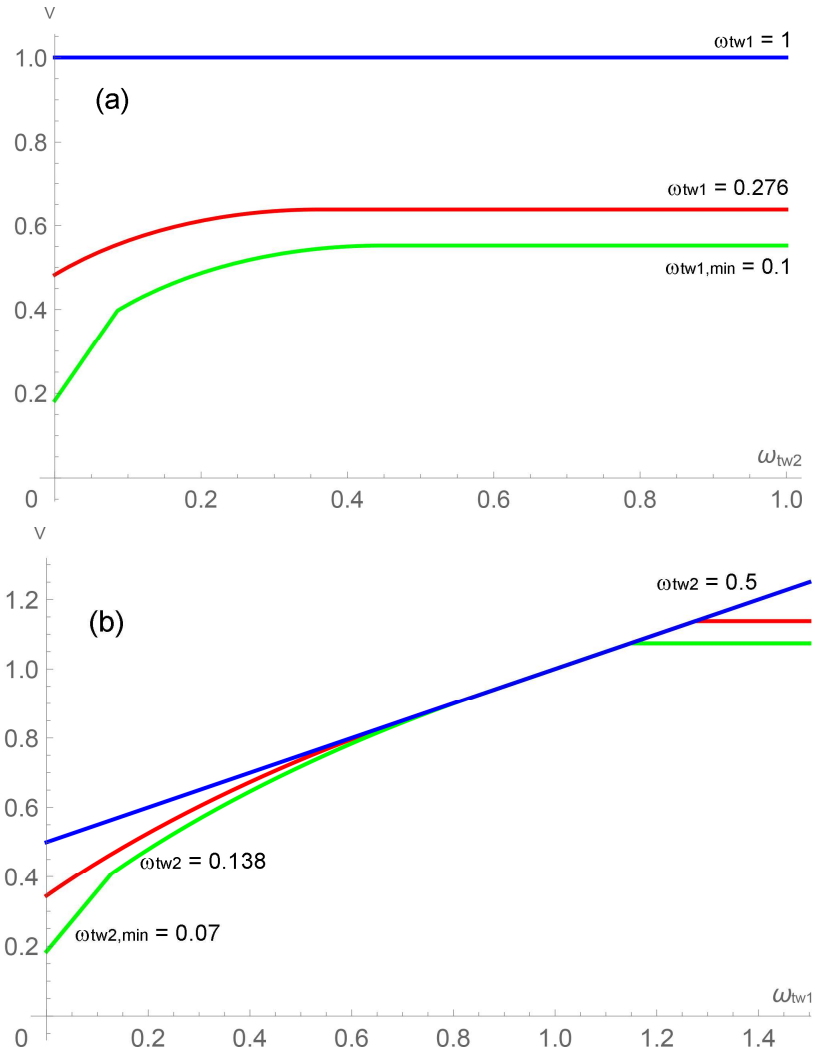

Figure 4.6 Case 1: non-dimensional shear strength vs.: ω_{tw2} for characteristic values of ω_{tw1} (a), ω_{tw1} for characteristic values of ω_{tw2} (b)

value of ω_{w2} are reported. They show that, by increasing the amount of inclined web reinforcement, the shear strength increases unless the mechanical ratio ω_{w1} is more than 1. Above the latter value, the shear resistance remains constant, because of the failure in compression of both the vertical web reinforcement and the web concrete, i.e. $\tilde{\sigma}_{tw2} = -1$ and $cot\theta = 1$. Only an increment of vertical web reinforcement, which are compressed in this over-reinforced configuration, is able to increase the shear strength, allowing the concrete strut to withstand the compressive forces of the truss mechanism.

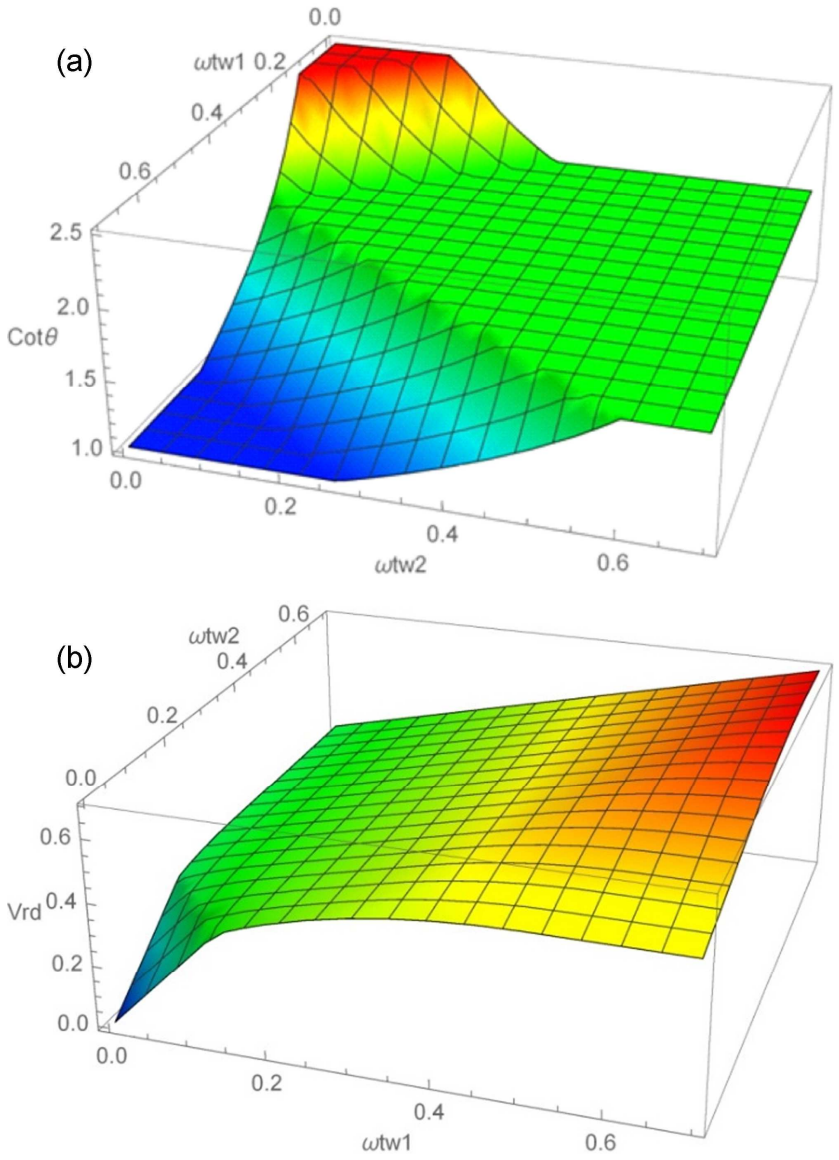

Figure 4.7 Case 2: inclination of web concrete stress field (cotθ) (a) and non-dimensional shear strength (b) vs. ω_{tw1} and ω_{tw2}

Figures 4.7-4.8 refer to the second case, where the first order of reinforcement represents the traditional vertical stirrups ($\alpha_1 = 90°$), while the second order has $\alpha_2 = 120°$. The stress trend of the two orders of transverse reinforcement is comparable to that described for case 1; thus it is not reported here. It can be noticed that inclined reinforcements with slope $\alpha_2 > 90°$ are only effective in small amounts for beams with a very small amount of vertical

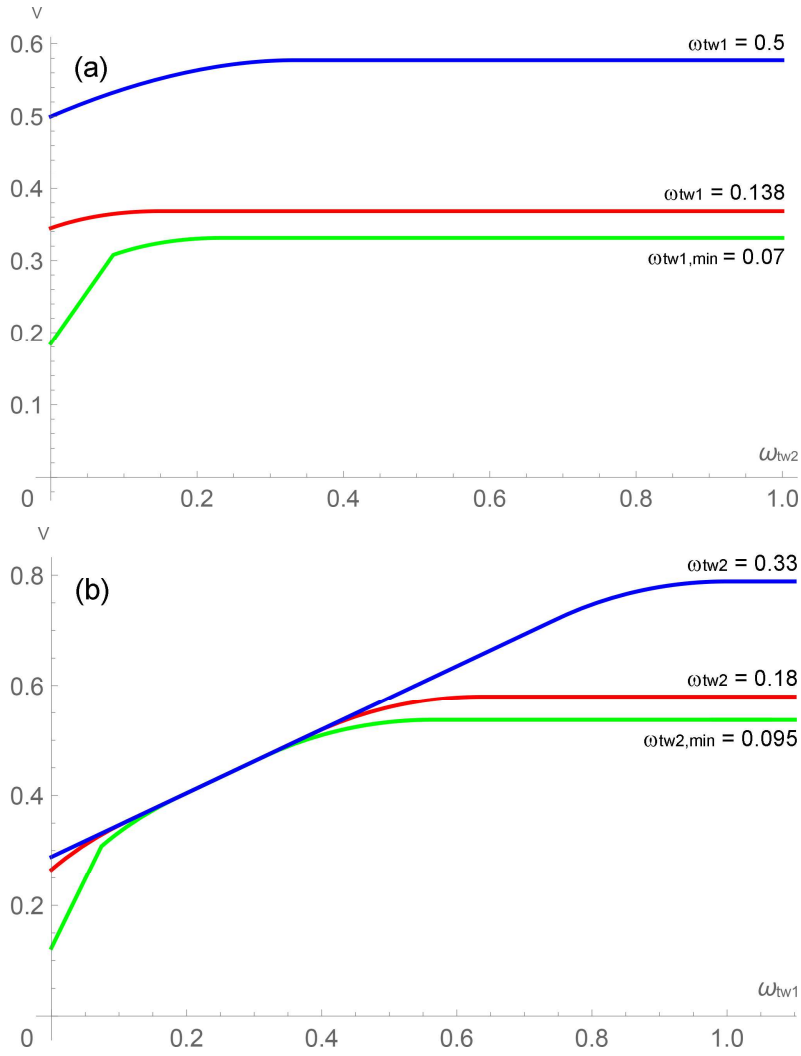

Figure 4.8 Case 2: non-dimensional shear strength vs.: ω_{tw2} for characteristic values of ω_{tw1} (a), ω_{tw1} for characteristic values of ω_{tw2} (b)

stirrups (green line in Figure 4.8a) or for over-reinforced beams (Figure 4.8b, $\omega_{tw1} > 0.5$).

4.5 Conclusions

A design-oriented model able to predict the shear capacity of HSTCBs and RC beams with transverse reinforcement arranged with two different inclinations was proposed. Since the evaluation of shear strength is obtained using the commonly-named "lower-bound solution" (Prager 1959; Nielsen and Hoang 2011), a closed-form procedure for maximizing the element shear

capacity by varying the stress in the two orders of web reinforcement and the value and inclination of the web concrete compressive strut was derived.

The analytical procedure depends on whether both the orders of web reinforcement have angles of inclination, with respect to the beam axis, in the range $45° \leq \alpha_i \leq 90°$ ($i = 1, 2$), or only the first-order inclination is in the range $45° \leq \alpha_1 \leq 90°$ while the second-order inclination is in the range $90° < \alpha_2 \leq 135°$. For each of the two aforementioned cases, and for any amount of mechanical ratio of web reinforcement, equations for evaluating the parameters influencing the shear resistance, namely slope of the web concrete strut and the stresses acting on the two orders of web reinforcement, were proposed. Moreover, equations able to consider premature failure of either the compressive or the tensile chord due to shear-flexure interaction were included. Referring to continuous variation of transverse reinforcement ratios $\omega_{w1} - \omega_{w2}$, regions characterized by homogeneous behaviour of the three abovementioned parameters were detected, and equations for evaluating the boundaries of these regions were determined. The comparison carried out between the analytical predictions provided by the model and experimental results of shear critical HSTCBs and ordinary RC beams demonstrated the accuracy of the model. The main equations constituting the model (e.g. (4.14) and (4.33)) prove that the proposed model represents a direct extension of the EN 1992:1-1 model for the shear assessment of ordinary beams with two orders of transverse reinforcement. Major issues deserving further research include the investigation of layout of HSTCB with added vertical stirrups, design effectiveness of different transverse reinforcement amounts and inclinations, as well as the use of a larger database covering all the regions identified by the model in order to prove its reliability thoroughly.

CHAPTER 5

MACRO-MODELLING OF THE CYCLIC BEHAVIOUR OF RC BEAM-COLUMN JOINTS

Beam-column joints are the structural members which transfer forces between columns and beams. Capacity design of seismic-resistant structures requires that the joints behave elastically, while the beams are supposed to undergo plastic deformations and dissipate seismic energy. To this aim, it is of crucial importance to properly design the geometry of the joint and the reinforcement passing through it. On the contrary, in the case of beam and column having small cross-sections and large-diameter longitudinal reinforcement, and small amount of transverse reinforcement within the joint, the latter is subjected to high shear forces due to seismic actions causing loss of stiffness and strength. These characteristics are common for joints of RC buildings realized by means of HSTCBs. For these reasons, a thorough analysis of these RC buildings, which will be carried out in Chapter 8, should take into account the inelastic behaviour of beam-column joints. Therefore, the main goal of this chapter is to derive an approach for the implementation in FE software packages, and calibration of the parameters of a model already proposed in the literature able to represent the cyclic behaviour of beam-column joints of ordinary frames. Its reliability in reproducing the behaviour of HSTCB-column joints is checked by reproducing experimental results of an RC subassembly of HSTCB-column joint subjected to reversed cyclic actions. More precisely, the chapter is organized as follows:

- in the first part the assessment of the forces acting on joints when subjected to cyclic actions and their resisting mechanisms are described. Then, phenomena influencing cyclic behaviour of joints are pointed out, outlined the common strategies used to mitigate the loss of strength and stiffness caused by them;
- in the second part, a model proposed by Lowes and Altoontash (2003), able to represent efficiently the cyclic response of beam-column joints, is presented;

- in the third part, the adopted approach and its constituting elements are described. Subsequently, two constitutive laws used to reproduce the different mechanisms characterizing the cyclic response of joints are introduced;
- the fourth part describes the application of the above-mentioned procedure to an RC subassembly realized with HSTCBs and experimental and numerical force-displacement curves are compared.

5.1 Cyclic behaviour of RC beam-column joints

5.1.1 Forces acting on the joint and internal resisting mechanisms

The forces transferred by beams and columns to an RC internal joint are illustrated in Figure 5.1. These forces include tensile and compressive forces T_S and C_S acting on the beam and column longitudinal bars, and the resultant of the compressive stresses C_C on concrete due to bending moment. Generally speaking, the real distribution of tangential stresses at the interface between panel zone, beams and columns is unknown. This uncertainty is due to the cracks generated by bending moment and potential slippage of the longitudinal bars caused by loss of bond strength. When the width of flexure-generated cracks is relatively small, shear forces can be transferred to the joint by considering the whole height of the beam or column cross-sectional height. By contrast, when the cracks widen, it is reasonable assuming that the shear forces are mainly transferred to the joint via the compressive areas due to bending moment.

In Figure 5.1a are schematized a group of diagonal crack developed within the panel zone oriented parallel to the principal compressive stresses. Once the joint is cracked, two different resisting mechanisms can be identified: *diagonal strut* (Figure 5.1b) and *truss mechanism* (Figure 5.1c). The whole shear resistance of the joint is the combination of the contributions given by the two above mechanisms, which however are effective at different steps of a cyclic loading process.

The diagonal strut mechanism (Figure 5.1b) absorbs the forces acting at the four external faces of the joint, i.e. C_C, column and beam shear force V_{col}, V_b, respectively, and a percentage of F_b, due to longitudinal bars, related to bond stresses within the nodal zone. In fact, compressive stresses due to bending moment generate ideal confinement conditions at the nodal zones of

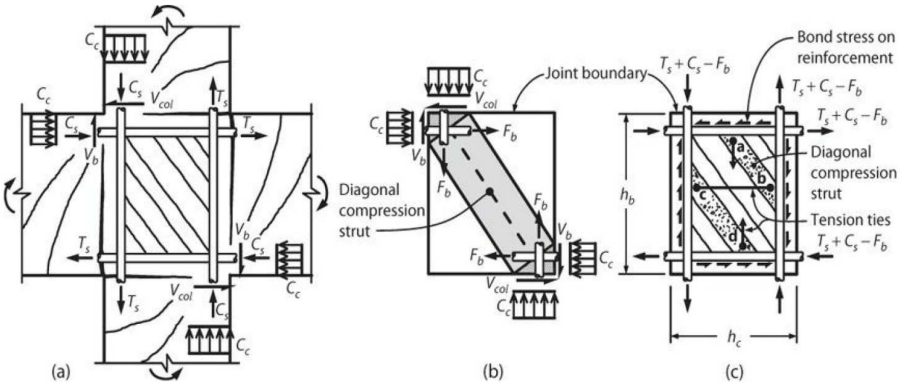

Figure 5.1 Resisting mechanisms of an RC internal joint (taken from Moehle 2014)

the diagonal strut; therefore, the force F_b is a significant fraction of the whole force transferred by the longitudinal reinforcement. The diagonal strut does not require transverse reinforcement to achieve equilibrium. Notwithstanding this, transverse reinforcement can be used to confined the panel zone, potentially increasing compressive strength and ductility.

Conversely, through the *truss resisting mechanism* (Figure 5.1c), the remaining fraction of the forces transferred by the longitudinal bars, namely $T_S + C_S - F_b$, are in equilibrium by exploiting shear strength of the panel zone. For simplicity's sake, bond stresses between concrete and bars are supposed uniformly distributed along the panel zone. Therefore, in order to be in equilibrium, bond stresses require the detection of a group of struts and ties. For instance, in Figure 5.1c, bond stresses developed near point **a** are in equilibrium by means of the horizontal component of the diagonal strut **ab**. At the same time, the latter requires a vertical tie at the point **a** to be in equilibrium. At the point **b**, forces acting on the strut **ab** are in equilibrium via bond stresses acting on **b** and tie **bc**. The anchorage of the latter to the point **c** is in equilibrium thanks to the strut **cd** and bond stress near to that point.
Ultimately, truss mechanism requires the detection of vertical and horizontal ties to equilibrate bond stresses related to longitudinal reinforcement. In the horizontal direction, ties are represented by the stirrups arranged within the joint, while in the vertical one these are identified in the longitudinal bars of the column, if are well distributed along height of the joint.

When considering a monotonic load, the aforementioned mechanisms are both able to carry a significant fraction of the whole shear acting on the joint. On the other hand, when a cyclic load is considered, a variation of the contributions provided by the two resisting mechanisms is observed, caused by the reduction of their strengths. This behaviour can be explained describing

some aspects of the cyclic response of beam-column joints. When an RC subassembly is pushed in one direction, longitudinal reinforcement of the beam subjected to tensile stresses yields. When unloading the subassembly, a residual flexural crack is observed at the interface between beam and joint. Subsequently, if the subassembly is pushed in the other direction, the whole compressive force due to bending moment will be absorbed by the longitudinal bars yielded in tension unless the crack is closed. During this step, the whole shear force experienced by the joint is transferred to it through the truss mechanism because concrete on the external faces of the joint is cracked and, thus, able not to transfer normal stresses. This leads to an increment in the contribution of the truss mechanism with respect to the diagonal strut. This scheme is effective unless the anchorage length of the longitudinal bars is sufficient to limit their slippage within the joint. As a matter of fact, when the subassembly is loaded in the opposite direction, an inadequate anchorage brings to significant slippage which causes crack closing, and therefore, concrete within the compressive areas due to bending moment is subjected to compressive stresses, transforming the resisting mechanism of the joint from truss mechanism to diagonal strut.

Having said that, the diagonal strut is the main resisting mechanism in the case of inadequate anchorage length of the longitudinal reinforcement, while the truss mechanism prevails when the anchorage length or the transverse reinforcement are sufficient. However, it should be emphasized that, the more the cracks caused by the cyclic action reduce the compressive strength of the diagonal strut, the more the confinement effect provided by the stirrups within the joint is reduced.

On the basis of the above considerations, nodal deformations caused by cyclic action are mainly due to the two phenomena described below (Figure 5.2):

- Bar slippage: the anchorage of the longitudinal bars of beams and columns leads to significant bond stresses. The slippage of the reinforcement with respect to the external face of the joint brings to rigid rotations of beams and columns;
- Shear distortion: joint undergoes shear forces which causes its shear distortion, leading to rigid rotations of beams and columns.

An adequate anchorage length brings to low bond stresses at the interface rebar-concrete. Therefore, loss of bond strength due to cyclic actions and slippage within the joint are dramatically reduced. On the contrary, an inadequate anchorage subjected to cyclic actions could show a significant

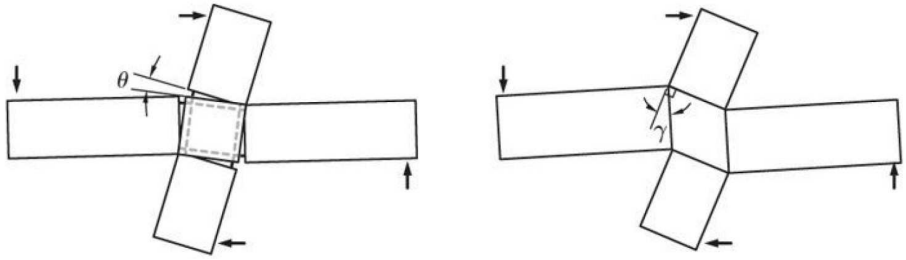

Figure 5.2 Phenomena affecting the deformations of the joints: bar slippage (left), shear distortion (right) (taken from Moehle 2014)

degrading bond strength which hampers the proper functioning of the longitudinal bars. This leads to a beam-column joint with reduced stiffness and energy dissipation capacity. Moreover, regarding those joints subjected to high shear forces, a loss of deformation capacity due to progressive damaging of the panel zone is also observed.

5.2 Model reproducing the cyclic behaviour of beam-column joints

Once the main mechanisms affecting the cyclic behaviour of RC joints were identified, a research in the literature was conducted aiming at searching for models focusing on these two aspects. As already discussed in Section 2.2.3, according to the suggestions of Pan et al. (2017), the mechanical model proposed by Lowes and Altoontash (2003) was adopted, the latter being one of the most reliable in reproducing the behaviour of joints. This model, represented in Figure 5.3, is constituted by a four-node, 12 DOFs super-element which comprises:

- a 2D element subjected to shear action only which mimics the stiffness and strength deterioration exhibited by the concrete core of the beam-column joint;
- eight linear springs reproducing the strength and stiffness degradation caused by slippage of the longitudinal reinforcement within the concrete core due to bond stress reduction;
- four linear springs emulating the decreased ability to transfer shear actions at the joint perimeter because of crack opening.

This model employs the Modified Compression Field Theory (MCFT) (Vecchio and Collins 1986) to evaluate the monotonic curve of the shear–stress vs. shear–strain relationship of the concrete core within the beam-column joint. As illustrated in Figure 5.3, the 2D element transfers all loads

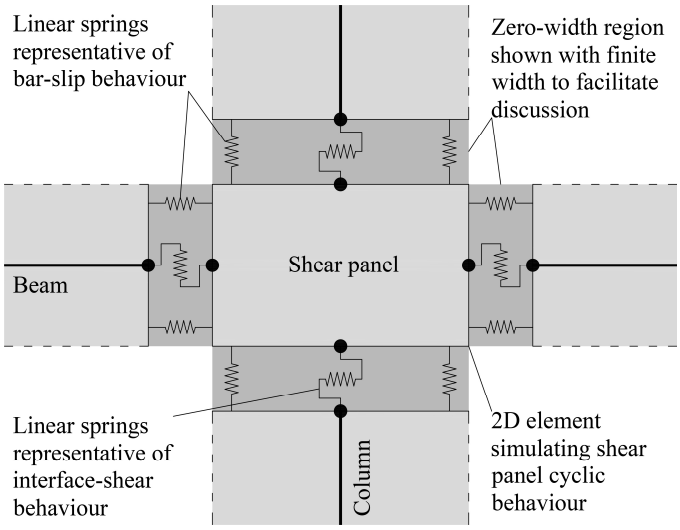

Figure 5.3 RC beam-column joint model (adapted from Lowes and Altoontash 2003)

via shear stresses. Consequently, the MCFT is employed setting to zero the normal stresses acting on the concrete shell, and neglecting normal strains. The cyclic response of beam-column joints is reproduced via constitutive laws calibrated on the basis of the experimental study carried out by Stevens, Uzumeri, and Collins (1991).

The monotonic curve of the bar–stress vs. the bar–slip is defined assuming several simplifications regarding the anchorage behaviour (Lowes and Altoontash 2003). First of all, the bond stress throughout the anchorage-zone of the longitudinal reinforcement was supposed to be constant if the bar was loaded below the elastic limit, or piecewise constant for bars experiencing yielding. Secondly, the bar slip determines the relative displacement between the bar and concrete core perimeter and it is related to the strain state experienced by the bar. Thirdly, no slip is assumed to occur at the section of zero normal stresses. In Figure 5.4 bond stresses and stress state along the anchorage-zone of a longitudinal reinforcement anchored within the concrete core of a beam-column joint loaded over the elastic limit are schematically illustrated.

The symbols used in Figure 5.4 are defined as follows:

- f_s: bar stress at the concrete core perimeter;
- f_y: the steel yield stress;
- τ_E: bond stress in case of elastic steel;
- τ_Y: bond stress in case of yielded steel;
- A_b: rebar cross-sectional area.

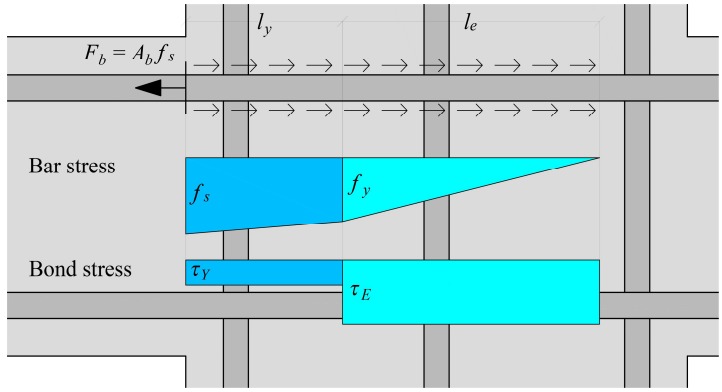

Figure 5.4 Bond stress and bar stress distribution for a bar anchored in a beam-column joint (adapted from Lowes and Altoontash 2003)

Moreover, l_e and l_y, are the rebar segments whose stresses are below or beyond the yield value. Once these simplifications have been defined, the equations which relate bar-stress and bar-slip in the monotonic behaviour are equal to:

$$\begin{cases} s = \dfrac{d_b f_s^2}{8E\tau_E} & f_s \le f_y \\ s = \dfrac{d_b}{4}\left\{\dfrac{f_y^2}{2E\tau_E} + \dfrac{f_s - f_y}{\tau_Y}\left[\dfrac{f_y}{E} + \dfrac{\left(f_s - f_y\right)}{2E_h}\right]\right\} & f_s > f_y \end{cases} \tag{5.1}$$

in which E is the steel elastic modulus; E_h the strain hardening modulus; and d_b the nominal rebar diameter.

It is well known that bond resistance drops when reinforcing bars experience a certain value of slippage (Eligehausen et al. 1983). As suggested in Lowes and Altoontash (2003), the slip threshold after which the bond strength decays is assumed equal to 3 mm.

With respect to the bond strength values to be adopted in (5.1), an experimental campaign focusing on anchorage behaviour of reinforcing bars (e.g. Eligehausen et al. 1983) pointed out that the bond strength is related to both the concrete condition and the state of stress surrounding the anchored-length bar and transverse reinforcement around the anchored bar. These factors are synthetically taken into account by Lowes and Altoontash in the values reported in Table 5.1.

Concerning the shear transfer mechanism, the flexural cracks at the joint perimeter reduce the capability of the joint to transfer shear forces. It is

Table 5.1 Average bond stress by varying the stress acting on the rebar (from Lowes and Altoontash 2003)

Stress acting on the bar, f_s (MPa)	Average bond stress (MPa)
$f_s < f_y$	$\tau_E = 1.8 f_c^{0.5}$
$f_s > f_y$	$0.05 f_c^{0.5} < \tau_Y < 0.4 f_c^{0.5}$

apparent that the amplitude of these cracks vary significantly when the joint is subjected to a cyclic action. For this reason, a simplified model which does not take into account the variation of the amplitude of these cracks would be too inaccurate. Furthermore, the contribution of this mechanism to the whole shear distortion of the joint is much lower than the other ones. In addition, very few experimental tests were conducted aiming at shedding a light on this mechanism. All the above considered, Lowes and Altoontash (2003) suggests to model the capacity to transfer shear actions at the joint perimeter by means of linear elastic springs.

5.3 Adapted model for FE software

The macro model described in the previous section is implemented in a FE software, and it will be validated by comparison of numerical and experimental cyclic curves. In this study, both the benchmark test on the subassembly and the analyses in Chapter 8 on RC frames are carried out using the software *SeismoStruct* (SeismoSoft, 2020). Structural members are modelled using distributed plasticity fibre-section elements with force-based formulation, while 2D shear-panel component and bar-slip linear springs are modelled by means of link elements. The latter are 3D elements, having uncoupled axial, shear and flexural behaviours, linking two coincident structural nodes defining a force-displacement or moment-rotation response relationship independent for each of its 6 DOFs. The advantage and limitations of using distributed plasticity model were discussed in Section 2.2.1. In Figure 5.5 the structural model employed to adapt the aforementioned beam-column joint model into the software is illustrated.

It is constituted by the following components:

- four rotational springs at the beam-to-joint and column-to-joint interfaces to simulate the relative rotation of the structural member due to slippage of the longitudinal reinforcement within the concrete core;
- one rotational spring at the centre of the beam-column joint to simulate the relative rotation between columns and beams due to

the shear deformation of the joint region;

- four linear springs representing the interface-shear behaviour.

Moreover, four rigid links were introduced between central nodes and nodes on the beam-to-joint and column-to-joint interfaces, assuming that the cyclic behaviour of the joint is totally represented by the central rotational spring. Lastly, deformations of the joint due to axial force and bending moment are negligible, being much smaller than those due to shear action.

The reason why is necessary to use bending moment acting on the central node instead of shear forces acting on the joint perimeter is illustrated in Figure 5.6, in which *h* and *w* are the height and the width of the joint, respectively. As formerly mentioned, the monotonic behaviour of the joint is assessed by using the Modified Compression Field Theory (MCFT). The use of MCFT requires the introduction of several assumptions regarding the mechanical response of the joint. As a matter of fact, MCFT is based on a constitutive model characterized by a plane stress, in which axial and tangential responses are coupled. As shown in Figure 5.3, the Lowes and Altoontash model is developed assuming that all the actions acting on the joint, including the axial force of the columns, are transferred by means of shear force. Therefore, when using the MCFT, normal stresses acting on the joint are set equal to zero. This assumption is also used in the adapted model, although the layout is different (Figure 5.5), because the MCFT is defined for RC panels for which only the thickness is known, and is not possible to couple axial force and in-plane bending moment. Furthermore, because of the

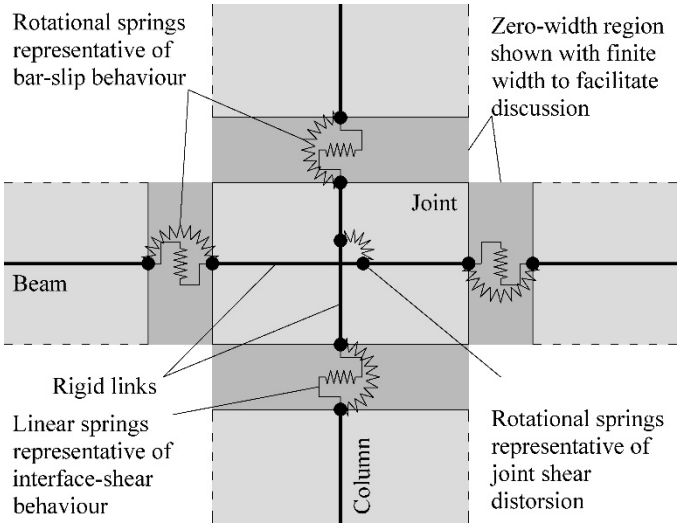

Figure 5.5 Structural model implemented in *SeismoStruct*

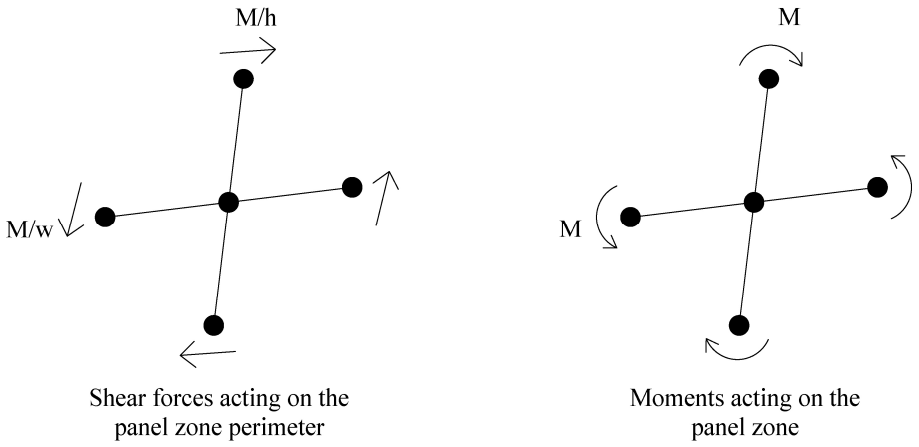

Figure 5.6 Forces acting on the joint in the adapted model

in-plane dimensions of the panel are unknown, the reinforcement has to be considered spread and uniformly distributed.

The rotational spring of the panel zone was modelled by means of a link element in which a moment-rotation behaviour is defined using the "multi-lin" constitutive law. The latter is based on the Polygonal Hysteretic Model (PHM) introduced by Sivaselvan and Reinhorn (1999), which is able to simulate both stiffness and strength deterioration and the pinching phenomenon. With regard to the bar-slip mechanism, the "gen-hyst" constitutive law is used. As for the interface-shear mechanism, this is modelled by means of linear elastic springs with very high stiffness, as already discussed in Section 5.2.

5.3.1 Polygonal Hysteretic Model (PHM)

Among the several constitutive model implemented in the software package *Seismostruct*, the Polygonal Hysteretic Model (PHM) was selected to reproduce the cyclic behaviour of the panel zone. The PHM has the advantage to easily take into account the loss of strength and stiffness and the pinching phenomenon, the latter being the contraction of the hysteresis loops. Fifteen parameters are required to characterize the behaviour of the PHM, the first eleven regarding the backbone curve and the other four concerning the cyclic response.

The first-order parameters (backbone curves) are the following:

- Initial flexural stiffness K_{cr};
- Cracking moment (positive) M^{+}_{cr};
- Yielding moment (positive) M^{+}_{y};

- Yielding rotation (positive) ϕ^{+}_{y};
- Ultimate rotation (positive) ϕ^{+}_{u};
- Post-yielding stiffness (positive), as a percentage of the elastic one α^{+};
- Cracking moment (negative) M^{-}_{cr};
- Yielding moment (negative) M^{-}_{y};
- Yielding rotation (negative) ϕ^{-}_{y};
- Ultimate rotation (negative) ϕ^{-}_{u};
- Post-yielding stiffness (negative), as a percentage of the elastic one α^{-}.

The second-order parameters (cyclic behaviour) are the following:

- Stiffness degradation δ;
- Ductility based strength decay β_2;
- Hysteretic energy based strength decay β_3;
- Slip parameter γ.

Equations governing degradation of strength and stiffness are the following, respectively:

$$M_y^{+/-} = M_{y0}^{+/-}\left[1-\left(\frac{\phi_{\max}^{+/-}}{\phi_u^{+/-}}\right)^{\frac{1}{\beta_2}}\right]\left[1-\frac{\beta_3}{1-\beta_3}\frac{H}{H_{ult}}\right] \tag{5.2}$$

$$R_k^{+} = \frac{M_{cur}+\delta M_y}{K_{cr}\,\phi_{cur}+\delta M_y} \tag{5.3}$$

In which:

- $M^{+/-}_{y0}$: undamaged positive/negative yielding moment;
- $\phi^{+/-}_{max}$: maximum positive/negative rotation;
- H: dissipated hysteretic energy;
- H_{ult}: dissipated hysteretic energy when monotonically loaded up to the ultimate rotation, excluding degrading phenomena;
- R^{+}_{k}: positive degrading stiffness factor;
- M_{cur}: current moment;
- ϕ_{cur}: current rotation.

To clarify the influence of the above parameters in the response of PHM, different analyses were carried out on a link element by varying the second-

order parameters, whose values are reported in Table 5.2, while the moment-rotation curves are illustrated in Figure 5.7. It can be observed that, by increasing the number of hysteresis loops, unloading branches loose stiffness (Figure 5.7a) with a low value of δ. Moreover, high values of β_2 and β_3 lead to hysteresis loops with reducing maximum strength depending on the maximum rotation achieved in the previous loop (Figure 5.7b) and the dissipated energy (Figure 5.7c). Lastly, pinched hysteresis loops are obtained when a low value of $\gamma$is used (Figure 5.7d).

Table 5.2 PHM: values of the second-order parameters used in four analyses on a link element

Second-order parameters	Analysis (a)	Analysis (b)	Analysis (c)	Analysis (d)
δ	4	200	200	200
β_2	0.001	0.6	0.001	0.001
β_3	0.001	0.001	0.6	0.001
γ	1	1	1	0.5

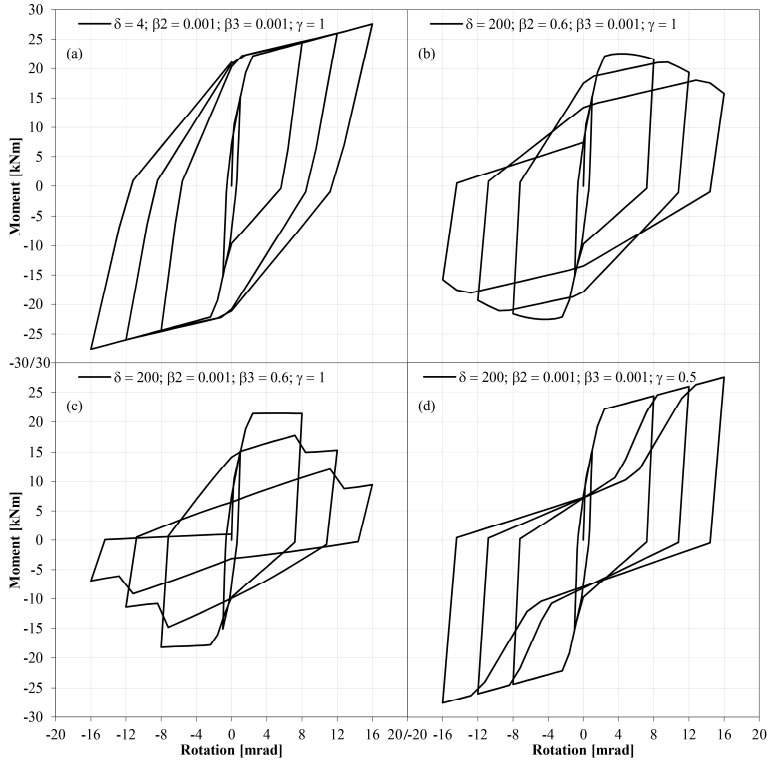

Figure 5.7 PHM: moment-rotation curves obtained by varying the values of the second-order parameters

5.3.2 Gen_Hyst Model (GHM)

To reproduce the cyclic behaviour of the bar-slip mechanism, the Gen_Hyst Model (GHM) was selected as the most suitable among the models implemented in *Seismostruct*. GHM is able to reproduce both pinching effect and degradation of strength and stiffness. Differently from PHM, GHM provides the opportunity to define a residual strength, the latter being of paramount importance in the bar-slip mechanism. Like the PHM, GHM is characterized by eleven parameters divided in two groups, the first one defining the backbone curves, while the second one defining the cyclic response.

The first-order parameters (backbone curves) are the following:

- Elastic stiffness K_e;
- Yielding moment (positive) M^+_y;
- Ultimate moment (positive) M^+_u;
- Ultimate rotation (positive) ϕ^+_u;
- Residual strength (positive) M^+_r;
- Yielding moment (negative) M^-_y;
- Ultimate moment (negative) M_u;
- Ultimate rotation (negative) ϕ_u;
- Residual strength (negative) M_r;

The second-order parameters (cyclic behaviour) are the following:

- Pinching factor γ;
- Degradation factor δ.

To clarify the influence of the above parameters in the response of GHM, different analyses were carried out on a link element by varying the second-order parameters, whose values are reported in Table 5.2, while the moment-rotation curves are illustrated in Figure 5.8. A low value of γ leads to pinched hysteresis loops (Figure 5.8a), while a high value of δ reduces post-yielding moment strength values (Figure 5.8b).

Table 5.3 GHM: values of the second-order parameters used in four analyses on a link element

Second-order parameters	Analysis (a)	Analysis (b)
δ	0.001	0.6
γ	0.5	1

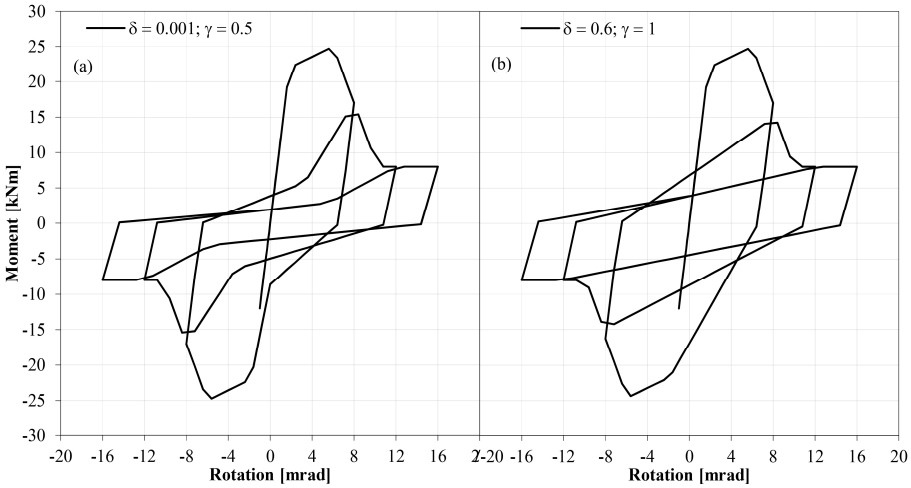

Figure 5.8 GHM: moment-rotation curves obtained by varying the values of the second-order parameters

5.4 Application of the adapted model

In order to assess the reliability of the FE model in reproducing the cyclic behaviour of beam-column joints of traditional RC frames made with HSTCBs, the results of a previously carried out experimental campaign are used, reported in Colajanni et al. (2016b). Geometrical and mechanical characteristics of specimens tested, as well as results obtained, were already described in Section 2.2.3. Among the three subassemblies tested, specimen no. 2, whose column was subjected to an axial load equal to 800 kN, was selected to calibrate the cyclic behaviour of the joint. The parameters characterizing the above-described constitutive models are calculated on the basis of the geometrical and mechanical properties of this subassembly. The procedures described below can be used to perform the blind prediction of the cyclic response of both the panel zone and the bar-slip mechanism. When reproducing experimental results, some critical parameters, such as the second-order parameters and the ultimate rotations of panel zone and bar-slip mechanism, can be suitably calibrated in order to obtain improved correspondence between numerical and experimental curves.

5.4.1 PHM parameters

As explained before, the monotonic behaviour of the panel zone is characterized by means of the MCFT, which is implemented in the software package *Shell-2000*, whose interface is shown in Figure 5.9. This software provides the shear force vs. shear strain response of a reinforced concrete shell

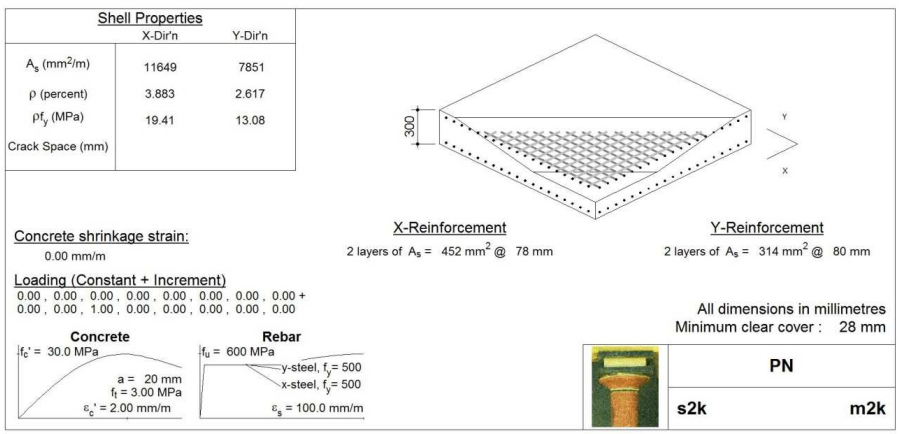

Figure 5.9 Interface of the software package *Shell-2000*

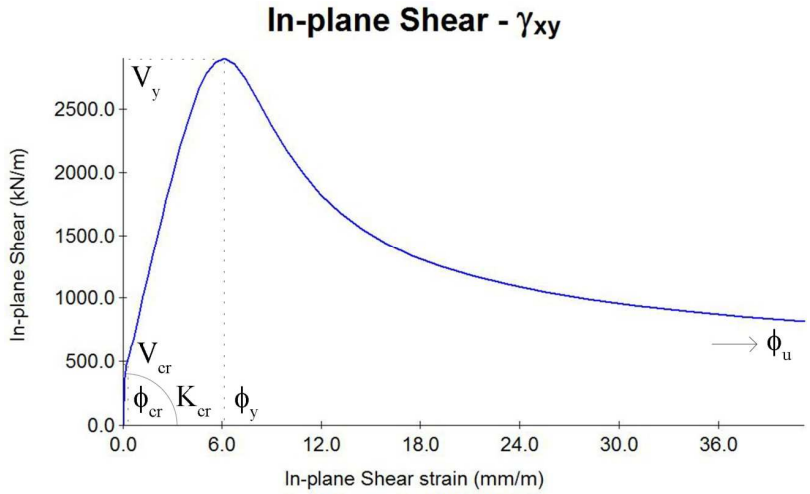

Figure 5.10 Shear force vs. shear strain curve of the panel zone obtained via *Shell-2000*

subjected, along the two directions, to axial forces and out-of-plane bending moments. The input parameters are thickness of the panel, geometrical ratios of reinforcement ρ and mechanical properties of materials. Longitudinal reinforcement of beams is arranged along the x-direction, while that of columns is arranged along the y-direction. In Figure 5.10 is illustrated the obtained shear force vs. shear strain curve.

The shear force is expressed in kN/m, thus the shear acting on the investigated panel zone is obtained by multiplying with the cross-section height of the column, $h = 0.4$ m:

$$\begin{aligned} V_{cr} &= 470 \cdot 0.4 = 188\,kN \\ V_y &= 2900 \cdot 0.4 = 1160\,kN \end{aligned} \tag{5.4}$$

To obtain cracking and yielding moment, the above values are multiplied with the height of the panel zone:

$$\begin{aligned} M_{cr} &= V_{cr}\, h = 188 \cdot 0.25 = 47\, kNm \\ M_{y} &= V_{y}\, h = 1160 \cdot 0.25 = 290\, kNm \end{aligned} \tag{5.5}$$

From Figure 5.10, the related rotations are equal to:

$$\phi_{cr} = 0.0002\, rad \qquad \phi_{y} = 0.006\, rad \tag{5.6}$$

The ultimate rotation is set to 0.2 rad. This value of ultimate rotation, which represents the rotation for which the moment capacity is equal to zero, was selected in order to obtain a loss of peak moment strength equal to 20% at the conventional ultimate rotation, which represents the failure of the panel zone. Lastly, post-yielding stiffness is assumed equal to 0.001.

Once the monotonic behaviour of the panel is defined, its response subjected to cyclic actions can be defined by means of the parameters proposed by Sivaselvan and Reinhorn (2000) for three different levels of damage, which are reported in Table 5.4. On the basis of the joint geometry and the forces to which is subjected, in the following numerical applications the parameters related to the "severe" level of damage are selected.

In the absence of experimental results, the ultimate rotation of the PHM should be chosen on the basis of the values suggested in international standards or in the literature for the conventional ultimate rotation. An example can be found in De Risi et al. (2017) and in Section 8.2. As for the parameters defining the cyclic behaviour of the panel zone, these should be selected on the basis of the geometrical and mechanical characteristics of the panel zone. For instance, a small-sized panel zone combined with rebars with large diameters are supposed to undergo a severe level of damage, thus the appropriate values given in Sivaselvan and Reinhorn (2000) should be used.

Table 5.4 Values of the second-order parameters proposed by Sivaselvan and Reinhorn (2000)

Second-order parameters		**Level of damage**		
		Small	**Medium**	**Severe**
Stiffness degradation	δ	15	10	4
Ductility based strength decay	$\beta 2$	0.001	0.3	0.6
Hysteretic energy based strength decay	$\beta 3$	0.001	0.15	0.6
Slip parameter	γ	1	0.75	0.5

5.4.2 GHM parameters

On the basis of the procedure previously described in Section 5.2, the parameters characterizing the GHM for the rebars of the beams are calculated below. Due to the high level of preload applied on the column and the high ratio between the bending moment resistance of column and beam, preliminary analyses showed that partialization of the column cross-section does not occur. So, for simplicity's sake, the rotational spring representative of the bar-slip mechanism at the column-to-joint interface is not modelled.

Regarding the HSTCBs, the sagging and hogging yielding moment are equal to, respectively:

$$M_y^+ = 91 kNm \qquad M_y^- = 165 kNm \tag{5.7}$$

By using the first of Eqs. (5.1), the slip at the yielding is given as follows:

$$s_y = \frac{d_b f_y^2}{8 E \tau_E} = \frac{24 \cdot 500^2}{8 \cdot 200000 \cdot 9.86} = 0.38 mm \tag{5.8}$$

It should be noticed that this equation does not include the anchorage length. In this study, consistently with Lowes and Altoontash (2003), values of $1.8 f_c^{0.5}$ and $0.2 f_c^{0.5}$ were adopted for τ_E and τ_Y, respectively, f_c being the compressive strength of concrete, equal to 30 MPa. The rotation of the section is computed by considering the distance between tensile chord and neutral axis approximately equal to 2/3 d:

$$\phi_y = s_y / (2d/3) = 0.38/151 = 0.0025 rad \tag{5.9}$$

The average elastic stiffness for both sagging and hogging moment is:

$$K_y = \left(M_y^+ / \phi_y + M_y^- / \phi_y \right) / 2 = 51200 kNm / rad \tag{5.10}$$

With regard to the post-yielding stiffness, it is assumed that the maximum slip beyond which the bond strength decreases is 3 mm, consistently with the suggestion of Lowes and Altoontash. Therefore, by using the second of Eqs. (5.1), the tensile stress acting on the longitudinal bar at the slip of 3 mm is computed as follows:

$$s_u = \frac{d_b f_y^2}{8 E \tau_E} + \frac{d_b f_y \left(f_s - f_y \right)}{4 E \tau_Y} + \frac{d_b \left(f_s - f_y \right)^2}{8 E_h \tau_Y} = 3 mm \tag{5.11}$$
$$\Rightarrow \qquad f_u = 528.5 MPa$$

The corresponding sagging and hogging moment are the following:

$$M^{+} = 96.5 kNm \qquad M^{-} = 175 kNm \tag{5.12}$$

The rotation of the section is given by the (5.9), substituting s_y with s_u:

$$\phi_u = s_u / (2d/3) = 3/151 = 0.01987 rad \tag{5.13}$$

Thus, the post-yielding stiffness is calculated as follows:

$$\begin{aligned} K_u^{+} &= \frac{M_u^{+} - M_y^{+}}{\phi_u^{+} - \phi_y^{+}} = \frac{96.5 - 91}{0.01987 - 0.0025} = 317\, kNm/rad \\ K_u^{-} &= \frac{M_u^{-} - M_y^{-}}{\phi_u^{-} - \phi_y^{-}} = \frac{175 - 165}{0.01987 - 0.0025} = 576\, kNm/rad \end{aligned} \tag{5.14}$$

Lastly, the post-yielding stiffness as ratio of elastic one is given by:

$$\alpha^{+} = \frac{K_u^{+}}{M_y^{+} / \phi_y^{+}} = 0.0087 \qquad \alpha^{-} = \frac{K_u^{-}}{M_y^{-} / \phi_y^{-}} = 0.0087 \tag{5.15}$$

The parameters characterizing the cyclic behaviour of the bar-slip mechanism are assumed equal to $\delta = 0.6$ and $\gamma = 0.5$, consistently with those reported in Table 5.4 in the case of "severe" degrading effects.

As already stated before, the preceding procedure can be used to perform the blind prediction of the monotonic moment-rotation curve of the bar-slip mechanism considering generic geometrical and mechanical characteristics. Regarding the parameters defining the cyclic behaviour of the bar-slip mechanism, these should be selected on the basis of the geometrical and mechanical characteristics of the bar and the anchorage length. For instance, an inadequate anchorage length combined with a bar with large diameter is supposed to undergo a severe level of damage, thus the corresponding values suggested by Sivaselvan and Reinhorn (2000) should be used.

5.4.3 Comparison between experimental and numerical results

Once all the parameters defining the cyclic response of PHM and GHM were computed, the beam-column subassembly is modelled with the software *Seismostruct*. During the experimental test, friction forces were observed at the beam ends due to the setup of restraints. Therefore, the first goal is to calibrate the amount of these friction forces by considering the joint rigid. In Figure 5.11 the comparison between the experimental and numerical force-

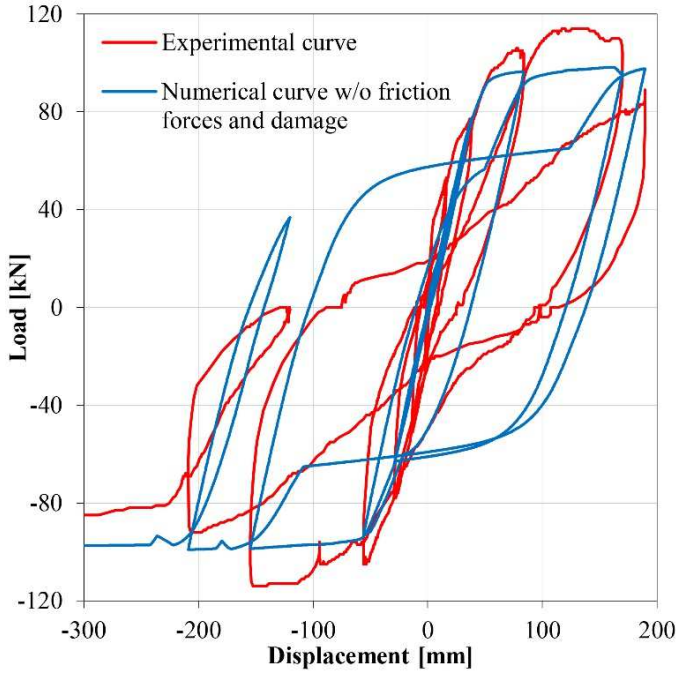

Figure 5.11. Comparison between experimental and numerical force-displacement curves without friction forces and considering the joint rigid

displacement curves is plotted.

Both force and displacement are referred to the base of the column. The curves clearly show the yielding of beams, but at different force values. This difference is due to the friction forces acting on the beam ends, which can be calculated as follows:

$$F_{friction} = \mu_c F_{num} \frac{H}{L} \tag{5.16}$$

in which F_{num} is the numerical shear force acting on the column, H and L are column height and beam length, respectively, while μ_c is the friction coefficient acting on beam end constraints, which can be given as:

$$\mu_c = \frac{F_{\exp,\max} - F_{num,\max}}{F_{num,\max}} \tag{5.17}$$

in which $F_{num,max}$ and $F_{exp,max}$ are the maximum forces of the post-yielding branches of the numerical and experimental curves, respectively. The force calculated with (5.16) is equally distributed on the two beam ends.

The absolute value of the peak response is 99 kNm for the numerical curve

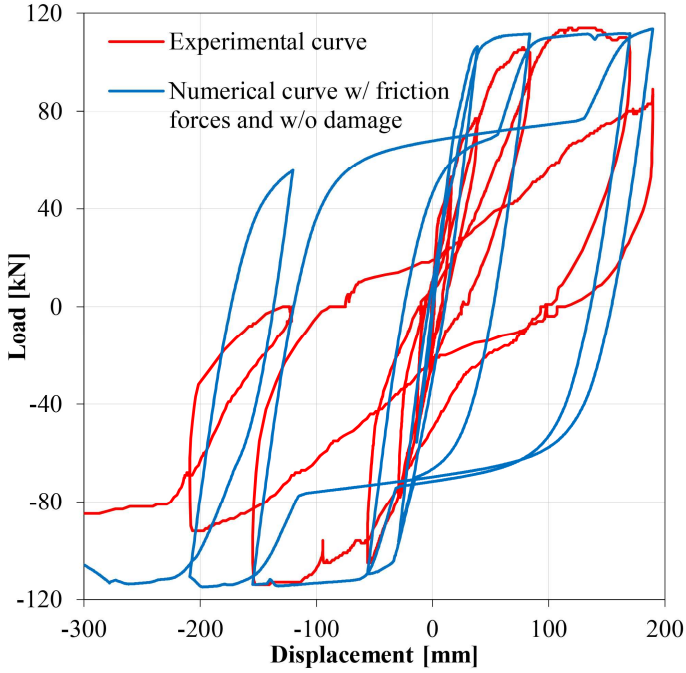

Figure 5.12. Comparison between experimental and numerical force-displacement curves with friction forces and considering the joint rigid

and 114 kNm for the experimental one, with a difference of 15%. It is worth comparing also the total energy dissipated by the experimental and the numerical curves, which are 67822 kNm and 79807 kNm, respectively, with a difference of about 18%.

The comparison between experimental and numerical force-displacement curves including friction forces is illustrated in Figure 5.12. It should be noted that the experimental and numerical post-yielding branches now exhibit the same value of force. Moreover, no degrading phenomena in terms of stiffness or strength are registered in the numerical curve, hence the differences with the experimental one are attributed to the joint.

The absolute peak response is equal to 114 kNm, which is the same value of the experimental one. With regard to the energy dissipated by the numerical curve, this is 108215 kNm, which is 60% more than that dissipated by the experimental one. This difference is clearly due to the absence of the above-mentioned degrading phenomena affecting the joint.

At this point, the element links representing the bar-slip mechanism and the shear distortion of the panel zone are modelled on the basis of the parameters calculated above. The comparison between experimental and numerical force-displacement curves with friction forces and considering the

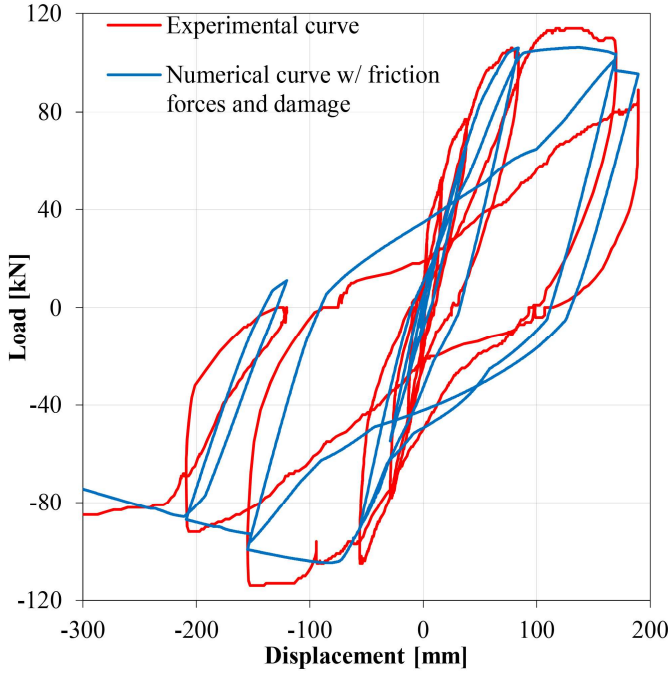

Figure 5.13. Comparison between experimental and numerical force-displacement curves with friction forces and degrading phenomena of joint

degrading phenomena of the joint is shown in Figure 5.13. It can be seen that the numerical model is reliable in reproducing stiffness and strength deterioration of the experimental curve. As for the pinching phenomenon, this is slightly underestimated, meaning that in the experimental test the joint experienced very high degrading phenomena.

The absolute peak response is equal to 105 kNm, which is slightly lower than that of the experimental one and to that obtained introducing the friction forces at the beam ends. This difference is due to the fact that the degrading phenomena influencing the mechanical response of the joint reduce its strength and, thus, the maximum strength of the subassembly.

The energy dissipated by the subassembly during the test for each loading cycle for both experimental and numerical results is compared in Figure 5.14. Regarding the capability of the model in reproducing the dissipated energy by the subassembly, the numerical results are in good agreement with the experimental ones, although some discrepancies can be observed for each loading cycle. The maximum value of the ratio between the difference of the dissipated energy during the i^{th} cycle calculated from the experimental and the numerical results, and the total energy dissipated during the experimental test, is observed at the 6^{th} cycle, and is about 6%. The trend of the energy dissipated

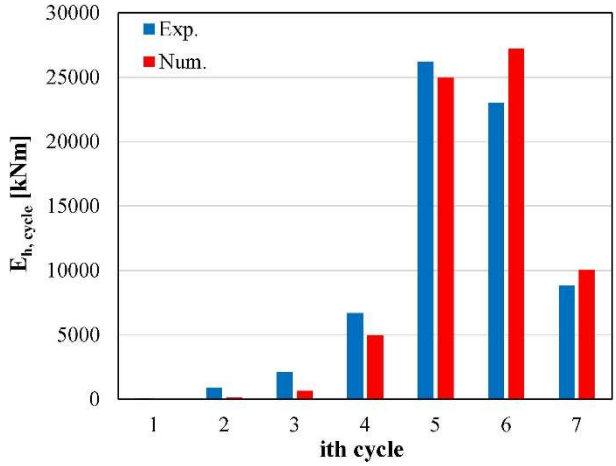

Figure 5.14. Energy dissipated by the subassembly for each loading cycle for both experimental and numerical results

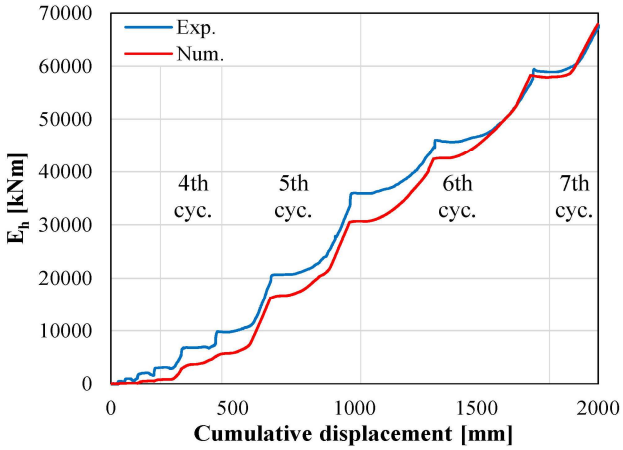

Figure 5.15. Trend of the energy dissipated by the subassembly versus cumulative displacement for both experimental and numerical results

by the subassembly during the test versus cumulative displacement is shown in Figure 5.15. It can be seen that, despite some differences, the overall trend is similar and the total amount of energy dissipated at the end of the test is almost equal.

5.5 Conclusions

In this chapter a numerical model able to reproduce the cyclic response of RC beam-column joints realized with HSTCBs was described. Initially, the mechanical behaviour of joints subjected to cyclic actions was analysed, focusing on the resisting mechanisms and phenomena influencing their

response.

With regard to the former, two main mechanisms were identified:

- *diagonal strut*, which equilibrates axial and shear forces acting on the external faces of the joint;
- *truss mechanism*, which equilibrates the forces transferred by longitudinal bars, exploiting the shear resistance of joint.

The diagonal strut is the main mechanism in the case of inadequate anchorage length of rebars, while the truss mechanism prevails when transverse reinforcement and anchorage length are adequate.

Concerning the phenomena affecting the response of joints, two main phenomena were detected:

- Bar-slip mechanism;
- Shear distortion.

Both of them cause relative rotations between beams and columns, reducing the stiffness, strength and dissipation capacity of the joint.

After that, the adopted approach to model the cyclic behaviour of joint was defined, as follows:

- four rotational springs at the beam-to-joint and column-to-joint interfaces to simulate the relative rotation of the structural member due to slippage of the longitudinal reinforcement within the concrete core;
- one rotational spring at the centre of the beam-column joint to simulate the relative rotation between columns and beams due to the shear deformation of the joint region.

Two constitutive laws implemented in the software *Seismostruct* were selected, able to appropriately reproduce the above-mentioned phenomena. Both of them account for loss of strength and stiffness and pinching effect.

Lastly, the effectiveness of the model in reproducing the behaviour of HSTCB-column joint was proved by comparison of the model outcome against an experimental test previously carried out on a HSTCB-column joint.

The comparison between experimental and numerical force-displacement curves highlighted that the adopted approach successfully reproduces the degrading strength and stiffness of the joint and the pinched hysteretic cycles. On the basis of these results, this approach will be used in Chapter 8 to simulate the cyclic behaviour of joints belonging to RC frames realized with HSTCBs endowed or not with the innovative devices that will be proposed in

Chapters 6 and 7.

CHAPTER 6

DESIGN PROCESS OF HSTCB-COLUMN FRICTION CONNECTIONS

In this chapter the design process of different beam-column friction connections realized with HSTCB is discussed. First, the design technological characteristics of the proposed connections, developed on the basis of the critical review of the already existing connections, discussed in Chapter 3, are described. Then, the modelling strategy adopted to assess the mechanical behaviour of the proposed connections is explained and validated. Subsequently, three solutions are described, having an increasing level of both detailing and performance. More precisely, the first one is characterized by a pin connection and vertical and horizontal slotted holes, the second one is characterized by a T stub connection and curved slotted holes, the third one is characterized by a vertical central plate passing throughout the beam height. For each solution, the calculation of the design parameters, the finite element model developed and the numerical results are described.

6.1 Technological characteristics of the proposed connections

In order to design the beam-column connection for cast-in-situ RC frames realized with HSTCBs, the considerations listed in Section 3.4 are taken into account. The solution with the dissipative device in vertical position is adopted, deemed more suitable for the aim of the present research, if compared to the horizontal one, the latter suffering of the bending moment contribution provided by T stubs during sliding phases. It is worth remembering that the vertical solution, as arranged by Latour et al. (2018), is influenced by an undesired contribution as well, provided by bolts of friction device that have to be dragged up and down during sliding phase. Nevertheless, a solution to this inconvenience will be proposed during the development of the proposed connection. With the aim of avoiding interferences with the slab in the upper part of the beam, the solution with friction devices at both the upper and lower

part of the beam is excluded. At the same time, the beam-column connection has to be provided with a centre of rotation, clearly identified to predict the kinematic of the connection. This centre of rotation should be placed as close as possible to the slab to limit its damage. The connection must exhibit proper shear strength in all the functioning phases. Lastly, the transfer of stresses from the HSTC beam to the steel elements to which is connected should avoid damage of concrete.

6.2 Validation of the adopted numerical procedure

In the absence of experimental tests, the mechanical behaviour of the proposed connections can be carefully analysed only by means of models exploiting numerical computational methods, such as the Finite Element Method (FEM). Generally speaking, FEM models are often used as a preliminary tool for validating the design procedure of structural members designed on the basis of analytical models, as well as for calibrating the mechanical behaviour of specimens to be tested. In this research, the 3D FEM software used to simulate the performance of the proposed connections is the well-known multiphysics FEM software ABAQUS/CAE 2016. Due to the complexity of this software (and, in general, of all 3D FEM software packages) different preliminary FEM analyses have to be carried out aimed at validating the ability of the modelling approach in reproducing the mechanical responses of structural members, similar to the proposed ones, already tested in the literature. To this aim, it is convenient to begin with simple models, and then increase the level of complexity. Therefore, the first Finite Element Analysis (FEA) aims at reproducing the mechanical behaviour of the linear friction damper device tested by Latour et al. (2015) subjected to reversed cyclic load. The specimen, whose geometrical characteristics are reported in Figure 3.35, is constituted by two steel plates, one with standard clearance hole and the other one with slotted holes, connected by means of a double cover butt joint having eight preloaded bolts M20 class 10.9 per side. Between the two steel plates and the cover plates are inserted two friction shims. The test here reproduced is endowed with the friction pads “M2”, while steel plates are made of S275 steel. The bolts clamping the steel plates together are preloaded with a torque T_b of 200 Nm, corresponding to a bolt preload of F_{pc} = T_b / (0.2 d) = 50 kN, being d the bolt diameter equal to 20 mm. The test is carried out by imposing to the steel plate endowed with slotted holes a displacement history. Experimental test showed that, during the first 10 cycles, the friction coefficient varies between 0.15 and 0.19. Therefore, an

average value of 0.17 is selected to be used in the numerical simulation. The 3D model of the device investigated is reported in Figure 6.1. At the end section of the plate with slotted holes, the cyclic displacement of ± 16 mm is imposed. The opposed end section of other central plate is fixed. The expected force for which the central plate begins to slide is calculated as follows:

$$F_{s,the} = \mu n_s n_b F_{pc} = 136kN \tag{6.1}$$

where μ is the friction coefficient (0.17), n_s the number of surfaces involved in the friction connection (2), n_b the number of bolts clamping the plates (8).

The analysis is divided in two steps: the first one in which the preload force is applied to bolts, the second one in which the displacement history is imposed to the end section of the central plate. The comparison between force-displacement curves of numerical analysis and experimental test are reported in Figure 6.2.

As can be seen, the numerical model satisfactorily reproduces the experimental test in terms of sliding force. The numerical sliding force is equal to 137.5 and 133.5 kN in case of positive and negative sliding direction, respectively. The maximum difference between analytical and numerical sliding force is 2%. It should be highlighted that, due to the fixed friction coefficient, the numerical friction force is substantially constant during the analysis. Considering a variation of the friction coefficient is out of the scope of the present research. As a matter of fact, a varying friction coefficient should be calibrated on the basis of several parameters, such as roughness of surfaces (obtained analysing the asperities of the surfaces at the microscale level), wearing of asperities (depending on the displacement undergone by surfaces), temperature of the elements (depending not only on the displacement undergone by surfaces but also on the sliding velocity) etc.

As regards the mechanical behaviour of HSTCBs, the effectiveness of FEM models in reproducing the experimental results was proven in several previously published papers. More precisely, different Authors already studied the most suitable modelling techniques for reproducing the flexural and shear behaviour of HSTCBs. Concerning the latter, several researches have been published over the last decade, such as Ballarini et al. (2017) and Monaco (2016), in which numerical models were developed and validated against experimental and analytical benchmarks. The modelling approach presented here is characterized by the main numerical and geometrical features of the studies mentioned above. The FEM model exploits the

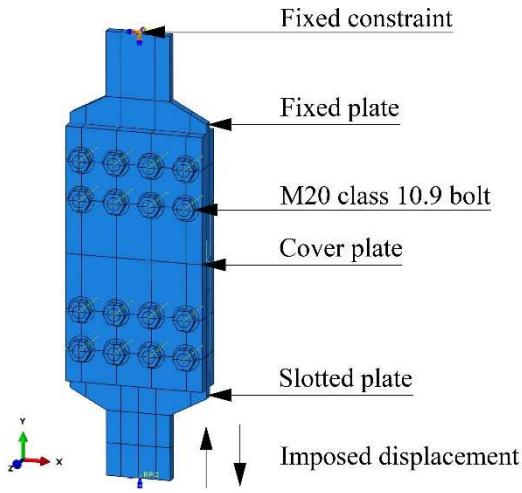

Figure 6.1 3D FEM model of the linear friction device tested by Latour et al. (2015)

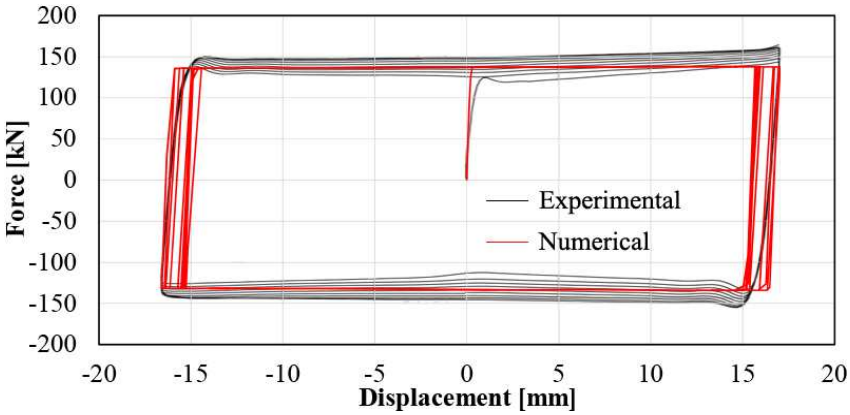

Figure 6.2 Comparison between experimental and numerical results of the friction device endowed with the friction pad "M2" tested in Latour et al. (2015)

knowledge, gathered over the last years, of several local phenomena influencing the mechanical behaviour of HSTCBs, such as buckling of bottom plate and inclined bars, that have been analysed comprehensively in several papers. Specifically, buckling of inclined bars constituting the steel truss of HSTCBs was studied both experimentally and analytically by Colajanni et al. (2014a, 2015b). With regard to buckling of bottom plate, this phenomenon is checked by using the formulation proposed in EN 1993:1-1 for slender compressed members. Concerning simulation of bond between steel and concrete, several papers have dealt with this phenomenon (e.g. Ballarini et al. 2020; Colajanni et al. 2015b, 2018a, 2018b) and two main modelling approaches were developed: the first one, which considers perfect connection between rebars and concrete, is used for simpler analysis, while the second

one, which employs a stress-slip constitutive law for the rebar-concrete interface, is used for more detailed analysis. Both of these approaches will be adopted in the subsequent analysis by using the same assumptions of the above-mentioned papers.

6.3 Solution with vertical and horizontal slotted holes

The first solution is illustrated in Figure 6.3, consisting in the adaptation to the HSTC beam of the vertical dissipative device with symmetric connection tested in Latour et al. (2018b). It includes a central vertical steel plate (here called rib plate) placed on a vertical plane including the beam axis, two steel angles, and two friction pads placed at the interface of the aforementioned elements. Two groups of slotted holes, one vertically-oriented on the steel angles, and the other one horizontally-oriented on the rib plate, allow the bolts to move in any direction. By doing so, bolts can slide with a curved trajectory limiting the damaging of the structural elements during the sliding step. The first difference with the device reported in Figure 3.12 is constituted by the rib plate of the friction device, which is welded, rather than bolted, to the steel plate at the lower part of the HSTC beam. Regarding the upper connection, differently from the solutions described in Chapter 3, a pin connection has been selected, being able both to determine the required centre of rotation, and to prevent the damage of the structural elements constituting the upper connection. The pin connection is constituted by 7 vertical holed plates, 3 connected to the column and 4 to the beam. The latter ones are connected to an end plate, to which are welded on the opposite face the top and bottom longitudinal reinforcement. To satisfy the requirements regarding the replaceability of the pin and to ensure a uniform stress distribution between pin and plates, the thickness of the latter ones must be 25 mm. The connection to the column, which will be further investigated in the following sections, is realized by means of threaded bars embedded through the height of the column cross-section. It should be stressed that, if the bond between threaded bars and concrete is adequately guaranteed, the deformability of the connection should not exceed the deformability of a traditional connection generally made with smaller diameter rebars, characterized by a reduced internal lever arm, and thus subjected to higher axial forces. The above-described beam-to-column connection lengthens the internal lever arm of the bending moment acting on the beam-column joint, reducing the stresses experienced by the panel joint, thus preventing its damaging and enhancing its cyclic performance. The 3D model of the first solution is shown in Figure 6.4.

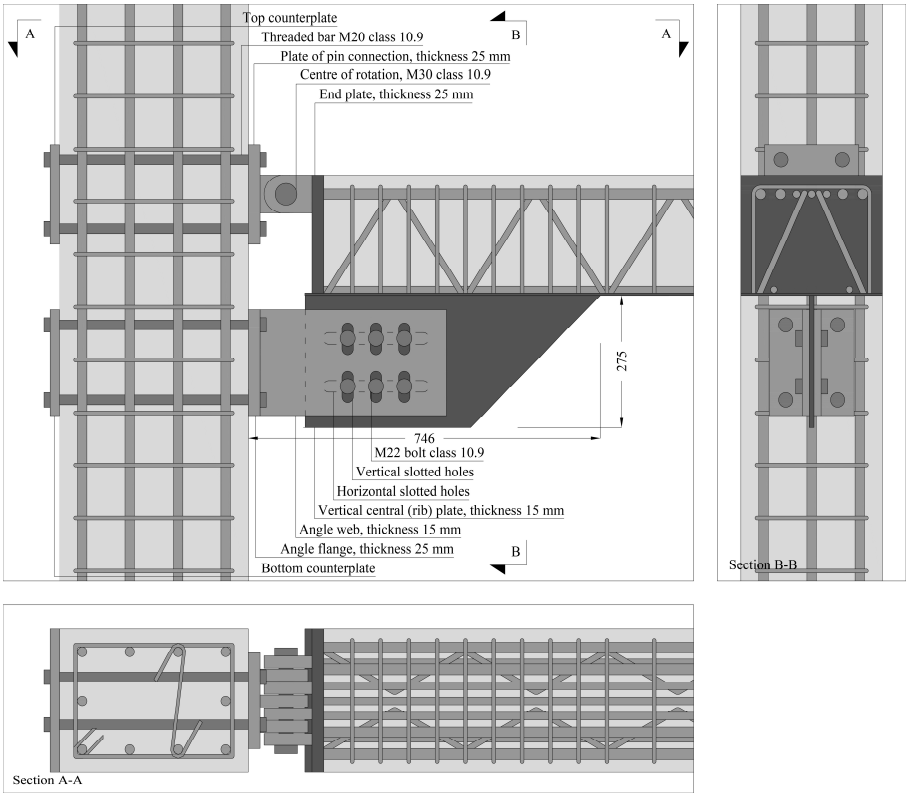

Figure 6.3 First solution with vertical and horizontal slotted holes and pin hinge

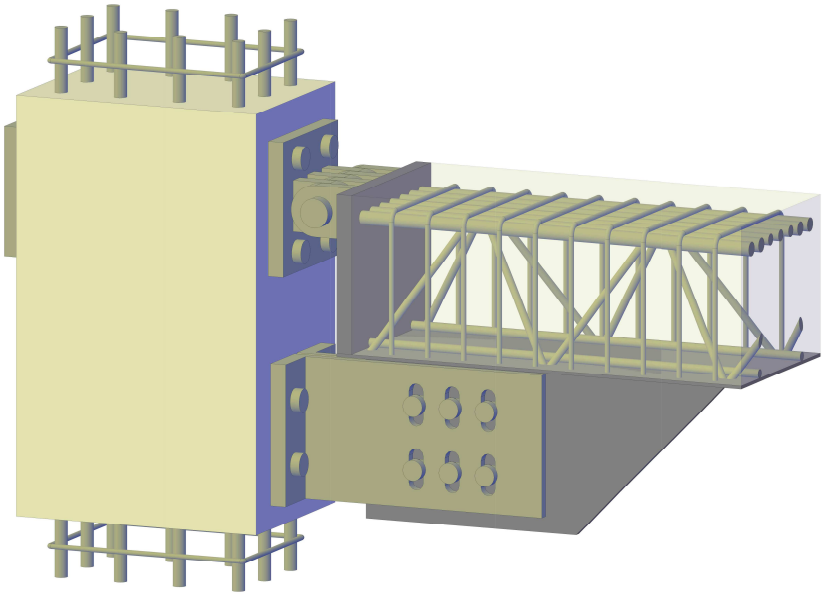

Figure 6.4 First solution: 3D view

With regard to the construction tolerances, these are taken into account at the connection between column and steel elements (pin connection and steel angles). Vertical tolerance can be solved by realizing vertical slotted holes on the steel plates used for connecting the device to the column. Conversely, for horizontal tolerance, the device should be positioned before concrete casting of the column in order to accommodate the tolerance. The steel truss of the beam is made shorter in the factory (as is done today as well) than the clear span and the remaining length (about 5-10 cm) is completed by cast-in-situ concrete (if the panel zone and the beam are cast together) or by cement grout (if the panel zone and the beam are cast at different times). A detailed evaluation of the connection to the column and the tolerances adopted for placing the device in situ are topics which play a decisive role in effective use of the device, and will be thoroughly studied in the third solutions.

As regards the undesired influence of the slab on the overall behaviour of the connection, as well as on the effect on the required tolerance of the slots, in the literature some suggestions have been made for effectively disconnecting the slab from the joint, such as those reported in Pampanin et al. 2006 and Priestley et al. 1999, shown in Figure 6.5 and Figure 6.6, respectively. These solutions were proposed to reduce the damage undergone by the slab caused by the geometric elongation of the beam which occurs during a seismic event. In fact, traditional slabs are not able to accommodate the beam elongation due to both the residual strain within the plastic hinges and the geometrical contribution given by the rotation of the beam. These phenomena cause cracks on the slabs, as well as increase the strength of the plastic hinges by restraining the elongation of beams.

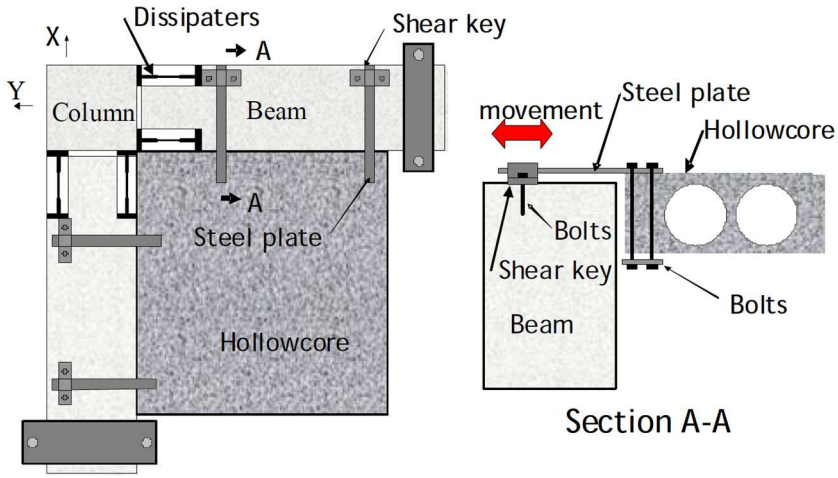

Figure 6.5 Articulated slab connection (taken from Pampanin et al. 2006)

Figure 6.6 X-shaped connection between slab and beam (taken from Priestley et al. 1999)

The identification of efficient technical solutions for minimizing the effects of slab interaction is still a challenge in the scientific literature, worthy of further study.

6.3.1 Calculation of the design parameters

The design process of the beam-column connection calls for the definition of the bending moment M_d which activates the slippage of the system. This value should be obtained from the analysis of the RC frame endowed with such devices. It has to be stressed that the connection should behave rigidly under serviceability limit state and slide during seismic events. Concerning the strategy to design the geometry of the proposed connection, an iterative procedure is adopted, with the purpose of minimizing the height of the vertical central plate. This procedure is outlined below: a tentative value of the internal lever arm z of the beam-to-column connection is selected according to both design bending moment and mechanical and geometrical properties of the beam (e.g. 1.5 times the effective depth of the beam). This value is suggested for beams with small effective depth (e.g. 25 cm), while for beams with larger effective depth is suitable a value of the internal lever arm z equal to 1.2÷1.3 times the effective depth. Then, the diameter and the number of the bolts required to achieve the design moment is computed. Successively, the geometries of steel angles, vertical central plate and slotted holes are defined on the basis of the minimum distances between holes and edges of the plates, as proposed by EN 1993:1-1 and EN 1993:1-8. Furthermore, the distance between steel angle and bottom plate as well as between vertical central plate and column must be adequate to accommodate the maximum rotation achieved by the connection, to avoid any undesired contact. If the above

prescriptions are satisfied, therefore the selected value of z might be greater than the minimum one and might be reduced until the optimal solution is found. On the contrary, if only one of the prescriptions is not satisfied, then the value of z is less the optimal one and a new iteration must be carried out, starting from a greater value of z.

In this study there are no specific structural details of the building in which this connection is inserted. Therefore, a design value of the bending moment should be arbitrarily assumed. On the basis of the hogging moment strength of the beam belonging to the subassembly described in Section 2.2.3, and considering an overstrength factor equal to 1.5, the design bending moment is equal to:

$$M_d = \frac{M_{Rd}^-}{\Omega_\mu} = \frac{165}{1.5} = 110\,kNm \tag{6.2}$$

By doing so, the geometrical characteristics of the beam and column belonging to the subassembly modelled below are the same of the experimentally tested subassembly. The overstrength factor is introduced with the aim of avoiding any damage formation to the surrounding RC members. The overstrength coefficient should be obtained through experimental tests carried out on friction damper devices, taking into account the variability of sliding force, static and dynamic friction coefficients, and preload acting on the bolts. In detail, the research groups of University of Salerno, Italy, and University of Naples "Federico II", Italy, proposed an overstrength factor calculated as follows (Latour et al., 2018):

$$\Omega_\mu = \frac{\mu_{st.95\%}}{\mu_{dyn.5\%}} \frac{N_{b.95\%}}{N_{b.5\%}} = 2 \tag{6.3}$$

in which $\mu_{dyn.\ 5\%}$ and $N_{b.\ 5\%}$ are the 5% fractiles of the dynamic friction coefficient and the bolt preload, respectively; $\mu_{st.\ 95\%}$ and $N_{b.\ 95\%}$ are the 95% fractiles of the static friction coefficient and the bolt preload, respectively. The values were obtained on the basis of the experimental results reported in Latour et al. (2014, 2015), Ferrante Cavallaro et al. (2017, 2018). The range of variability of the static and dynamic friction coefficients depend on the type of friction material used. In fact, the more the friction material provides stable and repeatable response during sliding, the less is the variability of the friction coefficients, leading to lower overstrength factors and more economical structural members.

The research groups of University of Auckland and University of

Canterbury which developed the SHJ already described in Section 3.1, proposed an overstrength factor of 1.4, based on the 95% fractile of the ratios between the experimental sliding force of several specimens of SHJs and the calculated one (Khoo et al. 2015).

In the present research, due to the absence of an experimental campaign aimed to evaluate the variability of the preceding parameters (i.e. sliding force, static and dynamic friction coefficients, and preload acting on the bolts) influencing the calculation of the overstrength factor, the latter is arbitrarly set equal to 1.5, as already specified above, on the basis of the values proposed by the preceding Authors.

Assuming a beam length of 5 m, the shear resistance must be at least equal to $V_{Rd} = 2\ M_{Rd}$ / L = 66 kN in the absence of distributed loads.

The friction damper device is designed to withstand a sliding force $F_{d,1}$ equal to the design bending moment M_d divided by the lever arm z_1, obtained via the above-mentioned iterative procedure, which is equal to 399 mm (Figure 6.7):

$$F_{d,1} = \frac{M_d}{z_1} = \frac{110}{0.399} = 275.7\,kN \tag{6.4}$$

Obviously, in absence of gravity loads acting on the beam, the same magnitude of this force is obtained if hogging or sagging moment is considered.

Six M16 bolts class 10.9 are used, whose resisting area is $A_{res,M16}$ = 157 mm^2 and yielding and ultimate strength are f_{yb} = 900 MPa and f_{ub} = 1000 MPa.

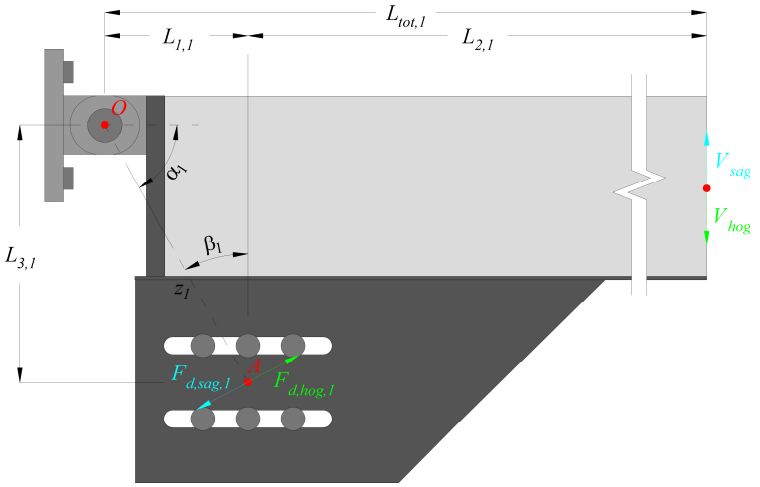

Figure 6.7 Forces acting on the beam calculating the equilibrium with respect to point *O*

So, the preloading force of each bolt is given as follows:

$$F_{pc,M16} = 0.7 f_{ub} A_{res,M16} = 109.9 kN \tag{6.5}$$

According to EN 1993:1-8, the sliding force $F_{s,1,Rd}$ is calculated through the following expression:

$$F_{s,1,Rd} = \frac{k_s n_b n_s \mu}{\gamma_{M3}} F_{pc} \tag{6.6}$$

being: - k_s coefficient that depends on the shape of the slotted hole (contrarily to what the European code prescribed, the value is herein assumed equal to 1); - n_b the number of bolts (6 in this case); - n_s the number of surfaces in contact (2 in this case); - μ the friction coefficient (assumed equal to 0.4); - γ_{M3} safety factor (assumed equal to 1). The value of the friction coefficient is selected consistently to the suggestion of EN1993 with reference to "surfaces blasted with shot or grit, spray-metallized with an aluminium or zinc based product".

Furthermore, regarding the preloading force, several studies in the literature show that the value of F_{pc} decreases progressively due to creep phenomena which are affected to the high amount of preloading force applied to the bolt. With the aim of limiting these effects, as already discussed in Section 3.1, Ferrante Cavallaro et al. (2017, 2018) propose to contain the bolt preload within the range 30-60% of the maximum load suggested by EN 1993:1-8. Therefore, in the present study, the design sliding force $F_{s,d,1}$ is:

$$F_{s,d,1} = t_{s,1} n_b n_s \mu F_{pc,M16} \tag{6.7}$$

where the parameter $t_{s,1}$ is introduced for representing the ratio between the effective and the code-consistent preload applied to the bolt, which is set between 0.3 and 0.6 as mentioned before. In particular, by equating Eq. (6.4) and Eq. (6.7) a ratio $t_{s,1}$ = 0.523 is obtained. Successively, the design preloading force $F_{pc,d,1}$ to be applied to each bolt results:

$$F_{pc,d,1} = t_{s,1} F_{pc,M16} = 0.523 \times 109.9 = 57.5 kN \tag{6.8}$$

The length of the horizontal and vertical slotted holes is designed on the basis of the displacement demand of the considered structure. By assuming that the structure collapses according to the global mechanism, the relation between the displacement demand at the top of the building δ_c, which can be evaluated by means of the elastic response spectrum, and the rotation demand

at the beam ends θ_c, can be approximated as follows:

$$\theta_{c,1} \approx \frac{\delta_c}{h_{str}} = 40 mrad \tag{6.9}$$

where h_{str} is the total height of the building. Subsequently, the minimum length of the horizontal and vertical slotted holes to ensure the movement of the bolts can be approximated as follows:

$$l_{horizontal\ slotted\ holes,\min,1} = \theta_{c,1}\, z_1 \cos\beta_1 = 14 mm \tag{6.10}$$

$$l_{vertical\ slotted\ holes,\min,1} = \theta_{c,1}\, z_1 \sin\beta_1 = 7.7 mm \tag{6.11}$$

These lengths are measured between the external face of the bolt shank and the slotted hole internal face. The group of six bolts used in the friction device are arranged on two horizontal rows. The two bottom steel angles are bolted to the rib plate by means of the aforementioned group of six M16 bolts. Each angle is subjected to one half of the force expressed by Eq. (6.4), whose horizontal and vertical components amplified by the overstrength factor are calculated below:

$$B_{h,1} = \frac{1}{2}\Omega_\mu F_{d,1} \sin(\alpha_1) = 180.8\ kN \tag{6.12}$$

$$B_{v,1} = \frac{1}{2}\Omega_\mu F_{d,1} \cos(\alpha_1) = 100.2\ kN \tag{6.13}$$

The horizontal component is a compressive force in the case of hogging moment, tensile force in the case of sagging one. The vertical component is oriented downward in the case of hogging moment, upward in the case of sagging one. The angle web is dimensioned considering the bending moment due to the shear force in the presence of axial force. With regard to the angle flange, the design is carried out according to the plastic failure mechanisms described in EN 1993:1-8. If the equilibrium is calculated with respect to the point *A* (Figure 6.7), the same forces reported in Eqs. (6.12) and (6.13) are obtained and can be used to design the pin connection consistently with EN 1993:1-8 prescriptions. As regards the connection to the column, this will be calculated in the third solution.

Lastly, some considerations regarding the geometrical restraints which control the design of the friction connection for an optimal functioning are

carried out. By referring to Figure 6.7, the lever arm z_1, can be easily calculated as $\sqrt{L_{1,1}^2 + L_{3,1}^2}$, where $L_{1,1}$ and $L_{3,1}$ are the horizontal and vertical distances between the points *A* and *O*, respectively. Hence, in the case of hogging moment, the equilibrium with respect to the point *O* is expressed as follows:

$$V_{hog} L_{tot,1} = F_{d,hog,1} \sqrt{L_{1,1}^2 + L_{3,1}^2} \tag{6.14}$$

The vertical component of the friction force $F_{d,hog,1}$ can be rewritten as follows:

$$F_{d,hog,1,v} = F_{d,hog,1} \sin \beta = F_{d,hog,1} \frac{L_{1,1}}{\sqrt{L_{1,1}^2 + L_{3,1}^2}} \tag{6.15}$$

Rearranging Eq. (6.15) with respect to $F_{d,hog,1}$ and substituting into Eq. (6.14), yields:

$$F_{d,hog,1,v} = \frac{V_{hog} L_{1,1} L_{tot,1}}{L_{1,1}^2 + L_{3,1}^2} \tag{6.16}$$

where $L_{tot,1}$ is the beam length. From Eq. (6.16) can be obtained the deemed-to-satisfy inequality for the optimal functioning of the friction connection, as follows:

$$\frac{F_{d,hog,1,v}}{V_{hog}} = \frac{L_{1,1} L_{tot,1}}{L_{1,1}^2 + L_{3,1}^2} \geq 1 \tag{6.17}$$

It is interesting to highlight that the above inequality involves only the geometry of the connection. For geometrical configurations satisfying Eq. (6.17), it is ensured that the vertical component of the friction force acting on the friction device is able to carry the shear force to which the beam is subjected. Moreover, in the case of ratio between $F_{d,hog,1,v}$ and V_{hog} greater than 1, this means that vertical equilibrium of the beam is ensured only if the top connection applies a shear force on the beam with the same direction of the vertical component of the external load acting on the beam and having a magnitude equal to the difference between $F_{d,hog,1,v}$ and V_{hog}. On the contrary, in the case of inequality not satisfied, the functioning of the connection could be hampered by a different orientation of the friction force with respect to the theoretical one or by a transfer of shear force to the T stub web, both cases caused by the need of satisfying the vertical equilibrium of the beam.

6.3.2 Finite element model

Once the geometry of the first solution was defined, 3D FEM analysis on a simplified equivalent structural model is carried out (Figure 6.8). A subassembly representing an exterior beam-column joint is modelled using the FEM software ABAQUS CAE, considering the column pinned at both the top and the bottom sections. Cross-section dimensions and length of both two half-columns and half-beam are equal to 300 × 400 mm and 3 m, 250 × 300 mm and 2.5 m, respectively. The first structural model is implemented aiming at investigating the behaviour of the friction connection, without paying attention to the transferring force mechanisms to beam and column, and it has the following characteristics: - beam and column with a linear elastic behaviour, without any reinforcement; - steel plate of the upper pin connection and lower steel angles are connected to the column with an idealised constraint; - realistic model of the contacts between the elements constituting the friction device (penalty in the tangential direction and hard contact in the normal one); - due to the need for simple construction solutions, the pin connection is not calibrated; thus, the initial configuration of the pin in an ideal centred position with respect to the hole in which is inserted, is assumed; therefore, it is not in contact with the pin shank. As regards materials, the steel elements are modelled using an elastic stress-strain curve. In particular, steel elements and bolts are modelled using the same elastic modulus E_s equal to 210 GPa. The analysis procedure used is “Static, General”, while the automatic stabilization option used is “Specify dissipated energy fraction”, set to the default value of 0.0002. The preceding options will be also used in the other two solutions analysed in the following sections. Concerning the bolt preload, this is simulated by using the dedicated tool already existing in the “Types for selected step” list, within the “Load” window, and named “Bolt load”. The bolt preload will be applied in the same way in the following solutions. Two displacement control tests have been simulated, by imposing a vertical displacement to the beam end section. The first one is monotonic downward up to 240 mm and the other one is cyclic with a displacement in the range ± 100 mm. Before application of the displacement history, the preloading force is applied to the bolts of the friction device.

6.3.3 Results

The moment-rotation curve of the monotonic test is reported in Figure 6.10, in which six different phases are emphasized. The moment is defined as the product between the vertical reaction force at the beam end section and the

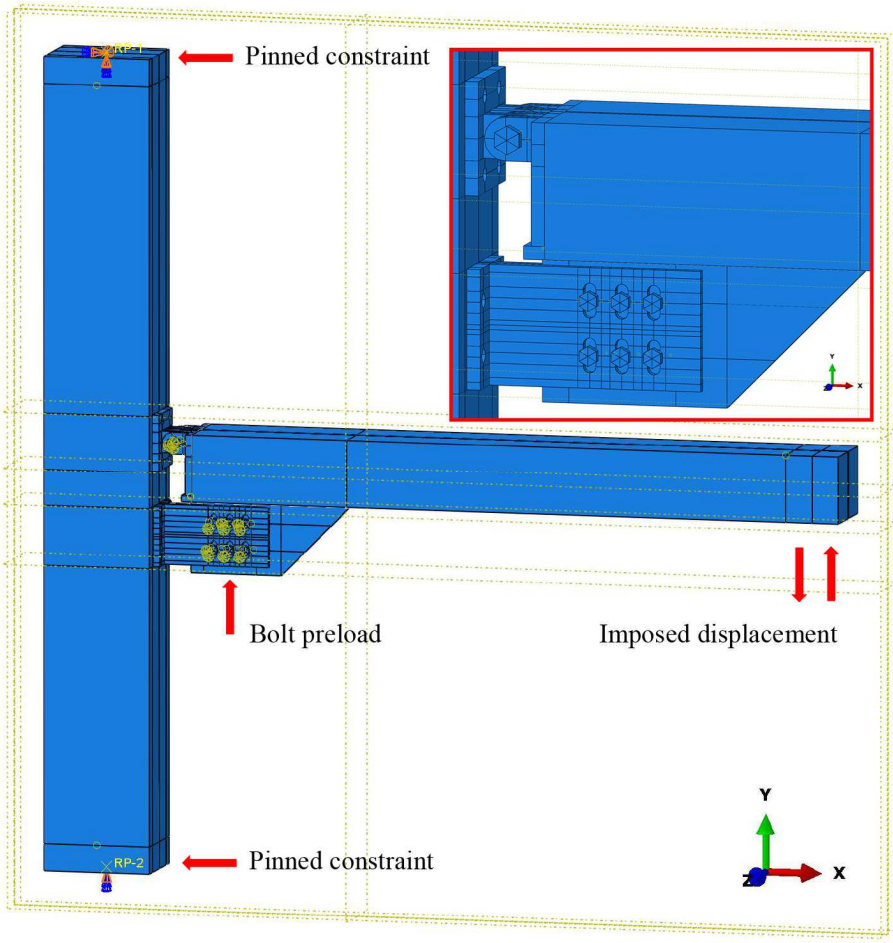

Figure 6.8 3D model of the first solution of dissipative system

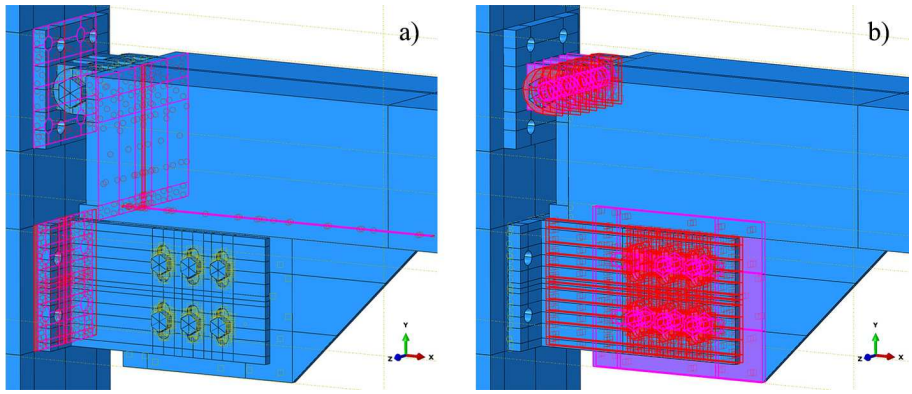

Figure 6.9 Surfaces involved in the definition of contacts: a) idealised contact between column and both steel plate of pin connection and angle flanges; b) realistic contact between elements constituting the friction device and the pin connection

distance between the beam end section and the axis of the pin connection. As for the rotation, it is given by the ratio between the displacement at the beam end section and the distance between the beam end section and the axis of the pin. The rotation values plotted in Figure 6.10 are given by the contributions provided by the beam, column and beam-column connection. The mechanism of transmission of the shear force will be discussed for each phase.

1. In the linear elastic branch the friction stresses at the interface of the dissipative device are able to avoid the sliding of the surfaces. Because the upper pin is not in contact with the holes of the steel elements in which is inserted due to the clearance hole, the bending moment and the shear force are totally absorbed by the friction shims;
2. In the second branch, the resistance provided by the friction stresses is achieved, structural elements slide mutually, and the beam rotates around a point identified within the plates constituting the dissipative device, until the pin is in contact with the holes of the steel elements (Figure 6.11);
3. The system assumes a new configuration in terms of stiffness, the distribution of the friction stresses on the dissipative device is modified, because the bending moment resistance of the beam-to-column connection is provided from the reaction of the pin and the friction forces at the dissipative device. The system behaves elastically again. In this step, the shear force experienced by the connection is still totally absorbed by the friction device;

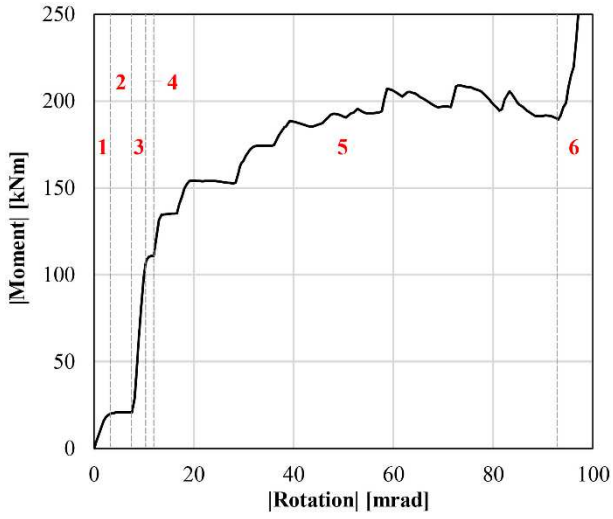

Figure 6.10 First solution: moment-rotation curve of the monotonic analysis

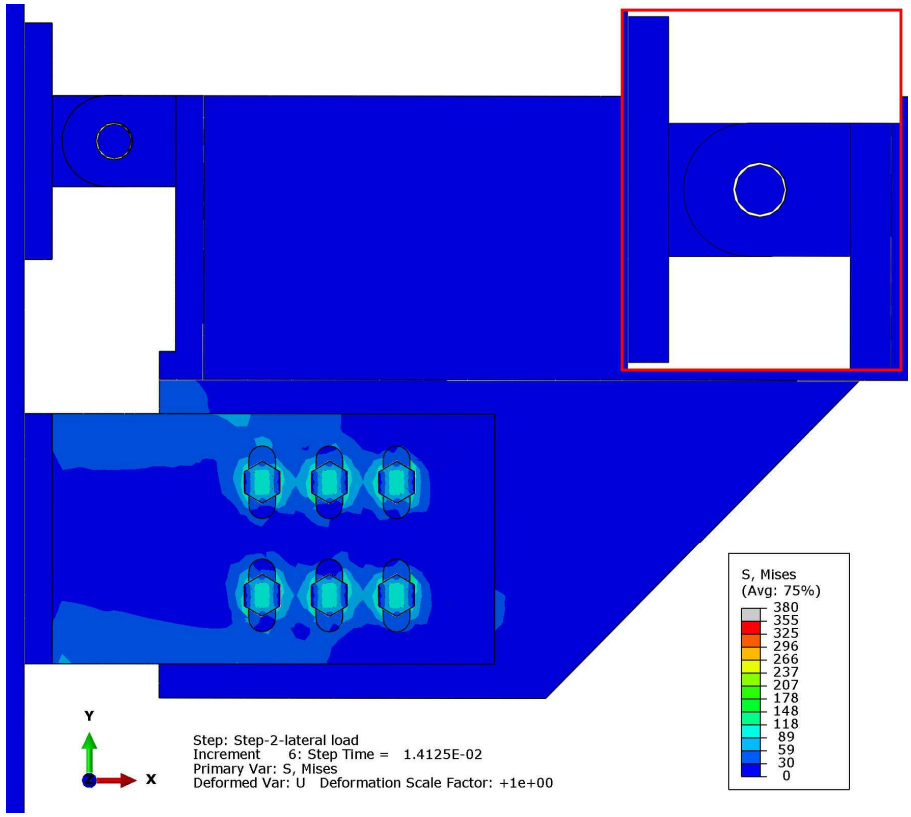

Figure 6.11 Stress state during phase 2

4. The sliding system activates and the beam rotates around the centre of rotation in the contact area between the pin and the steel elements (Figure 6.12). In this branch the moment-rotation relationship is perfectly plastic, namely the force value for which the device slides is constant while the beam rotation increases. The friction shims withstand the whole shear force in this step as well. The structural elements constituting the dissipative device behave elastically, reproducing the behaviour expected during the design procedure. The bending moment of the connection is approximately equal to 110 kNm;
5. Bolt shanks, which during previous steps were not in contact with the horizontal slotted holes of the rib plate, due to the hole clearance, go in contact with the latter ones. At the interface between bolts shanks and horizontal slotted holes of the rib plate, localized increments of the stress values are registered, as can be seen in Figure 6.13 (the right steel angle and bolt heads are removed). In order to keep rotating the system, bolts of the dissipative device have to be drawn below by the rib plate.

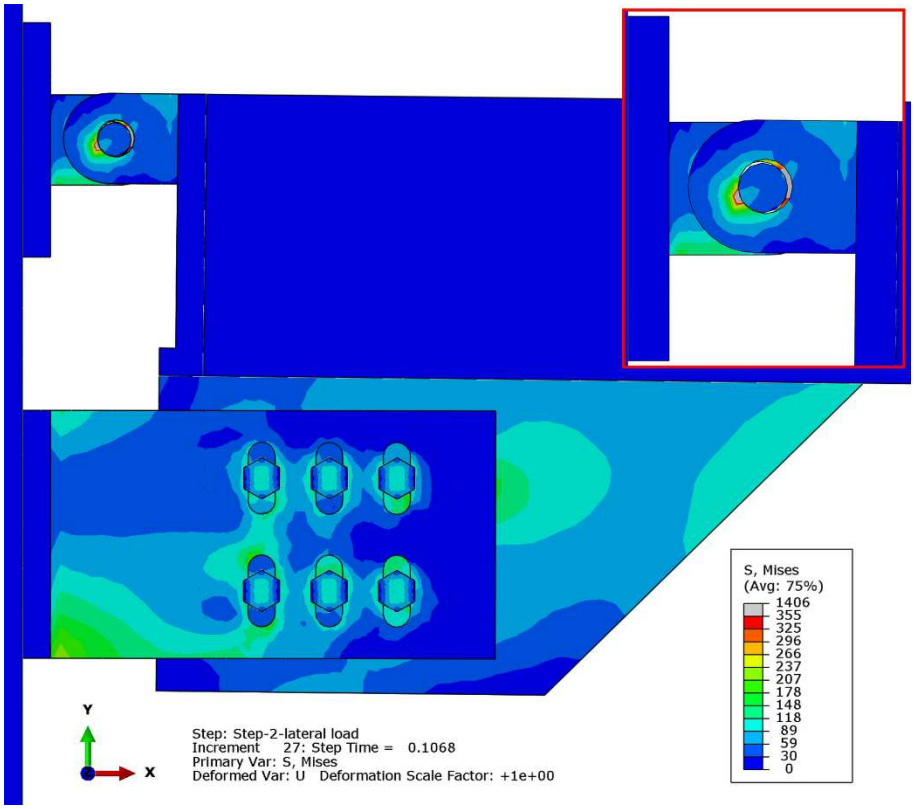

Figure 6.12 Stress state during phase 4

To do so, the friction forces between the bolt heads and the external faces of the steel angles have to be overcome. These friction forces, which usually are not considered in steel structures, cause the sawtooth-shaped progressive increment of the load, as shown in Figure 6.10. This increment is due to the contacts between horizontal slotted holes and bolts shanks which gradually occur while the beam rotation increases (Figure 6.13). As for the shear, the secondary friction forces cause an increment in the shear experienced by the web angles, already subjected to the whole shear force transferred by the beam. To maintain the vertical equilibrium of the beam, the pin connection provides a vertical reaction with the same direction of the external force acting on the beam and value equal to the difference between the shear force acting on the web angles and that acting on the beam;

6. The bolts of the friction device go in contact with the end of vertical slotted holes, thus the system exhibits a new stiffness. The displacement value for which this phenomenon is achieved is well beyond the design

rotation capacity for which the beam-to-column connection has been designed.

Once the results of the monotonic test have been discussed, confirming what was already faced in the literature and described in Section 3.1, the cyclic test was carried out, providing the moment-rotation response reported in Figure 6.14. From the analysis of this figure, some considerations can be carried out:

- The phenomenon registered in the previous test and described as "step 2", namely the step during which the pin is not in contrast with the steel elements, is become critical when the bending moment to which the connection is subjected, is reversed (it is emphasized in Figure 6.14 with the dashed rectangles). As a matter of fact, these two horizontal branches represent the resistance provided by the friction device when the pin moves inside the holes within is inserted. As a consequence, not only the stiffness,

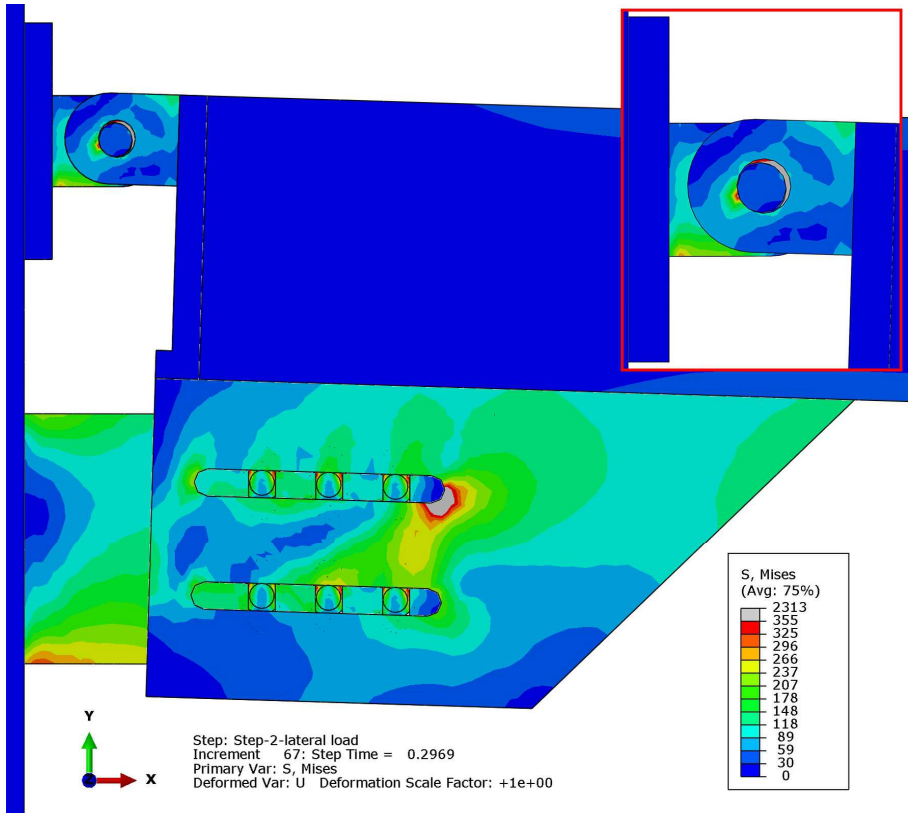

Figure 6.13 Stress state during phase 5

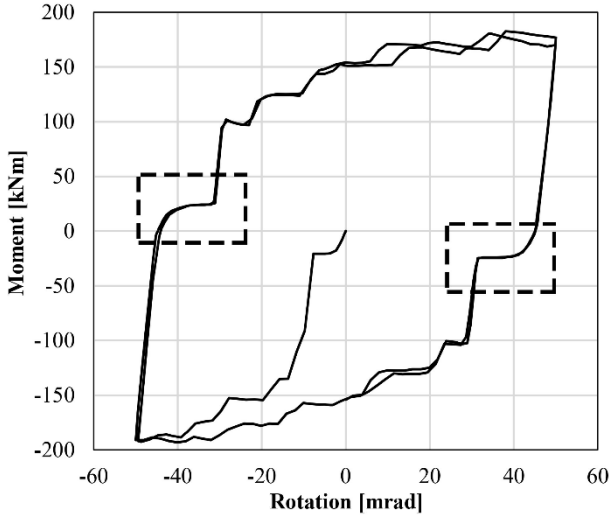

Figure 6.14 First solution: moment-rotation curve of the cyclic analysis

but also the dissipative capacity of the connection is highly influenced by this phenomenon;

- Wide and stable hysteretic cycles are obtained because the 3D FEM model does not include both degrading phenomena regarding the friction coefficient and loss of bolt preload.

6.4 Solution with curved slotted holes and T stub

Based on the above-discussed results, the second device scheme, illustrated in Figure 6.15, aims to solve the weaknesses of the first one, i.e. pinching of the connection response which depends on the position of the pin, and the additional resistance of the dissipative device when the bolts are dragged above and below. The first problem is solved by substituting the pin connection with a bolted connection constituted by a T stub and a C-shaped steel plate. The cross-sectional shape of the latter makes the steel element much stiffer than the T stub using the same cross-sectional area. At the same time, the C-shaped profile width is less than that of the beam to which is connected, in order not to obstacle the concrete pouring operation. As already known in the literature, and described in Chapter 3, the centre of rotation of the connection is supposed to form near the base section of the T stub. In the adopted solution, the cross-sectional area of the horizontal plate of the T stub is reduced by means of two holes, in order to force the system to form the plastic hinge at the reduced section, ensuring the definition of a centre of rotation. As for the second problem, namely the additional resistance due to

the secondary friction forces, the horizontal and vertical slotted holes were substituted with curved slotted holes realized on the rib plate. By doing so, the dissipative device is able to rotate and the bolts remain in their initial position. It should be emphasized that the presence of the slab and its possible interaction with the functioning of the proposed connection is not investigated. However, to accommodate possible different displacement from that assumed during design phases (i.e. displacement along the radial direction) caused by the interaction with the slab, a group of slotted holes arranged along the radial direction can be realized on the angle webs. This solution, that will be investigated when the presence of the slab will be considered in the FEM models, could avoid severe damaging of bolts in the case of malfunctioning of the friction connection.

Concerning the cross-sectional dimensions along the radial direction, the width is set 1.3 times the diameter of the bolts used in the friction device to ensure that the bolts shanks do not hit the curved slotted holes while the connection slides. As a result, both the bolts of the friction device and the vertical central plate are prevented from experiencing severe damage. On the basis of the above-defined centre of rotation, length and width of the curved slotted holes have been determined with the aim of ensuring the design rotation capacity, avoiding, once the sliding step is achieved, any contact between bolts shanks and slotted holes.

Preliminary analyses showed that the system exhibited no sufficient stiffness in the in-plane direction. Therefore, 12 mm diameter inclined rebars have been inserted connecting the bottom plate of the HSTCB and the top chord, as depicted in Figure 6.16. These web bars have variable inclination and allow the activation of the stress transfer mechanism between concrete, steel top chord and slotted-hole central plate.

With reference to the connection layout, beam end shape and stirrup layout are chosen in order to reduce interferences with the slab after the concrete casting phase, and to ensure the replaceability of the T-stub and the bolts used in the connection with the C-shaped profile. For this reason, the area under the upper connection must be empty. At the same time, it is necessary to ensure a proper stress transfer capability between bottom and top chord of the steel truss connecting the two chords throughout the length of the connection. To fulfil the above requirement, the concrete core in the proximity of the connection presents an inclined external face throughout the length of the top bolted connection (see the beam profile shown in Figure 6.15) and the layout of the inclined central stirrups is determined consequently. It is worth remarking that the number, inclination and position of the central stirrups

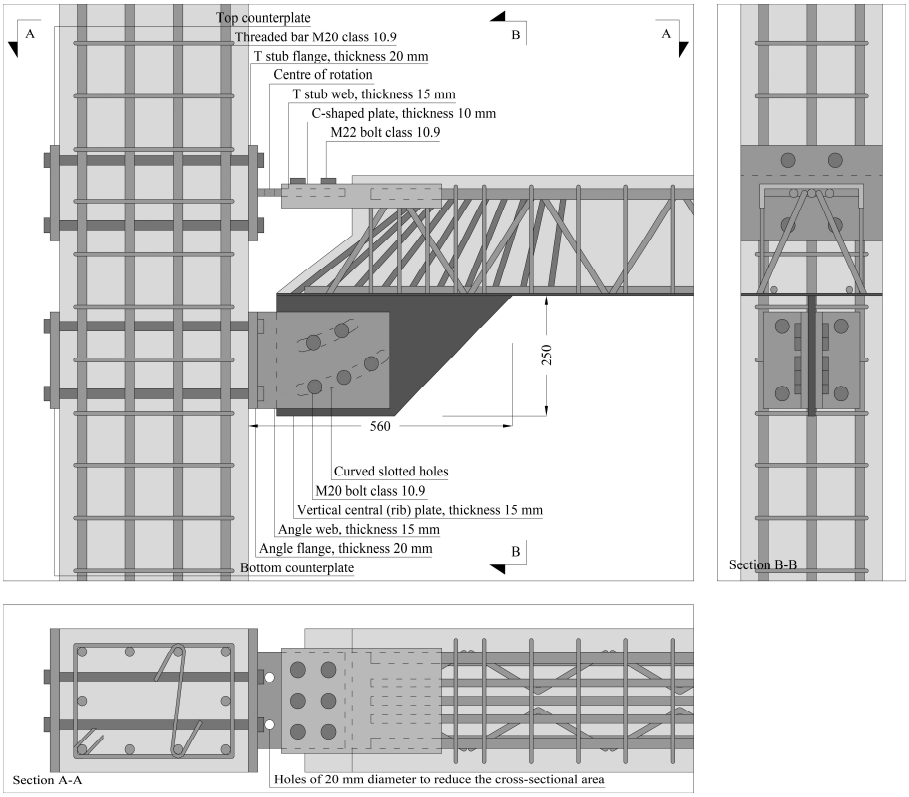

Figure 6.15 Second solution with curved slotted holes and T stub

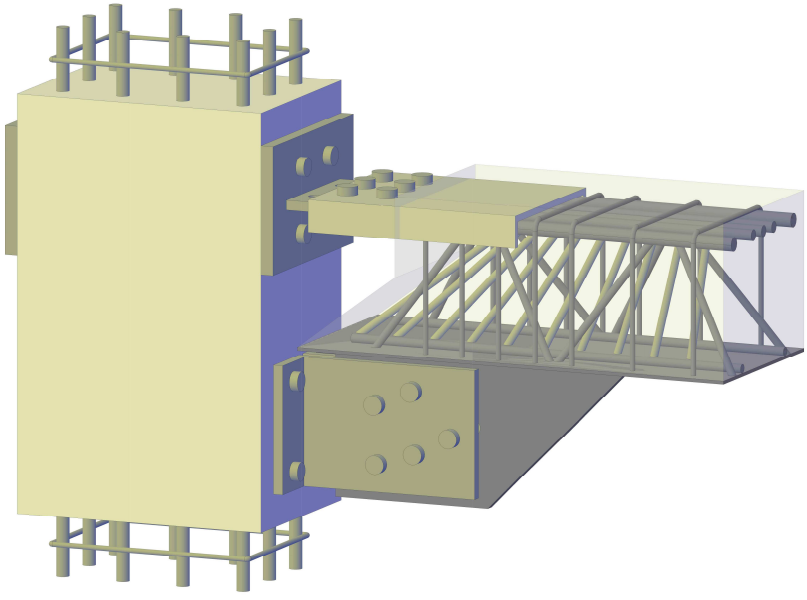

Figure 6.16 Second solution:3D view

might be optimised through a parametric study aimed at reducing structural complexity and improving the stress transfer mechanism between the vertical central plate, the top and bottom chord of the steel truss, and the concrete core of the beam along the length of the device.

6.4.1 Calculation of design parameters

Like the previous solution, the design bending moment is set to M_d = 110 kNm. The new geometrical configuration provides a different lever arm z_2 of the connection, which is 380 mm. Therefore, the sliding force $F_{d,2}$ is computed by modifying Eq. (6.4):

$$F_{d,2} = \frac{M_d}{z_2} = \frac{110}{0.380} = 289.5\,kN \tag{6.18}$$

As explained in Section 6.3.1, the same magnitude of this force is obtained if hogging or sagging moment is considered. In this solution, five M18 bolts 10.9 class are adopted, whose resisting area is $A_{res,M18}$ = 192 mm^2. So, the preloading force of each bolt is given as follows:

$$F_{pc,M18} = 0.7 f_{ub} A_{res,M18} = 134.4\,kN \tag{6.19}$$

The design sliding force $F_{s,d,2}$ is:

$$F_{s,d,2} = t_{s,2} n_b n_s \mu F_{pc,M18} \tag{6.20}$$

in which the meaning of parameters is already known. As done before, by equating Eq. (6.18) and Eq. (6.20) the ratio between the effective and the code-consistent preload applied to the bolt is calculated, which is equal to $t_{s,2}$ = 0.538. So, the design preloading force $F_{pc,d,2}$ to be applied to each bolt results:

$$F_{pc,d,2} = t_{s,2} F_{pc,M18} = 0.538 \times 134.4 = 72.3\,kN \tag{6.21}$$

Consistently with Section 6.3.1, the length of the curved slotted holes is designed on the basis of the displacement demand of the considered structure. In this case, a higher rotation demand $\theta_{c,2}$ is assumed, equal to 50 mrad. Therefore, the minimum length of the curved slotted holes to ensure that there is no contact between bolt shanks and slotted holes is given by:

$$l_{curved\,slotted\,holes,\min,2} = \theta_{c,2} z_2 = 19\,mm \tag{6.22}$$

This length is measured between the external face of the bolt shank and the

slotted hole face. The group of five bolts used in the friction device are arranged on two rows of curved holes. The two bottom steel angles are bolted to the rib plate by means of the above-mentioned group of five M18 bolts. Each angle is subjected to one half of the force expressed by Eq. (6.18), whose horizontal and vertical components amplified by the overstrength factor are calculated below:

$$B_{h,2} = \frac{1}{2}\Omega_{\mu} F_{d,2} \sin(\alpha_2) = 201.3\ kN \tag{6.23}$$

$$B_{v,2} = \frac{1}{2}\Omega_{\mu} F_{d,2} \cos(\alpha_2) = 81.4\ kN \tag{6.24}$$

in which α_2, being the angle between the beam axis and the lever arm z_2, is equal to 68°. The horizontal component is a compressive force in the case of hogging moment, tensile force in the case of sagging one. The vertical component is oriented downward in the case of hogging moment, upward in the case of sagging one. The angle web is dimensioned considering the bending moment due to the shear force in the presence of axial force. With regard to the angle flange, the design is carried out according to the plastic failure mechanisms described in EN 1993:1-8. As for the T stub, if the equilibrium is calculated with respect to the point *A* (Figure 6.17), the same forces reported in Eqs. (6.23) and (6.24), multiplied by 2, are obtained and can be used to design the standard bolted connection between T stub and C-shaped profile consistently with EN 1993:1-8 prescriptions.

As highlighted before, preliminary analyses showed that the concrete block of the beam tends to separate from the bottom plate, rotating around the point *B*, in the case of hogging moment, and the point *C*, in the case of sagging moment (Figure 6.17). Therefore, a group of vertical rebars with different inclinations were placed at the connection between vertical central plate and bottom plate. The moment acting on these stirrups can be easily calculated as follows:

$$M_{Ed,vertical\ inclined\ rebars,hog} = V_{hog,2} L_{4,2} = 66 \times 1.84 = 121.44\ kNm \tag{6.25}$$

$$M_{Ed,vertical\ inclined\ rebars,sag} = V_{sag,2} \left(L_{3,2} + L_{4,2} \right) = 66 \times 2.385 = 157.41\ kNm \tag{6.26}$$

It must be underlined that these rebars should behave elastically up to the design moment of the beam-column connection multiplied by the overstrength

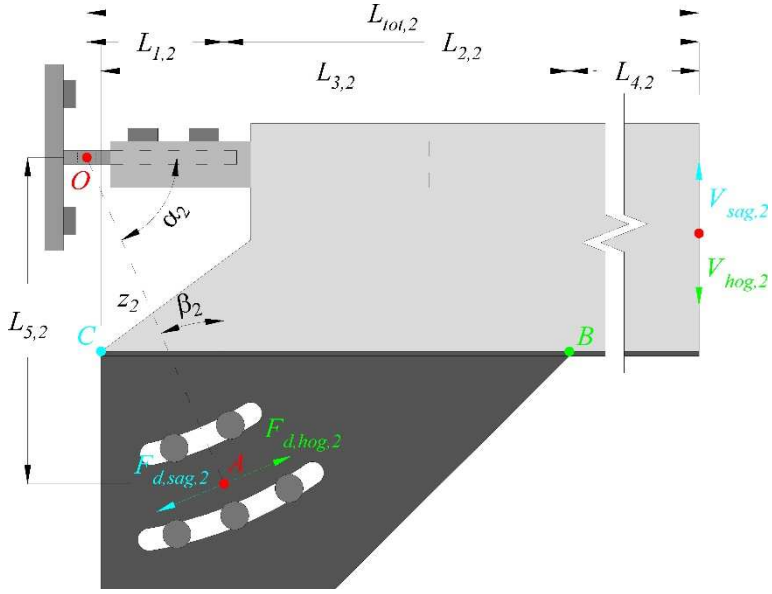

Figure 6.17 Forces acting on the beam calculating the equilibrium with respect to point *O*

factor. With regard to the connection to the column, this will be calculated in the third solution.

6.4.2 Finite element model

A more detailed FEM model is developed in order to accurately evaluate the mechanical behaviour, in terms of stiffness and strength, not only of the beam-column connection, but also of the connections between the friction device and beam, and between beam and column. Geometry of the beam-column subassembly as well as mechanical properties of steel elements are the same of the previous model. More in detail, the length of the beam is 2.6 m, while the load application point is placed 2.4 m from the column face. Regarding the concrete material, a compressive strength f_c of 25 MPa and an elastic modulus E_0 of 28960 MPa are adopted. The plastic behaviour of concrete is modelled by using the Concrete Damaged Plasticity model based on the theory of plastic continuous damage of quasi-brittle materials. The uniaxial stress-strain relationship of concrete in compression is computed via the following equation, proposed by Saenz (1964):

$$\sigma = \frac{E_0 \varepsilon}{1 + \left(E_0 \frac{\varepsilon_c}{f_c} - 2 \right) \frac{\varepsilon}{\varepsilon_c} + \left(\frac{\varepsilon}{\varepsilon_c} \right)^2} \tag{6.27}$$

Where ε_c is the strain at the peak stress assumed equal to 0.002. The compressive behaviour of concrete is assumed linear elastic until the 40% of the peak compressive stress. As for the damage model, the one proposed by Lubliner et al. (1989) is used. As a matter of fact, this model assumes that loss of stiffness occurs only once the peak stress is attained, i.e. in the softening branch, and is described by the following simple equation:

$$d = 1 - \frac{\sigma}{f_c} \tag{6.28}$$

in which d is the damage and σ is the post-peak compressive stress.

Regarding the tensile behaviour, the concrete is assumed to behave elastically until the attainment of the tensile strength equal to 2.56 MPa. The softening branch is modelled via the fracture energy method, whose value is computed as proposed by CEB-FIP Model Code (2010):

$$G_F = 73 f_c^{0.18} = 0.13 N/mm \tag{6.29}$$

The adopted values of the parameters describing the CDP model are reported in Table 6.1.

The compressive stress-strain curve of the concrete is shown in Figure 6.18.

With regard to the steel elements, they are characterized by three different grades. Rebars are made of steel grade B450C, which is the standard class required by the Italian Code, that of constructional steel is S355, while bolts are class 10.9. The yielding stresses of the grades are 500 MPa, 400 MPa and 900 MPa, respectively. These values are consistent with those reported in Colajanni et al. (2016b). The elastic-perfectly plastic stress-strain curve is used to simulate the inelastic behaviour of steel, with an elastic modulus E equal to 210 GPa.

FEM model uses first order tetrahedral element for all components, with the exception of column and C-shaped profile for which linear bricks are selected (Figure 6.19). The analysis is constituted by two steps: the first one in which the preloading force is applied to the bolts, the second one in which

Table 6.1 Adopted values of the parameters characterizing the CDP model

CDP parameters				
Dilation angle	Eccentricity	f_{b0}/f_{c0}	K	Viscosity
40	0.1	1.16	0.667	0.0001

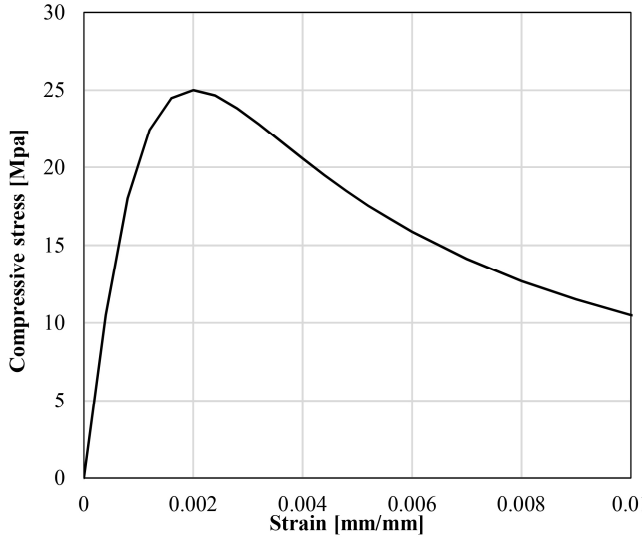

Figure 6.18 Compressive stress-strain curve of concrete used in FEM model

the displacement history is applied to the beam end.

With reference to the contact modelling, the FEM model comprises the following interactions:

- longitudinal, transverse and inclined reinforcement of the HSTC beam, modelled via truss elements, connected to the concrete core with an "embedded" constraint (with which nodes of a wire element embedded within a solid element are constrained to the nearest nodes of the solid element) (Figure 6.20a);
- the bottom plate of the HSTC beam connected to the transverse and inclined reinforcement through a "tie" constraint (with which nodes of an element are constrained to the nearest nodes of another element) (Figure 6.20b);
- the interaction between bottom plate and concrete core by means of a "frictionless" property (Figure 6.20c);
- the connection between C-shaped profile and longitudinal bars via "tie" constraint (Figure 6.20d);
- the interaction between C-shaped profile and concrete core by means of a "frictionless" property (Figure 6.20e).

Two groups of monotonic analyses are carried out, applying a displacement of 240 mm at the beam end downward for the first group, upward for the other one. For each group, two analyses are performed applying different preloading forces at the bolts belonging to the friction

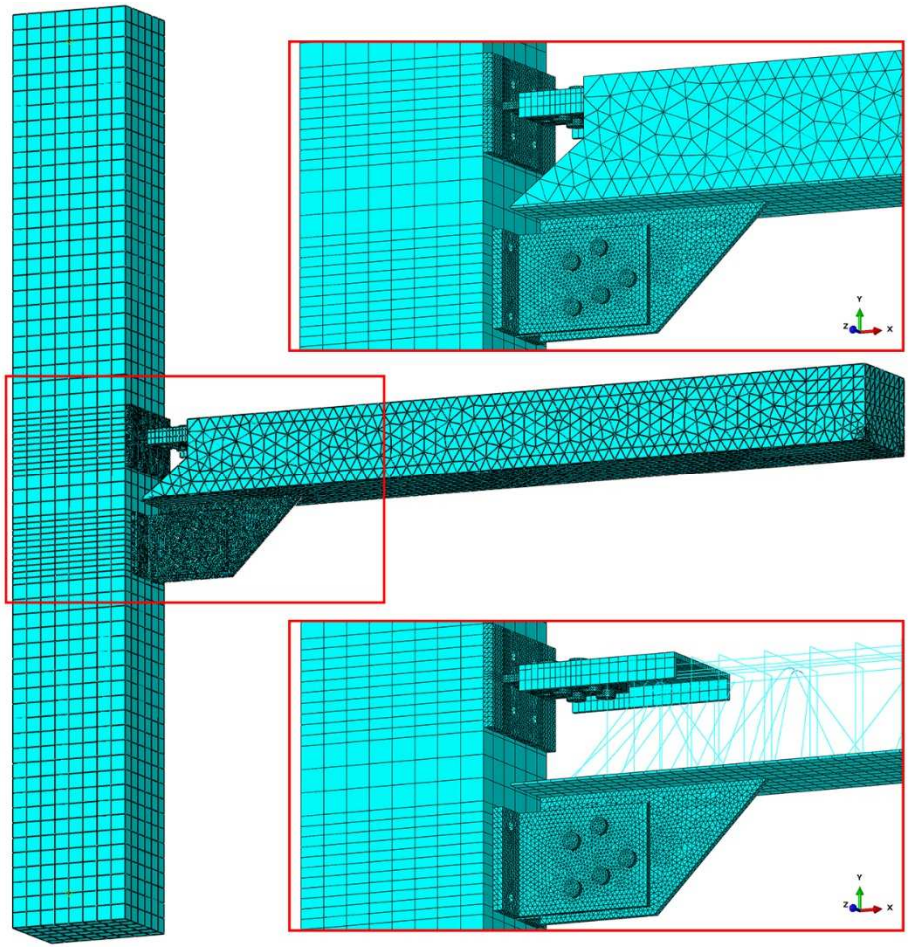

Figure 6.19 Second solution: mesh of the FEM model

device, to simulate different design moment values of the connection, namely M_d and 1.5 M_d. Then, two cyclic analyses are performed by varying the bolt preload as before. The loading protocol is constituted by two cycles of amplitude ± 100 mm.

6.4.3 Results

The results of the proposed connection responses are presented in terms of moment-rotation curves and stress contours for both monotonic and cyclic response. Figure 6.21 reports the monotonic moment-rotation curve that characterizes the response of the friction connection. As in the first solution, the moment is calculated as the product between the vertical reaction force at the free end of the beam and the distance between the assumed centre of

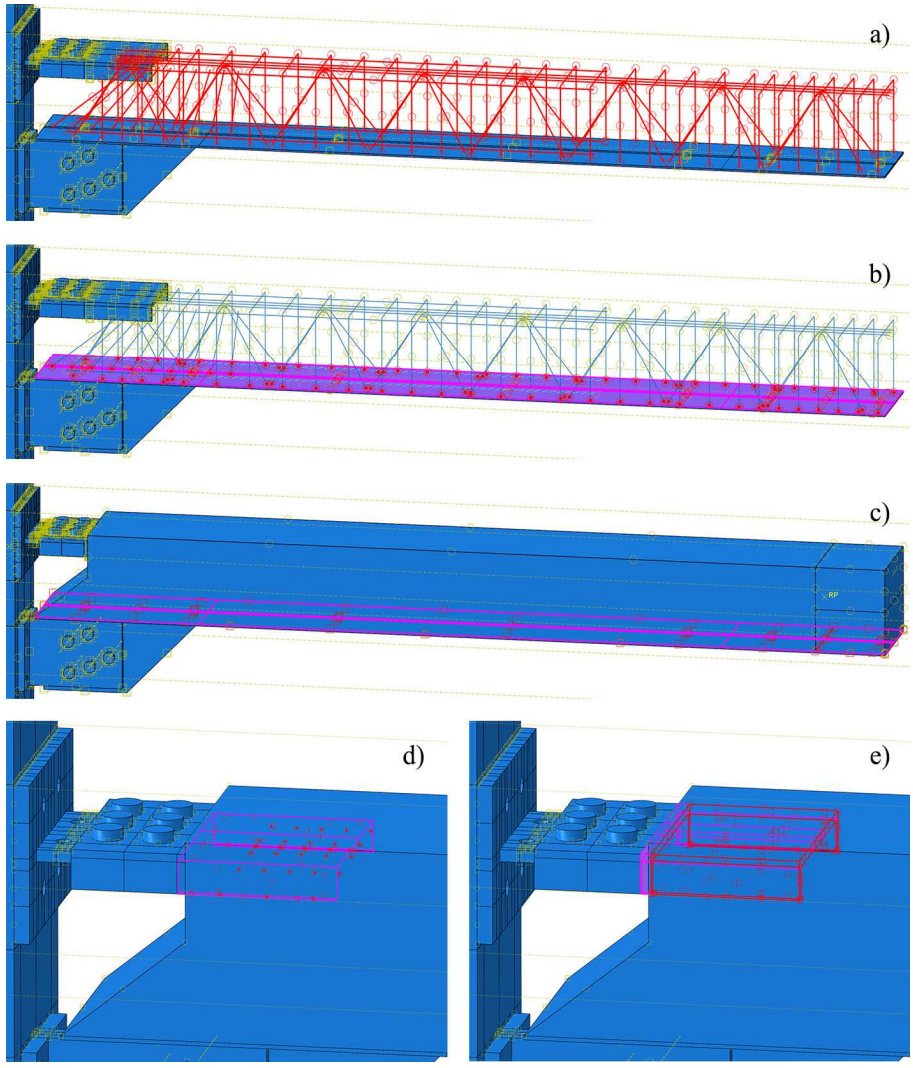

Figure 6.20 Interactions of the FEM model: a) longitudinal, transversal and inclined reinforcement within the HSTC beam; b) "tie" constraint between the bottom plate of the HSTC beam and the transversal and inclined reinforcement; c) interaction between bottom plate and concrete core; d) "tie" constraint between C-shaped profile and longitudinal bars; e) interaction between C-shaped profile and concrete core

rotation and the free end of the beam. As for the rotation, it is calculated by the ratio between the vertical displacement of the beam end and the distance between the assumed centre of rotation and the beam end. The rotation values shown in Figure 6.21 are given by the contributions provided by beam, column and beam-column connection.

The resisting moment of the connection shown by the FEM model is in good agreement with the corresponding design value calculated analytically.

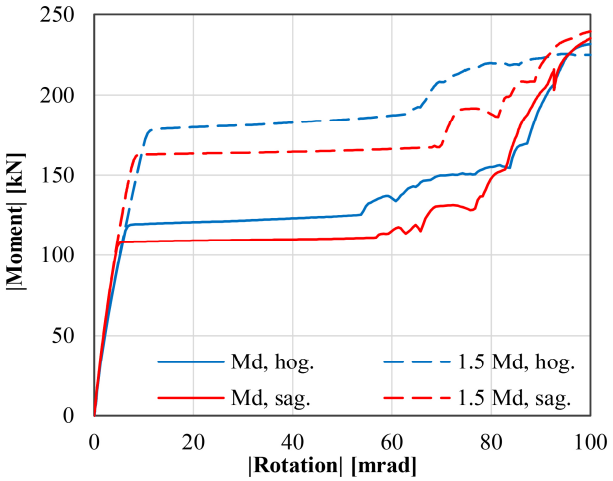

Figure 6.21 Second solution: moment-rotation curves of the monotonic analyses

In discussing the moment-rotation curves in detail, three phases can be identified:

1. the friction device does not slip and the system behaves elastically;
2. the sliding is activated and the behaviour of the system turns into an almost perfectly-plastic behaviour, exhibiting a slight hardening probably due to the plasticization of the base section of the T stub. The deformations of the top connection slightly move the centre of rotation supposed during the design;
3. the design displacement limit is reached; a progressive increment in the moment value is caused by the contact between the bolt shank and the slotted hole internal surfaces.

The responses provided by the two monotonic analyses are different both in terms of stiffness and strength. In fact, the moment values for which the friction device slides are 119 kNm for hogging moment and 108 kNm for sagging moment, 8% higher and 2% lower than the design moment, respectively. Moreover, the rotation for which the friction device slides is lower in the sagging moment analysis (5 mrad) than the hogging moment one (7 mrad). On the contrary, the rotation for which a bolt shank hits the curved slotted holes is higher in the sagging moment analysis (58 mrad) than the hogging moment one (54 mrad). The reason of the differences of such results can be found in the inadequate stiffness of both the C-shaped profile and its connection to the HSTC beam. As for the analyses with the bolt preload multiplied by 1.5, it can be seen that the moment values when the friction device slides are 179 kNm and 160 kNm for hogging and sagging moment,

respectively. These values are 8% higher and 3% lower, respectively. It should be noted that the differences between the design moment and the moment for which the device slides remain approximately constant by varying the bolt preload.

For the brevity's sake, only the results in terms of stress contour plot related to the hogging analyses are described below. Figure 6.22 reports the stress state in the device during the analyses between phase 1 and 2. The figure shows that all steel components of the device are in the elastic range of their constitutive behaviour. Moreover, the stress state seems to increase proportionally in all steel components when the moment strength is increased, proving the efficiency of the design procedure. In addition, it can be noticed that the inclined bars are effective in connecting the friction device to both the top chord and the concrete beam.

Figure 6.23 shows the minimum principal stresses of concrete, illustrating the half part of concrete core of beam only. Generally speaking, the compressive stress values are satisfactory in both analyses with the exception of the high stress values in the bottom part of the concrete core at the right side of the rib plate (highlighted by the circled area), where the bottom steel plate of the HSTCB is not effective in transferring the internal forces coming from the vertical slotted plate.

In Figure 6.24 the plastic maximum principal strains in the concrete are illustrated. Three different cracked areas can be individuated for both the analyses:

- beam upper part (1): here the concrete cracking is due to the flexural tensile stresses;
- concrete cover of the C-shaped profile (2): the deformations of the steel profile cause the damage of the concrete cover;
- bottom plate-concrete interface (3): concrete part near the bottom plate undergoes damage because of the significant tensile stresses due to the inclined stirrups.

Similarly, it is possible to analyse the numerical output in the transition between phase 2 and 3 previously described. More precisely, Figure 6.25a and Figure 6.25b show the stress state in the steel device for the analyses with M_d = 110 kNm and 165 kNm, which can be compared with Figure 6.22a and Figure 6.22b, respectively. The stress values in the steel elements are almost unchanged, except for the T stub and the C-shaped profile: the increase of the rotation of the system produces the increase of the flexure to which the two elements are subjected. It can also be noticed that the bending moment

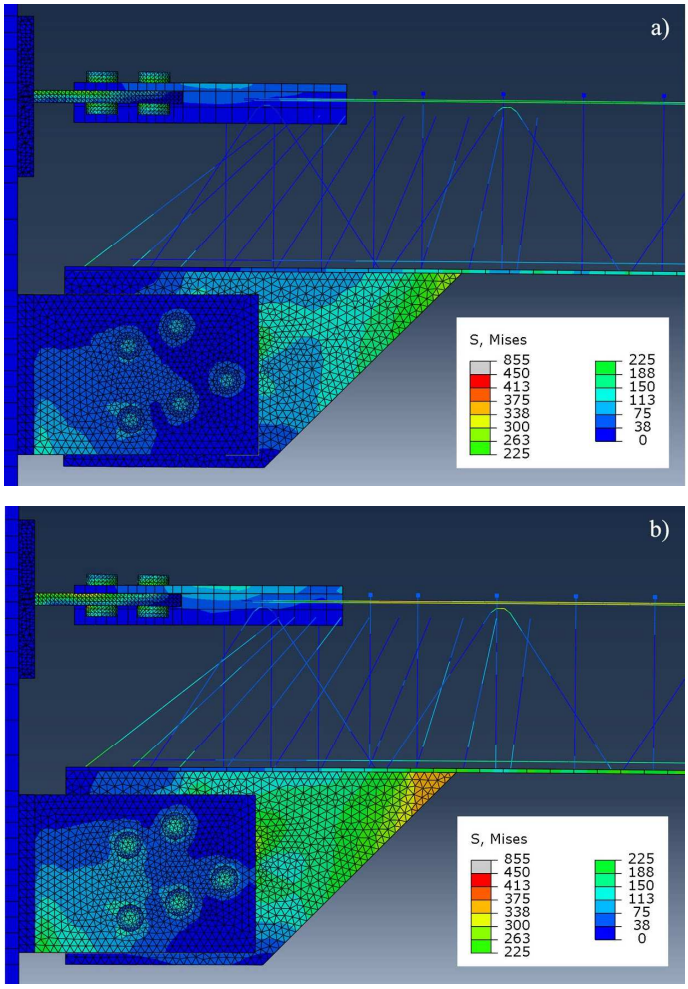

Figure 6.22 Stress state in the steel elements between phase 1 and 2 of the analyses with M_d = 110 kNm (a) and 165 kNm (b).

undergone by the C-shaped profile contributes to a slight shifting of the position of the centre of rotation from the assumed one. Nonetheless, the connection behaves according to the design requirements for displacement greater than the design one.

Likewise, the minimum principal stresses in the concrete of the two analyses illustrated in Figure 6.26a and Figure 6.26b are almost unchanged if compared to those of Figure 6.23a and Figure 6.23b, respectively, proving the capability of the friction connection to limit the forces to which the surrounding elements are subjected and preventing them from experiencing any plastic deformation.

Finally, Figure 6.27 shows the cracked concrete in the transition between

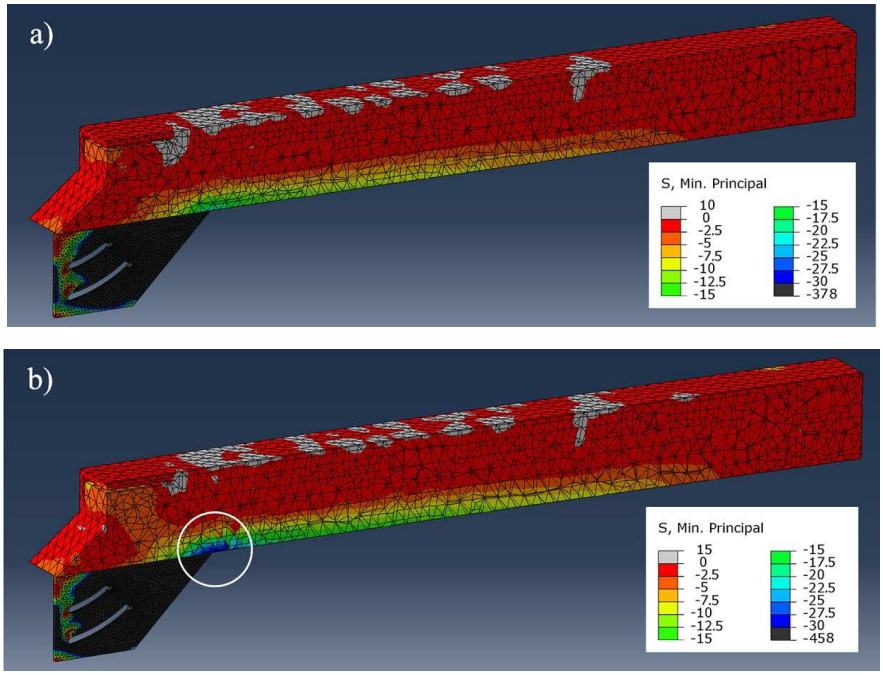

Figure 6.23 Minimum principal stresses in the concrete between phase 1 and 2 of the analyses with M_d = 110 kNm (a) and 165 kNm (b)

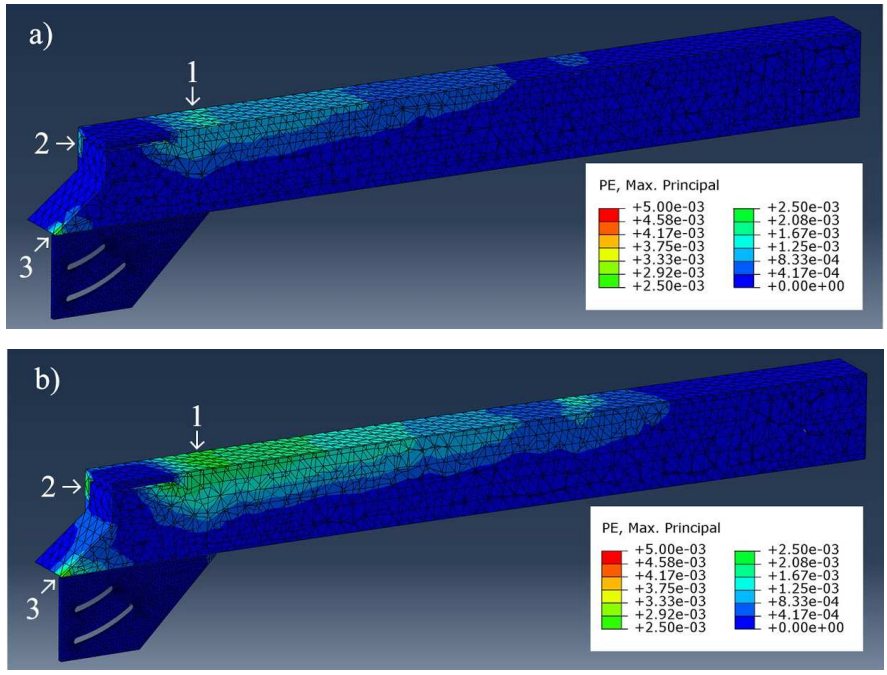

Figure 6.24 Maximum principal strains in the concrete between phase 1 and 2 of the analyses with M_d = 110 kNm (a) and 165 kNm (b).

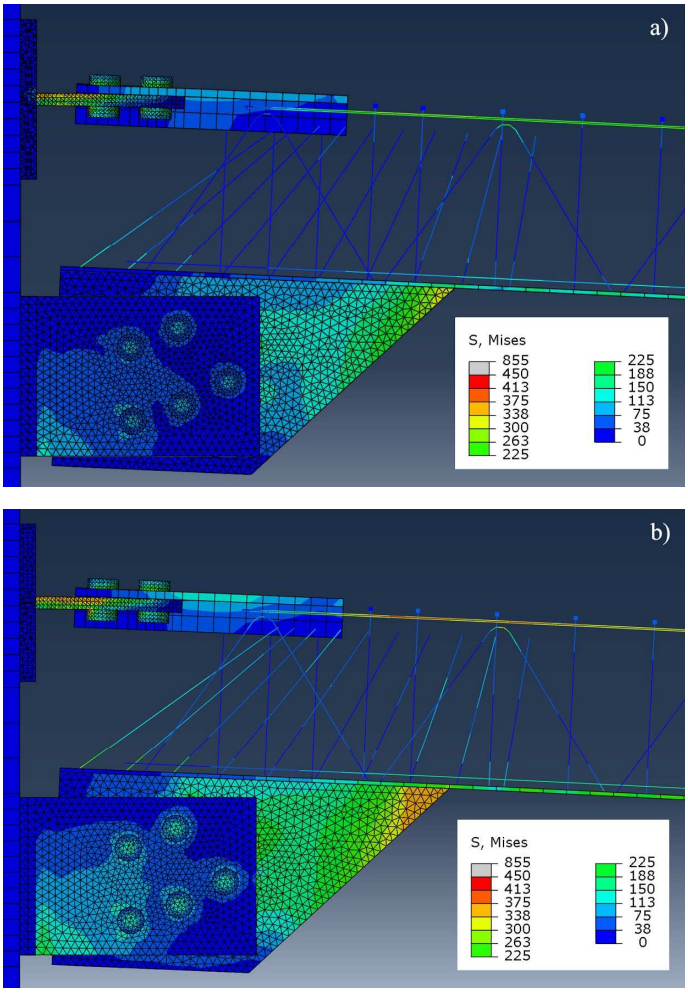

Figure 6.25 Stress state in the device between phase 2 and 3 of the analyses with M_d = 110 kNm (a) and 165 kNm (b).

phase 2 and 3. In particular, the maximum principal strain contour indicates that there is a slight increment of the crack propagation especially in the area next to the C-shaped profile embedded within the concrete. This phenomenon might be due to the significant increment of the flexure of the C-shaped profile. Such a flexure induces a progressive degradation of the concrete cover around the steel profile. Moreover, the cracking state at the beam extrados in the analysis with M_d = 110 kNm (Figure 6.27a) seems to increase significantly if compared to that of Figure 6.24a. By contrast, the cracking state at the beam extrados in the analysis with M_d = 165 kNm (Figure 6.27b) increases negligibly if compared to that in Figure 6.24b. Therefore, the limitation in the concrete strain proves that there is no condition for which the pinching

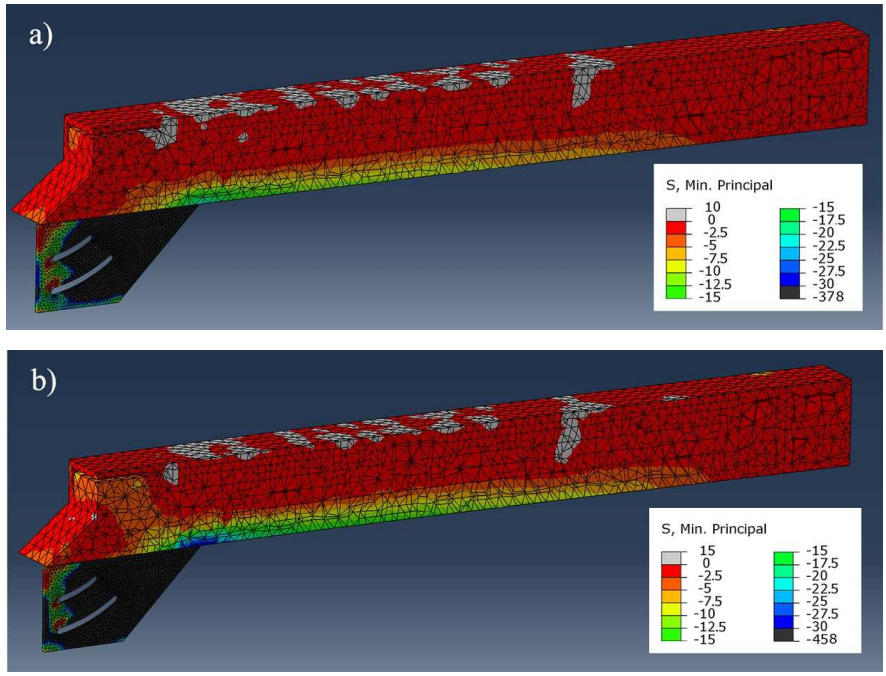

Figure 6.26 Minimum principal stresses in the concrete between phase 2 and 3 of the analyses with M_d = 110 kNm (a) and 165 kNm (b)

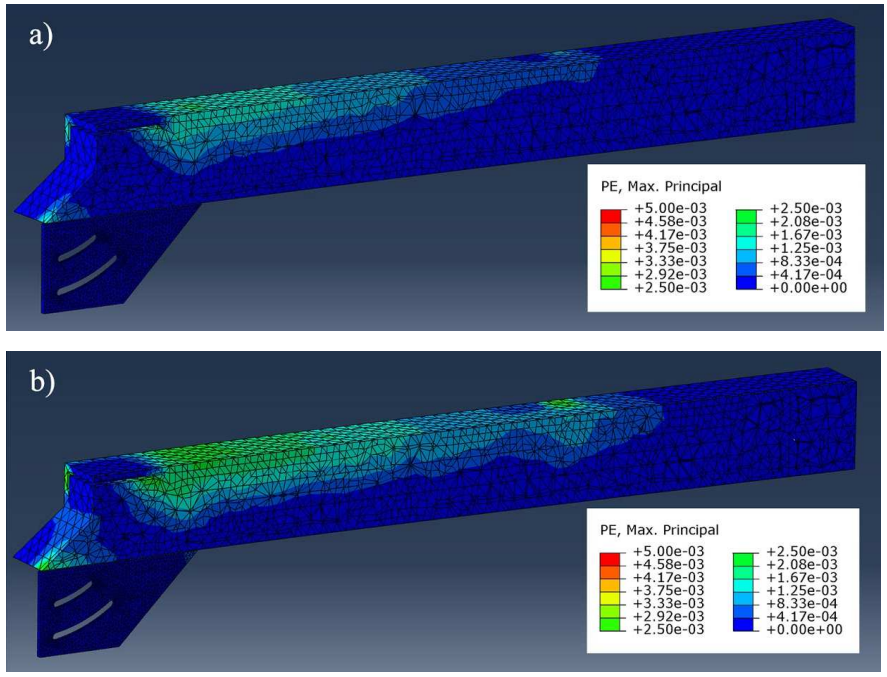

Figure 6.27 Maximum principal strains in the concrete between phase 2 and 3 of the analyses with M_d = 110 kNm (a) and 165 kNm (b).

phenomenon could be activated.

The output of phase 3 is not analysed because it refers to the behaviour of the device beyond the design condition.

From the moment-rotation curve of the cyclic test reported in Figure 6.28, it can be observed that the system behaves according to the design requirements, i.e. it exhibits a similar response for hogging and sagging bending moment and does not evidence any damage in the loading-unloading phases. The analysis of the stress state is the same already described for the monotonic test. Although the FEM analysis is not able to take into account the wearing of the friction pads and possible variation of the friction coefficient, the stability of the hysteresis cycles of the frictional dissipative connections, as attested by several papers in the literature (e.g. Khoo et al. 2015), can be obtained through a combination of low-wear materials able to maintain the friction coefficient as constant as possible (Khoo et al. 2012a) and disc springs able to keep constant the value of the preload acting on the bolts of the connection (Ramhormozian et al. 2019). Moreover, numerous experimental tests available in the literature prove the dissipative capacities and fatigue strength of the T stub as described in Latour et al. (2015).

With regard to the plasticization cumulated on the device components at the end of the cyclic test, Figure 6.29 reports the distribution of the equivalent plastic strains in the steel elements of the analyses with moment strength equal to 110 kNm (a) and 165 kNm (b): it can be observed that all steel elements of the former are in the elastic range with the exception of the horizontal flange of the T-stub which behaves in the plastic range according to the design

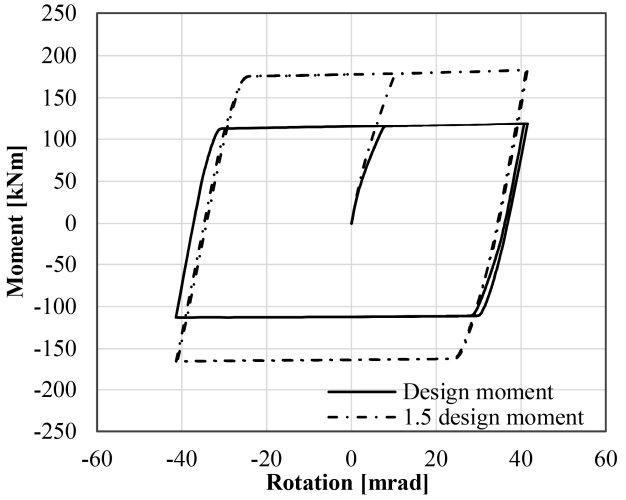

Figure 6.28 Second solution: moment-rotation curves of the cyclic analyses

requirements. The latter analysis also shows slight plasticization of the bottom plate and two of the inclined bars at the connection with the vertical central plate, due to the high stresses transferred, as already described in Figure 6.23 and Figure 6.26.

Concerning the concrete block, it can be noteworthy to assess the cracking state of the material on the basis of the equivalent tensile plastic strains represented in Figure 6.30a and Figure 6.30b for the analyses with M_d = 110 kNm and 165 kNm, respectively. As expected, in the inner rim of the beam, at its intrados, the concrete cracks when the beam is subjected to positive bending moment. At the same time, the cyclic action produces a greater deformation of the C-shaped profile of the upper connection with respect to the behaviour observed in the monotonic simulation, increasing the plastic strains of the surrounding concrete cover, leading to localized damage to the concrete corner in the first analysis, and to extensive damage concerning almost the whole concrete cover of the C-shaped profile in the second one.
This phenomenon is due to the combination of the thin concrete cover and the deformability of the C-shaped profile. In addition, slight damage to the concrete cover is also registered in Figure 6.30b at the connection between the bottom plate and the part of the concrete beam with the inclined shape, due to the forces transferred by the inclined bars. However, all the above-mentioned concrete damages are minor and do not influence the cyclic performance of the proposed connection.

Further comments can be drawn from the analysis of the peak stress and strain values referred to specific parts of interest of the model, summarized in Table 6.2. More precisely, for each component of the structural system, the stress and strain values are referred to the following areas:

- Concrete core of the beam: the contact area with the acute angle of the plate with curved slotted holes and the upper part near the connection with the C-shaped profile;
- Curved slotted hole plate: the acute angle of the plate in contact with the bottom plate of the beam;
- Steel angles: the base section of the web plate;
- T stub: the area between the base section and the row of bolts nearest to the column;
- C-shaped profile: the area between the other row of bolts and the mid-section of the profile.

It should be noted that the peak stress and strain values do not consider the areas subjected to the bolt preload. In Table 6.2, it can be seen that the

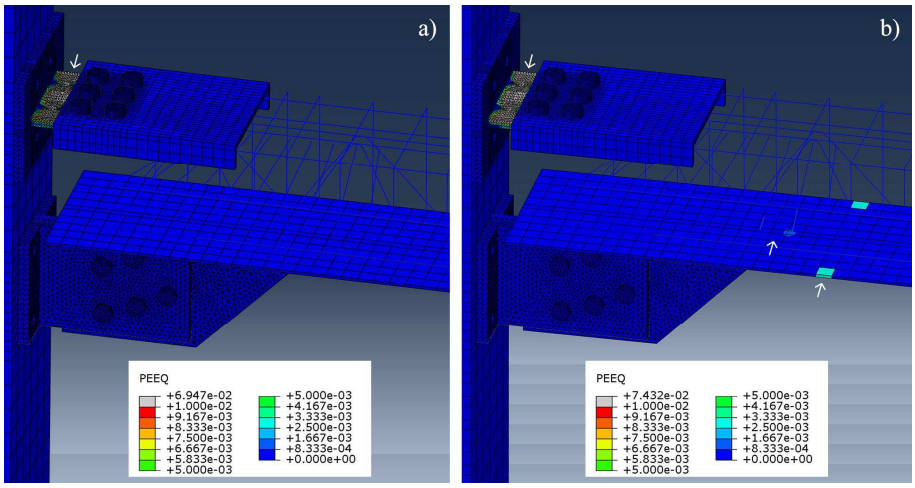

Figure 6.29 Plastic strain distributions at the end of the cyclic FE tests with M_d = 110 kNm (a) and 165 kNm (b)

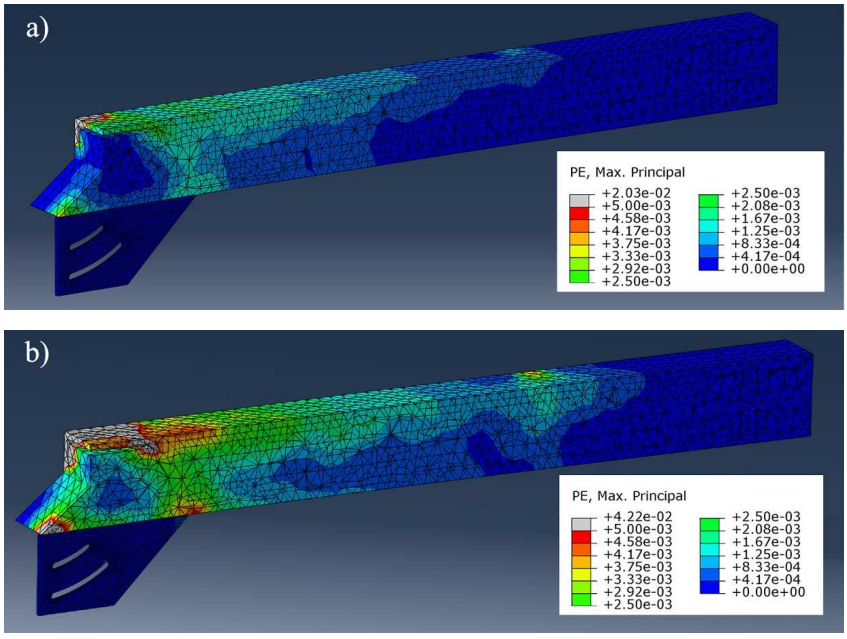

Figure 6.30 Maximum principal strains in the concrete at the end of the cyclic FE tests with M_d = 110 kNm (a) and 165 kNm (b)

maximum stress in the concrete material is less than the peak value (2.56 MPa) because the cracking of concrete on the top part of the beam was already achieved in previous steps of the analysis. On the contrary, the minimum stress for M_d = 165 kNm is above the uniaxial compressive strength of concrete

Table 6.2 Peak stress and strain values of the monotonic response with M_d =110 kNm and M_d = 165 kNm

	M_d =110 kNm			
	Transition step			
	Phase 1 - 2		*Phase 2 - 3*	
	$\sigma_{max/min}$ [MPa]	$\varepsilon_{max/min}$ [%]	$\sigma_{max/min}$ [MPa]	$\varepsilon_{max/min}$ [%]
Concrete core of the beam	2.46	0.14	2.34	0.15
	-21.5	-0.08	-22.3	-0.08
Curved slotted holes plate	-	0.05	-	0.05
	-340	-0.15	-365	-0.16
Steel angles	17.2	0.03	7.25	0.02
	-157	-0.07	-145	-0.07
T stub	365	0.16	520	0.64
	-62.3	-0.03	-380	-0.29
C profile	178	0.07	183	0.08
	-19.4	-0.01	-54.5	-0.03
	M_d =165 kNm			
	Transition step			
	Phase 1 - 2		*Phase 2 - 3*	
	$\sigma_{max/min}$ [MPa]	$\varepsilon_{max/min}$ [%]	$\sigma_{max/min}$ [MPa]	$\varepsilon_{max/min}$ [%]
Concrete core of the beam	2.45	0.24	2.29	0.26
	-28.7	-0.12	-29.5	-0.13
Curved slotted holes plate	-	0.13	-	0.15
	-445	-0.3	-463	-0.33
Steel angles	26.2	0.04	16.7	0.04
	-236	-0.11	-223	-0.1
T stub	423	0.25	550	0.9
	-91.7	-0.1	-415	-0.55
C profile	275	0.12	282	0.13
	-28.3	-0.01	-64.1	-0.04

implemented in FEM model. This phenomenon is due to the biaxial compressive state acting on the analysed area of concrete. With reference to the steel elements, the minimum stresses in the curved slotted hole plate slightly increase between the two considered numerical steps in both analyses, proving that, during the sliding of the system, the stress state of the components of the friction device are substantially unchanged. The minimum stress and strain values in the steel angles and the maximum values in C-shaped profile in the considered transition steps of the two analyses, are almost

directly proportional. As a final consideration, the maximum stresses and strains in the T stub show the formation of the plastic hinge after the transition step from phase 1 to phase 2 and subsequently the hinge is able to behave as centre of rotation of the system as supposed during the design process.

Lastly, Figure 6.31a and Figure 6.31b show the distribution of shear in the nodal area due to the hogging and sagging moments once the sliding force of the friction device is achieved, normalized with respect to the vertical component of the shear force acting on the beam V_{beam}. Such shear distribution is qualitatively comparable with the literature results reported in Latour et al. 2018b, proving the reliability of the presented model.

More precisely, Figure 6.31 shows that the shear forces to which the elements in the nodal area are subjected achieve values well beyond the shear acting on the beam (where the friction device is not present), the latter corresponding to the force applied on the beam end, and follow complex distribution, requiring particular attention during the design procedure.

Concerning the hogging moment analysis (Figure 6.31a), it can be seen that the shear experienced by the vertical central plate is more than twice the shear acting on the beam. To preserve the vertical equilibrium, the beam segment at the connection with the friction device is subjected to shear force, with opposite sign, almost twice that acting on the remaining length of the beam. As regards the connection elements to the column, it can be seen that the shear acting on the steel angles is higher than that acting on the beam, thus, in order to preserve the vertical equilibrium, the T-stub is subjected to shear force with opposite sign.

With reference to the sagging moment analysis (Figure 6.31b), the shear distribution is similar to the previous one, but with the opposite sign. Concerning the external vertical force absorbed by the inclined bars by axial force, it can be noticed that only the bars placed at the beginning and at the end of the rib plate are significantly loaded, while the group of bars in the middle are almost unloaded, as confirmed by the stress state of the steel elements reported in Figure 6.22 and Figure 6.25.

On the basis of these results, some recommendations can be drawn for the design of the beam within the nodal area, the vertical central plate and the steel angles. In detail, the beam should be designed to withstand a shear force which is at least equal to $2\ \Omega_\mu\ V_{Rd}$, in which $V_{Rd} = 2\ M_{Rd} / L$. With regard to vertical central plate and steel angles, these should be designed considering a shear force at least equal to $2.5\ \Omega_\mu\ V_{Rd}$ and $1.3\ \Omega_\mu\ V_{Rd}$, respectively.

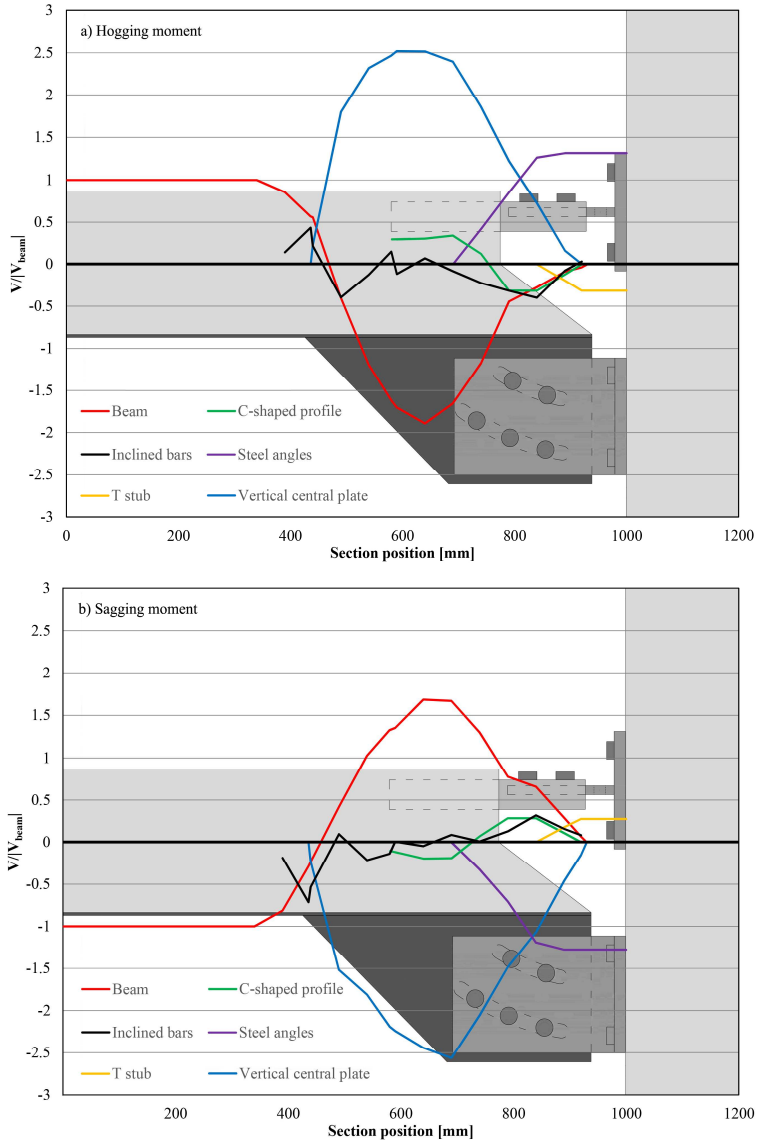

Figure 6.31 Second solution: Distribution of shear in the nodal area due to the hogging and sagging moments once the sliding force of the friction device is achieved

6.5 Solution with curved slotted holes and vertical plate

The second solution provided a promising performance. However, numerical results highlighted several flaws:

- Inadequate stiffness of the bolted connection between T stub and C-shaped profile;

- Inadequate stiffness of the C-shaped profile;
- Inadequate reduction of the T stub stiffness near the base section;
- Complex layout of the reinforcement between C-shaped profile and bottom plate;

With the purpose of solving the weaknesses of the second model, a third one is developed, characterized by the three following main differences: - the plate containing the curved slotted holes is extended throughout the beam depth and is welded to the bottom face of a new horizontal plate, on the top face of which are welded the longitudinal bars; the horizontal plate and the T stub are connected via a standard bolted connection; vertical studs connecting the bottom plate of the steel truss and the horizontal top plate, distributed along the horizontal length (parallel to the beam axis) of the vertical plate and covered by concrete (Figure 6.32). By connecting the friction device and the top bolted connection, it is guaranteed a high stiffness of the whole connection and a potential shift of the assumed centre of rotation is prevented.

The connection between the steel elements constituting the friction device and the beam is ensured by two groups of PerfoBond Connectors (PBCs), the first one arranged on the vertical central plate (which is the part of the vertical plate embedded within the concrete), the second one arranged on the top horizontal plate between the longitudinal bars. PBCs are a relatively innovative type of shear connectors for steel-concrete composite structures widely used, especially in Asia. They are constituted by a steel plate, embedded in concrete, on which are realized holes with circular or elongated geometry. The concrete dowel passing through the hole of the steel plate provides the shear resistance of the PBC. In addition, the holes on the top horizontal plate ensure a proper pouring of concrete.

Differently from the second solution, in order to clearly define the centre of rotation, the middle section of the length of T stub web between the T stub flange and the bolted connection to the beam is reduced, imitating the dog-bone-shaped beam ends of steel structures. By slightly reducing the height of the cross-section at the centre of rotation, the flexural stiffness and strength are reduced, easing the formation of the corresponding plastic hinge.

The studs have three main advantages, namely avoiding the slip between steel connection and concrete, providing confinement to the concrete core, and connecting the top horizontal plate and the bottom one to prevent any undesired relative displacement.

The connection to the column is realized by means of threaded bars passing throughout the cross-section height of the column and are connected each

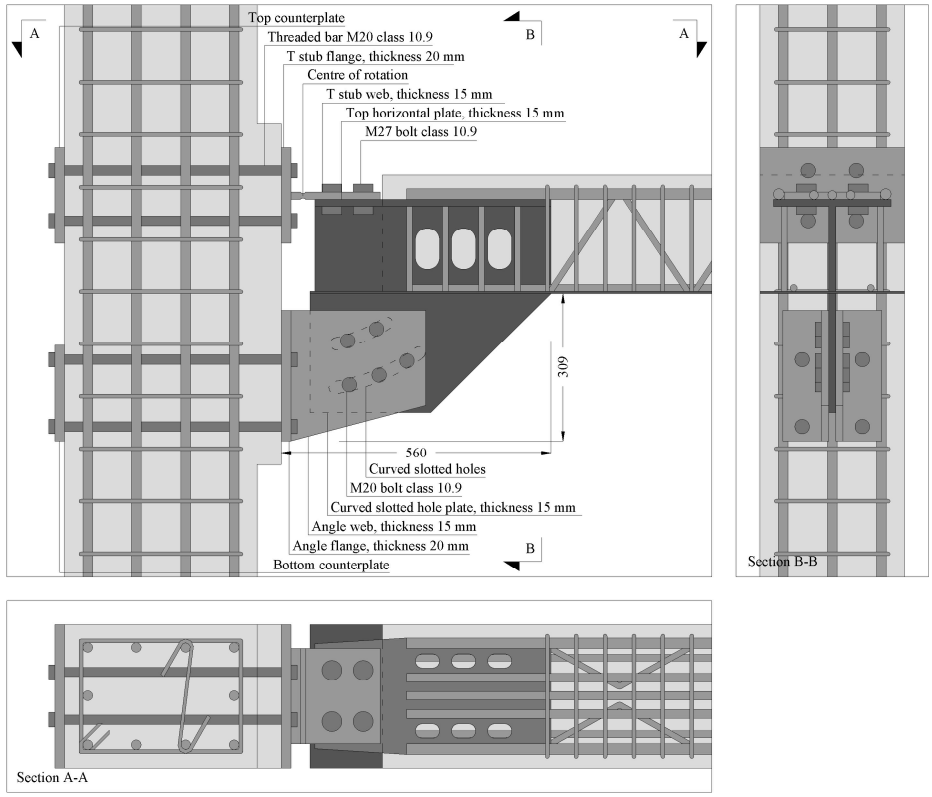

Figure 6.32 Third solution with curved slotted holes and vertical plate

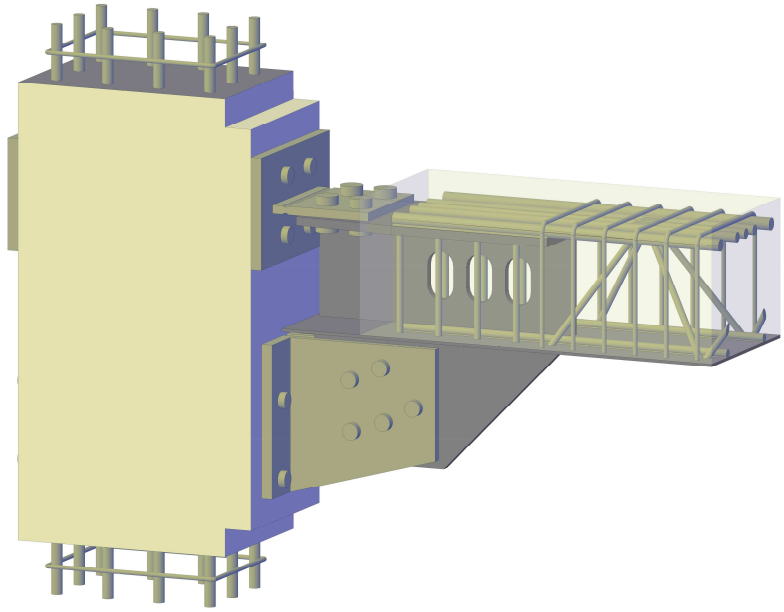

Figure 6.33 Third solution: 3D view

other on the opposite face of the column with counterplates in the case of perimeter beam-column joint, or with another beam-to-column connection in case of internal joint. The bars are designed to be smooth along the length embedded in the column, aiming at not transferring tensile forces through bond stresses. As a result, no significant damage is expected in the concrete due to cyclic actions. At the same time, a damaged bar could be potentially substitute. However, to prevent a loose connection between column and T stub/steel angles, which can lead to undesired deformability contributions to the overall behaviour of the connection, the threaded bars are preloaded once the concrete is cured. This feature improves considerably that advised in the second solution, in which the threaded bars were supposed to transfer the tensile forces to the column through bond stresses along the anchorage length. This detail could have led to severe damage at the steel-concrete interface, not to mention the fact that would have been impossible to substitute a potential damaged bar. Another advantage provided by the preloading of the threaded bars is the increment of the compressive strength of concrete of the panel zone, thanks to the biaxial compressive stress state to which is subjected, which leads to an improved mechanical performance of the panel zone.

Preliminary FEAs characterized by a detail modelling of the connection between column and steel angles, the latter having the same geometry plotted in Figure 6.15, showed an inadequate stiffness of this connection. In fact, the steel angles were subjected to a significant bending moment and the bolt connection with threaded bars was not rigid enough to provide the degree of restrain required. Therefore, the steel angles of the third solution are characterized by a web plate with variable height (Figure 6.32), whose direction of the bottom side with respect to the beam axis, is set parallel to that of the sliding force of friction device (as defined in Figure 6.34). Moreover, the threaded bar on the top side of the steel angle flange plate is positioned in order to have both threaded bars equidistant with respect to the projection of the above sliding force on the steel angle flange plate itself. By doing so, the threaded bars are more effective and provide a much more rigid connection.

6.5.1 Calculation of design parameters

Like the previous solution, the design bending moment is set to M_d = 110 kNm. The geometrical configuration provides a lever arm z_3 and an angle α_3 equal to 374 mm and 68°, respectively (Figure 6.34). As for the sliding force

$F_{d,3}$, this is computed by modifying Eq. (6.4):

$$F_{d,3} = \frac{M_d}{z_3} = \frac{110}{0.374} = 294.12\ kN \tag{6.30}$$

In this solution, the more common M20 bolts 10.9 class are adopted, whose gross area A_{M20} is 314 mm^2, resisting area $A_{res,M20}$ is 245 mm^2. Therefore, the code-consistent preloading force of each bolt is equal to:

$$F_{pc,M20} = 0.7 f_{ub} A_{res,M20} = 171.5 kN \tag{6.31}$$

The design sliding force $F_{s,d,3}$ is:

$$F_{s,d,3} = t_{s,3} n_b n_s \mu F_{pc,M20} \tag{6.32}$$

in which the meaning of parameters is already known. As already done in Section 6.4.1, by equating $F_{d,3}$ and $F_{s,d,3}$ the ratio between the effective and the code-consistent preload applied to the bolt $t_{s,3}$ is calculated, which is 0.429. Then, the design preloading force $F_{pc,d,3}$ to be applied to each bolt results:

$$F_{pc,d,3} = t_{s,3} F_{pc,M20} = 0.429 \times 171.5 = 73.5 kN \tag{6.33}$$

For what concerns the design of curved slotted holes, this is consistent with Section 6.4.1, and their minimum length is substantially the same, i.e. 19 mm.

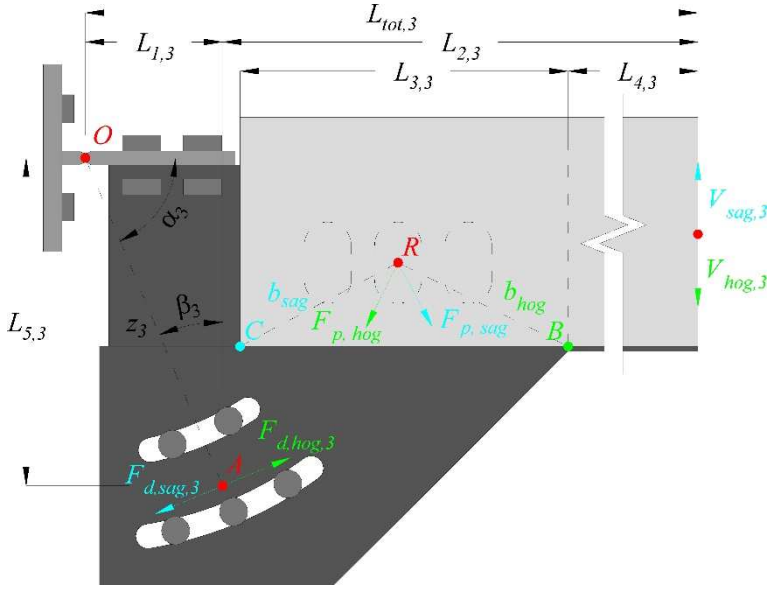

Figure 6.34 Forces acting on the beam calculating the equilibrium with respect to point *O*

As for the steel angles, the design axial and shear force for each element are calculated as follows:

$$B_{h,3} = \frac{1}{2}\Omega_{\mu} F_{d,3} \sin(\alpha_3) = 204.5\ kN \tag{6.34}$$

$$B_{v,3} = \frac{1}{2}\Omega_{\mu} F_{d,3} \cos(\alpha_3) = 82.6\ kN \tag{6.35}$$

As briefly explained before, this solution adopts the PerfoBond Connectors (PBCs) to connect the steel plates and the concrete core of the beam. This connection is ensured not only by PBCs on the vertical central plate, but also by those realized on the top horizontal plate, by the bottom plate, top horizontal plate and longitudinal bars. In order to simplify the calculation, PBCs are designed to withstand half of the design moment of the connection between steel plates and concrete core of the beam. The other half is withstood by the other above-mentioned resisting mechanisms. The shear resistance of each PBC is calculated by means of the equation proposed by Hosaka et al. (2000) employing the suggestion proposed by Zheng et al. (2016) to take into account the long-hole geometry:

$$F_{PBC} = 3.38 \sqrt{\frac{t_{vertical\ central\ plate}}{\sqrt{\frac{4A_{PBC}}{\pi}}}} \frac{4A_{PBC}}{\pi} f_c - 39000 = 191836\ N = 191.84\ kN \tag{6.36}$$

In which $t_{vertical\ central\ plate}$ is the thickness of the vertical central plate equal to 15 mm, A_{PBC} is the hole area equal to 3813 mm^2, f_c is the compressive strength of concrete equal to 30.31 MPa, consistent with the experimental value reported in Colajanni et al. (2016b). It should be stressed that the hole direction with respect to the shear direction does not influence significantly the shear strength of the PBC (Zheng et al. 2016).

Like the previous solution, the concrete block of the beam tends to separate from the bottom plate, rotating around the point *B* (Figure 6.34), in the case of hogging moment, and the point *C*, in the case of sagging moment. The design moment of the PBCs is given by:

$$M_{Ed,PBC,hog} = \frac{1}{2} V_{hog,3} L_{4,3} = \frac{1}{2} \times 66 \times 2.12 = 69.96\ kNm \tag{6.37}$$

$$M_{Ed,PBC,sag} = \frac{1}{2} V_{sag,2} \left(L_{3,3} + L_{4,3} \right) = \frac{1}{2} \times 66 \times 2.47 = 81.51 kNm \quad (6.38)$$

The moment strength of the PBCs can be calculated as follows:

$$M_{Rd,PBC,hog} = F_{p,hog} b_{hog} = 3 F_{PBC} b_{hog} = 3 \times 191.84 \times 0.202 = 116.25 kNm \quad (6.39)$$

$$M_{Rd,PBC,sag} = F_{p,sag} b_{sag} = 3 F_{PBC} b_{sag} = 3 \times 191.84 \times 0.190 = 109.35 kNm \quad (6.40)$$

The resisting moment is greater than the design one, thus the adopted geometry of PBCs is confirmed.

With regard to the connection to the column, this is calculated consistently with EN 1993:1-8 suggestions for standard bolted connection. The tension resistance of the group of four bars is equal to:

$$F_{t,Rd} = 4 \frac{0.9 f_{ub} A_{res,M20}}{\gamma_{M2}} = 4 \frac{0.9 \times 1000 \times 245}{1.25} = 705.6 kN \quad (6.41)$$

As regards the shear resistance of the group of four bars, this is given as follows:

$$F_{v,Rd} = 4 \frac{0.5 f_{ub} A_{M20}}{\gamma_{M2}} = 4 \frac{0.5 \times 1000 \times 314}{1.25} = 502.4 kN \quad (6.42)$$

It should be noted that in the above equation is used the gross section of the bar instead of the net area because the shear plane considered is not threaded.

As said before, the threaded bars are preloaded to avoid a loose connection. The preload value applied to each bolt $F_{pc,threaded\ bar}$ is equal to 50 kN. Therefore, the whole tension force acting on the group of four bars is equal to:

$$F_{t,Ed} = \Omega_{\mu} F_{d,3} \sin\left(\alpha_3\right) + 4 F_{pc,threaded\,bar} = 609.1\ kN \quad (6.43)$$

The shear force acting on the group of four bars is given by:

$$F_{v,Ed} = \Omega_{\mu} F_{d,3} \cos\left(\alpha_3\right) = 165.3\ kN \quad (6.44)$$

According to EN 1993:1-8, the combined shear and tension resistance of the group of four bars is calculated as follows:

$$\frac{F_{v,Ed}}{F_{v,Rd}} + \frac{F_{t,Ed}}{1.4 F_{t,Rd}} = \frac{165.3}{502.4} + \frac{609.1}{1.4 \times 705.6} = 0.946 < 1 \quad (6.45)$$

Therefore, the code requirement is satisfied.

The preceding procedure is summarized in the following step-by-step design procedure:

1. Evaluation of the design bending moment of the connection;
2. Tentative value of the lever arm of the connection;
3. Calculation of the sliding force (Eq. (6.30));
4. Design of the friction device (Eqs. (6.31-6.33));
5. Design of the curved slotted holes on the basis of the maximum expected rotation (Eq. (6.22) modified);
6. Design of the geometry of vertical central plate and steel angles;
7. If the geometry is consistent with EN1993 suggestions, then go to step 8, else go back to step 2 and select a longer lever arm;
8. Calculation of the design axial and shear force acting on the steel angles and T stub (Eqs. (6.34-6.35));
9. Design of the friction connection between T stub and top horizontal plate;
10. Design of the steel angles and T stub;
11. Design of the PerfoBond Connectors (Eqs. (6.36-6.40));
12. Design of the threaded bars connecting steel angles and T stub to the column (Eqs. (6.41-6.45));
13. Design of the beam, column, and panel zone on the basis of the capacity design criteria.

6.5.2 Finite element model

The FEM model is further developed in order to thoroughly take into account the interaction between beam reinforcement and concrete, as well as the connection between T stub, steel angles and threaded bars. More precisely, the bars constituting the steel truss are modelled as 3D elements and at the interface a cohesive interaction able to simulate the steel-concrete bond behaviour is employed. The proposed connection uses two different construction technologies, i.e. prefabricated steel truss and cast-in-situ concrete, which have different construction tolerances. Hence, to simulate the effect of the tolerances in the model, T stub and steel angles are distanced 50 mm from the face of the column, resulting in an overall height of the column cross-section at the beam-column connection of 450 mm.

All elements are modelled by using 8-node linear brick elements (C3D8R), except for the concrete core of the beam and the steel truss that use 4-node linear tetrahedron (C3D4) due to their complex geometries. Moreover, the

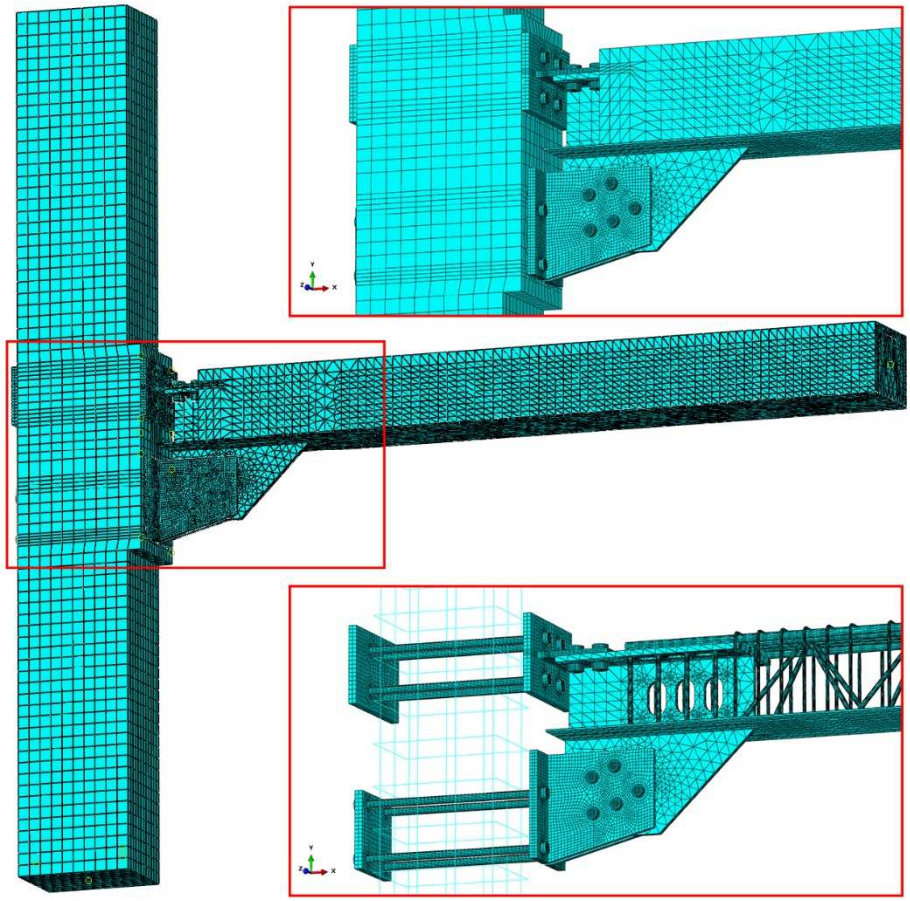

Figure 6.35 Third solution: mesh of the FEM model

longitudinal and transverse reinforcement within the column are modelled by using 2-node beam element (B3D2) and the interaction between these and the surrounding concrete is simulated by the "embedded" constraint (Figure 6.35).

Geometry of the beam-column subassembly is the same of the previous model, excepting the beam length equal to 2.73 m, while the distance between the beam end and the supposed centre of rotation is 2.635 m.

With regard to material properties, compressive strength of concrete is 30.31 MPa, while the elastic modulus of concrete E_0 is 30683 MPa, computed accordingly to EN1992-1-1 (2004). The modelling approach of concrete is the same used in the previous model.

As for the steel elements, a more refined approach is employed for rebars, steel plates and bolts. In fact, these steel elements are characterized by several steel grades. Longitudinal and transverse reinforcement are made of steel grade B450C, the standard class required by the Italian Code, steel grade of

constructional steel is S355, while bolts are class 10.9. For each of these grades a specific stress-strain relationship is defined. Stress-strain curves of rebars and constructional steel are defined on the basis of the model proposed by Yun and Gardner (2017), which schematizes the stress-strain relationship of steel with a quad-linear curve. The values of the four points describing the stress-strain curves of the two steel grades are reported in Table 6.3, while the curves are plotted in Figure 6.36. Yielding stresses used are those reported in Colajanni et al. (2016b).

As regards bolts and threaded bars, the model proposed by D'Aniello et al. (2017) is employed. The latter proposes an equation for the computation of an equivalent elastic modulus for bolts that takes into account the deformability of both the shank, the threaded length and the bolted members. Furthermore, a post-elastic stress-strain relationship is proposed for both HR and HV bolts. In this study, only HR bolts are adopted and the parameters describing the plastic behaviour of M20 bolts class 10.9 are reported in Table 6.4, while the post-elastic stress-strain curve is shown in Figure 6.37. With regard to the equivalent elastic modulus, this is 65742 MPa for the bolts belonging to the friction device, while is 142418 MPa for the threaded bars.

The model analysis is subdivided in three steps (excluding the initial one): 1) bolt preloading; 2) applying axial load on the column; 3) imposing displacement at the column base. Applied loads and boundary conditions are illustrated in Figure 6.38. Base and top of the column are constrained by using a roller and a hinge, respectively, while the beam end section is constrained with a roller. The hinge applied to the column top section is activated during the third step. The imposed displacement is applied to the column base section and not to the beam end, as done in the above-described FEM models. This simulates more accurately the real behaviour of a RC frame subjected to cyclic actions.

Table 6.3 Values of the four points characterizing the stress-strain curves of the steel classes S355 and B450C

		Steel S355		**Steel B450C**	
		σ [MPa]	ε [%]	σ [MPa]	ε [%]
Points	1	400	0.19	500	0.24
	2	400	2.05	500	2.63
	3	481	5.22	572	4.78
	4	530	14.72	615	11.22

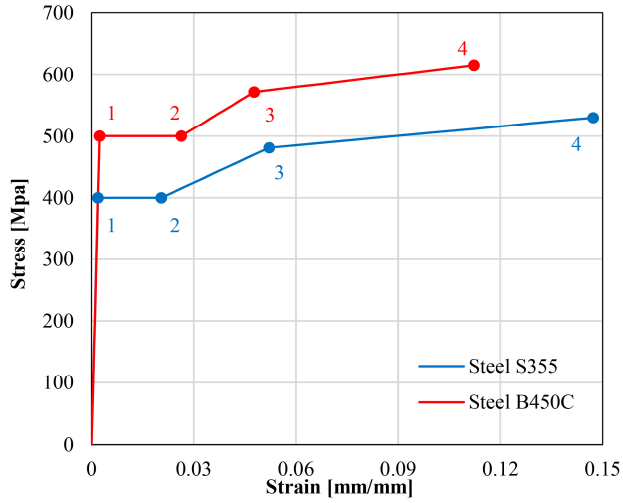

Figure 6.36 Stress-strain curves of steel grades S355 and B450C

Due to the high number of elements constituting the FEM model, several interactions are defined by using four different interaction properties, as illustrated in Figure 6.39. Steel-steel and steel-concrete interactions are modelled by using the Coulomb model of friction, with friction coefficient equal to 0.2, respectively. Moreover, friction coefficient of the interface between steel angles and curved slotted holes plate is set equal to 0.4. The interaction between the top surface of the bottom plate of the truss and the concrete core is modelled by using a frictionless interaction property. This assumption is based on the fact that not only the steel plate is smooth, but also the upper part of the steel plate is greased prior to the casting of concrete, leading to a negligible friction coefficient. The fourth interaction property is defined aiming at simulating the bond between rebars of the steel truss and the surrounding concrete. Therefore, a cohesive interaction property is selected, which is characterized by a linear-elastic behaviour up to the attainment of a

Table 6.4 Values of the five points characterizing the stress-strain curve of the plastic branch of M20 bolt class 10.9

		M20 bolt class 10.9	
		σ_{true} [MPa]	$\varepsilon_{true,\ plastic}$ [%]
Points	1	837.9	0
	2	889.2	0.5
	3	907.2	1.7
	4	804.2	36.08
	5	0	36.18

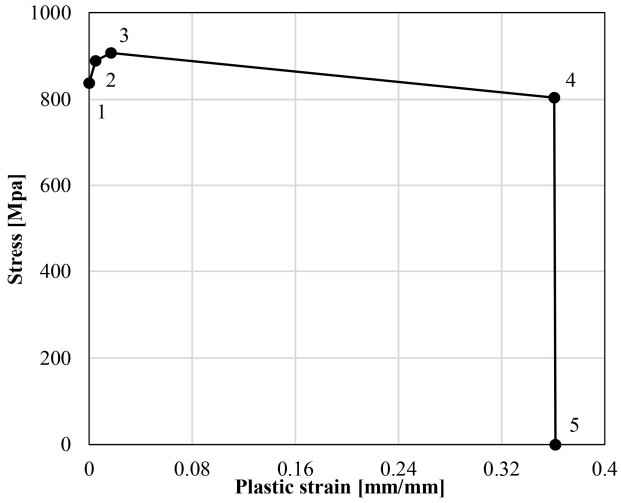

Figure 6.37 Post-elastic stress-strain curve of M20 bolt class 10.9

threshold, and post-elastic behaviour determined by a damage law. Considering an uncoupled behaviour, only the stiffness values of the two tangential directions (K_{ss}, K_{tt}) and the normal direction (K_{nn}) are defined. The latter one is set equal to zero, being negligible the separation resistance between steel and concrete in the normal direction. With reference to the damage, this is characterized by an initiation criterion and an evolution law. The former is defined as the attainment of the maximum tangential stress, while the latter is assumed as a linearly-increasing evolution law. The model selected to describe the rebar-concrete interaction is the well-known bond model proposed by Eligehausen et al. (1983). For simplicity's sake, a linear damage evolution law is selected. Both the elastic and the post-elastic stiffness can be defined on the basis of an energy criterion. More exactly, the elastic branch is calculated by equating the areas under the curves up to the slip value of 1 mm, while the post-elastic branch is obtained considering the areas under the curves by assuming an ultimate slip of 12 mm. Bond stress-slip curves of Eligehausen et al. and the equivalent linearized one are plotted in Figure 6.40.

The high number of interactions lead to convergence problems which require the definition of a specific strategy to overcome them. To this aim, the contact control is used on the interactions involving the threaded bars passing through the column, activated only on the first step regarding the bolt preloading. The contact control option is used to help the contact initiation between several elements in which rigid body motions are not contrained.

Two groups of monotonic analyses are carried out, applying a displacement of 270 mm at the column base rightward for the first group,

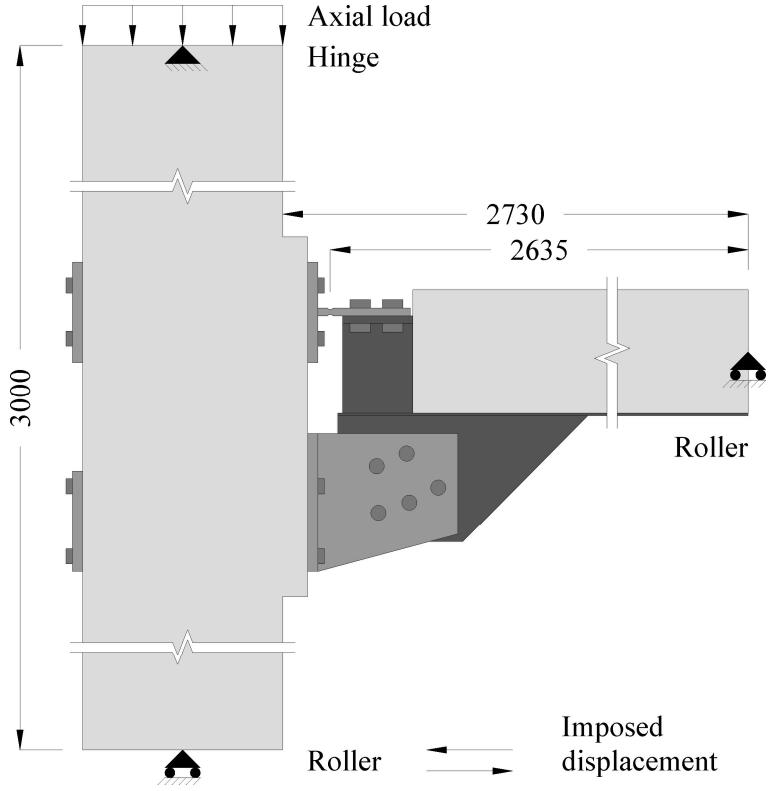

Figure 6.38 Applied loads and boundary conditions of the FEM model

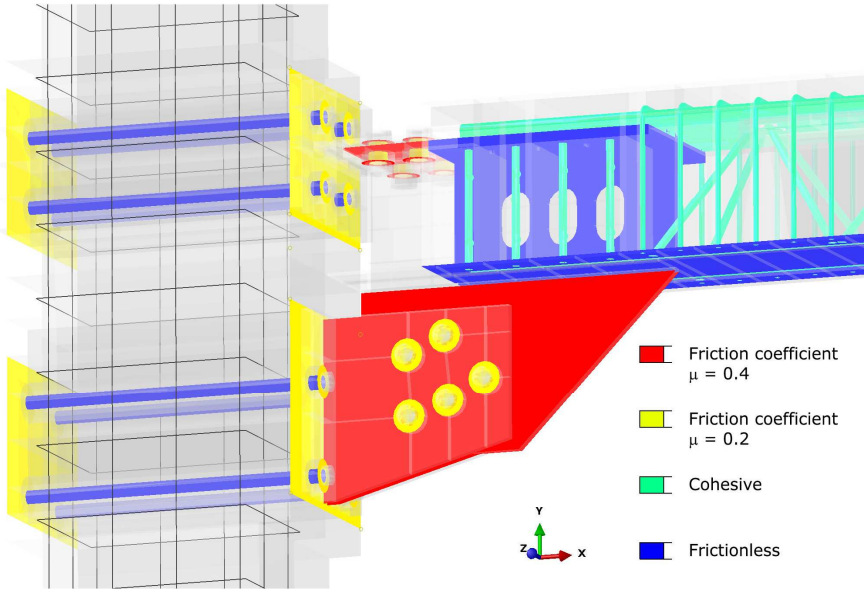

Figure 6.39 Interaction properties of the FEM model

Table 6.5 Values of the four points characterizing the stress-strain curves of the steel grades S355 and B450C

		Eligehausen et al.		**Equivalent linearized**	
		τ	s	τ	s
		[MPa]	[mm]	[MPa]	[mm]
Points	1	13.76	1	13.76	0.6
	2	13.76	3	0	20
	3	5.51	10		

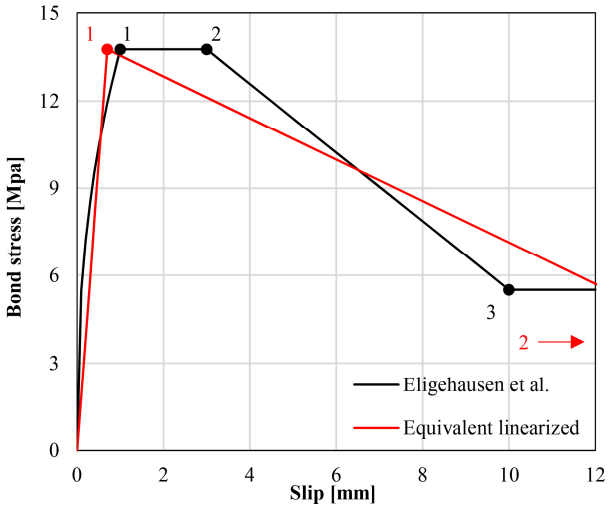

Figure 6.40 Bond stress-slip relationship at the bar-concrete interface

leftward for the other one. For each group, three analyses are performed applying different preloading forces at the bolts belonging to the friction device aiming at simulating different design moment values of the connection, namely 0.5 M_d, M_d and 1.5 M_d. Then, three cyclic analyses are performed by varying the bolt preload as described above. The loading protocol applied at the column base is reported in Figure 6.41. This displacement history is defined on the basis of the suggestions proposed in ACI 374.2R-13. In fact, the amplitudes of the cycles are determined by using the yield rotation multiplied by an increasing coefficient. Yield rotation θ_y is obtained by the monotonic analysis, and it is assumed 7 mrad. In order to limit the computational effort, three cycles are defined, having amplitude of $\pm\,\theta_y$, $\pm\,4\theta_y$ and $\pm\,7\theta_y$.

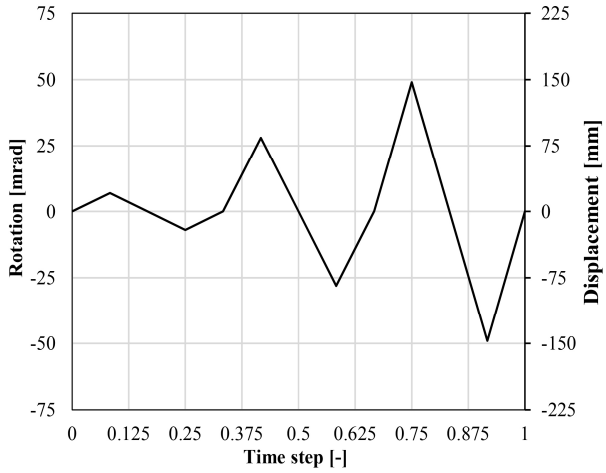

Figure 6.41 Loading protocol of the cyclic analyses

6.5.3 Results

As already done in Section 6.4.3, the results of the third solution are presented in terms of moment-rotation curves and stress contours for both monotonic and cyclic response. Figure 6.42 reports the monotonic moment-rotation curve of the subassembly. In these analyses, the moment is obtained as the product between the vertical reaction force at the beam end and the distance between the assumed centre of rotation and the beam end. With regard to the rotation, this is computed as the ratio between the horizontal displacement imposed to the column base section and the column height. The rotation values illustrated in Figure 6.42 are given by the contributions provided by the beam, column and beam-column connection, as well as threaded bars, T stub and steel angles.

Like the second solution, the moment strengths of the third connection obtained numerically agree satisfactorily with the corresponding analytical value. Once again, three phases can be identified:

1. the friction device does not slip and the system behaves elastically;
2. the sliding is activated and the behaviour of the system turns into an almost perfectly-plastic behaviour, exhibiting a slight hardening probably due to the plasticization of the base section of the T stub;
3. the bolts shanks go in contact with the curved slotted holes at the end of sliding, for a rotation much higher than the design one.

The responses provided by the six monotonic analyses are analogous in terms of stiffness, considering the elastic and the post-elastic ones for both

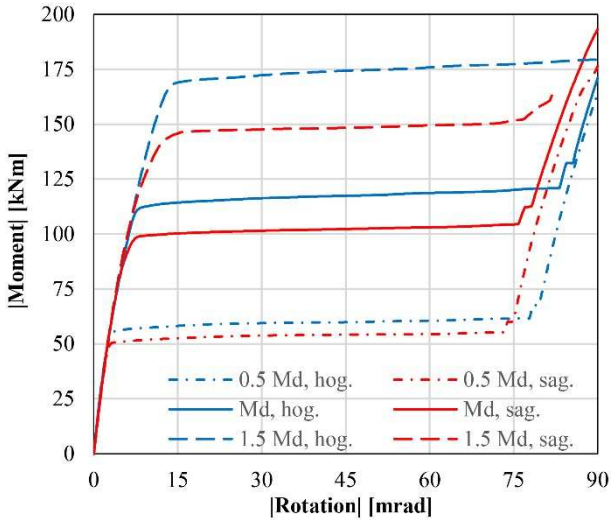

Figure 6.42 Third solution: moment-rotation curves of the monotonic analyses

hogging and sagging moment. The end of the almost horizontal post-elastic branch is characterized by the contact between bolts shanks and the end section of the curved slotted holes. This phenomenon is registered for a rotation of at least 70 mrad in all the analyses, due to the fact that the connection rotates around the assumed centre of rotation and the latter does not shift in any configuration. The above considerations confirm that the stiffness of all the elements and the connections constituting the third solution is adequate. With regard to the strength, different behaviour is obtained. As a matter of fact, in the case of M_d = 110 kNm, the moment values for which the friction device slides are 112 kNm for hogging moment and 99 kNm for sagging moment, 2% higher and 10% lower than the design moment, respectively. Moreover, in the case of M_d = 165 kNm, the moment values for which the friction device slides are 170 kNm for hogging moment and 146 kNm for sagging moment, 3% higher and 12% lower than the design moment, respectively. Lastly, in the case of M_d = 55 kNm, the moment values for which the friction device slides are 55 kNm for hogging moment and 50 kNm for sagging moment, equal to and 9% lower than the design moment, respectively. It can be pointed out the differences between numerical and analytical values tend to amplify when the design moment strength increases. It should be pointed out that the rotation values are given as the sum of the rotations of beam, column and beam-column connection. Therefore, the stiffness of the proposed connection should be evaluated by subtracting the rotations given by beam and column.

For the brevity's sake, only the results related to the hogging and sagging

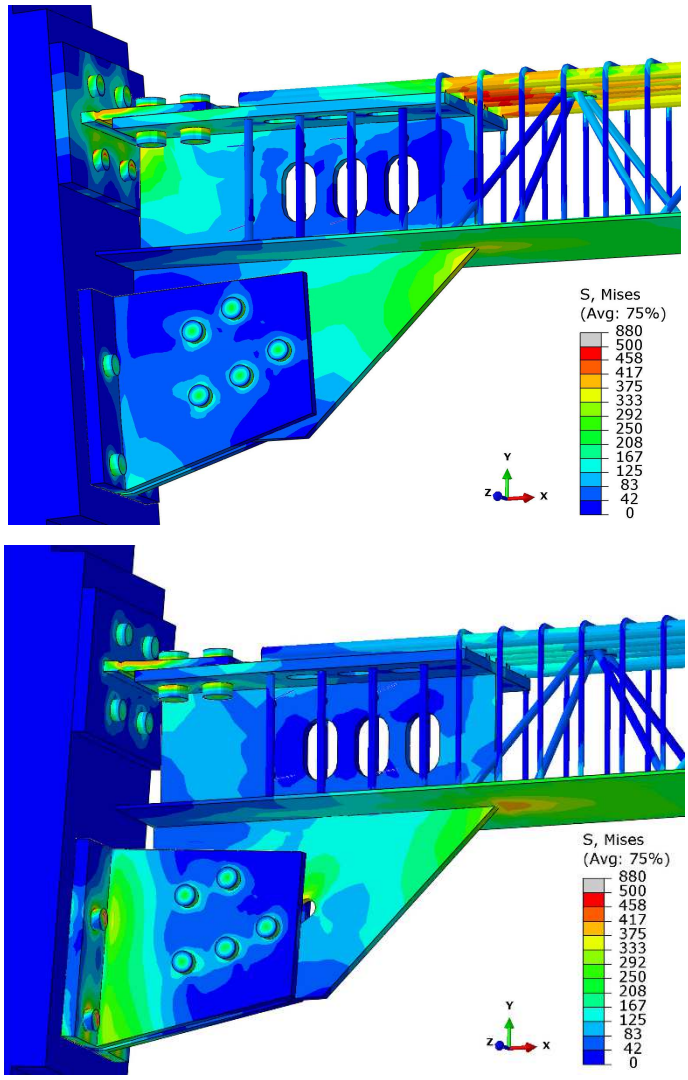

Figure 6.43 Stress state in the steel elements at the rotation of 70 mrad for hogging and sagging moment

analyses with moment strength 1.5 times the design moment are described below, this being the upper limit of functioning of the connection. Figure 6.43 reports the stress state in the steel elements at the rotation of 70 mrad. The figure shows that all the steel components of the device behave elastically, with high stress values at the acute angle of plate with curved slotted holes and the area of the bottom plate near to it. Moreover, longitudinal bars close to the top horizontal plate are near to the elastic limit in the hogging moment analysis. With regard to the T stub, high stress values can be seen at the assumed centre of rotation and at the top face of T stub in the area comprised

between the centre of rotation and the nearest bolt row. This means that, despite of the reduced section near the base of the T stub, the effective centre of rotation is slightly shifted from the assumed position. Nevertheless, as already seen in Figure 6.42, this phenomenon does not affect the monotonic behaviour of the connection. As for the vertical central plate, a severe stress concentration, especially in the case of the hogging moment analysis, is registered near the end section of the vertical central plate at the connection with the T stub. This is due to the shear force transferred by the T stub (as will be further observed in Figure 6.48), whose value is equal to that calculated in Eq. (6.40). This phenomenon confirms the effectiveness of the vertical central plate in transferring the shear force between T stub and beam, ensuring a rigid connection.

Figure 6.44 shows the minimum principal stresses of concrete at the rotation of 70 mrad, illustrating the half part of concrete members only.

With regard to the hogging moment analysis, two main stress concentrations can be noticed: the first one is the area comprised between the acute angle of the plate with curved slotted holes, the bottom plate and the vertical central plate, the second one is near the lower hole of the bottom connection to the column through which is inserted the preloaded threaded bar. Other minor stress concentrations are on the upper part of the holes belonging to the top connection to the column, due to the shear force acting upward transferred by the T stub via the threaded bars. By focusing on the concrete dowels passing through the vertical central plate, several stress concentrations with different positions can be noticed. These are consistent with the resisting mechanism assumed in Figure 6.34, in which the centre of rotation *B* corresponds to the first main concentration described above.

Concerning the sagging moment analysis, only one significant stress concentration is registered, which is near the connection with the T stub and due to the compressive force transferred by it. Other minor stress concentrations are noted on the upper part of the holes belonging to the bottom connection to the column, due to the shear force acting upward transferred by the steel angles through the threaded bars. The high compressive stress value near the bottom part of the beam end section is consistent with the resisting mechanism reported in Figure 6.34, representing the centre of rotation *C*. Differently from the analysis with hogging moment, slight stress concentration are registered on the vertical concrete dowels, while the horizontal ones withstand significant compressive stresses.

As a final point, the diagonal strut of the beam-column joint is clearly identified in both cases. From the analysis of the contour plot, it can be

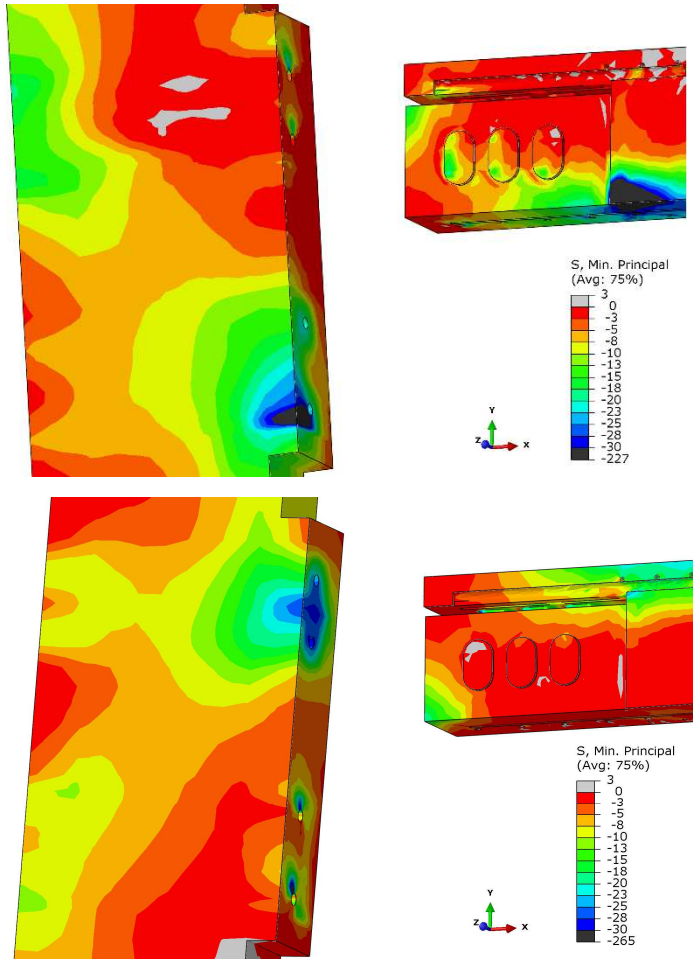

Figure 6.44 Minimum principal stresses in the concrete members at the rotation of 70 mrad for hogging and sagging moment

assumed that the joint panel is comprised between the mid-sections of top and bottom connections with threaded bars.

Once again, the results obtained during phase 3 are not reported because they refer to the mechanical behaviour of the connection well beyond the design limit.

The moment-rotation curves of the three cyclic test are plotted in Figure 6.45. It can be stated that the proposed connection satisfies the design requirements, namely wide and stable hysteresis cycles, showing a proportional response among the three curves by changing the bolt preload. The only flaw is the variation of the bending moment values belonging to the sliding phase obtained during the cycles, in the case of moment strength equal to 1.5 times the design moment. This is attributable to the fact that, being the

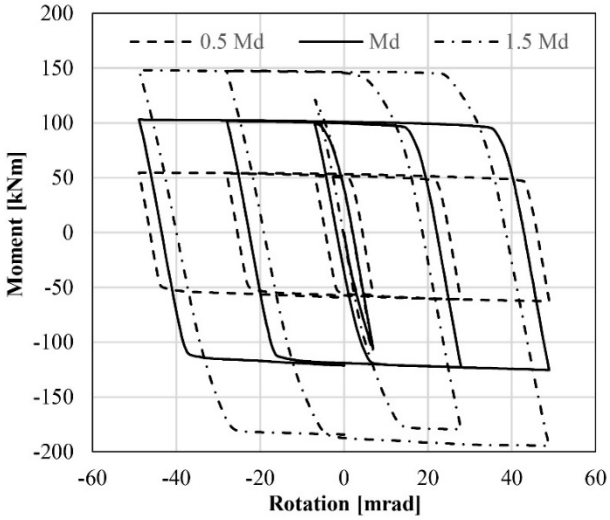

Figure 6.45 Third solution: moment-rotation curves of the cyclic analyses

connection at the upper limit of functioning, some slight changes in the resisting mechanisms and the position of the centre of rotation are triggered. Nevertheless, this phenomenon does not influence significantly the overall response of the connection.

The equivalent plastic strains cumulated on the steel elements at the end of the cyclic analysis are shown in Figure 6.46. It can be seen that all the steel components behave elastically except for the horizontal plate of the T stub, the longitudinal bars near the top horizontal plate and the area between the acute angle of the plate with curved slotted holes and the bottom plate. As for the T stub, this undergoes plastic deformations according to the design requirements. However, these plasticizations are not localized at the assumed centre of rotation, but extend between the centre of rotation and the nearest bolt row. This confirms that the centre of rotation shifted its position during the cyclic analysis, potentially triggering the variation of the moment capacity.

Regarding the longitudinal bars near the top horizontal plate and the area between the acute angle of the plate with curved slotted holes and the bottom plate, these elements experienced negligible plastic deformations which do not hamper the functioning of the whole connection and its reusability.

Concerning the concrete members, the compressive damage and the equivalent plastic tensile strain obtained at the end of the cyclic analysis with M_d = 165 kNm are plotted in Figure 6.47. With reference to the former, slight damage is registered on the upper concrete cover of the beam at the connection between longitudinal bars and top horizontal plate, as well as on the concrete dowels passing through the top horizontal plate. These damages are localized

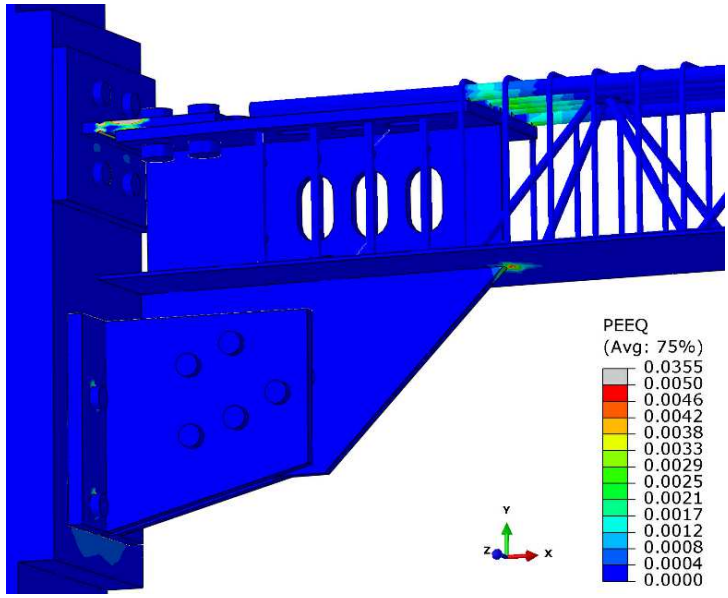

Figure 6.46 Equivalent plastic strain of steel elements at the end of the cyclic test with M_d = 165 kNm

and do not hinder the functioning of the connection. Regarding the equivalent plastic tensile strain, concrete members undergo several crack patterns:

- horizontal cracks near the connection with preloaded threaded bars are registered, due to the combination of different phenomena, namely bolt preload, tensile/compressive force transferred by T stub/steel angles, deformed shape of bolt shank due to the rotation of bolt head;
- vertical cracks across the beam cross-section between steel plates characterizing the connection (i.e. vertical central plate, top horizontal plate) and the remaining part of the beam. This cross-section of the beam is the most critical because it has to transfer forces between the two segments of the beam;
- cracks surrounding the concrete dowels, both the vertical and the horizontal ones. This crack pattern confirms the design strategy of the perfobond connectors and their efficiency in connecting the concrete core with the steel plates.

Despite of these different cracks, it can be stated that they do not influence the cyclic performance of the connection, as already seen in Figure 6.45. As a final consideration, it has to be emphasized that the plastic deformations of steel elements and the crack widths are significantly lower or null in the case

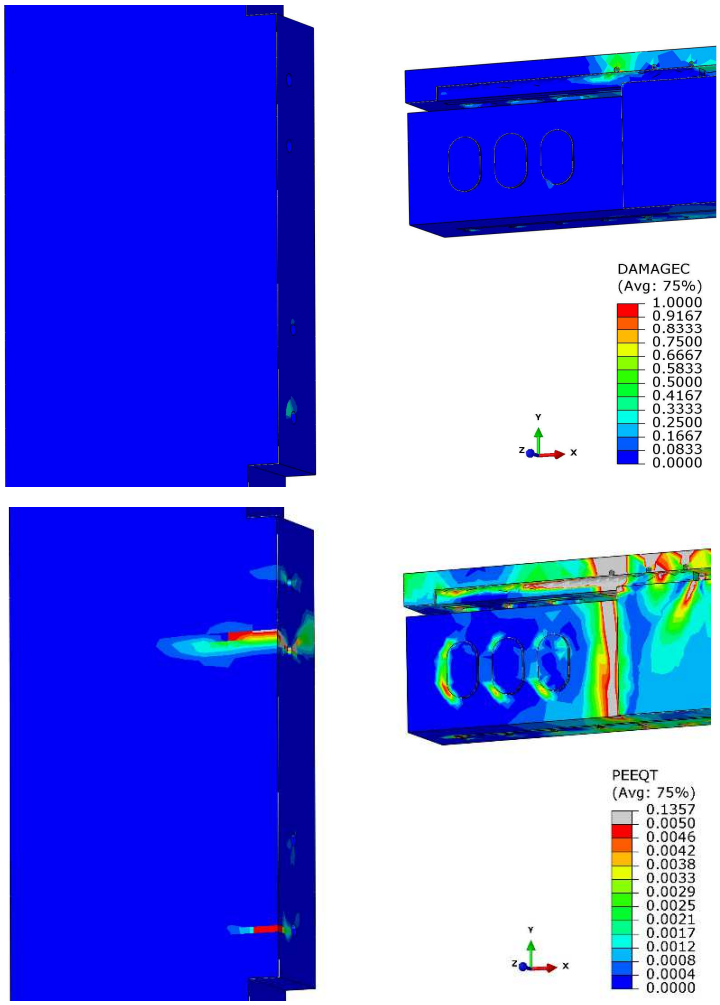

Figure 6.47 Compressive damage of concrete and equivalent plastic tensile strain of concrete at the end of the cyclic test with Md = 165 kNm

of M_d = 110 kNm.

All the above considered, it can be stated that the construction tolerance, simulated by distancing 50 mm flange plates of T stub and steel angles from the column, does not influence the mechanical performance of the connection.

The distribution of shear in the nodal area obtained for hogging and sagging moment, normalized with the vertical shear force acting on the beam V_{beam}, is shown in Figure 6.48a and Figure 6.48b. These values are obtained from the cyclic analysis with moment strength equal to 165 kNm at the time step 1 and 0.833 (Figure 6.41), respectively. The shear distribution can be qualitatively compared with those reported in Figure 6.31 and in Latour et al. (2018b), confirming the reliability of the model.

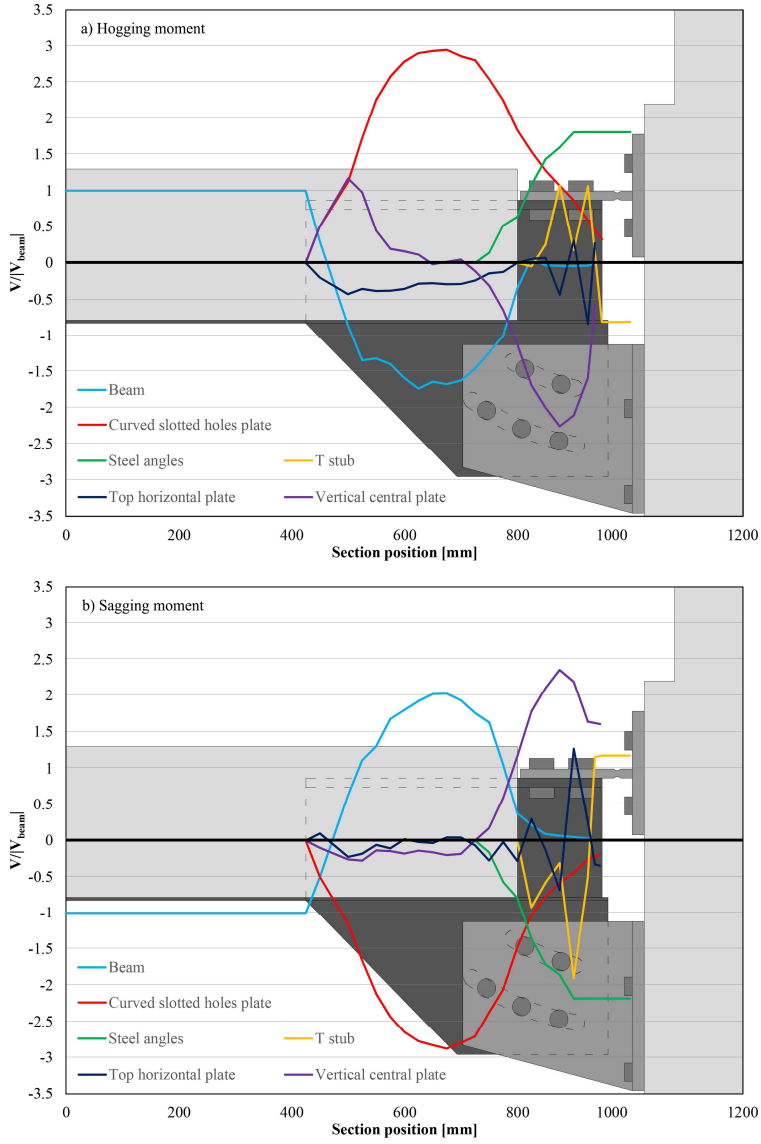

Figure 6.48 Distribution of shear in the nodal area due to the hogging and sagging moments once the sliding force of the friction device is achieved

In detail, Figure 6.48 shows that several elements constituting the connection experience shear forces which are much greater than the shear acting on the beam. As regards the hogging moment analysis (Figure 6.48a), it can be observed that the curved slotted holes plate undergoes a shear force almost three times that acting on the beam. To ensure the vertical equilibrium, the beam segment at the connection with the friction device experiences a shear force almost twice that acting on the remaining part of the beam. With

reference to the steel elements connecting the beam to the column, it can be seen that the steel angles undergo a shear force which is about 1.8 times that acting on the beam and, therefore, the equilibrium is ensured by the shear force acting on the T stub having opposite sign. This shear force is transferred to the vertical central plate, confirming the need of this steel plate in order to properly ensure the stiffness and strength of the proposed connection. About the sagging moment analysis (Figure 6.48b), the shear distribution is comparable to the above one, having the opposite sign. The only remarkable difference is the higher shear force acting on the steel angles and T stub, being almost 2.2 and 1.2 times that acting on the beam, respectively.

The results discussed above emphasize the need to pay particular attention to the design of all the elements constituting the proposed connection.

More precisely, similarly to the second solution, beam and vertical central plate should be designed to withstand a shear force which is at least equal to $2\ \Omega_\mu\ V_{Rd}$ and $2.5\ \Omega_\mu\ V_{Rd}$, respectively. Moreover, curved slotted holes plate, steel angles and T stub should be designed considering a shear force at least equal to $3\ \Omega_\mu\ V_{Rd}$, $2.2\ \Omega_\mu\ V_{Rd}$ and $1.2\ \Omega_\mu\ V_{Rd}$, respectively. The factor Ω_μ is added in order to provide adequate overstrength to the structural elements with respect to the maximum forces they could experience.

Lastly, it is interesting to compare the construction costs of the preceding solution with those of the standard HSTCBs. The construction costs are estimated on the basis of the price per kg of steel, as is usually done when using constructional steel. Considering a beam length of 5 m, a standard HSTCB having the geometrical characteristics of that used in the preceding FEAs weighs 182 kg. A HSTCB endowed with the dissipative device of the third solution at both ends weighs 278 kg, thus almost 53% heavier than the standard one. The cost of structural steelwork, including transport and bolts, can be roughly estimated as 4 € / kg, while the cost of mounting the structural steel elements in the construction site can be evaluated as 2 € / kg. It should be underlined that these costs do not take into account the economies generated in the case of making several similar elements and repeated working operation on site. On the basis of the preceding price, a standard HSTCB would cost 1092 €, while an innovative HSTCB would cost 1668 €. To the cost of the innovative HSTCB should be added the cost of the friction pads that can be estimated as 300 €, for a total cost of 1968 €. It is apparent that the increment of construction costs is significant. However, the proposed solution becomes competitive when considering, during the whole life-time of the structure, its superior performance in the case of seismic event.

6.6 Conclusions

In this chapter, three different solutions for a beam-column connection endowed with friction device and realized with HSTCBs, were described. The solutions take advantage of the considerations outlined by analysing the beam-column connections reported in the literature. The first solution is characterized by a vertical friction device with horizontal and vertical slotted holes and a pin connection on the top side of the beam. FEA results showed an inadequate performance due to the shift of the pin connection within the holes and the contact of the bolt shanks with the horizontal holes of the rib plate which leads to a significant increment of the resisting moment. On the basis of these results, the second solution is developed in order to solve the above-mentioned flaws. Thus, this is characterized by a friction device with curved slotted holes and a bolted connection between a T stub and a C-shaped profile on the top side of the beam. The curved slotted holes prevent the contact between the bolts shanks and the steel plate, avoiding the increment of the resisting moment, while the bolted connection with T stub prevents the variations of the resisting moment due to the shift of the pin within the holes. A more detailed FEM model were developed, characterized by inelastic behaviour of concrete of the beam and rebars within the concrete core of the beam. Preliminary FEAs showed an inadequate stiffness between concrete core of the beam and the plate with curved slotted holes. Thus, a group of bars with varying inclination in the vertical plane containing the beam axis, were added within the concrete core connecting the C-shaped profile with the bottom plate of the HSTCB. FEA results showed that the connection behaved accordingly to the analytical prediction. Moreover, negligible damage was observed in the structural elements, confirming the design requirements. Notwithstanding this, some deficiencies arose, namely the inadequate stiffness of the bolted connection between T stub and C-shaped profile, inadequate stiffness of the C-shaped profile, complex layout of the reinforcement between C-shaped profile and bottom plate. To solve these issues, the third solution substitutes the reinforcement between C-shaped profile and bottom plate, and the C-shaped profile itself with two steel plates, one vertical and the other horizontal, embedded within the concrete core of the beam. The vertical plate is welded both on the top and the bottom plates, ensuring the resisting mechanisms able to transfer the forces among the top connection and the friction device. To enhance the connection between the steel plate and the concrete core of the beam, two groups of perfobond

connectors are realized, the first one on the vertical central plate and the second one on the top horizontal plate. The FEM model was further detailed, taking into account the connection with the column, the inelastic behaviour of concrete of the column and rebars within the concrete core of the column. Moreover, the rebars within the beam were modelled as 3D elements to accurately reproduce their interaction with concrete. Satisfactory results were obtained by means of FEAs. More precisely, the flaws of the second solution were adequately solved and no significant damage were experienced by all the elements constituting the connection.

CHAPTER 7

PROPOSAL OF A SELF-CENTRING FRICTION CONNECTION FOR COLUMN BASE CONNECTION

This chapter focuses on the proposal of a self-centring connection for column base connection of RC frames with HSTCBs. The main characteristics of the proposed connection, as well as the advantages with respect to those already proposed in the literature, are discussed. Equations to assess moment-rotation curves for uniaxial bending are provided. After that, the modelling strategy used to evaluate the mechanical performance of the proposed connection is described and corroborated against experimental results and/or analytical predictions. Lastly, numerical results of FEM analyses both in terms of moment-rotation curves and stress contours are discussed.

7.1 Description of the column base connection

The critical review of the solutions proposed in the literature, reported in Section 3.2, revealed that the combination of friction devices and threaded bars coupled with disc springs ensures adequate energy dissipation capacity and self-centring behaviour. However, the mechanics of all the solutions analysed is highly dependent on the axial force acting on the column, because it helps to guarantee the self-centring capability of the connection. For this reason, a variation of the axial force leads to different moment strength, hampering the functioning of the connection and the predictability of its mechanical behaviour. This phenomenon influences especially external columns, where shear forces due to seismic actions provoke significant variations of the axial force acting on the column base. Moreover, the contribution provided by the vertical component of the seismic action should be also taken into account. On the other hand, the use of the axial force to self-centre the connection is an effective and economic strategy, and a solution which does not take it into account could lead to a more cumbersome and expensive configuration.

With all the above in mind, the proposed solution, which is shown in Figure

7.1, adopts a system designed in order to take into account the contribution of the axial force to the whole response of the connection the least possible. This system is constituted by a spherical cap connected to the column base and a concave steel bearing connected to a cross-shaped steel plate which transfers the forces to the foundation. In fact, this system is designed to withstand both

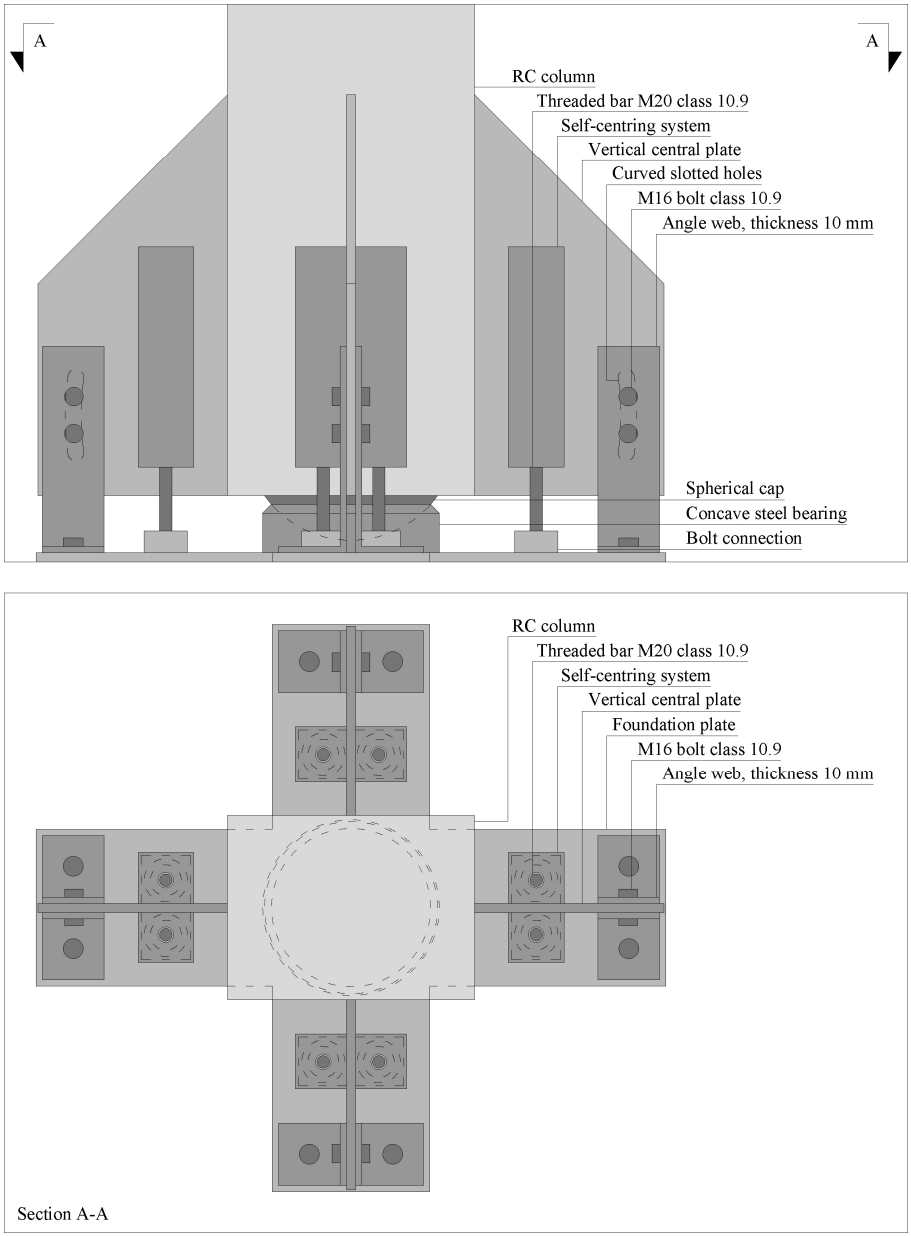

Figure 7.1 Proposed column base connection

axial and shear forces transferred between column and foundation. By doing so, the other devices constituting the connection are supposed to withstand the forces due to the bending moment only. The spherical cap and the concave bearing have the same radius of curvature R and, thus, the connection is supposed to rotate around the point O, centre of the sphere, which lays on the longitudinal axis of the RC member. To ensure symmetrical behaviour of the connection, each steel plate is endowed with two self-centring systems and a friction device. The latter is constituted by vertically-oriented steel angles clamped together by bolts passing through curved slotted holes. These ones are centred in O to prevent any contact between the central steel plate and the bolts shanks. With regard to the self-centring system, this is constituted by a stack of disc springs through which is inserted a preloaded threaded bar. This system is inserted through a vertically-oriented box-shaped steel case welded on the vertical central plate. Two flat washers are inserted at the ends of the stack of disc springs. The system is designed in order to undergo compression forces only and, thus, provide self-centring capacity in both directions. To do so, the system must be preloaded before the installation within the box-shaped case, the latter built without clearance between end plates and threaded bar in order to avoid any undesired displacement and ensure proper self-centring capacity of the system (Figure 7.2). The horizontal component of the displacement due to the rotation of the connection is absorbed by introducing a spherical connection between the bolt shank and the foundation plate. By doing so, the damaging of bolts shanks is limited and the self-centring capacity

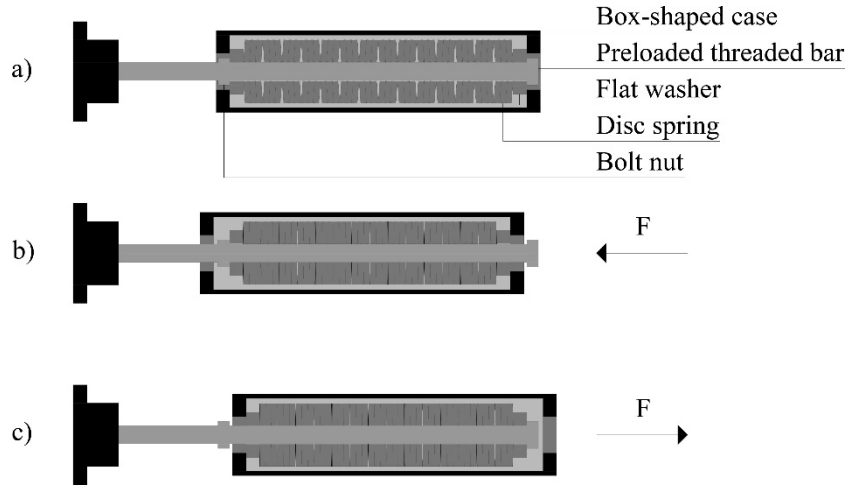

Figure 7.2 Self-centring system layout: resting position (a), when the box-shaped case is pushed towards the foundation (b) when the box-shaped case is pulled away from the foundation (c)

of the system is not hindered.

Disc springs are a reliable and cost-effective solution to prevent loss of bolt preload and avoid bolt yielding. Thanks to their conical shape, they can be combined to obtain the desired mechanical behaviour. In fact, a group of n springs stacked in parallel (i.e. one on the other oriented towards the same direction) provides a reaction force which is n times that given by a single spring, with the same deflection. On the other hand, a group of n springs stacked in series (i.e. one on the other alternatively oriented towards opposite direction) provides a deflection which is n times that given by a single spring, with the same reaction force. The pre-setting procedure is applied to the disc springs used in the proposed solution. During the manufacturing process, the disc springs are deflected to flat. This procedure causes residual stress while the disc spring returns to its conical shape. In this way, the disc spring will not yield again in the subsequent deflections.

The proposed solution, whose 3D model is shown in Figure 7.3 takes advantage of the solutions successfully developed by Xu et al. (2017) and Fan et al. (2019) as for the self-centring system, similarly constituted by a threaded

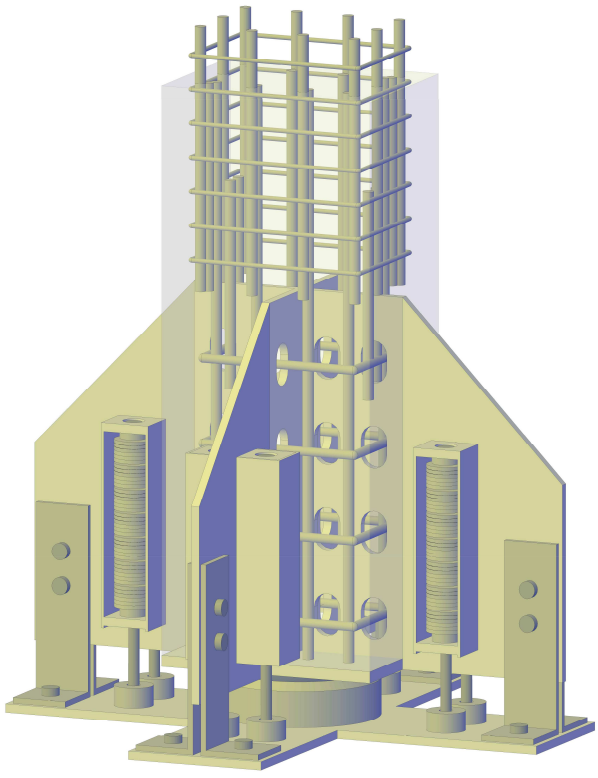

Figure 7.3 Proposed column base connection: 3D model

bar passing through a stack of disc springs already preloaded, and of the spherical bearing proposed by Froli et al. (2019) in the TROCKSISD device.

The design of the radius of curvature R is of paramount importance to ensure the proper functioning of the system. In fact, a too long R leads to a less concave bearing which could not work properly as a shear key. Therefore, the ideal solution would be to assume R equal to half the column minimum cross-section dimension. By doing so, the centre O would lay on the bottom cross-section of the column. However, the curved slotted holes centred in O and realized on the vertical central plates, should be inclined, requiring larger vertical central plate and steel angle, and making the connection more cumbersome. In the configuration investigated below, the centre of rotation is placed about 100 mm above the end section of the RC column.

In the general configuration, the column base connection is endowed with a vertically-oriented steel plate for each column face.

The proposed connection is built in the shop and then its components are assembled in the construction site. First of all, the cross-shaped base plate is arranged on the foundation before pouring of concrete. Once the concrete is cured, the main element of the connection constituted by the vertical central plates and the spherical bearing is positioned. After that, friction devices and self-centring systems are added. Lastly, in the case of cast-in-situ column, concrete of the column is poured once its reinforcement is arranged.

7.2 Calculation procedure

7.2.1 General method

The mechanics of the proposed connection is characterized by two main steps: the first one, in which the system behaves almost rigidly; the second one in which the sliding of the spherical surface occurs and the column starts to rotate. The assumption of rigid behaviour up to the attainment of the yielding moment is used to simplify the formulation. In fact, due to the different stiffness of friction devices and self-centring systems, the monotonic moment-rotation curve might be represented more accurately by a multi-linear curve, in which the first branch is characterized by the stiffness of all the resisting mechanisms. Once the friction devices slide, the stiffness of the connection is ruled by the elastic stiffness of the self-centring systems. Once the stacks of disc springs of the self-centring systems farthest from the centre of rotation O start to deflect, the whole connection assumes a new stiffness. The connection shows a stable post-yielding stiffness up to the attainment of

the ultimate rotation once the stacks of disc springs of all the self-centring systems deflect.

The external forces acting on the column base connection are illustrated in Figure 7.4. The connection is supposed to rotate around the point *O*, thus the yielding moment in the case of uniaxial bending, i.e. the design moment activating the rotation of the system may be expressed as:

$$M_y = M_{sc} + M_f + M_b \tag{7.1}$$

where M_{sc} is the moment strength provided by the self-centring system, M_f is the contribution given by the friction devices, while M_b is that provided by the friction forces acting at the spherical bearing. As previously mentioned,

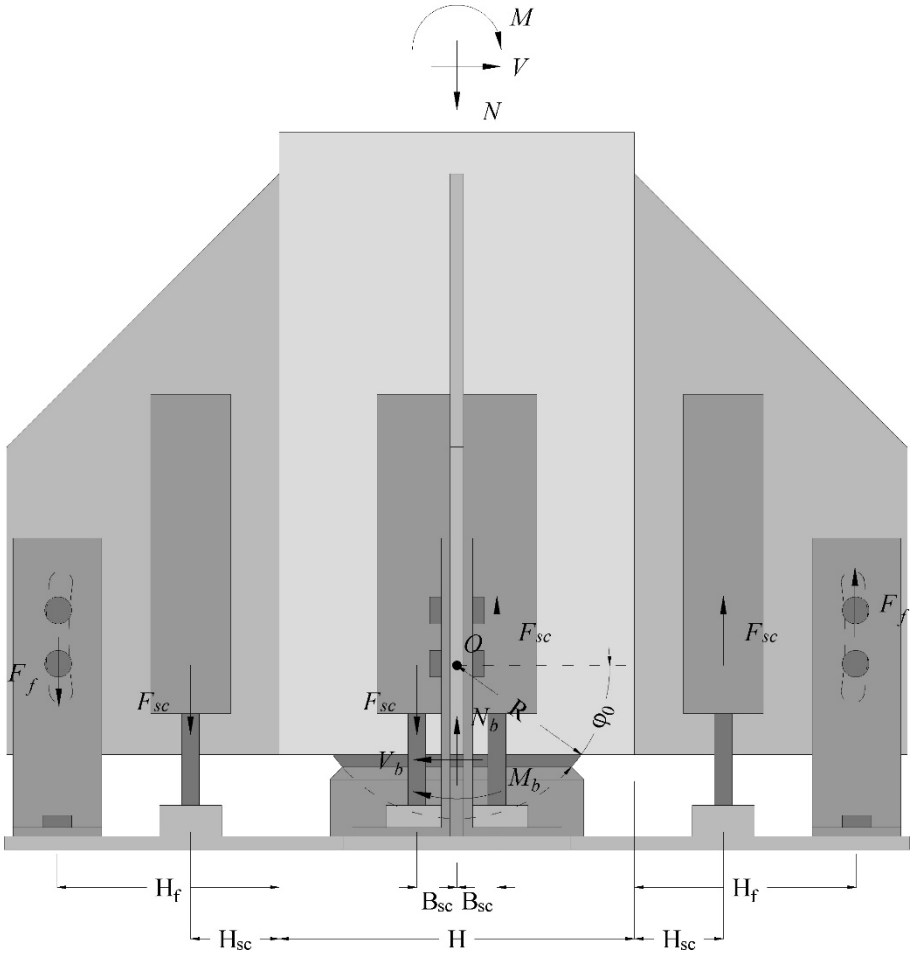

Figure 7.4 Proposed column base connection: forces acting on the connection calculating the equilibrium with respect to point *O*

the bearing defines the centre of rotation of the system. With respect to this point, the contributions to the yielding moment provided by both self-centring systems and friction devices are assessed.

On the basis of the connection illustrated in Figure 7.1, the terms in Eq. (7.1) may be expressed as follows:

$$M_{sc} = 4F_{sc}\left(\frac{H}{2} + H_{sc}\right) + 4F_{sc}\,B_{sc} \tag{7.2}$$

$$M_{f} = 2F_{f}\left(\frac{H}{2} + H_{f}\right) \tag{7.3}$$

$$M_{b} = \mu_{b} N R \Phi\left(\varphi_{0}\right) \tag{7.4}$$

where F_{sc} is the applied preload of each threaded bar, F_f is the friction force of the device aligned along the column strong axis, N is the axial load acting on the column, R is the radius of the spherical bearing, while $\Phi(\varphi_0)$ is a parameter depending on the bearing geometry (Froli et al. 2019). The contribution to the moment capacity of the connection provided by the steel angles bent in the out-of-plane direction is neglected. It is calculated on the basis of the angle φ_0, which is the complementary angle of the zenith one. The parameter $\Phi(\varphi_0)$ is calculated with the following equation:

$$\Phi\left(\varphi_{0}\right) = \frac{3}{2\pi\left(1-\sin^{3}\left(\varphi_{0}\right)\right)} \int_{0}^{2\pi} \int_{\varphi_{0}}^{\frac{\pi}{2}} \frac{\sin\left(\varphi\right)\cos\left(\varphi\right)}{\sqrt{\sin^{2}\left(\varphi\right) + \cos^{2}\left(\varphi\right)\sin^{2}\left(\theta\right)}}\, d\varphi d\theta \tag{7.5}$$

It should be noted that the first two terms of Eq. (7.1), that constitute most of the whole yielding moment of the connection, do not depend on the axial force acting on the column. To ensure self-centring capability to the connection, and to obtain a flag-shaped hysteresis loop (Figure 7.5), the contribution provided by the self-centring systems must be greater than that given by friction forces:

$$M_{sc} > M_{f} + M_{b} \tag{7.6}$$

To this aim, it is assumed to attribute a 60% of the yielding moment to the self-centring system, while the other 40% is given by friction devices and spherical bearing.

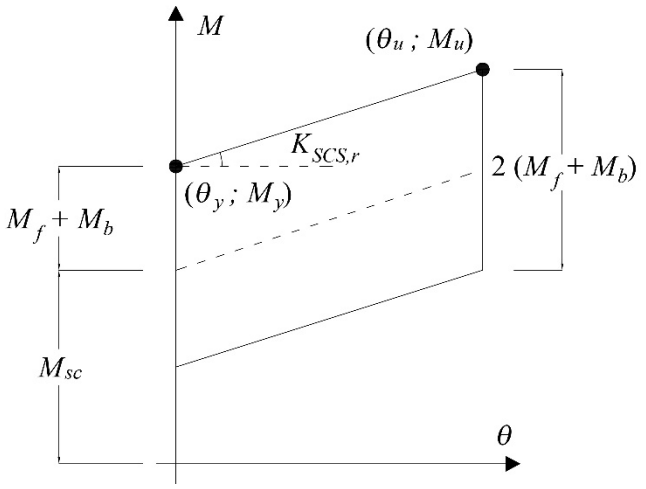

Figure 7.5 Proposed column base connection: analytical moment-rotation curve

Therefore, Eq. (7.2) yields:

$$M_{sc} = 0.6\,M_y \quad \rightarrow \quad F_{sc} = \frac{0.6\,M_y}{4\left(\frac{H}{2} + H_{sc} + B_{sc}\right)} \tag{7.7}$$

For simplicity's sake, it is assumed that all the self-centring systems achieve the yielding force at the same time.

As for M_b, it is difficult to tune its value, because it depends on the axial load acting on the column, the geometry of the bearing and the friction coefficient of the surfaces in contact. For this reason, tuning of moment strength is based on the contribution provided by the friction devices. Eqs. (7.3) and (7.4) may be rewritten as:

$$M_f + M_b = 0.4M_y \quad \rightarrow \quad F_f = \frac{0.4M_y - \mu_b NR\Phi\left(\varphi_0\right)}{2\left(\frac{H}{2} + H_f\right)} \tag{7.8}$$

The friction force provided by the devices may be computed with the equations already used in Chapter 6:

$$F_f = t_s n_b n_s \mu_f F_{pc} \tag{7.9}$$

in which t_s is the ratio between the effective and the code-consistent preload applied to the bolt, n_b is the number of bolts, n_s is the number of surfaces involved by the connection, μ is the friction coefficient, while F_{pc} is the code-consistent bolt preload.

The latter is calculated as:

$$F_{pc} = 0.7 f_{ub} A_{res} \tag{7.10}$$

where f_{ub} is the ultimate strength of steel, while A_{res} is the effective cross-sectional area of the bolt shank.

The post-yielding branch of the connection is characterized by the stiffness of the self-centring system, i.e. bolt shank and stack of disc springs. The latter is calculated with the aim of preventing the yielding of the threaded bar up to the ultimate rotation. Two main parameters affect the design of the stack of disc springs, i.e. the external force to which is subjected, and the overall deflection. The strength is ensured by the number of springs stacked in parallel (n_{par}), while the deflection is provided by those arranged in series (n_{ser}).

The design of the self-centring system is iterative. A tentative disc spring is selected, characterized by a conical disc height h_0, maximum allowable deflection and force equal to $0.75h_0$ and $F_{0.75h0}$, respectively, and a secant stiffness K_{sec} calculated as $F_{0.75h0}/(0.75h_0)$. The number of disc springs arranged in parallel is estimated as follows:

$$n_{par} \geq F_{sc} / F_{0.3h_0} \tag{7.11}$$

in which $F_{0.3h0}$ is the reaction force of the disc spring at a deflection of 30% of the conical disc height. This tentative value of deflection is assumed in order to ensure adequate deflection capability of the disc spring in the post-yielding branch.

Then, the equivalent stiffness of the stack of disc springs is calculated as:

$$K_{stack} = n_{par} K_{\sec} / n_{ser} \tag{7.12}$$

in which n_{ser} is still undetermined. The deflection of the stack of disc springs before yielding of the connection is equal to:

$$\delta_{sc} = \frac{F_{sc}}{K_{stack}} = \frac{F_{sc}}{K_{\sec}} \frac{n_{ser}}{n_{par}} \tag{7.13}$$

At this point, n_{ser} can be computed aiming at ensuring adequate deflection of the stack of disc springs up to the ultimate rotation of the connection:

$$n_{ser} \geq \frac{\frac{F_{sc}}{K_{\sec}} \frac{n_{ser}}{n_{par}}}{0.75 h_0} + \frac{\theta_u \left(\frac{H}{2} + H_{sc} \right)}{0.75 h_0} \tag{7.14}$$

where θ_u is the ultimate rotation of the connection. The two terms of the above equation are related to the phases at yielding, and at the ultimate rotation. Eq. (7.14) can be arranged as follows:

$$n_{ser} \geq \frac{\theta_u \left(\frac{H}{2} + H_{sc} \right) K_{\sec} n_{par}}{0.75 h_0 K_{\sec} n_{par} - F_{sc}} \tag{7.15}$$

The corresponding threaded bar passing through the disc springs is characterized by the following stiffness:

$$K_{tb} = \frac{E_{tb} A_{tb}}{l_{tb}} \tag{7.16}$$

in which E_{tb}, A_{tb} and l_{tb} are respectively the Young modulus, the average cross-sectional area and the length of the threaded bar. At this point, several checks must be performed: at the maximum allowable deflection of the whole stack of disc springs, the threaded bar should behave elastically to ensure the self-centring behaviour of the connection; the system has to be geometrically compatible with the remaining part of the connection (e.g. avoiding too long stack of disc spring); surrounding structural elements must behave elastically when withstanding the maximum force transferred by the self-centring system. If all the checks are satisfied, the rotational stiffness along the strong-axis direction, which is x axis, of the self-centring system may be expressed as:

$$K_{SCS,r,x} = \frac{1}{\left[\left(\frac{1}{\frac{H}{2} + H_{sc}} \right)^2 + \left(\frac{1}{B_{sc}} \right)^2 \right] \left(\frac{1}{n_{tb} K_{tb}} + \frac{1}{n_{tb} K_{stack}} \right)} \tag{7.17}$$

in which n_{tb} is the number of threaded bars. The ultimate moment of the whole connection M_u can be calculated with the following equation:

$$M_u = M_y + K_{SCS,r,x} \theta_u \tag{7.18}$$

7.2.2 Case study

The column base connection investigated hereinafter is designed on the basis of the above procedure. The design moment capacity of the connection

along the strong-axis $M_{y,x}$ is set equal to 200 kNm, which corresponds to 75% of the bending moment capacity of the column belonging to the subassembly described in Section 2.2.3. By using the assumptions of Eqs. (7.7) and (7.8), the following values of the contributions provided by self-centring system, friction devices and spherical bearing are obtained:

$$\begin{aligned} M_{sc,x} &= 0.6\,M_{y,x} = 120\,kNm \\ M_{f,x} + M_b &= 0.4 M_{y,x} = 80 kNm \end{aligned} \tag{7.19}$$

For simplicity's sake, the connection is endowed with friction devices and self-centring systems along the strong-axis only. Therefore, the applied preload of each threaded bar F_{sc} can be easily calculated by modifying

Eq. (7.7), setting H_{sc} = 100 mm:

$$F_{sc} = \frac{0.6\,M_{y,x}}{4\left(\frac{H}{2} + H_{sc}\right)} = \frac{120\times10^6}{4\left(200+100\right)} = 100000\,N \tag{7.20}$$

With regard to M_f and M_b, setting μ_b = 0.1, N = 200 kN and H_f = 250 mm, the force activating the sliding of the device is calculated by using Eq. (7.8):

$$F_f = \frac{0.4 M_{y,x} - \mu_b N R \Phi\left(\varphi_0\right)}{2\left(\frac{H}{2} + H_f\right)} = 84685\,N \tag{7.21}$$

This value can be obtained by using 2 bolts M20 class 10.9 for each friction device, having net cross-sectional area A_{res} of 245 mm^2 and ultimate strength f_{ub} of 1000 MPa. Each friction device involves two friction surfaces characterized by a friction coefficient μ_f of 0.4. The value of the friction coefficient is selected consistently to the suggestion of EN1993 with reference to "surfaces blasted with shot or grit, spray-metallized with an aluminium or zinc based product". Rearranging Eq. (7.9), the ratio between the effective and the code-consistent preload applied to the bolt can be computed as follows:

$$t_s = \frac{F_f}{n_b n_s \mu_f\, 0.7\, f_{ub} A_{res}} = 0.31 \tag{7.22}$$

The low value of axial force acting on the column is selected in order to limit its beneficial effect in maintaining the spherical cap within the concave

steel bearing. In fact, the shear force acting on the column tends to move it outside the concave bearing, and the more is the axial force, the less this effect can be observed.

Finally, $M_{f,x}$ and M_b are equal to 76.22 kNm and 3.78 kNm, respectively. As already said before, the only contribution to the moment strength of the connection which depends on the axial load acting on the column is that provided by spherical bearing. Therefore, in order to simulate the effect of the variation of axial load acting on the column due to seismic action, M_b is calculated also by using an axial load much higher than that used to design the friction devices. Considering an axial load of 400 kN, one obtains M_b equal to 7.57 kNm. This difference increases the whole moment strength of the connection of no more than 2%, thus its influence is negligible.

With regard to the self-centring system, its design is carried out by using the iterative procedure expressed by Eqs. (7.11)-(7.17). First of all, the ultimate rotation θ_u assumed to design the self-centring system is set to 35 mrad. So, by using threaded bars with diameter 20 mm, a disc spring with the geometrical characteristics reported in Table 7.1 is selected.

Reaction force at 75% of the maximum deflection $F_{0.75h0}$ is 85.82 kN, while secant stiffness K_{sec} is 65.29 kN/mm. The iterative procedure is satisfied by using 14 groups of disc springs arranged in series, each group constituted by 3 disc springs arranged in parallel. Therefore, by using Eq. (7.12) the stiffness of the stack of disc springs K_{stack} can be calculate, obtaining a value of 13991 N/mm. With an overall length of the threaded bar l_{tb} of 475 mm, its stiffness K_{tb}, given by Eq. (7.16), is 106253 N/mm. Then, rotational stiffness of the self-centring system $K_{SCS,r,x}$ is assessed by using Eq. (7.17), obtaining a value of 4450.75 kNm/rad. Lastly, the moment strength of the connection at the ultimate rotation $M_{u,x}$ can be evaluated by using Eq. (7.18), which yields:

$$M_{u,x} = M_{y,x} + K_{SCS,r,x}\,\theta_u = 355.78\,kNm \tag{7.23}$$

As for yielding moment along the weak-axis $M_{y,y}$, this is obtained by summing the contributions provided by self-centring systems and spherical bearing only:

$$M_{y,y} = M_{sc,y} + M_b = 4F_{sc}\,B_{sc} + M_b = 21.78\,kNm \tag{7.24}$$

Table 7.1 Geometrical characteristics of the disc spring used

D_e [mm]	D_i [mm]	h_0 [mm]	l_0 [mm]	t [mm]	h_0/t -
69.85	20.75	1.75	8.23	6.48	0.27

having assumed B_{sc} equal to 45 mm. The ultimate moment along the weak-axis $M_{u,y}$ is given as follows:

$$M_{u,y} = M_{y,y} + K_{SCS,l}\,\theta_u\,B_{sc}^2 = 25.29\,kNm \tag{7.25}$$

7.3 Validation of the adopted numerical procedure

The proposed connection is constituted by several mechanical parts (e.g. disc spring, self-centring system). Similarly to the procedure already adopted in Section 6.2, the accuracy of the numerical models in reproducing the mechanical properties of the connection, is assessed starting from simple models which involve single components, gradually increasing the level of complexity. To this aim, assuming the capability of reproducing accurately the mechanical performance of friction device on the basis of the findings reported in Chapter 6, the first model focuses the attention on the disc spring. After that, the second model analyses the self-centring system. However, this model is computationally expensive, and thus a third model is analysed, in which an equivalent version of the self-centring system is evaluated. For each model, numerical results are compared with analytical predictions to demonstrate the reliability of the modelling strategy.

7.3.1 Disc spring

To verify the ability to reproduce an experimental test on a disc spring by means of FEAs, one of the experimental results reported by Bagavathiperumal et al. (1991) is used. Geometrical characteristics of the disc spring tested are listed in Table 7.2, while the meaning of symbols is illustrated in Figure 7.6.

With regard to the mechanical characteristics of the disc spring, Young Modulus E is 206 GPa, Poisson ratio ν is 0.3, and yielding stress f_y is 2100 MPa. The FEM model is constituted by three elements, namely the disc spring, a base on which the disc spring lays and a steel disc pushing against the disc spring (Figure 7.7). The mesh is realized by using C3D8R elements. The analysis is constituted by one step only, in which is imposed a displacement to the steel disc equal to the maximum deflection of the disc spring. This analysis, as well as all the other ones below, consider geometric non-linearity.

The analysis procedure and the automatic stabilization option used are respectively “Static, General” and “Specify dissipated energy fraction”, set to the default value of 0.0002. These options will be also used in the other analyses carried out in the following sections.

Different analyses were carried out by varying the friction coefficient at

the interface between disc springs and the other elements, aiming at understanding the influence of this feature to the whole behaviour of the disc spring. Specifically, analyses considering a friction coefficient equal to 0, 0.4, 0.5, and 0.6 were performed.

The force-displacement curve of the disc spring is also analytically calculated using the formulation proposed by EN16984 (2016). In the case of disc spring without contact surfaces, like the tested one and the other ones used hereinafter, the spring force is given as follows:

$$F(s) = \frac{4E}{1-\nu^2}\frac{t^4}{K_1 D_e^2}\frac{s}{t}\left[\left(\frac{h_0}{t}-\frac{s}{t}\right)\left(\frac{h_0}{t}-\frac{s}{2t}\right)+1\right] \tag{7.26}$$

in which s is the deflection of the disc spring, K_1 is a constant calculated as follows:

$$K_1 = \frac{1}{\pi}\frac{\left(\frac{\delta-1}{\delta}\right)^2}{\frac{\delta+1}{\delta-1}-\frac{2}{\ln\delta}} \tag{7.27}$$

Table 7.2 Geometrical characteristics of the disc spring tested by Bagavathiperumal et al. (1991)

D_e [mm]	D_i [mm]	h_0 [mm]	l_0 [mm]	t [mm]	h_0/t -
66	33	2.0	4.9	2.9	0.7

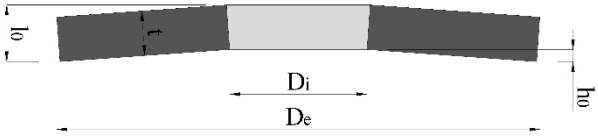

Figure 7.6 Disc spring: geometrical characteristics

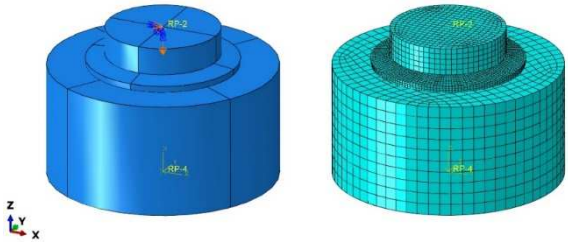

Figure 7.7 Disc spring: FEM model and mesh of the experimental test carried out by Bagavathiperumal et al. (1991)

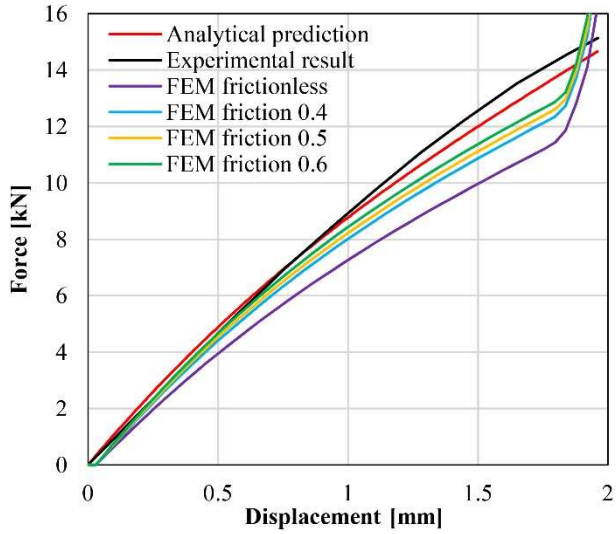

Figure 7.8 Disc spring: experimental, analytical and numerical force-displacement curves of the specimen tested by Bagavathiperumal et al. (1991)

where $\delta = D_e/D_i$. The maximum stress experienced by the disc spring in the mid-section may be expressed as:

$$\sigma_{OM} = -\frac{4E}{1-\nu^2}\frac{t^2}{K_1 D_e^2}\frac{s}{t}\frac{3}{\pi} \tag{7.28}$$

Satisfactory agreement between experimental results and analytical prediction can be found, up to 75% of the maximum deflection of the disc spring. Above this value, the force increases steeply because the disc spring is getting flattened.

The comparison between experimental, analytical and numerical force-displacement curves, plotted in Figure 7.8, demonstrates the capability of the FEM model to accurately reproduce the mechanical behaviour of the disc spring tested in the displacement range smaller than 75% of the ultimate deflection of the spring.

7.3.2 Self-centring system - detailed model

The detailed FEM model of the self-centring system is complex, involving numerous elements and interactions. The column base connection is endowed with several self-centring systems and, thus, FEAs would require a significant computational effort. For this reason, it is preferred to numerically analyse this system only, assessing the reliability of FEA by comparing the results with analytical predictions. Then, an equivalent element, having an analogous

mechanical behaviour, is defined and its response is compared to that of the self-centring system.

The geometrical characteristics of the self-centring system were already described in Section 7.2. The FEM model, which is illustrated in Figure 7.9, uses C3D8R elements. The yielding stress of the disc springs is 2100 MPa, while that of other steel elements is 900 MPa. With regard to the bolt preload, this is simulated by using the dedicated tool already existing in the "Types for selected step" list, within the "Load" window, and named "Bolt load". The bolt preload will be applied in the same way in the following analyses.

The analysis is divided into six steps:

1) Bar preloading: the preload is applied to the threaded bar;
2) Bar unloading: the threaded bar is unloaded. The first two steps aim at simulating the presetting procedure of disc springs;
3) Bar preloading: the threaded bar is preloaded again;
4) Rest;
5) Push down: a distributed pressure on the top flat washer is applied to simulate the reaction of the box-shaped case in which the self-centring system is inserted;
6) Push up: a distributed pressure on the bottom flat washer is applied with the same goal of the above step.

Several analyses are carried out in order to highlight the contribution of friction to the overall behaviour of the self-centring system. More precisely, friction coefficient equal to 0.2, 0.4, and 0.6 are used.

The stress contours of the most significant phases of the analysis with friction coefficient equal to 0.2 are plotted in Figure 7.10. High stress values can be noticed at the internal edges of disc springs in all the phases (except for step time 2 in which there are no forces acting on the model). At step time 4.5, the maximum deflection of disc springs is achieved, with an overall shortening of the stack of about 18 mm. It should be seen that in this step the portion of threaded bar inserted through the disc springs is no longer preloaded because bolt head is not in contact with the flat washer. Moreover, the force acting on the disc springs is transferred on the bolt nut, loading the lower portion of the threaded bar. At step time 5, the internal portion of bolt shank is loaded again, while the lower one is unloaded. At step time 5.5, the maximum deflection of the stack of disc spring is achieved again, and the bolt shank is subjected to the tensile force transferred by the top flat washer to the bolt head. At step time 6, the system comes back to the initial condition, with slight differences in the stress contours of the flat washers.

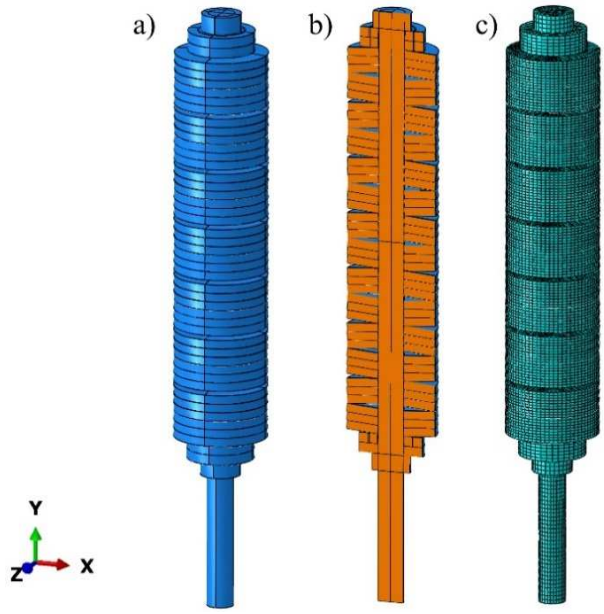

Figure 7.9 Self-centring system - detailed model: FEM model (a), its cut-view (b), and mesh (c)

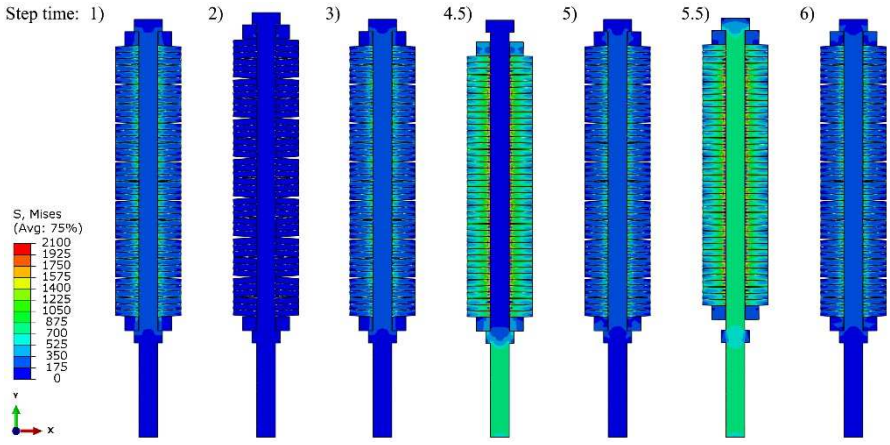

Figure 7.10 Self-centring system - detailed model: stress contours at different step times

In Figure 7.11 are plotted the trends of the relative shortening of the disc springs and the reaction force at the bolt base during the analysis. It can be seen that the presetting procedure leads to a residual shortening of the disc springs due to the flattening of the contact points (step time 2). Moreover, when the disc springs are subjected to the bolt preload (step time 1, 3-4, 5 and 6), the relative shortening is substantially the same, with a negligible reduction over the analysis. This phenomenon is due to the progressive flattening of the

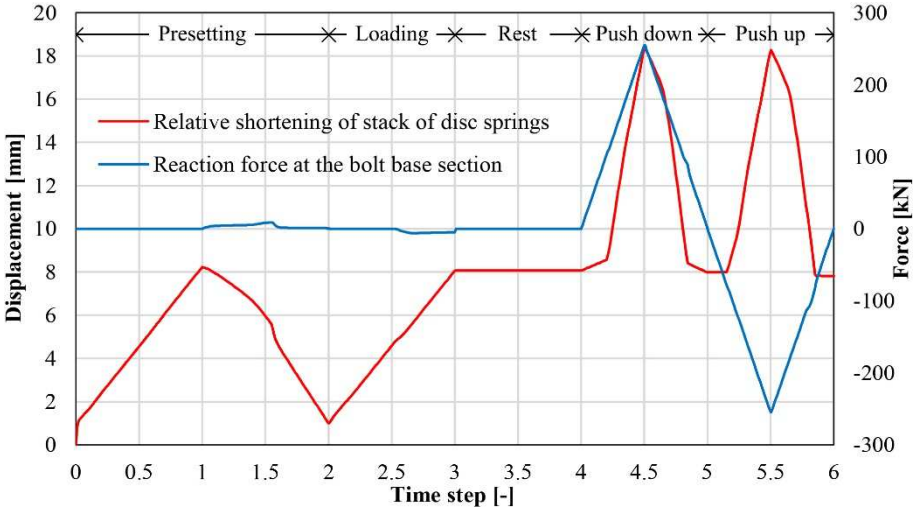

Figure 7.11 Self-centring system - detailed model: relative shortening of the disc springs (red line) and the reaction force at the bolt base (blue line)

contact points between disc springs, flat washers, bolt head and nut. Concerning the reaction force, negligible values are registered during the first four steps, while at step time 4.5 and 5.5, a force value almost equal to that causing the expected deflection of disc springs is registered.

The relative shortening of the stack of disc springs registered in the three analyses at step time 1, 4.5, and 5.5, and the corresponding ones calculated analytically, are reported in Table 7.3. The results show that the friction coefficient affects significantly the behaviour of the self-centring system. In fact, the more is the friction coefficient, the less are the deflections for the three steps investigated. The comparison with the analytical values shows that none of the three values of friction coefficient used is able to accurately reproduce the deflections of the three steps considered. Indeed, deflection at time step 1 (*presetting*) is reproduced well by FEA with friction coefficient of 0.6, while deflections at time step 4.5 and 5.5 (i.e. *push down* and *push up*) are replicated by FEA with friction coefficient 0.2.

To better understand the influence of the friction coefficient on the cyclic behaviour of the self-centring system, in Figure 7.12 is plotted the reaction force at step 5 vs. the shortening of the stack of disc springs at step 5 (i.e. not considering the shortening of the stack undergone in previous steps) for each analysis, and the analytical prediction. In the loading phase, the response can be divided in two steps: the first one characterized by the same stiffness, despite the different friction coefficient used; the second one whose stiffness depends on the friction coefficient. The friction coefficient value which

Table 7.3 Relative shortening of the stack of disc springs: analytical prediction vs. numerical results obtained with different friction coefficient

		Step time		
		1	**4.5**	**5.5**
		Relative shortening		
		[mm]	**[mm]**	**[mm]**
Friction coefficient μ	0.2	8.23	18.38	18.26
	0.4	7.44	16.48	16.36
	0.6	6.68	14.67	14.58
Analytical prediction		6.91	18.4	

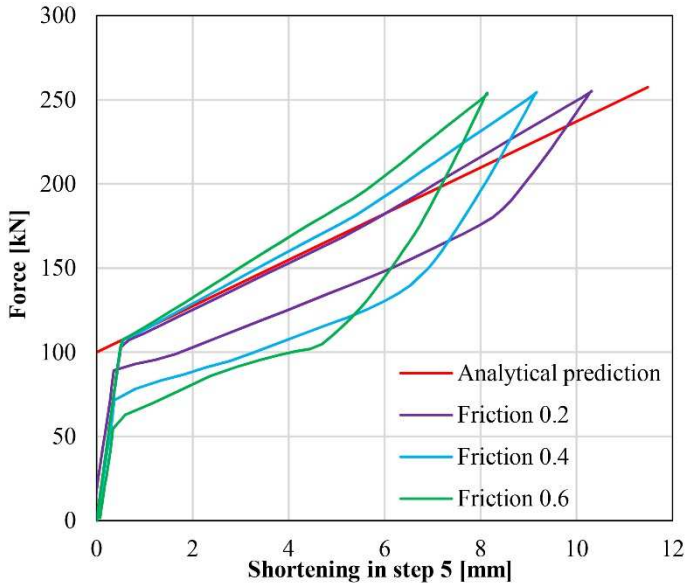

Figure 7.12 Self-centring system - detailed model: reaction force vs. shortening of the stack of disc springs at step 5

reproduces better the stiffness of the second branch is 0.2. It can also be noticed that higher friction coefficient leads to wider hysteresis loops, due to the sliding of the disc springs arranged in parallel. This would be a positive aspect in terms of dissipative capacity of the whole connection. However, the combination with friction devices could hamper the self-centring capacity, because of the lower unloading branch.

On the basis of the above considerations, the friction coefficient which reproduces better the analytical curve is 0.2. This differs from what was found out in Figure 7.8, where the numerical result was satisfactory with friction coefficient equal to 0.6. This may be explained by the fact that the self-

centring system is characterized by three disc springs arranged in parallel and the friction forces generated between the surfaces in contact are less negligible.

7.3.3 Self-centring system - equivalent model

The equivalent system is constituted by a cylinder having outside diameter 50 mm and inside one 21 mm. The elastic modulus E_{eq} is calculated to achieve a deflection of the system equal to that obtained with the stack of disc springs. The effective cross-sectional area of the cylinder $A_{cylinder}$ is 1617 mm^2. The whole height of the stack of disc springs h_{stack} is 295.88 mm. The equivalent longitudinal strain at the maximum allowable deflection is:

$$\varepsilon_{eq} = \frac{n_{ser} 0.75 h_0}{h_{stack}} = \frac{14 \times 0.75 \times 1.7526}{295.88} = 0.0622 mm/mm \quad (7.29)$$

Then, the equivalent elastic modulus is:

$$E_{eq} = \frac{n_{par} F_{0.75 h_0}}{A_{cylinder} \varepsilon_{eq}} = \frac{3 \times 85823}{1617 \times 0.0622} = 2559.91 MPa \quad (7.30)$$

Lastly, the Poisson ratio is calibrated via FEAs: the adopted value is 0.05. In Figure 7.13 are shown the FEM model and the mesh. The same mesh elements and mechanical properties of steel elements are used. Moreover, the analysis is divided in six steps as well, having the same descriptions of those used for the detailed model.

The stress contours of the most significant phases are plotted in Figure 7.14. Generally speaking, the behaviour of the equivalent system is in good agreement with that previously described and plotted in Figure 7.10.

In Figure 7.15 are plotted the trends of the relative shortening of the cylinder and the reaction force at the bolt base during the analysis. In this case, no residual shortening is registered at the end of the presetting procedure, because no contact points get flat (step time 2). In addition, loading and unloading branches show limited changes in stiffness. Like the detail model, when the cylinder subjected to the bolt preload (step time 1, 3-4, 5 and 6), the relative shortening is substantially the same, with a negligible reduction over the analysis. As for the reaction force, negligible values are registered during the first four steps, while at step time 4.5 and 5.5, a force value almost equal to that causing the expected deflection of the cylinder is registered.

The relative shortening of the cylinder at step time 1, 4.5, and 5.5, the

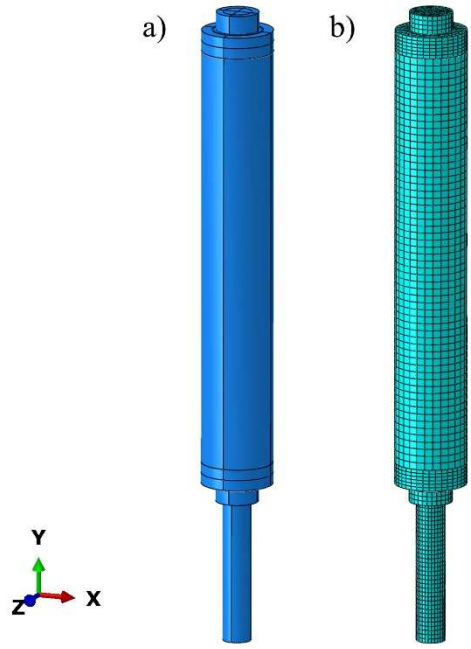

Figure 7.13 Self-centring system - equivalent model: FEM model (a), and mesh (b)

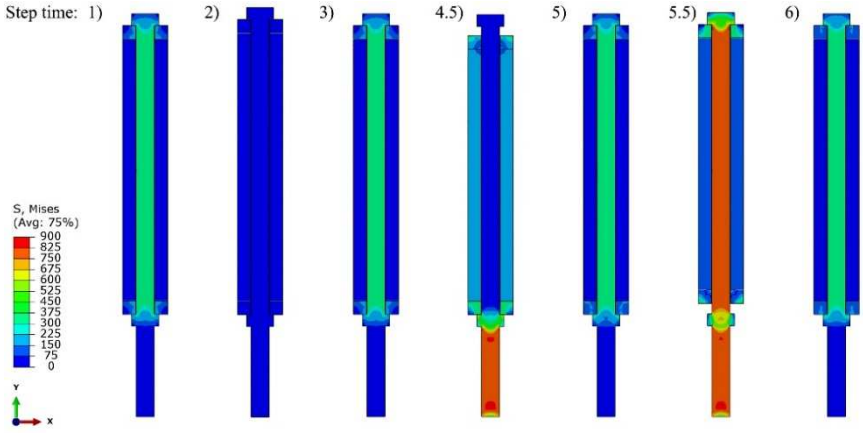

Figure 7.14 Self-centring system - equivalent model: stress contours at different step times

corresponding ones of the detailed model and those calculated analytically, are compared in Table 7.4. The results show that the equivalent model satisfactorily reproduces the macroscopic mechanics of the stack of disc springs.

In Figure 7.16 the reaction force at step 5 vs. the shortening of the cylinder at step 5 is compared with those of the detailed model and the analytical prediction. Generally speaking, the results of the equivalent model are in good

Table 7.4 Relative shortening of the stack of disc springs: analytical prediction vs. numerical results obtained with different friction coefficient

	Step time		
	1	**4.5**	**5.5**
	Relative shortening		
	[mm]	**[mm]**	**[mm]**
Detailed model (friction coefficient $\mu = 0.2$)	8.23	18.38	18.26
Equivalent model	7.11	17.69	17.71
Analytical prediction	6.91	18.4	

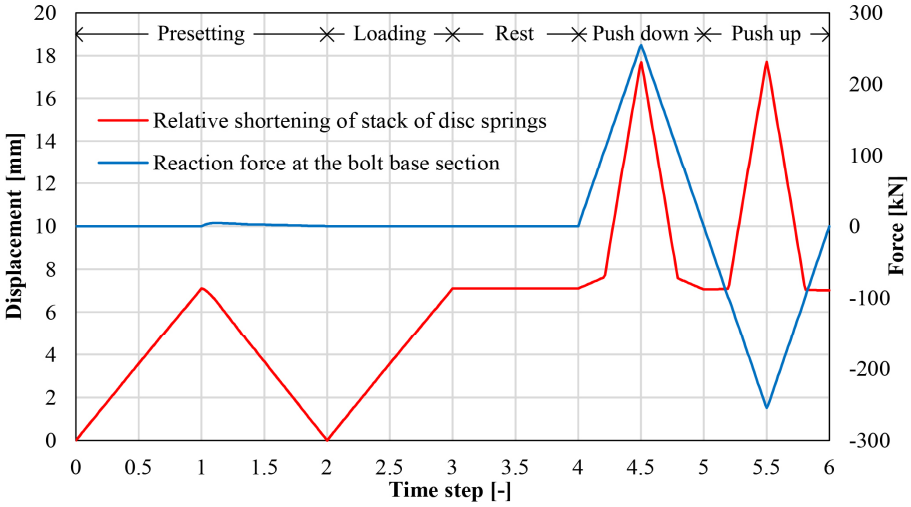

Figure 7.15 Self-centring system - equivalent model: relative shortening of the disc springs (red line) and the reaction force at the bolt base (blue line)

agreement with those of the detailed one, proving the accuracy of the simplified modelling strategy. Moreover, it can be observed that the equivalent model provides loading and unloading curves practically coincident, with no energy dissipation. This is due to the fact that, in the equivalent model, the friction forces generated at the interface between disc springs arranged in parallel are missing.

7.4 Finite element model

The FEM model aims at focusing on the macroscopic mechanical performance of the proposed connection. For this reason, the modelling does not include the connection between concrete column with friction devices and spherical bearing and concrete column. Moreover, the connections with the RC foundation are not modelled as well.

The model analysed includes a column with height of 900 mm between

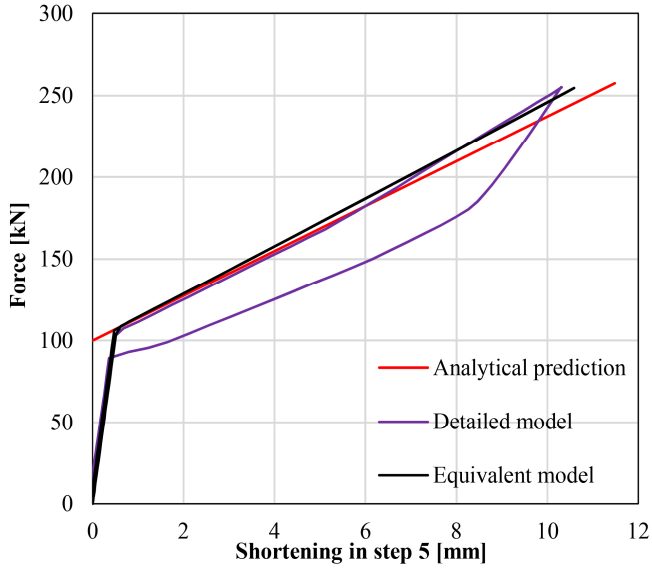

Figure 7.16 Self-centring system - detailed model: reaction force vs. shortening of the stack of disc springs at step 5

centre of rotation *O* and mid-point of column top section, four self-centring systems modelled consistently with the procedure outlined in Section 7.3.2, two friction devices and the spherical bearing (Figure 7.17).

Thanks to the simple model geometry, all elements are modelled by using 8-node linear brick elements (C3D8R), as shown in Figure 7.18.

Concerning material properties, all the elements are characterized by a linear elastic behaviour with Young modulus equal to 206 GPa.

Each analysis is divided into four steps:

1) Bolts and bars preloading: the preload is applied to bolts and threaded bars;
2) Rest: some interaction properties are changed;
3) Applying axial load on the column: a distributed pressure on the column top section is applied;
4) Imposing displacement at the column top section.

On the column top section is applied a uniform pressure whose resultant is equal to 200 kN. Moreover, the displacement history is applied to the centre of the above section. The connection of all steel elements to the foundation is simulated by introducing fixed constraints, excepting for threaded bars, for which pinned constrains are used.

The complexity of the FEM model requires the definition of several interactions characterized by different interaction properties. With regard to

the spherical bearing, the interaction is modelled by means of the Coulomb model of friction, with friction coefficient of 0.1 (Figure 7.19a). Concerning the friction devices, the same modelling strategy is used, characterized by a friction coefficient equal to 0.4 (Figure 7.19b). As for the interactions involving the self-centring systems, some of them depend on the analysis step. In fact, as already described before, the internal length of the box-shaped case must be equal to that of the stack of disc spring already preloaded, in order to avoid any undesired displacement of the column base connection due to a loose self-centring system. To simulate this constructional aspect, during the first analysis step, i.e. preloading of threaded bars, the interactions between the flat washers and the external blocking plates of the box-shaped case (Figure 7.19e), and between the flat washers and the stack of disc springs (Figure 7.19f), are characterized by a cohesive property with very high stiffness in the normal direction. By doing so, while the stack of disc springs shortens due to the preloading of the threaded bar, flat washers and external blocking plate remains in contact with disc springs. During the second analysis step, the interaction property of these interactions is changed to the Coulomb model of friction, with friction coefficient equal to 0.2, to simulate the real behaviour of these components during the functioning of the connection. To reproduce the mechanical continuity between the external blocking plates and the other plates of the box-shaped case, during the second analysis step are

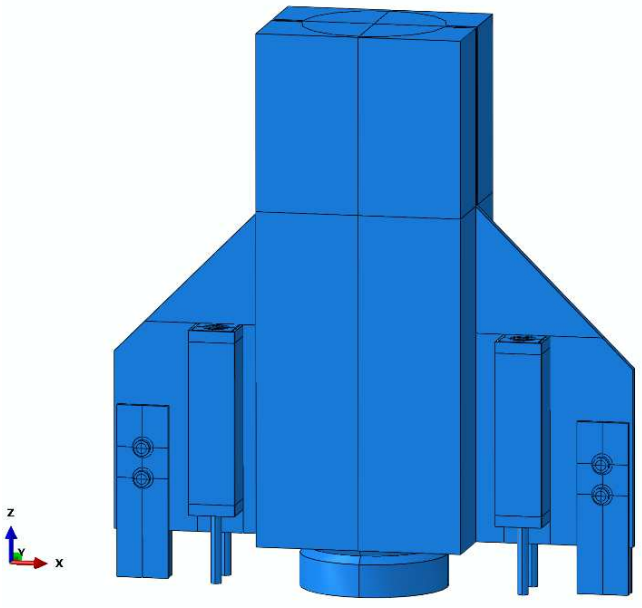

Figure 7.17 Proposed column base connection: 3D FEM model

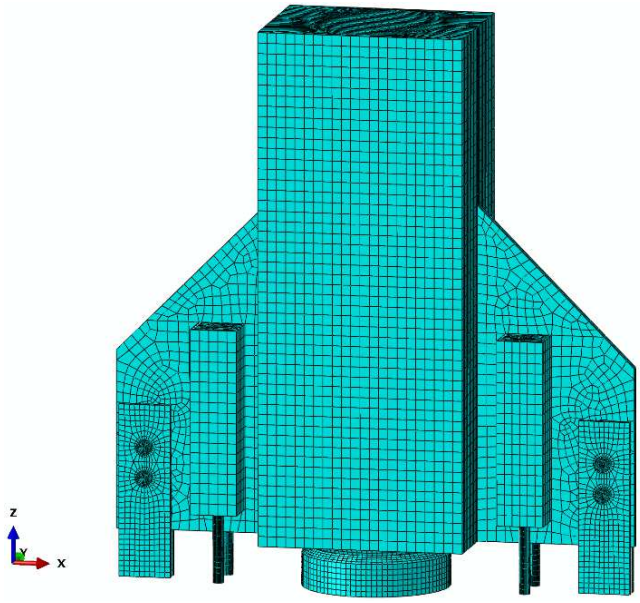

Figure 7.18 Proposed column base connection: mesh of the FEM model

activated several interactions having cohesive property with very high stiffness (Figure 7.19g). With regard to the interactions between bolt head and nut with external blocking plate and flat washers (Figure 7.19c, d), these are modelled with friction coefficient equal to 0.2 and are introduced since the first analysis step. Lastly, the interaction between shank of the threaded bar and internal surface of the cylinder mimicking the mechanical response of the stack of disc springs (Figure 7.19h), is modelled as frictionless.

Three groups of cyclic analyses are carried out:

1) bending along the strong-axis direction;
2) bending along the weak-axis direction;
3) bidirectional bending.

Four analyses belong to the first group, three of which focus only on one of the three resisting mechanisms each (i.e. spherical bearing, friction devices, self-centring systems), while the fourth one analyses the whole connection with all the resisting mechanism together. This is done to assess the accuracy of the numerical model in reproducing the mechanical behaviour of each resisting mechanism of the proposed connection. The other two groups consist of one analysis each.

The first two groups employ the loading protocol shown in Figure 7.20, while the third one uses that plotted in Figure 7.21. As already done in Section 6.5.2, these displacement histories are defined on the basis of the suggestions

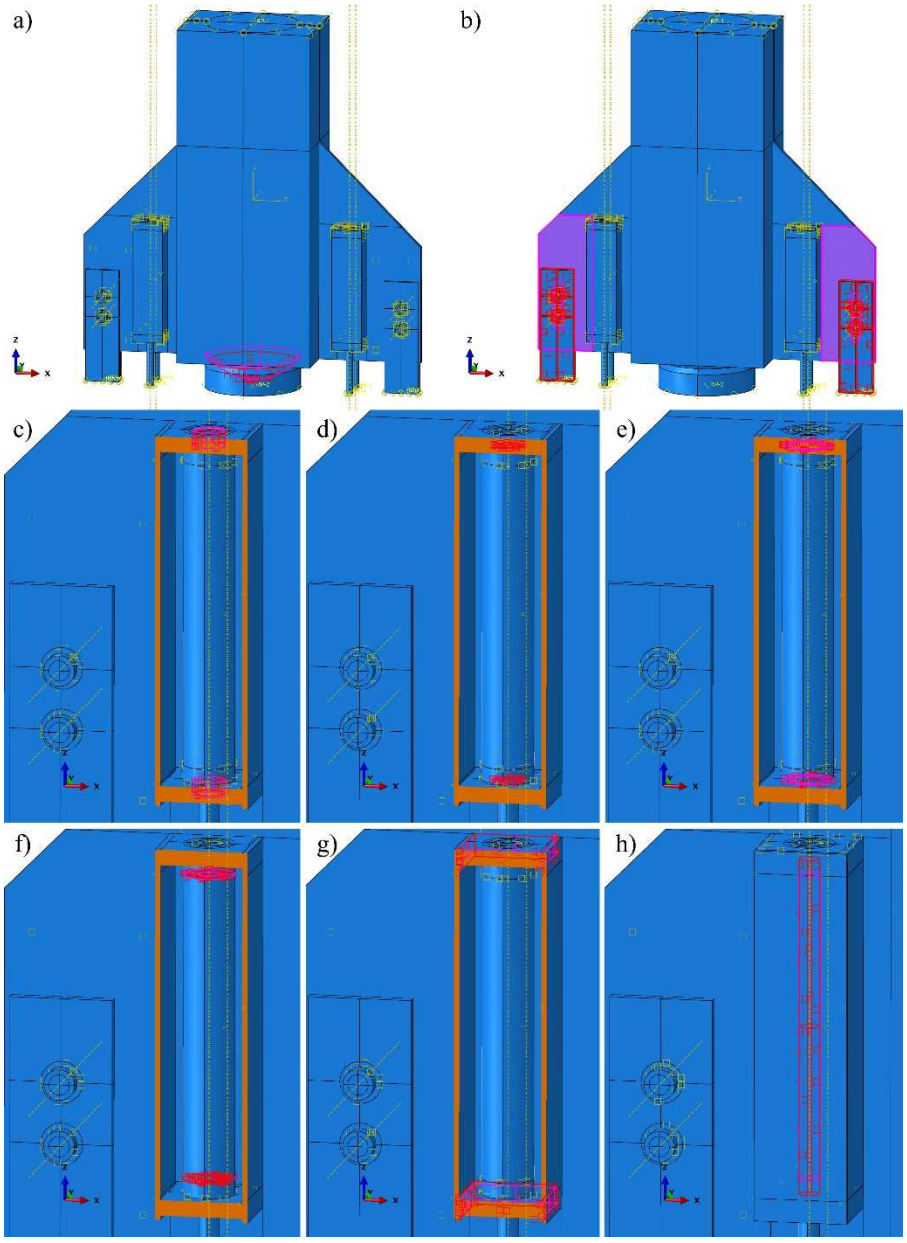

Figure 7.19 Proposed column base connection, interaction of the FEM model: a) spherical bearing, b) friction devices, c) bolt head and nut with external blocking plate, d) bolt head and nut with flat washers, e) flat washers with external blocking plates, f) flat washers and stack of disc springs, g) external blocking plates and other plates of the box-shaped case, h) shank of the threaded bar and internal surface of the cylinder mimicking the mechanical response of the stack of disc springs

of ACI 374.2R-13. However, preliminary analyses showed that the yield rotation of the connection is very low. For this reason, the amplitudes of the

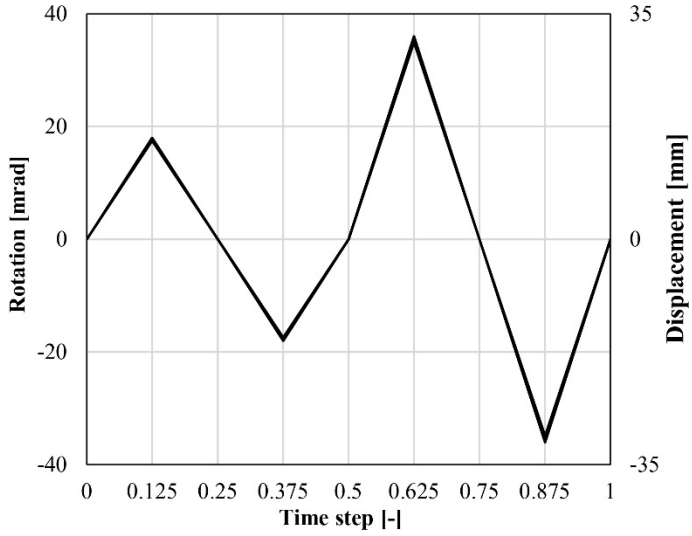

Figure 7.20 Proposed column base connection: loading protocol of the unidirectional analyses

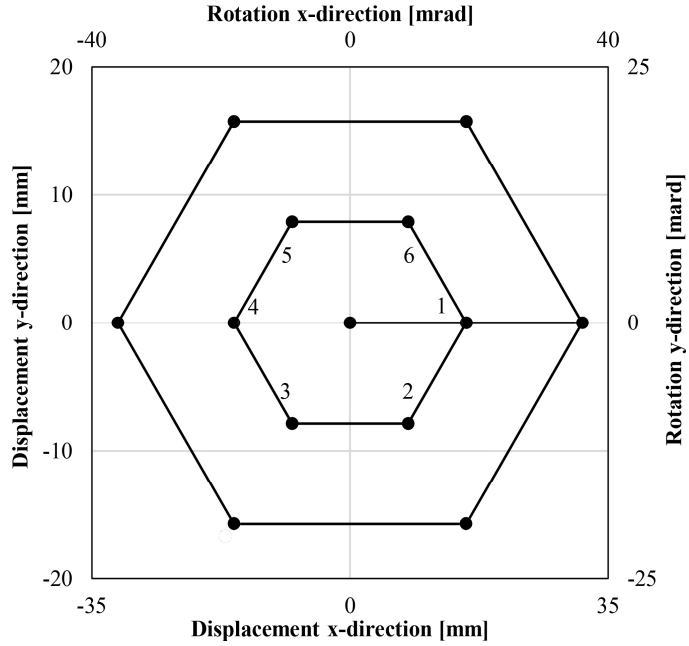

Figure 7.21 Proposed column base connection: loading protocol of the bidirectional analysis

cycles are defined on the basis of the ultimate rotation of the connection. To limit the computational effort, only two cycles are performed, having amplitude of ± 0.5 θ_u, and θ_u, respectively.

7.5 Results

As already done in Chapter 6, the results are presented in terms of moment-rotation curves and stress contours. The moment is obtained as the product between the horizontal reaction force at the mid-point of the column top section and the distance between the assumed centre of rotation (which is the point *O* of Figure 7.4) and the column top section. The rotation is computed as the ratio between the horizontal displacement imposed to the column top section and the distance between the centre of rotation *O* and the column top section.

Figure 7.22 reports the cyclic moment-rotation curves obtained considering only the spherical bearing, the friction devices, and the self-centring systems. It can be observed good agreement between numerical result and analytical prediction for each resisting mechanism. As for the results obtained with the whole connection, plotted in Figure 7.23, they confirm the design expectations, namely repeatable hysteresis loops and self-centring capability. It can be also observed that the assumption of initial rigid behaviour of the whole connection does not lead to significant error in the analytical evaluation of the moment-rotation curve.

In Figure 7.24 are shown the stress contours of the proposed connection during analysis with bending along strong-axis at the ultimate rotation θ_u. It can be observed that the high values of stress on the curved slotted holes plates near the self-centring systems, as well as on the box-shaped cases, are caused by the reaction forces transferred by these systems. Specifically, those on the top side of the left plate are due to the compressive forces transferred by the self-centring systems, while those on the bottom side of the right plate are due to the tensile forces transferred by the systems. As for friction devices, the stress contours reveal that they are subjected to in-plane bending moment due to the uneven sliding occurring on their internal surfaces. This effect could be also due to the fact that, as the spherical bearing has slightly moved outside the concave steel bearing (as it will be described below), a small amount of the shear force acting on the column is now absorbed by steel angles. This phenomenon is magnified by the idealized fixed constraint at their bases which avoid any rotation, which instead could be expected in such a connection (shown in Figure 7.1). Therefore, the connection of the proposed solution to the foundation must be thoroughly investigated with a more detailed FEM model.

In Figure 7.25 are plotted the stress contours of the connection cutting the model along a vertical plane passing through the threaded bars. From the

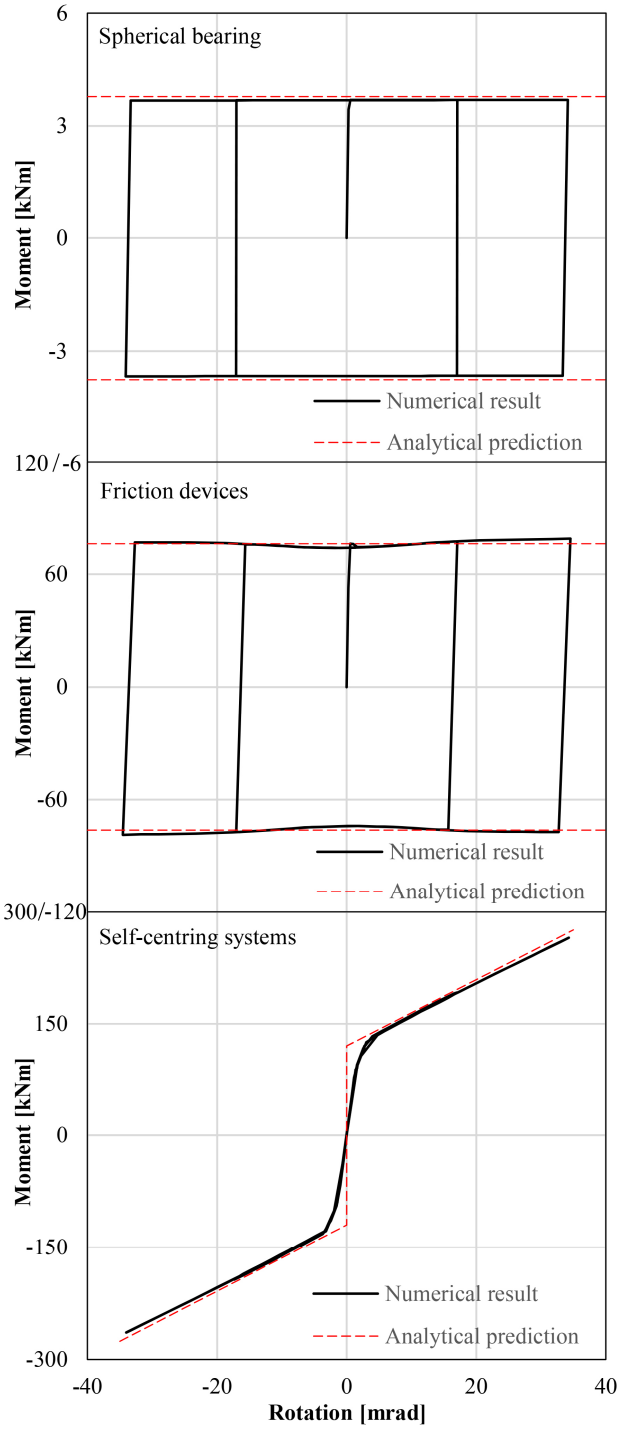

Figure 7.22 Proposed column base connection: moment-rotation curves obtained with spherical bearing, friction devices, self-centring systems

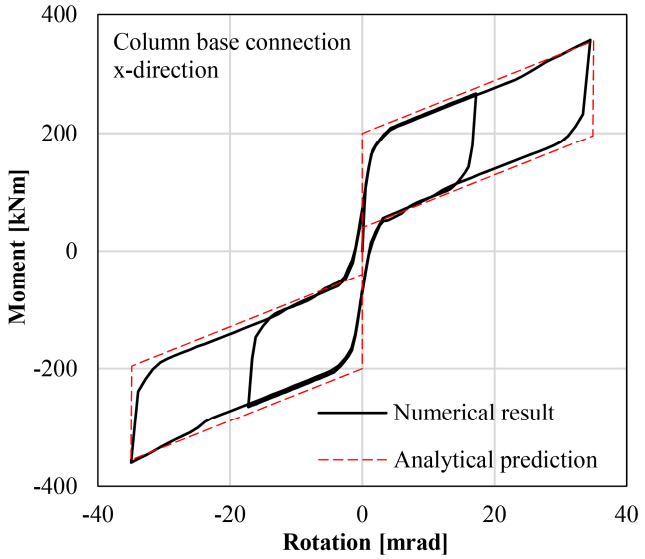

Figure 7.23 Proposed column base connection: moment-rotation curve of the whole connection along strong-axis

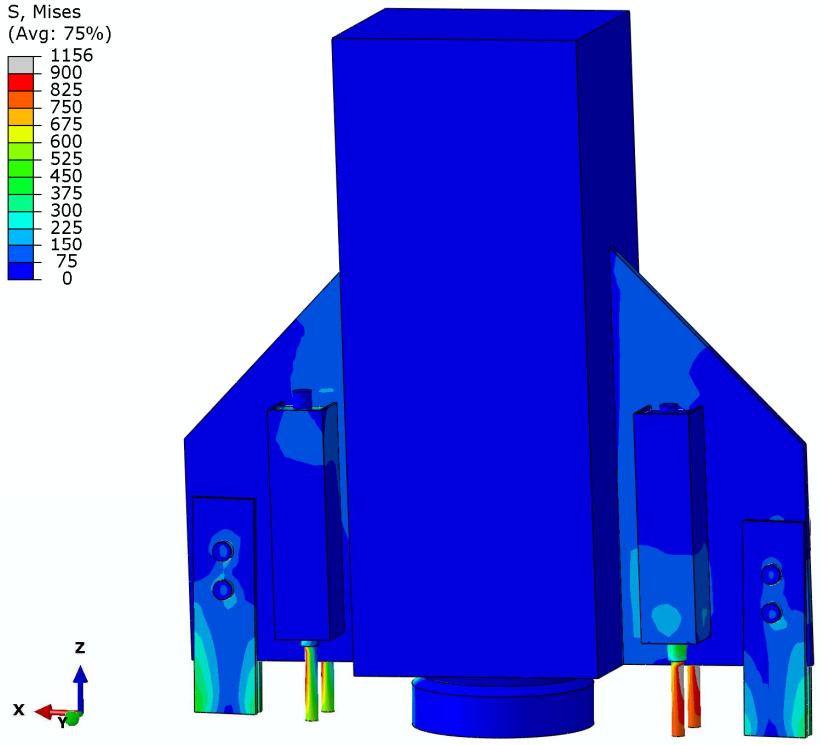

Figure 7.24 Proposed column base connection: stress contours of the proposed connection during analysis with bending along strong-axis at the ultimate rotation θ_u - whole view

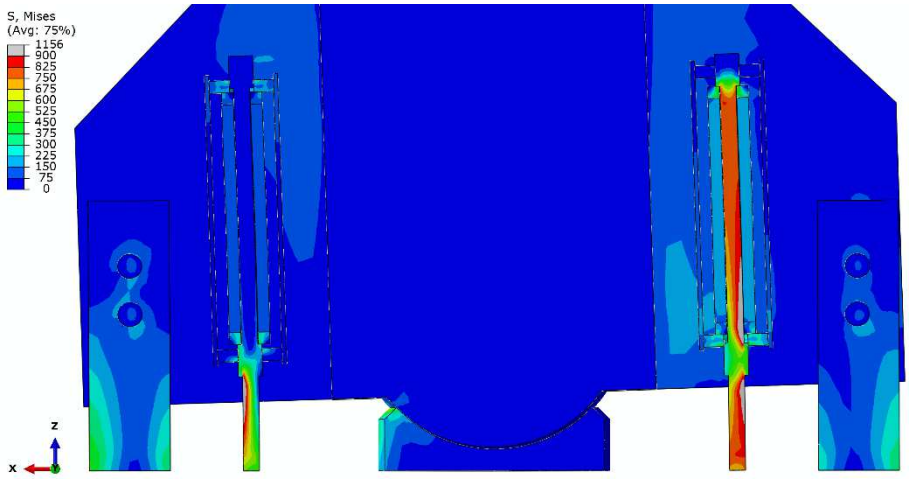

Figure 7.25 Proposed column base connection: stress contours of the proposed connection during analysis with bending along strong-axis at the ultimate rotation θ_u - cut view

deformed shape it can be stated that the self-centring systems are bent by the external blocking plates due to the rotation of the whole connection. However, thanks to the pinned connection of the self-centring systems, the bending of the shanks of the threaded bars, and its possible detrimental effect, is low. Nonetheless, threaded bars are still subjected to considerable bending moment, potentially leading to unexpected plastic deformations. This phenomenon, which could hinder the self-centring capability of the whole connection, must be investigated further. With reference to the spherical bearing, it can be seen that the spherical cap transfers shear and axial load to the concave steel bearing on a limited part of it. This means that there is no full contact between spherical cap and concave steel bearing, the column being affected by rocking behaviour. This is due to the fact that the frictional force on the effective contact surface of the spherical bearing, which is generated by the component of shear and axial load normal to this contact surface (i.e. N_n and V_n in Figure 7.26), is greater than the difference between the components of the axial and shear load parallel to this effective contact surface (i.e. N_p and V_p in Figure 7.26), which should ensure that the connection keeps rotating instead of sticking on this effective contact surface. In this case, having a low axial load, the column tends to show an undesired rocking behaviour. Nevertheless, as already seen in Figure 7.23, this unexpected phenomenon does not noticeably influence the overall mechanical response of the connection.

With regard to the Von Mises stress values, in general no component experiences stress values greater than the yielding strength (assuming that they

are realized with steel grade S355), excepting for the threaded bars, which suffer stress values beyond the yielding strength (i.e. f_{yb} = 900 MPa). For this reason, further analysis should be performed to better understand this phenomenon and develop a possible solution.

Concerning the mechanical response of the connection along weak-axis, in Figure 7.27 can be observed significant difference between numerical and analytical moment-rotation curve. This can be explained by the fact that, due to the out-of-plane rotation of the curved slotted holes plates, the threaded bars are bent (as shown by stress contours plotted in Figure 7.28 and Figure 7.29), providing an undesired contribution to the moment capacity of the whole

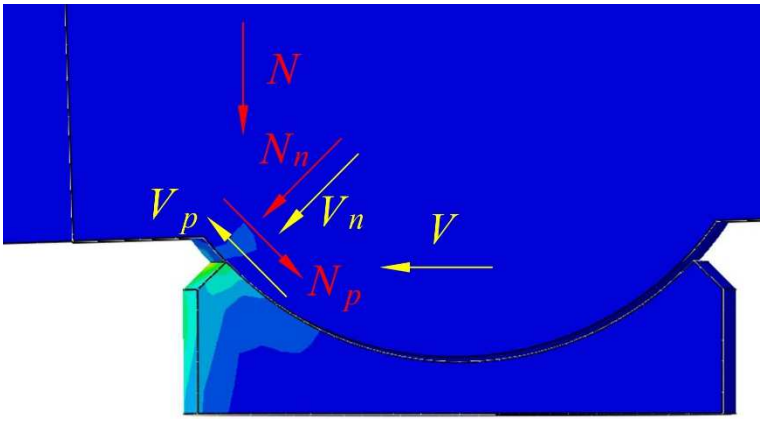

Figure 7.26 Proposed column base connection: forces acting on the spherical bearing

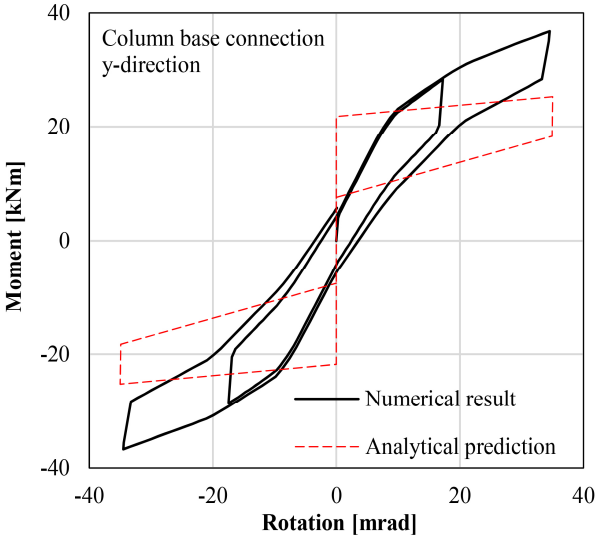

Figure 7.27 Proposed column base connection: moment-rotation curve of the whole connection along weak-axis

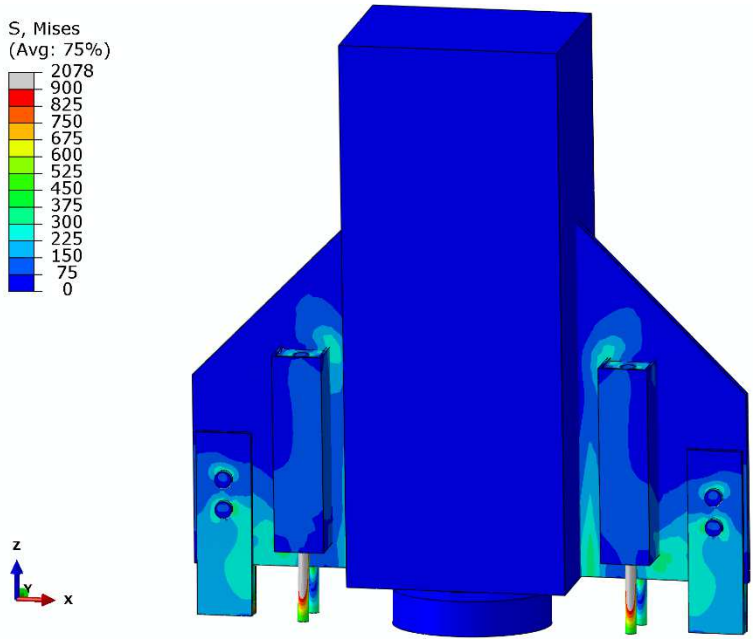

Figure 7.28 Proposed column base connection: stress contours of the proposed connection during analysis with bending along weak-axis at the ultimate rotation θ_u - whole view

connection. Moreover, it can be seen that the steel angles of friction devices are bent also, adding another contribution to the whole moment capacity which was not considered in the design procedure. With reference to the behaviour of the connection during biaxial bending analysis, in Figure 7.30 and Figure 7.31 are represented the moment-rotation curve along strong-axis and the interaction curve between moment along x- and y-direction, respectively. Concerning the former, it can be seen that, by comparing Figure 7.30 and Figure 7.23, the response of the connection is practically the same to that obtained during the uniaxial bending analysis. However, it must be pointed out that the hysteresis loops seem to widen in the elastic branch in which the stack of disc springs is not deflected (i.e. between about -5/5 mrad). This phenomenon does not affect the overall response of the connection, and its self-centring capability. As for the interaction curve, the peak values of the moment capacity along x-direction are coupled with non-null moment values along y-direction. This may be due to a position of the effective contact surface between spherical cap and concave bearing no longer laying on the vertical plane oriented along the x-direction containing the point of application of the displacement history on the column top section. By looking at the negative peak values of the moment capacity in x-direction, the non-null moment values along y-direction are practically the same, meaning that this

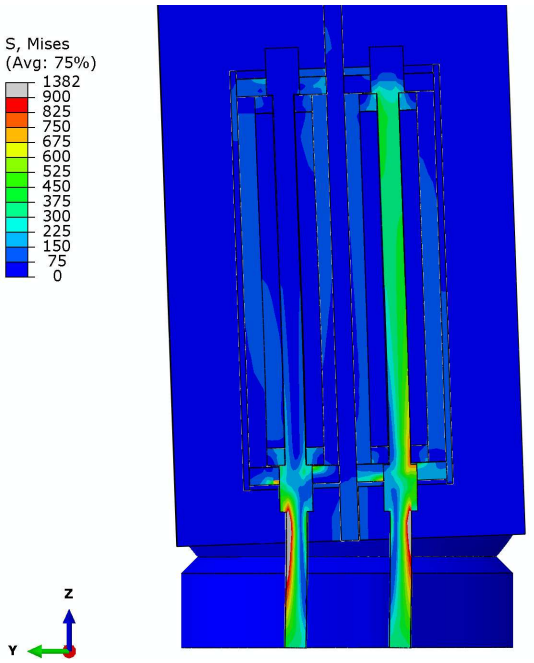

Figure 7.29 Proposed column base connection: stress contours of the proposed connection during analysis with bending along weak-axis at the ultimate rotation θ_u - cut view

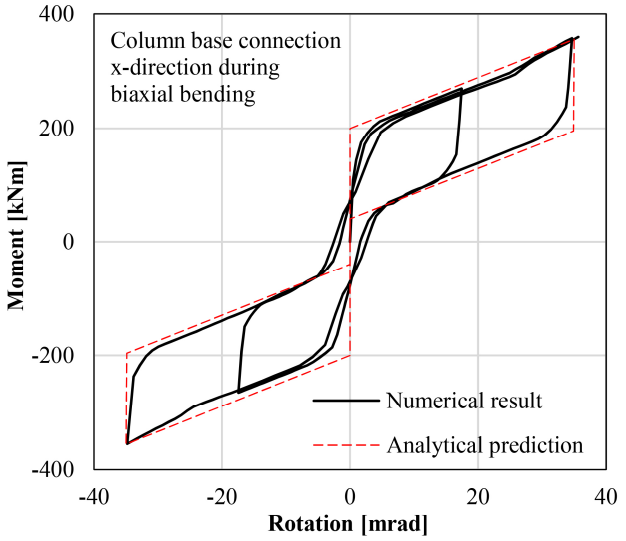

Figure 7.30 Proposed column base connection: moment-rotation curve of the whole connection along strong-axis during biaxial bending

issue does not evolve by increasing the number of cycles.

Lastly, it is interesting to evaluate the construction costs of this solution. As already done in Chapter 6, the construction costs are estimated on the basis

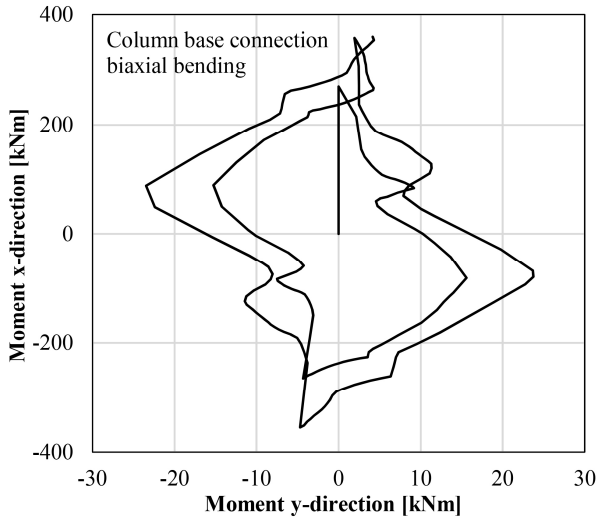

Figure 7.31 Proposed column base connection: interaction curve between moment along x- and y-direction

of the price per kg of steel, as is usually done when using constructional steel. However, in this case there are several components which require particular procedure to be built, such as the spherical bearing and the connection between the threaded bars and the cross-shaped steel plate. Thus, an accurate estimation of their costs is difficult. Nevertheless, to provide a rough estimation of the costs of the overall solution, the construction costs are evaluated by using the weight of these components and the price per kg of steel as well. The cost of structural steelwork, including transport and bolts, can be roughly estimated as 4 € / kg, while the cost of mounting the structural steel elements in the construction site can be evaluated as 2 € / kg. Considering the solution shown in Figure 7.3, it weighs 262 kg, including 20 studs beneath the cross-shaped steel plate. On the basis of the preceding price, the cost of the steel members constituting the proposed connection would be equal to 1575 €. The cost of the disc springs is roughly estimated as 20 € each, thus considering 112 discs the total cost of the disc springs is 2240 €. This cost, which is much higher than that of the steel members, does not take into account the economies generated in the case of ordering a very high number of disc springs. The total cost of the connection is 3815 €, which represents a significant increment of the construction costs with respect to that of the traditional frame. Yet, as already stated in Chapter 6, the construction costs should be evaluated considering the superior performance of the proposed connection provided in the case of seismic event over the whole life-time of the structure.

7.6 Conclusions

In this chapter, a new self-centring friction connection for column base connection of RC structures was proposed. This solution was developed on the basis of the critical review of the column base connections presented in the literature. The main advantage of this proposal is to take into account the contribution provided by the axial force to the whole response of the connection the least possible. To do so, a spherical bearing was introduced, constituted by a spherical cap connected to the column base section and a concave steel bearing connected to the foundation. This bearing withstands both axial and shear forces, and thus the other devices of the connection, namely self-centring systems and friction devices, withstand forces due to bending moment only. The self-centring system is constituted by a stack of disc springs through which is inserted a preloaded threaded bar. This system is designed to undergo compression forces only and, thus, provide self-centring capacity in both directions. The friction device is constituted by vertically-oriented steel angles clamped together by high-strength bolts passing through curved slotted holes. Equations to assess the moment-rotation curves along strong- and weak-axis were proposed. To assess the performance of the proposed connection, several Finite Element Analyses (FEAs) were carried out. First of all, some preliminary FEAs on some critical parts of the connection (e.g. disc spring, self-centring system) were performed to evaluate the capability of the FEM models in accurately reproducing experimental results and/or analytical predictions. Consequently, FEAs on the whole connection were carried out, first by analysing each resisting mechanism (i.e. spherical bearing, friction devices, self-centring systems), and then by considering all of them simultaneously. The results of FEAs for uniaxial bending along strong-axis were in remarkable agreement with the analytical predictions, for all the four cases above. On the other hand, FEA for uniaxial bending along weak-axis gave a numerical result significantly different from that analytically calculated. This was due to the fact that the threaded bars were bent, providing an undesired contribution to the whole moment capacity of the connection. Lastly, FEA was performed imposing biaxial bending to the connection. The results proved the correspondence of the moment-rotation curve in the strong-axis direction with that obtained during uniaxial bending. Moreover, the interaction curve of the moment along x- and y-direction proved the stability of the mechanical response of the connection, despite of the non-null moment values in y-direction at the peak values of moment in x-direction. This phenomenon was due to the different position of the effective

centre of rotation with respect to the loading point on the column top section. On a final note, the mechanics of the proposed connection is promising. However, several aspects need to be further investigated, such as the bending of the threaded bars, and the variation of the position of the centre of rotation. Moreover, a more detailed FEM model must be carried out, to better understand the behaviour of the connection between steel elements and concrete, as well as of the connection between steel elements and foundation.

CHAPTER 8

SEISMIC PERFORMANCE OF RC FRAMES MADE WITH HSTC BEAMS AND FRICTION DEVICES

This chapter focuses on the seismic performance of RC frames realized with HSTCBs and endowed with the friction connections proposed in the previous chapters. The aim is to prove that the use of the proposed connections within a RC frame effectively lead to an earthquake-resilient structure. With reference to the Beam-to-Column Connection (BCC), the second (or the mechanically equivalent third) solution of Friction Damper Device (FDD) described in Chapter 6 will be used. Concerning the Column-to-Foundation Connection (CFC), the solution developed in Chapter 7 will be employed. The cyclic behaviour of HSTCB-column joints is defined on the basis of the procedure described in Chapter 5. Four different types of RC frames are investigated: the first one is the Traditional Frame (TF); the second one is the Innovative Frame with FDDs at the BCCs (IF); the third one is the Innovative Frame + a version of the connection proposed in Chapter 7 endowed with the self-centring systems only, that are constituted by Threaded Bars and disc springs (IF-TB); the fourth one is the Innovative Frame + the proposed connection constituted by preloaded threaded bars, disc springs and Friction Devices (IF-FD).

The seismic response of the RC frames is assessed by means of both pushover analyses and Non-Linear Time History Analyses (NLTHAs). The former are carried out to prove that the use of innovative systems in MRFs is effective in preventing the damaging of RC members for drift values up to the attainment of the ultimate rotation of these systems. NLTHAs are carried out to assess the global and local responses of the different frames subjected to seismic excitation. To highlight the advantage in using the innovative systems, the different amount of damage undergone by the RC members belonging to the four types of frames is calculated by means of the Park and Ang Index (Park and Ang 1985) for beam ends, column bases and joints.

The chapter is organized in two main parts:

- first, RC frames, and seismic input are described. Moreover, the parameters characterizing the cyclic response of FDD and CFCs are calculated and the validation of the numerical models used is carried out;
- then, the results of the seismic response analyses performed for the four types of RC frames are commented.

8.1 RC frames and seismic input

In order to perform a comparison between the seismic response of RC frames endowed or not with friction devices, a generic RC frame having two stories 3 m high and two spans 5 m long is considered. This frame is the 1-y (or the equivalent 4-y) frame of the spatial structure having three bays in y-direction and two in x-direction whose structural model is represented in Figure 8.1. The column longitudinal and transverse reinforcement is that of the subassembly described in Chapter 2, except columns of 2/3-y frames whose cross-sectional dimensions are 400×500 mm. All the columns have the strong-axis oriented along the x-direction, excepting the four external columns of the six ones that belong to 2/3-y frames. The structure is located in Reggio Calabria (Italy), that is a highly seismic area, whose elastic and design spectra are reported in Figure 8.2. The behaviour factor q used is 3.

The dead load of the floor and the live load acting on it in seismic load combination is equal to 14.5 kN/m^2. The one-way slabs are supported by the beams oriented along y-direction. Therefore, top and bottom reinforcement of

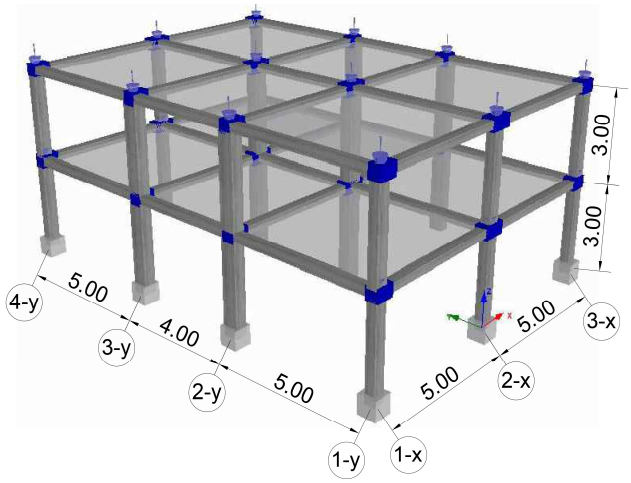

Figure 8.1 Structural model of the RC structure considered

the beams oriented along x-direction are the same and equal to 4ϕ24. Column bases are fixed and Rayleigh damping equal to 5% calculated on the basis of the 1st and 2nd periods of vibration of the structure is used. The tributary area for seismic masses belonging to the analysed RC frame leads to a distributed mass of 3.8 ton/m added on each beam, in addition to the dead load.

Four types of frame are considered: the first one is the Traditional Frame (TF), the second one is the Innovative Frame with FDDs at the BCCs (IF), the third one is the Innovative Frame + preloaded Threaded Bars and disc springs as self-centring system (IF-TB), and the fourth one is the Innovative Frame + the proposed connection constituted by preloaded threaded bars, disc springs and Friction Devices (IF-FD). It has to be underlined that the connection used in the third frame is a version of the column base connection investigated in Chapter 7 without friction damper devices. The reason for studying two different versions of the proposed connection, namely with and without friction devices, lies in the need of better understanding the influence of the different features of friction devices placed at the column base on the seismic response of the RC frame.

The fundamental period of the TF is 0.5 sec, while that of the IFs, due to the lengthened panel zone and, consequently, shortened column, is 0.48 sec.

Seismic input is modelled by 30 artificial accelerograms, generated by using the procedure developed by Vanmarcke and Gasparini (1977) in the recursive form proposed by Cacciola, Colajanni and Muscolino (2004). The modulating function in amplitude is the one proposed by Jennings, Housner and Tsai (1969). Each accelerogram has a duration equal to 30 seconds, with a strong motion phase of 20 seconds. With the aim of assessing the residual drift of the frame, 5 seconds are added at the end of the seismic action in which the structure performs free oscillation. Preliminary analyses showed that, when the frames are subjected to generated accelerograms with amplitude compatible with the code elastic spectrum, limited damage was registered in the structural members. In order to investigate the system response to destructive seismic events, able to produce drift similar to that attained during the experimental test, which is about 2.5%, and thus causing besides the formation of plastic hinges, also extensive cracking of panel zones and reinforcement bond losses, the accelerograms were scaled to 170% of the design intensity. In Figure 8.2 the response spectra and the average one of the 30 accelerograms generated are shown, while in Figure 8.3 one of these acceleration time histories is reported.

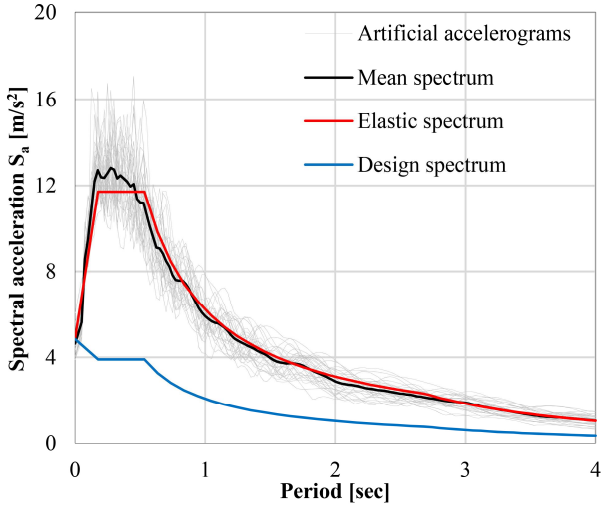

Figure 8.2 Elastic and design spectra (red and blue), response spectra and the average one of the group of artificial accelerograms used (grey and black)

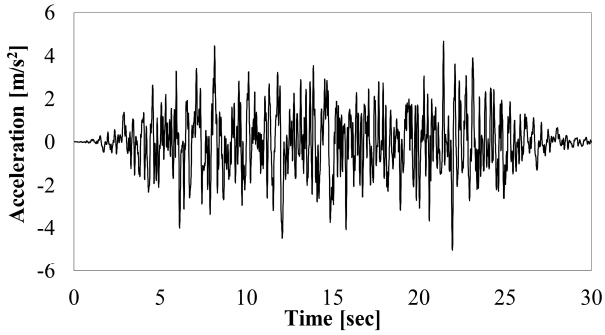

Figure 8.3 Acceleration time history of one of the artificial accelerograms used

8.1.1 Traditional frame (TF)

In TF, the beam-column joint is modelled as described in Chapter 5 and illustrated in Figure 5.5, with two types of non-linear rotational springs, representative of joint shear deformation and bar-slip mechanism, respectively. The parameters of these two rotational springs are reported in Table 8.1 and Table 8.2, respectively.

8.1.2 Innovative frame (IF)

In Figure 8.4 the node modelling scheme in the case of RC frame with friction device is shown. A non-linear rotational spring representative of joint shear deformation is used, while the friction device is represented by means of a bilinear kinematic rotational spring. The parameters of the former are

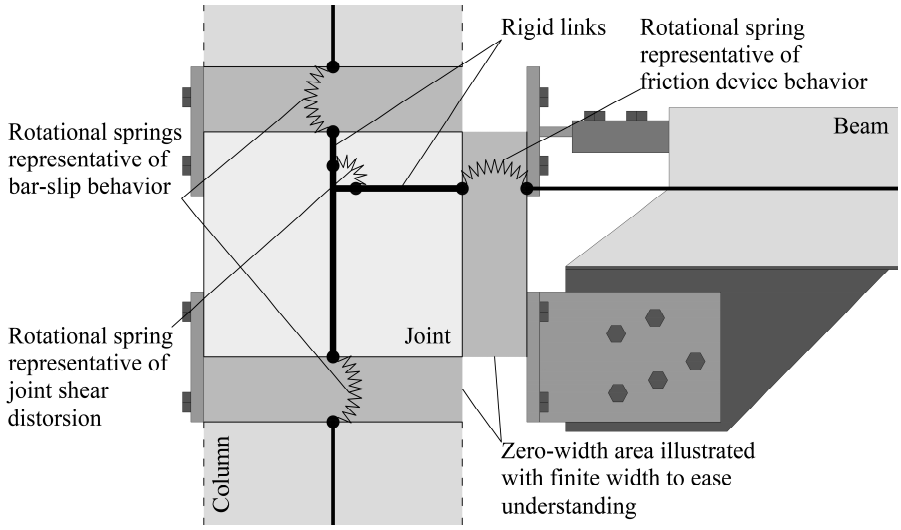

Figure 8.4 Node modelling scheme for RC frame with friction device

Table 8.1 Parameters of the rotational spring element for modelling the cyclic behaviour of the Panel Zone in the Traditional Frame (PZ-TF) and Innovative one (PZ-IF)

		PZ-TF	**PZ-IF**
First-class parameters (backbone curve)	Initial rotational stiffness (kNm/rad)	245000	330000
	Cracking moment (kNm)	49	66
	Yield moment (kNm)	298	406
	Yield rotation (rad)	0.006	0.006
	Ultimate rotation (rad)	0.2	0.2
	Post-yield stiffness ratio as % of elastic	0.001	0.001
Second-class parameters (hysteresis shape)	Stiffness degradation	4	4
	Ductility based strength decay	0.6	0.6
	Hysteretic energy based strength decay	0.6	0.6
	Slip parameter	0.5	0.5

Table 8.2 Parameters of the rotational spring element for modelling the cyclic behaviour of the Bar-Slip mechanism in the Traditional Frame (BS-TF)

		BS-TF
First-class parameters (backbone curve)	Elastic stiffness (kNm/rad)	65000
	Yield moment (kNm)	174/-169
	Rotation at peak moment strength (rad)	0.02/-0.02
	Peak moment strength (kNm)	184/-179
	Residual moment strength (kNm)	1.86/-1.73
Second-class parameters (hysteresis shape)	Pinching factor	0.5
	Deterioration factor	0.6

Table 8.3 Parameters of the bilinear kinematic rotational spring for modelling the cyclic behaviour of the friction device

Initial rotational stiffness (kNm/rad)	10^6
Yield moment (kNm)	110
Post-yield stiffness ratio as % of elastic	10^{-4}

reported in Table 8.1, calculated consistently with the procedure described in Chapter 5, while those of the latter are reported in Table 8.3, defined in order to simulate the behaviour of the friction device, i.e. rigid in the elastic branch and with a very small stiffness in the post-yielding branch. As already discussed in the previous chapters, the rotational springs representative of the bar-slip behaviour at the column-to-joint interface are not modelled.

8.1.3 Innovative Frame with self-centring Friction Device (IF-FD)

For brevity's sake, the design and modelling of IF-FD are now reported, and those related to IF-TB are presented below as particular case of IF-FD.

The column base connection used is the one proposed in Chapter 7. However, to make it suitable for the current application, its geometrical and mechanical properties are modified. The moment capacity of the connection is negligibly influenced by the variation of axial force acting on the column. Therefore, for simplicity's sake, the flexural behaviour along the strong-axis of the self-centring friction connection applied to the column bases of the IF-FD is modelled by a non-linear rotational spring employing the "scb" constitutive law; its parameters were computed referring to Figure 7.5. The rotational spring is applied between two coincident nodes, the first one being the base node of the column, the second one is the node to which is applied the fixed constraint. With regard to the axial and shear behaviour, these are modelled using linear elastic constitutive laws characterized by high values of the elastic modulus, in order to simulate a rigid behaviour.

The yielding moment of the connection M_y^{FD} is kept equal to 200 kNm, corresponding to 75% of the yielding moment of the column. The contribution of each resisting mechanism is reported below:

$$\begin{aligned} M_{sc} &= 0.6\,M_y = 120\,kNm \\ M_f + M_b &= 0.4 M_y = 80 kNm \end{aligned} \tag{8.1}$$

Consistently with the connection already investigated, this connection is endowed with friction devices and self-centring systems along the strong-axis

only. However, to reduce the gap opening during the post-yielding behaviour and, thus, require a lower number of disc springs, the distance between the self-centring system and the column H_{sc} is reduced to 50 mm. So, the preload to be applied to each threaded bar is calculated by rearranging Eq. (7.7):

$$F_{sc} = \frac{0.6\,M_{y,x}}{4\left(\frac{H}{2}+H_{sc}\right)} = \frac{120\times10^{6}}{4\left(200+50\right)} = 120000\,N \tag{8.2}$$

With regard to M_f and M_b, setting $\mu_b = 0.1$, $N = 200$ kN and $H_f = 200$ mm, the force activating the sliding of the device is calculated by using Eq. (7.8):

$$F_f = \frac{0.4M_{y,x} - \mu_b NR\Phi\left(\varphi_0\right)}{2\left(\frac{H}{2}+H_f\right)} = 95270\,N \tag{8.3}$$

This friction force is obtained with 2 bolts M20 class 10.9 for each friction device, having net cross-sectional area A_{res} of 245 mm^2 and ultimate strength f_{ub} of 1000 MPa. Each friction device involves two friction surfaces having a friction coefficient μ_f of 0.4. By means of Eq. (7.9), the ratio between the effective and the maximum preload applied to the bolt is computed as follows:

$$t_s = \frac{F_f}{n_b n_s \mu_f\ 0.7\ f_{ub} A_{res}} = 0.35 \tag{8.4}$$

Lastly, M_f and M_b are equal to 76.22 kNm and 3.78 kNm, respectively.

With the aim of ensuring the elastic behaviour of the threaded bars, a group of disc springs has to be designed and coupled to the bars. In this application the ultimate rotation of the system θ_u is set to 40 mrad, leading to a gap-opening Δ equal to:

$$\Delta = \theta_u\left(\frac{H}{2}+H_{sc}\right) = 10mm \tag{8.5}$$

In order to satisfy the abovementioned strength and displacement requirements, the self-centring system is designed by using the iterative procedure reported in Eqs. (7.11)-(7.17).

Both the same threaded bar and disc spring used in Chapter 7 are selected, the former having diameter equal to 20 mm, the latter having internal diameter equal to 20.75 mm, external diameter 69.85 mm, overall height 8.23 mm and thickness 6.48 mm, with a secant stiffness of about 65.29 kN/mm.

The stack of disc spring coupled to each bar is composed by 20 groups in series of 3 disc springs in parallel, with a whole stiffness K_{stack} of 9.8 kN/mm.

The last step to define the moment-rotation behaviour of the connection is to calculate the stiffness of the branch after the attainment of M_y^{FD}. Firstly, the stiffness of the threaded bar is computed as follows:

$$K_{tb} = \frac{E_{tb} A_{tb}}{l_{tb}} = 81.12\, kN/mm \tag{8.6}$$

Then, the rotational stiffness of the connection considering both the stiffness of the threaded bars and the group of disc springs is expressed as:

$$K_{SCS,r}^{FD} = \frac{1}{\left(\frac{1}{\frac{H}{2} + H_{sc}}\right)^2 \left(\frac{1}{n_{tb} K_{tb}} + \frac{1}{n_{tb} K_{stack}}\right)} = 2193\, kNm/rad \tag{8.7}$$

Lastly, the moment strength at the ultimate rotation is M_u^{FD} = 288 kNm. To prevent the formation of a plastic hinge at the column base up to the ultimate rotation, 2ϕ20 are added to the column in order to increase the moment strength along strong-axis direction.

The parameters characterizing the "scb" constitutive law employed in the rotational spring elements used to model the above-described connection are summed up in Table 8.4.

8.1.4 Innovative Frame with preloaded threaded bars (IF-TB)

The parameters characterizing the connection are the same of the above-mentioned self-centring friction connection, except for the contribution to the moment strength provided by the friction devices, that in this connection is

Table 8.4 Parameters of the rotational spring element for modelling the cyclic behaviour of the self-centring systems used in IF-TB and IF-FD

Self-centring systems	IF-TB	IF-FD
Initial rotational stiffness $K_{\theta 1}$ (kNm/rad)	10^6	10^6
Yield moment (kNm)	120	200
Post-yield stiffness $K_{\theta 2}$ (kNm/rad)	2193	2193
Ratio of forward to reverse yield moment	10^{-4}	0.8

neglected. Therefore, the yielding moment of the connection M_y^{TB} is equal to 120 kNm, given by the preload acting on the threaded bars and the axial force acting on the column. The stiffness of the post-yielding branch is $K_{SCS,r}^{FD}$, and thus the ultimate moment strength of the connection M_u^{TB} is equal to 208 kNm.

8.1.5 Validation of numerical models

To validate the design procedures presented above, a comparison between FEM results or experimental tests versus numerical models of the friction device and the self-centring friction connection is carried out. More precisely, the results of the FEM cyclic analysis of the second solution of BCC presented in Chapter 6 and that of the numerical model employed here are compared and reported in Figure 8.5a. Regarding the self-centring friction CFC, the results of the FEM cyclic analysis of the solution proposed in Chapter 7, shown in Figure 7.23 are compared with that of the numerical model used in here, and plotted in Figure 8.5. Both the comparisons confirm the reliability of the adopted design procedures.

8.2 Analysis of results

The performance of the four types of frames are assessed by means of pushover analyses and NLTHAs.

Pushover analyses calculate the yielding and ultimate rotations of plastic hinges by means of the equations reported in EN 1998 (2004). Generally speaking, the group of frames endowed with innovative devices provides capacity curves with stiffer elastic branches, if compared to that of the traditional frame, because of the shorter columns due to the lengthened panel zones (Figure 8.6). Moreover, the innovative frames show a lower maximum base shear due to the lower design moment strength of the friction devices, chosen in order to ensure the capacity design criterion. This means that innovative frames are designed assuming a higher behaviour factor *q* than that of the traditional frame. It can be noticed also a different behaviour of the curve once the yielding of the CFC is achieved. In fact, IF-TB and IF-FD show a hardening behaviour in the post-yielding branch of the capacity curve, ensured by the stiffness of the post-yielding branch of the CFC employed, able to overcome the P-Δ second-order effect. On the contrary IF shows a softening behaviour due to the degrading strength of the plastic hinge at the column base and the Elastic-Perfectly Plastic (EPP) behaviour of the BCC. As regards TF,

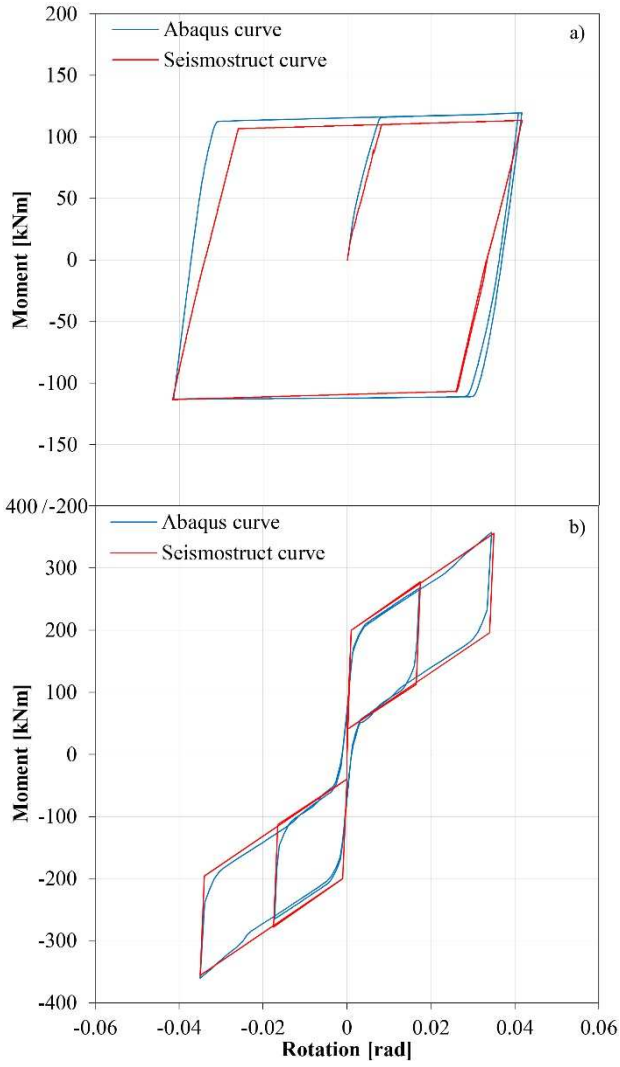

Figure 8.5 Abaqus result of the second solution proposed in Chapter 6 and Seismostruct result of the friction device for BCC (a), Abaqus result of the solution proposed in Chapter 7 and Seismostruct result of the self-centring friction device for CFC (b)

the hardening behaviour of the HSTCB plastic hinge compensate the P-Δ second-order effect, exhibiting an EPP base shear-roof displacement capacity curve. None of the RC members belonging to IF-TB and IF-FD undergoes plastic hinge formation for a global drift higher than 5% (top displacement = 0.30 m). Above this drift value, consistently with design provisions, the ultimate rotation of the friction devices is achieved.

Concerning NLTHAs, several parameters were inspected with the aim of understanding the local and global behaviour of the above-described

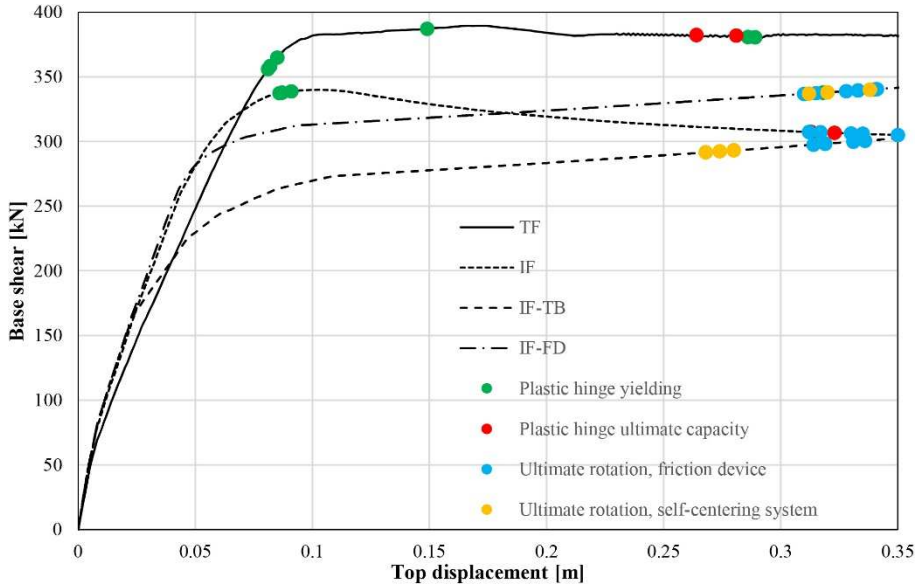

Figure 8.6 Capacity curves of the four types of frames investigated

structures. The structural parameters investigated are the following: mean and CoV of Maximum Interstorey Drift Ratios (MIDRs) and Residual Interstorey Drift Ratios (RIDRs); moment-rotation curves of beam end sections, column-base sections, link elements representing panel zone, bar-slip mechanism, friction device and self-centring systems. Moreover, the Park and Ang damage Index (PAI) (Park and Ang 1985) is evaluated for the main elements experiencing cyclic actions.

In Table 8.5 average and CoV of MIDRs and RIDRs of the four types of RC frames analysed are reported. As can be seen, similar average values of MIDRs are provided by TF and IF, with a slight decrement of the values in the case of frames endowed with friction devices. However, the average RIDRs obtained with the IF are between three- and four-fold higher than those provided by the TF, with almost half of the analyses providing RIDR values higher than the permissible residual drift considered, i.e. 0.5 %, the latter value proposed by McCormick et al. (2008).

By looking at the results of the IF-TB, it can be noticed that the adoption of a self-centring system with a much lower yield moment leads to an increase of the average MIDR, due to a stiffness loss at the CFC. Nevertheless, the RIDR average values are considerably lower if compared to those of the IF, proving the efficiency of the self-centring system. On the other hand, the comparison with the results of the TF highlights a behaviour which is not ideal, with a reduction of the RIDR average value at the first floor, and an

Table 8.5 Average and CoV of maximum interstorey drift ratios of the four types of RC frames

Story		Maximum IDR				Residual IDR			
		TF	**IF**	**IF-TB**	**IF-FD**	**TF**	**IF**	**IF-TB**	**IF-FD**
1	Avg	2.72%	2.56%	3.17%	2.57%	0.17%	0.47%	0.10%	0.09%
	CoV	13.3%	18.1%	12.6%	13.9%	78.0%	79.7%	86.6%	70.9%
2	Avg	2.91%	2.84%	3.10%	2.65%	0.14%	0.59%	0.24%	0.19%
	CoV	11.2%	16.6%	17.0%	17.9%	78.7%	78.2%	79.6%	77.0%

increment of that at the second floor. Indeed, 3 analyses give RIDR values of the second floor beyond the permissible threshold. Among the four configuration of frames investigated, the most satisfactory results are provided by the IF-FD. As a matter of fact, IF-FD gives practically the lowest mean MIDRs and similar mean RIDRs to those of the TF, and only one of the RIDR values is greater than the permissible value of 0.5 %. These results highlight that the combined use of innovative systems both at the BCC and CFC, with yielding strength lower than the strength of the connected members, is able to limit MIDR and RIDR. It must be stressed that the main goal of the adoption of friction devices and self-centring systems is not to mandatorily reduce MIDR and RIDR, compared to those obtained with traditional frames, but to mitigate damage in structures.

In order to stress the achievement of this goal, the different sources of energy dissipation for the four RC frame configurations are highlighted by comparison of the hysteresis cycles of dissipative elements for one of the accelerograms. For the sake of brevity, only the moment-rotation curves of the following elements are reported:

- Right end of the first-story second-span beam (Figure 8.7a for TF, Figure 8.7b for IF);
- Link element representing the beam-column joint shear distortion of the first-story internal joint (Figure 8.7c for TF, Figure 8.7d for IF);
- Link element connected to the right end of the aforementioned beam representing the bar-slip mechanism (in case of TF) (Figure 8.7e);
- Link element connected to the right end of the aforementioned beam representing the friction device (in case of IF) (Figure 8.7f);
- Link element connected to the base of the central column representing: the preloaded threaded bars and disc springs (in case of IF-TB) (Figure 8.8a); the self-centring friction connection

proposed in Chapter 7 (in case of IF-FD) (Figure 8.8b);

- Base of the first-story central column (Figure 8.8c for TF, Figure 8.8d for IF, Figure 8.8e for IF-TB, Figure 8.8f for IF-FD).

The moment-rotation curves are selected considering the same time-history analysis for all the frames. The investigated beam end of the TF

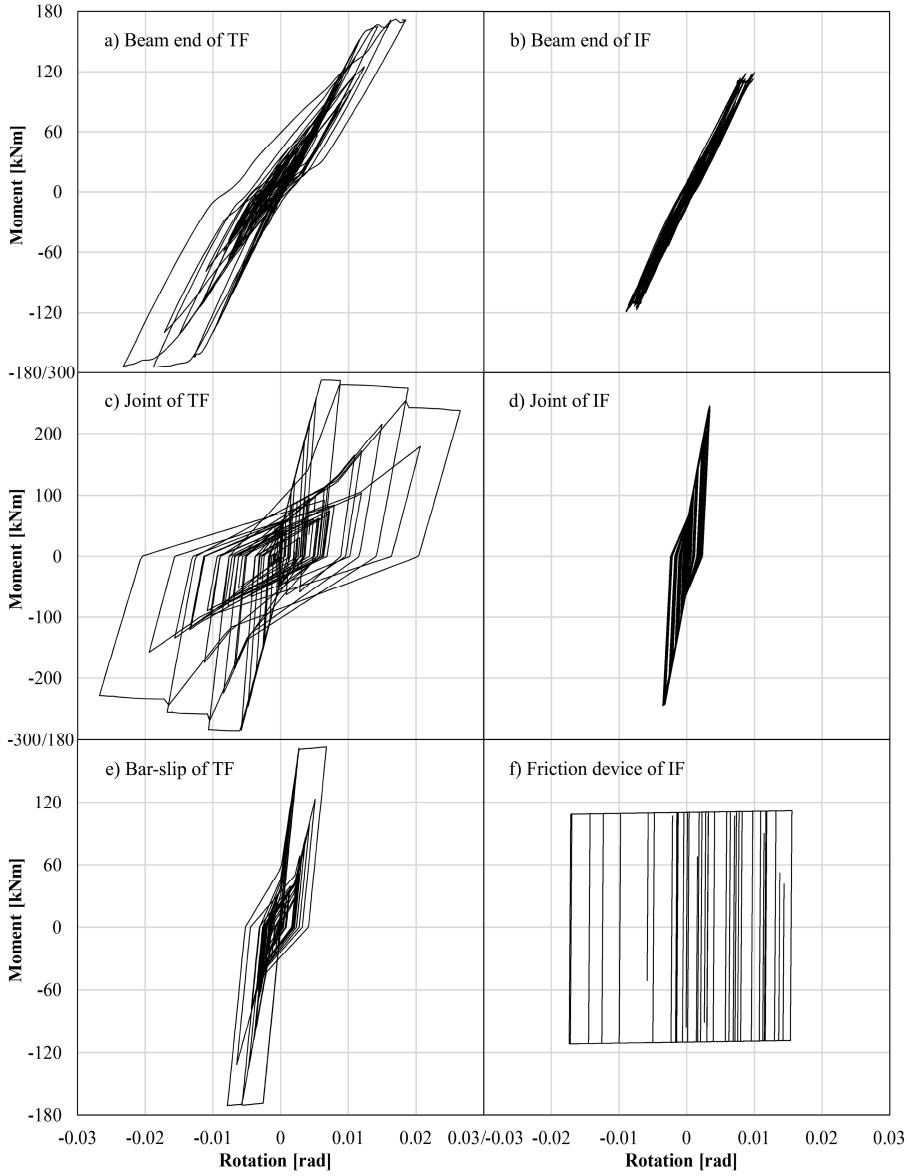

Figure 8.7 Moment rotation curve of: beam end section of TF (a), IF (b); beam-column joint shear deformation of TF (c), IF (d); bar-slip mechanism of TF (e); friction device of IF (f)

(Figure 8.7a) underwent slight plastic deformations due to the yielding of the bottom longitudinal bars. By contrast, consistently with design provisions, the investigated beam end of the IF (Figure 8.7b) showed an elastic moment-rotation curve.

Regarding the link elements representing the cyclic behaviour of the beam-column joint investigated, it can be seen that the panel zone of the TF (Figure 8.7c) experienced loss of strength and stiffness, achieving a significant level of damage. By contrast, the panel zone of the innovative frame (Figure 8.7d) did not reach the yield moment; thus no degrading phenomena affecting the strength and stiffness were registered. As a result, the damage undergone by the panel zone was negligible, being limited to crack formation.

In the TF, the link element representing the bar-slip phenomenon (Figure 8.7e) showed the first appearance of a degrading cyclic behaviour, contributing to the global level of damage experienced by the beam-column joint of the TF.

With respect to the link element representing the friction device (Figure 8.7f), it can be noticed that the seismic energy previously absorbed by the panel zone and the plastic hinges of beams is dissipated, in the IF, by the friction devices. The hysteretic cycles of the FDD are wide and stable, having assumed that the cyclic performance of the device is not dependent on the cumulative displacement experienced.

A comparison between Figure 8.8a and Figure 8.8b highlights that the connection with preloaded threaded bars and disc springs used in IF-TB undergoes lower maximum moment and larger rotation, if compared to those experienced by the self-centring friction connection used in IF-FD. Thus, a reduced overstrength factor could be used in the design of the column base.

However, the lower yield moment leads to a weaker frame and, as already seen in Table 8.5, higher average MIDR values. Moreover, the system constituted by threaded bars and disc springs only is not ideally able to dissipate energy, differently from the self-centring friction connection which dissipates a considerable amount of energy thanks to its flag-shaped moment-rotation curve.

As for the moment-rotation curves of the column bases illustrated in Figure 8.8c-f, it can be stated that the use of the FDD at the BCC alone in the IF does not prevent formation of a plastic hinge. By contrast, the column bases behave elastically when threaded bars and disc springs or self-centring friction connections are used in the IF-TB and IF-FD, respectively.

To shed light on the different level of damaging of the RC members in the

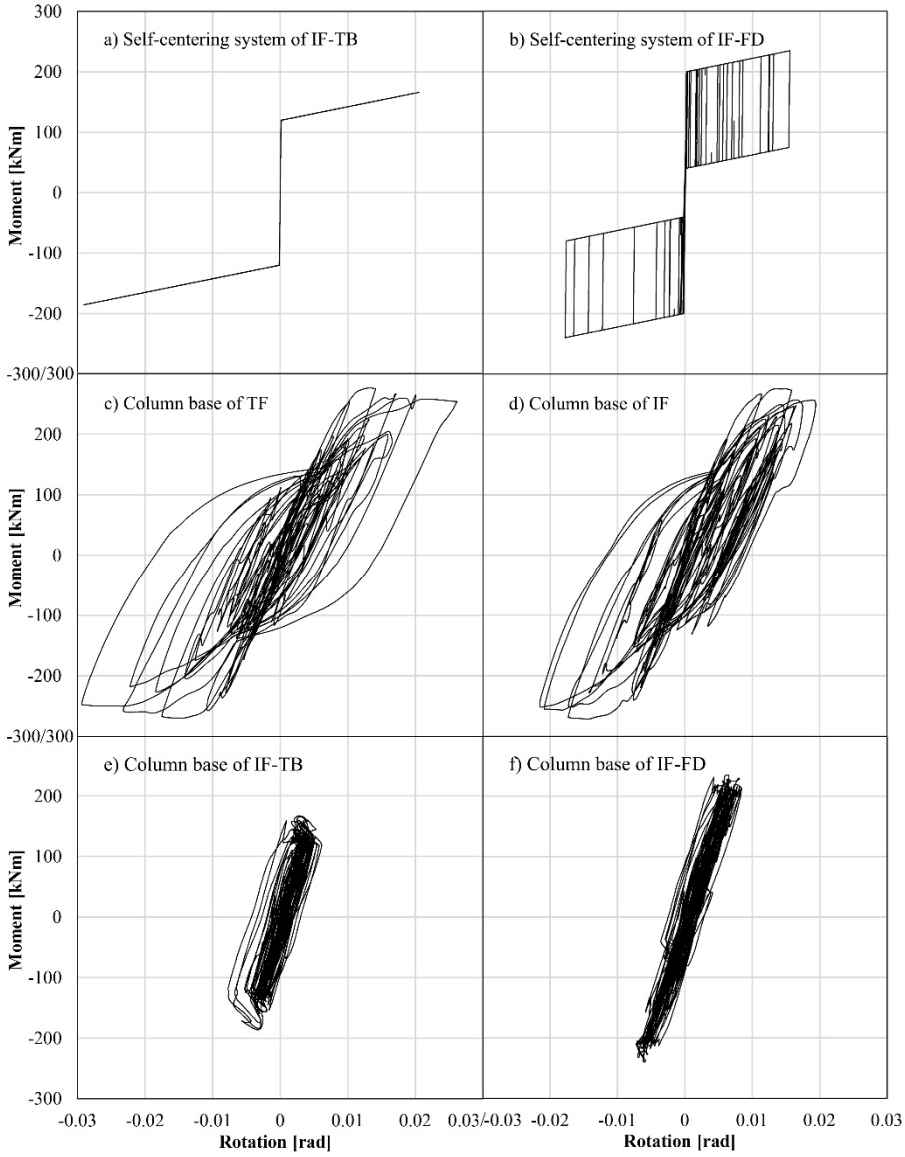

Figure 8.8 Moment-rotation curve of: the connection with preloaded threaded bars + disc springs of IF-TB (a); the self-centring friction connection of IF-FD (b); the column base in case of: TF (c); IF (d); IF-TB (e); IF-FD (f)

four types of frames investigated, the Park and Ang damage Index (PAI) (Park and Ang, 1985) in the modified version proposed by Kunnath et al. (1992) is calculated for all the elements included in the above list, considering also left end of the first-story first-span beam. PAI is given by the sum of two terms, synthetically representing the kinematic and hysteretic behaviour showed by an RC member during a time-history analysis, respectively. The improved

version of PAI is given as:

$$PAI = \theta + E = \frac{\theta_{\max} - \theta_y}{\theta_u - \theta_y} + \frac{\beta}{M_y \theta_u} \int dE \tag{8.8}$$

in which θ_{max} is the maximum rotation experienced by the RC member, θ_y is the yielding rotation, θ_u is the ultimate rotation, M_y is the yielding moment, $\int dE$ is the dissipated energy, and β is the model parameter, set equal to 0.15 for beams and columns as proposed by Cosenza et al. (1993), and 0.25 for joint panels as suggested by Altoontash (2004). θ_y and θ_u of beams and columns are obtained by using the equations proposed by EN 1998 (2004). Concerning joint panels, θ_y is obtained via MCFT, while θ_u is selected as suggested by De Risi, Ricci and Verderame (2017). In Table 8.6 are reported θ_y, θ_u, M_y, average and CoV values of kinematic and hysteretic terms θ and E, and PAIs for the elements of the list above, considering the group of 30 analyses. Generally speaking, the results prove that the use of innovative systems are effective in limiting or preventing the damaging of RC members. More precisely, with regard to beams, small average PAI values for TF confirm that slight damage occurs at beam ends, mainly due to hysteretic behaviour. By contrast, average kinematic and hysteretic terms equal to 0 for beam ends belonging to innovative frames mean that these RC members experience no plastic rotation and do not dissipate energy in any analysis. Concerning column bases, large average and small CoV PAI values for TF mean that the bulk of central columns are near to the failure condition. Conversely, in the case of IF, even if damage indexes of the columns are reduced by about 20% compared to those of the TF, their values are well beyond the limit of repairability, assumed equal to 0.4 (Park and Ang 1985). The efficiency to use specific devices at the CFC is confirmed by the average PAI values of the column of IF-TB and IF-FD, which are about 0.1 in both cases. Moreover, their reliability is proven by the small CoV PAI values. Kinematic and hysteretic terms of panel joints demonstrate the effectiveness of FDDs in the mitigation of structural damage. With regard to TF, average PAI value near to 1 and low scatter imply that the investigated panel joint is near collapse in all the analyses, and it achieves failure condition in almost half of them. By contrast, none of the panel joints in innovative frames reaches the yield moment, leading to kinematic terms equal to 0, while hysteretic terms are drastically reduced if compared to that of TF. Lastly, a relatively small average PAI value characterizes the bar-slip mechanism. However, since the

Table 8.6 Average and CoV values of Park and Ang damage Index (PAI), kinematic (θ) and hysteretic (E) terms for the left- and right-end of the first-story beams, column base, first-story internal joint, bar-slip mechanism of first-story beam

Parameters				θ	E	PAI
Left end of the first-story first-span beam	θ_y = 0.021 rad θ_u = 0.08 rad M_y^- = 169 kNm	TF	Avg	0.012	0.084	0.095
			CoV	182.98%	19.75%	36.07%
		IF/ IF-TB/ IF-FD	Avg	0	0	0
			CoV	-	-	-
Right end of the first-story second span beam	θ_y = 0.021 rad θ_u = 0.08 rad M_y^+ = 174 kNm	TF	Avg	0.018	0.083	0.101
			CoV	218.39%	17.69%	50.75%
		IF/ IF-TB/ IF-FD	Avg	0	0	0
			CoV	-	-	-
Base section of the central column	θ_y = 0.013 rad θ_u = 0.056 rad M_y = 278 kNm (for TF, IF, IF-TB) M_y = 326 kNm (for IF-FD)	TF	Avg	0.370	0.502	0.872
			CoV	26.72%	8.35%	13.42%
		IF	Avg	0.287	0.413	0.701
			CoV	38.59%	10.43%	19.50%
		IF-TB	Avg	0	0.118	0.118
			CoV	-	8.36%	8.36%
		IF-FD	Avg	0	0.080	0.080
			CoV	-	6.96%	6.96%
First-story internal joint	θ_y = 0.006 rad θ_u = 0.065 rad M_y = 298 kNm (for TF) M_y = 406 kNm (for IF, IF-TB, IF-FD)	TF	Avg	0.331	0.651	0.982
			CoV	25.41%	7.21%	10.63%
		IF	Avg	0	0.179	0.179
			CoV	-	6.56%	6.56%
		IF-TB	Avg	0	0.178	0.178
			CoV	-	7.03%	7.03%
		IF-FD	Avg	0	0.184	0.184
			CoV	-	7.48%	7.48%
Bar-slip mechanism	θ_y = 0.002 rad θ_u = 0.022 rad M_y = 169 kNm	TF	Avg	0.222	0.119	0.342
			CoV	63.07%	76.25%	65.67%

CoV value is large, a small number of analyses are characterized by a bar-slip mechanism with PAI value above the limit of repairability.

8.3 Conclusions

A comparison among the seismic response of RC frames realized with HSTCBs endowed or not with Friction Damper Devices FDDs was carried out. Besides the Traditional Frame (TF), three different configurations of the Innovative Frame (IF) were investigated, characterized by: FDDs at the Beam-to-Column Connections (BCCs) alone (IF), FDDs and Column-to-Foundation Connections (CFC) endowed with preloaded Threaded Bars coupled with disc springs (IF-TB) or self-centring Friction Devices (IF-FD). The model for joint shear distortion and slippage of the longitudinal bars within the panel zone was validated by experimental test on beam-column subassemblies realized by means of HSTCBs.

The seismic response of RC frames was assessed by means of both pushover analyses and Non-Linear Time History Analyses (NLTHAs), monitoring maximum and residual story drift ratios, element hysteretic responses and damage indexes.

Analysis of TF seismic response proves that panel zone and first story column base section are the elements prone to the greatest damage which, even if adequately designed, in the presence of high intensity earthquakes easily exceed the repairability threshold, up to the failure condition.

Conversely, the IF provides structural performance consistent with design forecasts, i.e. beam end sections with a nearly-elastic behaviour and panel zones which experience negligible level of damage. Nevertheless, the column bases of the IF still experience significant damage. Moreover, the average RIDR obtained with the IF is much higher than that provided by the TF, with almost half of the analyses providing RIDR values higher than the permissible residual drift assumed to consider the structure functional, i.e. 0.5%. The use of self-centring systems in the IF-TB and IF-FD is able to remedy the aforementioned drawbacks, leading to columns bases behaving elastically and an average RIDR similar with that given by the TF. However, a higher average MIDR is provided by the IF-TB, due to the limited dissipative capacity of the system constituted by column base connection made of preloaded threaded bars and disc springs only. By contrast, the IF-FD provides complete prevention of any damage and interruption of use, ensuring an average MIDR comparable to that of the TF, and smaller RIDR.

CHAPTER 9

CONCLUDING REMARKS AND RECOMMENDATIONS

9.1 Comparison between aims and results

The main goal of the thesis was to propose a comprehensive solution to build earthquake-resilient RC frames realized with HSTC beams. This solution involved the development of innovative friction damper devices for both BCC and CFC, with the aim of achieving the following properties:

- elastic behaviour up to the yielding moment, which corresponds to the moment value for which friction device(s) start(s) to slide;
- capacity to attain the design ultimate rotation experiencing negligible damage;
- limiting the damage experienced by the connection to specific structural elements, designed to be replaceable;
- avoiding the damaging of the surrounding RC members;
- cyclic response characterized by wide and stable hysteresis loops;

To this aims, initially, the review of the state of art on HSTCBs design procedure revealed that the shear capacity evaluation and the mechanical performance of HSTCB-column joints are still topics deserving further research efforts.

To reduce this lack of knowledge, a design-oriented model for shear strength evaluation of HSTCBs was proposed. The accuracy of this model, based on the truss mechanism with variable inclination of the concrete strut, was proved against a database of experimental tests on both HSTCBs and ordinary RC beams having two orders of transverse reinforcement.

Secondly, it was satisfactorily defined an approach for the application, in FE software packages, of an already-existing macro model developed to simulate the cyclic behaviour of RC beam-column joints, extending it to the case of HSTC beams.

Then, three different innovative connections for the BCC were proposed.

In detail, the first one is characterized by a pin connection and a friction device with vertical and horizontal slotted holes; the second one is characterized by a T stub connection and a friction device endowed with curved slotted holes; the third one, besides the friction device and the T stub connection above-mentioned, is characterized by a vertical central plate passing throughout the beam height.

With regard to the CFC, a solution characterized by friction devices and preloaded threaded bars coupled with disc springs was developed. The solution is endowed with a spherical bearing capable of making the contribution of the axial force to the whole response of the connection negligible.

It can be stated that the third solution developed for the BCC, as well as the solution proposed for the CFC, were able to fully satisfy the performance requirements listed above.

As regards the capability of the proposed connections in ensuring low-damage RC frames, this was successfully confirmed by comparing the results of the seismic performance of traditional and innovative frames realized with HSTC beams.

The above-mentioned achievements must be considered within the framework of the limitations listed in Section 9.2.

9.2 Limitations of the results

The results reported in this thesis have to be interpreted in the light of several limitations, which are listed below:

- with reference to the connections proposed, the main limitation is represented by the fact that their effectiveness was assessed by means of numerical analyses only. Moreover, they were validated by using a geometrical and mechanical configuration only;
- the role of the slab in modifying flexural and rotational capacity of the connection was not considered;
- the suitability of the self-centring connection for column base sections was limited to the steel elements only and did not involve the connections to both the foundation and the column;
- the FEM analyses were carried out by using values of the friction coefficient not based on experimental test results;
- the possible thermal effect influencing the mechanical response of the connections was not taken into account;

- the effectiveness of the proposed innovative connections in providing an earthquake-resilient RC frame was demonstrated focusing on a geometrical configuration of frame only.
- with regard to the shear capacity model, its accuracy was validated against a limited database that covers a small amount of possible geometrical and mechanical configurations;
- concerning the approach to reproduce the cyclic response of beam-column joints, this was proved effective considering only one geometrical and mechanical configuration.

9.3 Recommendations for future research

Starting from the above limitations, the following recommendations for future research are suggested:

- carrying out tests on friction shims to obtain real friction coefficient values to be used in the design of the proposed connections;
- the influence of the slab in modifying flexural and rotational capacity of the connection has to be numerically and experimentally investigated;
- carrying out tests on full-scale specimens of subassemblies including beam and column, in the case of BCC, or column and foundation, in the case of CFC;
- the use of the proposed bidirectional connections should be investigated both numerically and experimentally;
- the reliability of the proposed connections has to be proved considering a wide range of geometrical and mechanical characteristics;
- the capacity of the proposed connections in providing damage-proof RC frames has to be assessed considering different geometrical configurations, as well as different construction sites. Moreover, the behaviour of 3D RC structures should be evaluated as well;
- the effect of the variability of the moment capacity of BCC and CFC, caused by the uncertainties on both the friction coefficient and the preload acting on the bolts, on the seismic performance of the innovative RC frames should be investigated.

REFERENCES

Aiello, M.A. 2008. Analisi sperimentale della connessione acciaio-calcestruzzo nelle travi reticolari miste (Experimental Analysis of Steel-Concrete Connection in Hybrid Truss Beams). Proceedings of the 7th Italian Workshop on Composite Structures, Benevento, Italy, 23–24 October 2008; pp. 33–42.

Altoontash A. 2004. Simulation and damage models for performance assessment of reinforced concrete beam-column joints. PhD dissertation, Stanford University, CA.

Amadio, C., L. Macorini, and G. Suraci. 2008. Structural performance of a new hybrid RC-encased steel joint system. In Advances in Reinforced Concrete and Precast Constructions; Di Prisco, M., Ed.; Strarrylink: Milan, Italy, pp. 19–29.

Amadio, C. L. Macorini, S. Sorgon, and G. Suraci. 2011. A novel hybrid system with RC-encased steel joists. *European Journal of Environmental and Civil Engineering* 15:1433–1463. doi: 10.1080/19648189.2011.9723353.

Badalamenti, V. 2010. Analisi teorico-sperimentale del comportamento ciclico delle connessioni tra travi prefabbricate reticolari miste e pilastri in cemento armato. (Theoretical and Experimental Analysis of the Cyclic Behaviour of Hybrid Steel Trussed Concrete Beam-to-Column Connections). Ph.D. Thesis, Dipartimento di Ingegneria Strutturale, Aerospaziale e Geotecnica, Università degli Studi di Palermo, Palermo, Italy, 2010.

Badalamenti, V., L. La Mendola, and P. Colajanni. 2010. Seismic behaviour of hybrid steel trussed concrete beams. *Proceedings of the 14th European Conference Earthquake Engineering*, Ohrid, Republic of Macedonia, 30 August–3 September 2010; pp. 1–8.

Bagavathiperumal, P., K. Chandrasekaran, and S. Manivasagam. 1991. Elastic load-displacement predictions for coned disc springs subjected to axial loading using the finite element method. *The Journal of Strain Analysis for Engineering Design* 26 (3):147-152. doi: 10.1243/03093247V263147.

Bagheri, H., A. Hashemi, S. M. M. Yousef-Beik, P. Zarnani, and P. Quenneville. 2020. New self-centring tension-only brace using resilient slip-friction joint: experimental tests and numerical analysis. *Journal of Structural Engineering ASCE* 146 (10):04020219. doi: 10.1061/(ASCE)ST.1943-541X.0002789.

Ballarini, R., L. La Mendola, J. Le, and A. Monaco. 2017. Computational study of failure of hybrid steel trussed concrete beams. *Journal of Structural Engineering ASCE* 143 (8):04017060. doi: 10.1061/(ASCE)ST.1943-541X.0001792.

Ballarini, R., L. La Mendola, J. Le, and A. Monaco. 2020. Computational assessment of the structural performance of concrete beams with encased steel joist. *Proceedings of the 6th European Conference on Computational Mechanics: Solids, Structures and Coupled Problems (ECCM 6)*, Glasgow (UK), 11-15 June 2018, Edited by: Roger Owen, René de Borst, Jason Reese and Chris Pearce, 1187-1198, ISBN: 978-84-947311-6-7.

Belleri, A., A. Marini, P. Riva, and R. Nascimbene. 2017. Dissipating and re-centring devices for portal-frame precast structures. *Engineering Structures* 150:736-45. doi: 10.1016/j.engstruct.2017.07.072.

Borzouie, J., G. A. MacRae, J. G. Chase, G. W. Rodgers, and G. C. Clifton. 2015. Experimental studies on cyclic performance of column base weak axis aligned asymmetric friction connection. *Journal of Constructional Steel Research* 112 (Sep):252-62. doi: 10.1016/j.jcsr.2015.05.007.

Borzouie, J., G. A. MacRae, J. G. Chase, G. W. Rodgers, and G. C. Clifton. 2016. Experimental studies on cyclic performance of column base strong axis-aligned asymmetric friction connections. *Journal of Structural Engineering ASCE* 142 (1):04015078-1-10. doi: 10.1061/(ASCE)ST.1943-541X.0001327.

Cacciola, P., P. Colajanni, and G. Muscolino. 2004. Combination of modal responses consistent with seismic input representation, *Journal of Structural Engineering ASCE* 130 (1):47–55. doi: 10.1061/(ASCE)0733-9445(2004)130:1(47).

Campione, G., P. Colajanni, and A. Monaco. 2016. Analytical evaluation of steel–concrete composite trussed beam shear capacity. *Materials and Structures* 49 (8):3159-3176. doi: 10.1617/s11527-015-0711-6.

Cancelliere, N., P. Colajanni, and L. La Mendola. 2012. On bottom steel plate to concrete anchorage in hybrid steel trussed concrete beams. Proceedings of the STESSA 2012—Behaviour of Steel Structures in Seismic Areas, Santiago, Chile, 9–11 January 2012; CRC Press/Balkema Publishers—Taylor & Francis Group: London, UK, 2011; pp. 243–248, ISBN 9780415621052.

CEB-FIB. 2010, fib Model Code 2010. Comité Euro-International du Béton.

Chanchi Golondrino, J. C., G. A. MacRae, J. G. Chase, G. W. Rodgers, and G. C. Clifton. 2019. Asymmetric Friction Connection (AFC) Design for Seismic Energy Dissipation. *Journal of Constructional Steel Research* 157:70-81. doi: 10.1016/j.jcsr.2019.02.027.

Chisari, C., and C. Amadio. 2014. An experimental, numerical and analytical study of hybrid RC-encased steel joist beams subjected to shear. *Engineering Structures* 61 (1):84-98. doi: 10.1016/j.engstruct.2013.12.035.

Colajanni, P., L. La Mendola, and A. Recupero. 2013. Experimental test results vs. analytical prediction of welded joint strength in Hybrid Steel Trussed Concrete Beams (HSTCBs). *European Journal of Civil and Environmental Engineering* 17, 742-759. doi: 10.1080/19648189.2013.815135.

Colajanni, P., L. La Mendola, and A. Monaco. 2014a. Stress transfer mechanisms investigation in hybrid steel trussed-concrete beams by push-out tests. *Journal of Constructional Steel Research* 95:56-70. doi: 10.1016/j.jcsr.2013.11.025.

Colajanni, P., L. La Mendola, G. Mancini, A. Recupero, and N. Spinella. 2014b. Shear capacity in concrete beams reinforced by stirrups with two different inclinations. *Engineering Structures* 81:444-453. doi: 10.1016/j.engstruct.2014.10.011.

Colajanni, P., L. La Mendola, and A. Monaco. 2015a. Stiffness and strength of composite truss beam to RC column connection in MRFs. *Journal of Constructional Steel Research* 113:86-100. doi: 10.1016/j.jcsr.2015.06.003.

Colajanni, P., L. La Mendola, M. Latour, A. Monaco, and G. Rizzano. 2015b. FEM analysis of push-out test response of Hybrid Steel Trussed Concrete Beams (HSTCBs). *Journal of Constructional Steel Research* 111:88-102. doi: 10.1016/j.jcsr.2015.04.011.

Colajanni, P., L. La Mendola, A. Monaco, and A. Recupero. 2016a. Validation of shear model for RC and hybrid beams with two different inclinations of transversal reinforcement. *Applied Mechanics and Materials* 847:505-512. doi: 10.4028/www.scientific.net/AMM.847.505.

Colajanni, P., L. La Mendola, A. Monaco, and N. Spinella. 2016b. Cyclic behaviour of composite truss beam-to-RC column joints in MRFs. *Key Engineering Materials* 711:681-9. doi: 10.4028/www.scientific.net/KEM.711.681.

Colajanni, P., L. La Mendola, M. Latour, A. Monaco, and G. Rizzano. 2017a. Analytical prediction of the shear connection capacity in composite steel-concrete trussed beams. *Materials and Structures* 50 (1) art. no. 48. doi: 10.1617/s11527-016-0931-4.

Colajanni, P., L. La Mendola, A. Recupero, and N. Spinella. 2017b. Stress field model for strengthening of shear-flexure critical RC beams. *Journal of Composites for Construction ASCE* 21 (5). doi: 10.1061/(ASCE)CC.1943-5614.0000821.

Colajanni, P., L. La Mendola, and A. Monaco. 2017c. Experimental Investigation on the Shear Response of Precast Steel-Concrete Trussed Beams. *Journal of Structural Engineering ASCE* 143, 04016156. doi: 10.1061/(ASCE)ST.1943-541X.0001642.

Colajanni, P., L. La Mendola, and A. Monaco. 2018a. Review of push-out and shear response of hybrid steel-trussed concrete beams. *Buildings* 8 (10): art. n. 134. doi: 10.3390/buildings8100134.

Colajanni, P., L. La Mendola, and A. Monaco. 2018b. Stress transfer and failure mechanisms in steel-concrete trussed beams: experimental investigation on slab-thick and full-thick beams. *Construction and Building Materials* 161 (1):267-81. doi: 10.1016/j.conbuildmat.2017.11.134.

Colajanni, P., L. La Mendola, and A. Monaco. 2019. Shear models of RC-encased steel joist beams in MRFs. *Ingegneria Sismica* 36 (2):14-30.

Cosenza, E., G. Manfredi, and R. Ramasco. 1993. The use of damage functionals in earthquake engineering: a comparison between different methods. *Earthquake Engineering and Structural Dynamics* 22 (10):855-68. doi: 10.1002/eqe.4290221003.

D'Aniello, M., D. Cassiano, and R. Landolfo. 2017. Simplified criteria for finite element modelling of European preloadable bolts. *Steel and Composite Structures* 24 (6):643-658. doi: 10.12989/scs.2017.24.6.643.

D'Antimo, M., M. Latour, G. Ferrante Cavallaro, J. P. Jaspart, S. Ramhormozian, and J. F. Demonceau. 2020. Short- and long-term loss of preloading in slotted bolted connections. *Journal of Constructional Steel Research* 167: 105956. doi: 10.1016/j.jcsr.2020.105956.

De Risi, M. T., P. Ricci, and G. M. Verderame. 2017. Modelling exterior unreinforced beam-column joints in seismic analysis of non-ductile RC frames. *Earthquake Engineering and Structural Dynamics* 46:899-923. doi: 10.1002/eqe.2835.

Elettore, E., F. Freddi, M. Latour, G. Rizzano. 2019. Design and analysis of a steel seismic resilient frame equipped with self-centring column bases with friction devices. In 2019 Conference of the Society for Earthquake and Civil Engineering Dynamics, London, UK.

Eligehausen, R., E. P. Popov, and V. V. Bertero. 1983. Local bond stress-slip relationships of deformed bars under generalized excitations. UCB/EERC-83/23, College of Engineering, University of California, Berkeley, CA.

EN 1992. 2005. Design of concrete structures – Part 1-1: General rules and rules for buildings. CEN.

EN 1993:1-8. 2005. Design of steel structures – Part 1-8: design of joints. CEN

EN 1998. 2004. Design of structures for earthquake resistance – Part 1-1: general rules, seismic actions and rules for buildings. CEN.

EN 16984. 2016. Disc spring – Calculation. CEN.

Fan, X. W., L. H. Xu, X. S. Xie, Y. S. Sun, and Z. X. Li. 2019. Hysteresis analysis of pre-pressed spring self-centring energy dissipation braces using different models. *Advances in Structural Engineering* 22 (12):2662-71. doi: 10.1177/1369433219849844.

Ferrante Cavallaro, G., A. Francavilla, M. Latour, V. Piluso, and G. Rizzano. 2017. Experimental behaviour of innovative thermal spray coating materials for FREEDAM joints. *Composites Part B: Engineering* 115:289-99. doi: 10.1016/j.compositesb.2016.09.075.

Ferrante Cavallaro, G., M. Latour, A. B. Francavilla, V. Piluso, and G. Rizzano. 2018. Standardised friction damper bolt assemblies time-related relaxation and installed tension variability. *Journal of Constructional Steel Research* 141:145-55. doi: 10.1016/j.jcsr.2017.10.029.

Freddi, F., C. A. Dimopoulos, and T. L. Karavasilis. 2017. Rocking damage-free steel column base with friction devices: design procedure and numerical evaluation. *Earthquake Engineering and Structural Dynamics* 46:2281-300. doi: 10.1002/eqe.2904.

Freddi, F., C. A. Dimopoulos, and T. L. Karavasilis. 2020. Experimental evaluation of a rocking damage-free steel column base with friction devices. *Journal of Structural Engineering ASCE* 146 (10):04020217. doi: 10.1061/(ASCE)ST.1943-541X.0002779.

Froli, M., L. Giresini, and F. Laccone. 2019. Dynamics of a new seismic isolation device based on tribological smooth rocking (TROCKSISD). *Engineering Structures* 193:154-169. doi: 10.1016/j.engstruct.2019.05.014.

Grigorian, C. E., and E. P. Popov. 1994. Energy dissipation with slotted bolted connections. UCB/EERC-94/02, College of Engineering, University of California, Berkeley, USA.

Hashemi, A., P. Zarnani, R. Masoudnia, and P. Quenneville. 2017. Seismic resistant rocking coupled walls with innovative Resilient Slip Friction (RSF) joints. *Journal of Constructional Steel Research* 129:215-26. doi: 10.1016/j.jcsr.2016.11.016.

Hashemi, A., P. Zarnani, F. M. Darani, A. Valadbeigi, G. C. Clifton, and P. Quenneville. 2018. Damage avoidance self-centring steel moment resisting frames (MRFs) using innovative resilient slip friction joints (RSFJs). *Key Engineering Materials* 763:726-34. doi: 10.4028/www.scientific.net/KEM.763.726.

Hashemi, A., S. M. M. Yousef-Beik, M. Darani, G. C. Clifton, P. Zarnani, and P. Quenneville. 2019. Seismic performance of a damage avoidance self-centring brace with collapse prevention mechanism. *Journal of Constructional Steel Research* 155:273-85. doi: 10.1016/j.jcsr.2018.12.019.

Heistermann, C., M. Veljkovic, R. Simões, C. Rebelo, and L. Simões da Silva. 2013. Design of slip resistant lap joints with long open slotted holes. *Journal of Constructional Steel Research* 82: 223-233. doi: 10.1016/j.jcsr.2012.11.012.

Hosaka, T., K. Mitsuki, H. Hiragi, Y. Ushijima, Y. Tachibana, and H. Watanabe. 2000. An experimental study on shear characteristics of perfobond strip and its rational strength equations. *Journal of Structural Engineering JSCE* 46A:1593-1604..

Jennings, P. C., G. W. Housner, and C. Tsai. 1969. Simulated earthquake motions for design purpose. In *4th World Conference on Earthquake Engineering,* A (1):145–160, Santiago, CL.

Ju, Y. K., J. Y. Kim, and S. D. Kim. 2007. Experimental evaluation of new concrete encased steel composite beam to steel column joint. *Journal of Structural Engineering ASCE* 133 (4):519–529. doi: 10.1061/(ASCE)0733-9445(2007)133:4(519).

Khoo, H. H., C. Clifton, J. Butterworth, G. MacRae, and G. Ferguson. 2012a. Influence of steel shim hardness on the Sliding Hinge Joint performance. *Journal of Constructional Steel Research* 72:119-29. doi: 10.1016/j.jcsr.2011.11.009.

Khoo, H. H., C. Clifton, J. Butterworth, G. MacRae, S. Gledhill, and G. Sidwell. 2012b. Development of the self-centring sliding hinge joint with friction ring springs. *Journal of Constructional Steel Research* 78:201-11. doi: 10.1016/j.jcsr.2012.07.006.

Khoo, H. H., C. Clifton, J. Butterworth, and G. MacRae. 2013. Experimental study of full-scale self-centring sliding hinge joint connections with friction ring springs. *Journal of Earthquake Engineering* 17:972-97. doi: 10.1080/13632469.2013.787378.

Khoo, H. H., C. Clifton, G. MacRae, H. Zhou, and S. Ramhormozian. 2015. Proposed design models for the asymmetric friction connection. *Earthquake Engineering and Structural Dynamics* 44:1309-24. doi: 10.1002/eqe.2520.

Koetaka, Y., P. Chusilp, Z. Zhang, M. Ando, K. Suita, K. Inoue, and N. Uno. 2005. Mechanical property of beam-to-column moment connection with hysteretic dampers for column weak axis. *Engineering Structures* 27:109-117. doi: 10.1016/j.engstruct.2004.09.002.

Kuramoto, H., and I. Nishiyama. 2004. Seismic performance and stress transferring mechanism of through column-type joints for composite reinforced concrete and steel frames. *Journal of Structural Engineering ASCE*, 130 (2):352–360. doi: 10.1061/(ASCE)0733-9445(2004)130:2(352).

Kunnath, S. K., A. M. Reinhorn, and J. F. Abel. 1992. IDARC V3.0: a program for the inelastic damage analysis of RC structures. NCEER 92–0022: National Center for Earthquake Engineering Research, State University of New York at Buffalo, Buffalo, USA.

Larkin, A. S., D. H. Sanders, and M. S. Saiidi. 2012a. Unbounded prestressed columns for earthquake resistance. *Center for Civil Engineering Earthquake Research*, Department of Civil and Environmental Engineering, University of Nevada, Reno, Nevada, Report No. CCEER-12-02.

Larkin, A. S., D. H. Sanders, and M. S. Saiidi. 2012b. Unbounded prestressed columns for earthquake resistance. In *15th World Conference on Earthquake Engineering*, Lisboa, PT.

Latour, M., V. Piluso, and G. Rizzano. 2014. Experimental analysis on friction materials for supplemental damping devices. *Construction and Building Materials* 65:159-76. doi: 10.1016/j.conbuildmat.2014.04.092.

Latour, M., and G. Rizzano. 2015. Design of X-shaped double split tee joints accounting for moment-shear interaction. *Journal of Constructional Steel Research* 104:115-126. doi: 10.1016/j.jcsr.2014.10.015.

Latour, M., V. Piluso, and G. Rizzano. 2015. Free from damage beam-to-column joints testing and design of DST connections with friction pads. *Engineering Structures* 85:219-33. doi: 10.1016/j.engstruct.2014.12.019.

Latour, M., V. Piluso, and G. Rizzano. 2018a. Experimental analysis of beam-to-column joints equipped with sprayed aluminium friction dampers. *Journal of Constructional Steel Research* 146:33-48. doi: 10.1016/j.jcsr.2018.03.014.

Latour, M., M. D'Aniello, M. Zimbru, G. Rizzano, V. Piluso, and R. Landolfo. 2018b. Removable friction dampers for low-damage steel beam-to-column joint. *Soil Dynamics and Earthquake Engineering* 115:66-81. doi: 10.1016/j.soildyn.2018.08.002.

Latour, M., G. Rizzano, A. Santiago, and L. S. da Silva. 2019. Experimental response of a low-yielding, self-centring, rocking column base joint with friction dampers. *Soil Dynamics and Earthquake Engineering* 116:580-92. doi: 10.1016/j.soildyn.2018.10.011.

Li, X., Y. C. Kurama, and G. Wu. 2020. Experimental and numerical study of precast posttensioned walls with yielding-based and friction-based energy dissipation. *Engineering Structures* 212:110391. doi: 10.1016/j.engstruct.2020.110391.

Lowes, L. N., and A. Altoontash. 2003. Modeling reinforced-concrete beam-column joints subjected to cyclic loading. *Journal of Structural Engineering ASCE* 129 (12):1686-97. doi: 10.1061/(ASCE)0733-9445(2003)129:12(1686).

Lubliner, J., J. Oliver, S. Oller, and E. Oñate. 1989. A plastic-damage model for concrete. *International Journal of Solids and Structures* 25 (3): 299–326.

MacRae, G. A., C. R. Urmson, W. R. Walpole, P. Moss, K. Hyde, and C. Clifton. 2009. Axial shortening of steel columns in buildings subjected to earthquakes. *Bulletin of the New Zealand Society of Earthquake Engineering* 42 (4):275-287. doi: 10.5459/bnzsee.42.4.275-287.

McCormick, J., H. Aburano, M. Ikenaga, and M. Nakashima. 2008. Permissible residual deformation levels for building structures considering both safety and human elements. In *14th World Conference on Earthquake Engineering*, Beijing, CN.

Mitra, N., and L. N. Lowes. 2007. Evaluation, calibration and verification of a reinforced concrete beam-column joint model. *Journal of Structural Engineering* ASCE 133 (1):105-120. doi: 10.1061/(ASCE)0733-9445(2007)133:1(105)").

Moehle, J. P. 2014. Seismic design of reinforced concrete buildings. *McGraw-Hill Professional*, New York, USA.

Mohammadyan-Yasouj, S.E., A. K. Marsono, R. Abdullah, and M. Moghadasi. 2015. Wide beam shear behaviour with diverse types of reinforcement. *ACI Structural Journal* 112 (2):199-208. doi: 10.14359/51687299.

Monaco, A. 2014. Experimental analysis, numerical and analytical modelling of shear strength mechanisms in Hybrid Steel Trussed Concrete Beams. Ph.D. Thesis, Department of Civil, Environmental, Aerospace and Material Engineering, University of Palermo, Palermo, Italy, 2014.

Monaco, A. 2016. Numerical Prediction of the Shear Response of Semi-Prefabricated Steel-Concrete Trussed Beams. *Construction and Building Materials* 124:462-74. doi: 10.1016/j.conbuildmat.2016.07.126.

Monti, G. and F. Petrone. 2015. Shear resisting mechanisms and capacity equations for composite truss beams. *Journal of Structural Engineering ASCE* 141, 04015052. doi: 10.1061/(ASCE)ST.1943-541X.0001266.

Morgen, B. G., and Y. C. Kurama. 2004. A friction damper for post-tensioned precast concrete moment frames. *PCI Journal* 49 (4):112-33. doi: 10.15554/pcij.07012004.112.133.

Morgen, B. G., and Y. C. Kurama. 2007. Seismic design of friction-damped precast concrete frame structures. *Journal of Structural Engineering ASCE* 133 (11):1501-11. doi: 10.1061/(ASCE)0733-9445(2007)133:11(1501)

Morgen, B. G., and Y. C. Kurama. 2008. Seismic response evaluation of posttensioned precast concrete frames with friction dampers. *Journal of Structural Engineering ASCE* 134 (1):132-45. doi: 10.1061/(ASCE)0733-9445(2008)134:1(132).

Nielsen, M.P., and L. C. Hoang. 2011. Limit Analysis and Concrete Plasticity, 3rd edition. CRC Press. doi: 10.1201/b10432.

NTC 2018. Italian Construction Building Code (in Italian).

Oh, S. H., Y. J. Kim, and H. S. Ryu. 2009. Seismic performance of steel structures with slit dampers. *Engineering Structures* 31:1997-2008. doi: 10.1016/j.engstruct.2009.03.003.

Pampanin, S., A. Amaris, U. Akguzel, and A. Palermo. 2006. Experimental Investigations on High-Performance Jointed Ductile Connections for Precast Frames. *Proceedings of the First European Conference on Earthquake Engineering and Seismology* Geneva, Switzerland.

Pampanin, S. 2015. Towards the "Ultimate Earthquake-Proof" Building: Development of an Integrated Low-Damage System. In: Ansal A. (eds) *Perspectives on European Earthquake Engineering and Seismology. Geotechnical, Geological and Earthquake Engineering*, 39. Springer, Cham. doi: 10.1007/978-3-319-16964-4_13.

Pan, Z., S. Guner, and F. J. Vecchio. 2017. Modeling of interior beam-column joints for nonlinear analysis of reinforced concrete frames. *Engineering Structures* 142:182-91. doi: 10.1016/j.engstruct.2017.03.066.

Park, Y., and A. H. Ang. 1985. Mechanistic seismic damage model for reinforced concrete. *Journal of Structural Engineering ASCE* 111 (3):722-39. doi: 10.1061/(ASCE)0733-9445(1985)111:4(722).

Prager, W. 1959. An introduction to plasticity, Reading, MA, Addison-Wesley.

Priestley, M. J. N., S. Sritharan, J. R. Conley, and S. Pampanin. 1999. Preliminary Results and Conclusions From the PRESSS Five Storey Precast Concrete Test Building. *PCI Journal* 44 (6):42-67.

Puhali, R., and I. Smotlack. 1980. Relazione sulle prove di push-out atte a determinare le leggi di carico-scorrimento delle travi in sistema composto tipo"REP" (Report on the Push-Out Tests Fit for the Determination of Load-Slip Laws of REP Composite Truss Beams). Science of Constructions Institute Acts, University of Trieste: Triest, Italy.

Ramhormozian, S., G. C. Clifton, G. A. MacRae, and G. P. Davet. 2017. Stiffness-based approach for Belleville springs use in friction sliding structural connections. *Journal of Constructional Steel Research* 138:340-356. doi: 10.1016/j.jcsr.2017.07.009.

Ramhormozian, S., G. C. Clifton, G. A. MacRae, and H. H. Khoo. 2018. The sliding hinge joint: final steps towards an optimum low damage seismic-resistant steel system. *Key Engineering Materials* 763:751-60. doi: 10.4028/www.scientific.net/KEM.763.751.

Ramhormozian, S., C. G. Clifton, G. A. MacRae, G. P. Davet, and H. H. Khoo. 2019. Experimental studies on Belleville springs use in the sliding hinge joint connection. *Journal of Constructional Steel Research* 159:81-94. doi: 10.1016/j.jcsr.2019.03.031.

Recupero, A., A. D'Aveni, and A. Ghersi. 2003. N–M–V interaction domains for box and I-shaped reinforced concrete members. *ACI Structural Journal* 100 (1):113-119. doi: 10.14359/12445.

Recupero, A., A. D'Aveni A, and A. Ghersi. 2005. Bending moment-shear force interaction domains for prestressed concrete beams. *Journal of Structural Engineering ASCE* 131 (9):1413-1421. doi: 10.1061/(ASCE)0733-9445(2005)131:9(1413).

Richart, F.E. 1927. An investigation of web stresses in reinforced concrete beams. *Bulletin No. 166*, Engineering Experiment Station, University of Illinois, Urbana.

Saenz, L. P. 1964. Discussion of "Equation for the stress-strain curve of concrete," by Desayi and Krishnan. *ACI Structural Journal* 61 (9):1229-1235.

Sassone, M., and M. A. Chiorino. 2005. Design Aids for the Evaluation of Creep Induced Structural Effects; Shrinkage and Creep of Concrete; Gardner & Weiss: New York, NY, USA; pp. 239–259.

SeismoSoft. SeismoStruct – a computer program for static and dynamic nonlinear analysis of frames structures, 2020. Available at http://www.seismosoft.com

Shen, Y., C. Christopoulos, N. Mansour, and R. Tremblay. 2011. Seismic design and performance of steel moment-resisting frames with nonlinear replaceable links. *Journal of Structural Engineering ASCE* 137 (10): 1107-1117. doi: 10.1061/(ASCE)ST.1943-541X.0000359.

Sivaselvan, M. V., and A. M. Reinhorn. 1999. Hysteretic models for cyclic behaviour of deteriorating inelastic structures. MCEER-99-0018, Multidisciplinary Center for Earthquake Engineering Research, State University of New York at Buffalo, Buffalo, USA.

Sivaselvan, M. V., and A. M. Reinhorn. 2000. Hysteretic models for deteriorating inelastic structures. *Journal of Engineering Mechanics ASCE* 126 (6):633-40. doi: 10.1061/(ASCE)0733-9399(2000)126:6(633).

Song, L. L., T. Guo, and C. Chen. 2014. Experimental and numerical study of a self-centring prestressed concrete moment resisting frame connection with bolted web friction devices. *Earthquake Engineering and Structural Dynamics* 43 (4):529-45. doi: 10.1002/eqe.2358.

Stevens, N. J., S. M. Uzumeri, and M. P. Collins. 1991. Reinforced-concrete subjected to reversed-cyclic shear – Experiments and constitutive model. *ACI Structural Journal* 88 (2):135-46.

Takagi, J., and A. Wada. 2019. Recent earthquakes and the need for a new philosophy for earthquake-resistant design. *Soil Dynamics and Earthquake Engineering* 119:499-507. doi: 10.1016/j.soildyn.2017.11.024.

Tesser, L. and S. Scotta. 2013. Flexural and shear capacity of composite steel truss and concrete beams with inferior precast concrete base. *Engineering Structures* 49, 135–145. doi: 10.1016/j.engstruct.2012.11.004.

Tsampras, G., R. Sause, D. Zhang, R. B. Fleischman, J. I. Restrepo, D. Mar, and J. Maffei. 2016. Development of deformable connection for earthquake-resistant buildings to reduce floor accelerations and force responses. *Earthquake Engineering and Structural Dynamics* 45 (9):1473-94. doi: 10.1002/eqe.2718.

Tsampras, G., R. Sause, R. B. Fleischman, and J. I. Restrepo. 2018. Experimental study of deformable connection consisting of friction device and rubber bearings to connect floor system to lateral force resisting system. *Earthquake Engineering and Structural Dynamics* 47 (4):1032-53. doi: 10.1002/eqe.3004.

Tullini, N. and F. Minghini. 2013. Nonlinear analysis of composite beams with concrete-encased steel truss. *Journal of Constructional Steel Research* 91, 1–13. doi: 10.1016/j.jcsr.2013.08.011.

Vanmarcke, E. H., and D. A. Gasparini. 1977. Simulated earthquake ground motions. In *4th international conference on Smirt*, K1/9, San Francisco, USA.

Vecchio, F. J., and M. P. Collins. 1986. The modified-compression field theory for reinforced-concrete elements subjected to shear. *ACI Structural Journal* 83 (2):219-31.

Vincenzi, L., and M. Savoia. 2010. Stabilità di tralicci PREM in prima fase (Stability of PREM-beams in the first phase). *Proceedings of the 18th C.T.E. Congress*, Brescia, Italy, 11–13 November 2010; pp. 849–858. (In Italian).

Xu, L. H., X. W. Fan, and Z. X. Li. 2017. Cyclic behaviour and failure mechanism of self-centring energy dissipation braces with pre-pressed combination disc springs. *Earthquake Engineering and Structural Dynamics* 46:1065-80. doi: 10.1002/eqe.2844.

Yang, T. S., and E. P. Popov. 1995. Experimental and analytical studies of steel connections and energy dissipators. UCB/EERC-95/13, College of Engineering, University of California, Berkeley, USA.

Yousef-Beik, S. M. M., S. Veismoradi, P. Zarnani, A. Hashemi, and P. Quenneville. 2021. Experimental study on cyclic performance of a damage-free brace with self-centring connection. *Journal of Structural Engineering ASCE* 147 (1):0002869. doi: 10.1061/(ASCE)ST.1943-541X.0002869.

Yun, X., and L. Gardner. 2017. Stress-strain curves for hot-rolled steels. *Journal of Constructional Steel Research* 133:36-46. 10.1016/j.jcsr.2017.01.024.

Zhang, Z., R. B. Fleischman, J. I. Restrepo, G. Guerrini, A. Nema, D. Zhang, U. Shakya, G. Tsampras, and R. Sause. 2018. Shake-table test performance of an inertial force-limiting floor anchorage system. *Earthquake Engineering and Structural Dynamics* 47 (10):1987-2011. doi: 10.1002/eqe.3047.

Zheng, S., Y. Liu, T. Yoda, and W. Lin. 2016. Parametric study on shear capacity of circular-hole and long-hole perforbond shear connector. *Journal of Constructional Steel Research* 117:64-80. doi: 10.1016/j.jcsr.2015.09.012.